



HAL
open science

Searching for Dark Matter and New Physics in the Neutrino sector with Cryogenic detectors

Julien Billard

► **To cite this version:**

Julien Billard. Searching for Dark Matter and New Physics in the Neutrino sector with Cryogenic detectors. Cosmology and Extra-Galactic Astrophysics [astro-ph.CO]. Université Claude Bernard Lyon 1, 2021. tel-03259707

HAL Id: tel-03259707

<https://theses.hal.science/tel-03259707v1>

Submitted on 14 Jun 2021

HAL is a multi-disciplinary open access archive for the deposit and dissemination of scientific research documents, whether they are published or not. The documents may come from teaching and research institutions in France or abroad, or from public or private research centers.

L'archive ouverte pluridisciplinaire **HAL**, est destinée au dépôt et à la diffusion de documents scientifiques de niveau recherche, publiés ou non, émanant des établissements d'enseignement et de recherche français ou étrangers, des laboratoires publics ou privés.

Searching for Dark Matter and New Physics in the Neutrino sector with Cryogenic detectors

Diplome d'Habilitation à Diriger des Recherches

Julien BILLARD
Université Lyon 1

Soutenu le 19 Janvier 2021, devant le jury composé de:

Corinne Augier – Présidente
Andrea Giuliani – Rapporteur
Jacob Lamblin – Rapporteur
David Lhuillier – Rapporteur
Christine Marquet – Examinatrice
Frédéric Mayet – Examineur
Alessandro Monfardini – Examineur

Institut de Physique des 2 Infinis de Lyon

Contents

1	Direct detection of Dark Matter	5
1.1	The dark matter puzzle	5
1.1.1	Evidence	5
1.1.2	Candidates	6
1.2	WIMP direct detection	9
1.2.1	Direct Detection principle	10
1.2.2	Experimental techniques and state of the art	13
1.2.3	The neutrino background	17
1.3	Searching for low-mass dark matter with EDELWEISS	21
2	A light Dark Matter search from the IP2I above ground cryogenic facility	25
2.1	Introduction	25
2.2	EDELWEISS-Surf	26
2.2.1	Detector	26
2.2.2	Experimental setup	26
2.3	Dark Matter search	27
2.3.1	Data processing	27
2.3.2	Detector calibration and stability	31
2.3.3	Data analysis	32
2.4	Results	37
2.4.1	Weakly Interacting Spin-independent Dark Matter	37
2.4.2	Strongly Interacting Dark Matter	38
2.4.3	Migdal Search	39
2.4.4	Spin-dependent Interactions	41
2.5	Conclusion and outlook	42
2.5.1	On the direct detection of light dark matter	42
2.5.2	On the future RICOCHET experiment at ILL	43
3	The future RICOCHET low-energy neutrino observatory	45
3.1	Introduction	45
3.2	Experimental state of the art	46
3.2.1	The first CENNS detection	46
3.2.2	Ongoing and planned cryogenic CENNS experiments	47
3.3	The RICOCHET experiment at ILL	48
3.3.1	The cryogenic detectors	49

3.3.2	The ILL-H7 nuclear reactor site	50
3.3.3	Preliminary experimental setup	50
3.3.4	RICOCHET CENNS sensitivity	51
3.4	Shielding optimization and expected backgrounds	52
3.5	Searching for new physics with RICOCHET	55
3.6	Signal systematics	58
3.6.1	Anti-neutrino reactor flux predictions	58
3.6.2	Low-energy nuclear recoil energy calibration	59
3.6.3	In-situ neutron background monitoring	60
3.7	Characterization of the ILL site	61
3.7.1	The neutron background	61
3.7.2	Vibration levels	64
3.8	Conclusion and perspectives	65
4	CryoCube design optimization and expected CENNS sensitivity with RICOCHET	67
4.1	Electro-thermal model and heat resolution optimization	68
4.1.1	Steady state	69
4.1.2	Time domain	69
4.1.3	Frequency domain	71
4.1.4	Results and discussion	73
4.2	Electrostatic simulation and electrode optimization	76
4.2.1	Basics of the ionization signal	76
4.2.2	Electrode design optimization for FID38 and PL38	78
4.2.3	Results and discussion	81
4.3	Expected CryoCube CENNS sensitivity	84
4.3.1	Timing resolution and muon-veto coincidence	85
4.3.2	Heat Vs Ionization based particle identification	88
4.3.3	The hypothetical Heat Only background	91
4.3.4	The muon veto cut optimization	93
4.3.5	CryoCube sensitivity study: results and discussion	94
4.4	Conclusion	97
5	Ongoing CryoCube detector R&D	99
5.1	The IP2I cryogenic facility	99
5.2	Vibration mitigation and cryogenic suspension	101
5.2.1	An elastic-pendulum based cryogenic suspended tower	101
5.2.2	Characterization of the vibration levels	103
5.2.3	Cryogenic detector performance improvement	105
5.3	Overview of recent experimental results	107
5.3.1	Heat energy resolution and detector mass optimization	108
5.3.2	Ionization channel experimental characterization and performance	111
5.3.3	Timing resolution	114
5.3.4	IP2I background characterization	115
5.3.5	Low-noise HEMT-based electronics	119
5.4	Conclusions	121

Introduction

The nature of invisible dark matter (DM) that constitutes some 26% of the mass-energy balance of the Universe remains one of the most fundamental puzzles in physics today. The most compelling solution to the DM enigma is provided by postulating some new elementary particle that must be outside of the spectrum of the Standard Model (SM) – which in fact provides one of the strongest arguments in support of “new physics” beyond the SM (BSM). From Galactic dynamics we know that if this DM particle has a non-zero coupling to the ones from the SM, then an Earth-based experiment may be able to detect its existence and characterize its properties. In 1985, following the initial idea from Goodman and Witten, the field of direct detection of dark matter was born and nowadays about 40 experiments worldwide, based on a host of techniques, are searching for DM. The EDELWEISS-III experiment, using cryogenic germanium semiconductor detectors, is now lowering its DM particle mass range from the GeV/c^2 - down to the eV/c^2 -scales in order to extend its sensitivity to this elusive particle.

However, as upcoming and future direct detection experiments are increasing their sensitivity, they will soon become affected by the ultimate cosmic neutrino background. Indeed, the coherent elastic neutrino-nucleus scattering (CENNS) of these neutrino with the nuclei from the detector material will prevent future experiments to genuinely identify a positive detection of DM candidates with cross sections below the so-called “neutrino floor”. This fundamental limitation can however be significantly reduced thanks to a low-energy and precise measurement of the CENNS process which can be done with dedicated experiments, using similar detector technologies, placed in proximity to a nuclear reactor. To that end, the future RICOCHET experiment will be installed 8 m away from the ILL research reactor in order to provide a low-energy and high precision CENNS measurement down to the sub-100 eV energy-scale. On top of reducing the systematics associated with the CENNS cross section, it will also have unprecedented sensitivity to various new physics scenarios in the electroweak sector. These include for instance the existence of sterile neutrinos and of new mediators, that could be related to the DM problem, and the possibility of Non Standard Interactions that would have tremendous implications on the global neutrino physics program.

A brief introduction to the dark matter puzzle and the field of direct detection, with a particular emphasis on the neutrino background issue and the EDELWEISS experiment, is given in Chapter 1.

An above-ground dark matter search, demonstrating the low-mass reach achievable with the EDELWEISS technology, is presented in Chapter 2. This result also demonstrates the feasibility to achieve sub-100 eV energy threshold on 30 g-scale Ge crystals operated from the surface, as planned for the forthcoming RICOCHET experiment.

Chapter 3 gives a detailed overview of the future RICOCHET low-energy neutrino observatory, hosting two cryogenic detector arrays – CryoCube and QArray–, that will be deployed at ILL in the coming years. A preliminary experimental setup, as well as background estimates and new physics reaches will be presented. Additionally, we also give an extensive discussion about various systematics that may affect our measurement, and how we plan on mitigating them. Eventually, we present our onsite characterizations, including fast neutron and vibration measurements which are both major threats to RICOCHET’s CENNS sensitivity.

Chapter 4 describes the CryoCube detector design consisting in an array of 27 Ge crystals of about 30 g heat sunk at 10 mK and readout with dedicated HEMT-based preamplifiers. Firstly, the chapter reviews the electrothermal modeling and optimization of the heat channel, then it discusses the electrostatic modelling and optimization of the ionization channel. Lastly, the chapter assesses the CryoCube sensitivity to CENNS with the RICOCHET experiment at ILL, and demonstrates that discovery significance ranging from 17-to- 5σ , depending on the various background and setup assumptions, should be achievable after only one reactor cycle.

Finally, this manuscript ends with Chap. 5 which summarizes the various individual 30 g-scale Ge detector performance, how they compare with the modeling from the previous chapter, and how we plan to further improve them in order to achieve the CryoCube targeted performance.

1

Direct detection of Dark Matter

1.1 The dark matter puzzle

Diverse astronomical and cosmological observations, on scales ranging from galaxies to the entire Universe, provide powerful evidence that 85% of the matter in the Universe is in the form of cold, non-baryonic dark matter (CDM). *The following section largely follows the 2020 APPEC dark matter direct detection report to which I was one of the author [1].*

1.1.1 Evidence

1) Astronomical and Cosmological Evidence for Non-Baryonic Dark Matter

The rotation curves of disc galaxies are close to flat at large radii, rather than having a Keplerian, $r^{-1/2}$, decline as expected from the luminous components. According to Newton's law, this indicates that these galaxies are surrounded by invisible, extended, close to spherical, DM halos (for a historical review see Ref. [2]). Using measurements of the velocity dispersion of galaxies and the virial theorem, clusters of galaxies have been shown to contain a large fraction of DM [3]. Furthermore the energy spectrum and radial flux of the X-rays emitted by the hot gas in clusters demonstrate that the majority of the matter they contain is non-baryonic (e.g., Ref. [4]), while gravitational lensing observations allow the mass distribution to be mapped out (e.g., Ref. [5]). Dark matter is also required for the small initial density perturbations to grow sufficiently to produce the observed large scale structure and also to explain the heights of the acoustic peaks in the Cosmic Microwave Background (CMB) angular power spectrum (e.g., Ref. [6]).

1.1 The dark matter puzzle

2) Observational Probes of the Nature and Abundance of Dark Matter

The anisotropies in the CMB allow precise measurements of the cosmological parameters. A combined analysis, including large scale structure data (baryon acoustic oscillations), gives $\Omega_{\text{CDM}}h^2 = 0.119 \pm 0.001$, where the CDM relic density parameter, $\Omega_{\text{CDM}} \equiv \rho_{\text{CDM}}/\rho_c$, is the present day CDM density, relative to the critical density ρ_c and h is the Hubble constant in units of $100 \text{ km/s/Mpc}^{-1}$ [7]. Using the same data the baryon density parameter is $\Omega_b h^2 = 0.0223 \pm 0.0001$ [7], consistent with the measurement from Big Bang Nucleosynthesis (BBN) and the primordial abundances of the light elements [8], so that $\approx 85\%$ of the matter is cold DM. The event rate in WIMP direct detection is directly proportional to the local (*i.e.* at the Solar location) DM density. This can be measured via a variety of methods (for reviews see Ref. [9, 10]) and a standard value of $\rho_0 = 0.3 \text{ GeV}/c^2/\text{cm}^3$ is usually adopted. On small scales density fluctuations can be erased by the free-streaming of DM. The observed clustering of galaxies is reproduced by numerical simulations in which the majority of the DM is cold, *i.e.* non-relativistic during structure formation [11]. Constraints on the free-streaming scale from Lyman- α forest data place a constraint on the mass of generic thermal relic DM, with the same temperature as the SM, of $m > 5.3 \text{ keV}/c^2$ [12, 13].

The CMB anisotropies are sensitive to energy injection due to, for instance, DM annihilation into electromagnetically charged final states. Using Planck data, this places a constraint on the WIMP annihilation cross section into electrons where m_χ is the WIMP mass and $\langle\sigma v\rangle$ the thermally averaged annihilation cross section [7]. The separation of the baryonic and total mass in merging galaxy clusters, like the Bullet cluster, places an upper limit on the DM self-interaction cross section $\sigma/m_\chi < \mathcal{O}(1) \text{ cm}^2/\text{g}$ (see discussion in Ref. [14]).

1.1.2 Candidates

Some general properties of DM particle candidates can be established already from observational evidence and numerical simulations alone. Firstly, most of them favour cold dark matter, as described above, although some arguments favour warm dark matter (WDM).¹ Secondly, CMB properties indicate that dark matter is non-baryonic, and that it is electrically neutral and colorless. As a matter of fact, DM particles should interact with ordinary matter preferably only weakly, where weak may stand for the familiar weak force, or instead some other sub-weak force defined by some non-negligible coupling to the Standard Model (SM) particles. Lastly, DM particles should also be either perfectly stable, or extremely long lived (at least 160 Gyr [15]). Finally, the DM particle mass range can span nearly 50 orders of magnitude, from values as tiny as 10^{-21} eV (fuzzy DM) for bosons with de Broglie wavelength of the order of typical sizes of dwarf galaxies [16] up to the (reduced) Planck scale $\bar{M}_P \simeq 2 \times 10^{18} \text{ GeV}$ (above which it is difficult to consider DM particles as elementary). This is as much as we can be fairly confident about the general properties of DM which, however, is only a first step towards identifying its real nature, since they can be easily satisfied by a wide range of specific particle candidates, or in fact classes of candidates.

¹DM relics can be classified as hot, cold, or warm, depending on how relativistic they are around the time of matter-radiation equality and how large is their free-streaming length during structure formation.

1) Thermal WIMP dark matter

The class of DM candidates that has received the most attention over the last decades is the so-called thermal WIMP. Thermal WIMPs were produced during the very early and hot stage of the Universe, when the SM and DM particles were in thermal equilibrium. However, as the Universe expanded and cooled, the WIMP annihilation rate Γ_{ann} decreased as it was getting harder and harder for a DM particle to find a partner to annihilate. Thermal WIMPs eventually froze out when the annihilation rate became lower than the expansion rate of the Universe $\Gamma_{\text{ann}} \leq H \propto T_f^2/\overline{M}_P$, where T_f corresponds to the freeze out temperature. Assuming that the DM particle's lifetime is greater than the age of the Universe, or even stable, after freeze out its comoving density remained constant. The thermal WIMP relic density can be computed by solving numerically the covariant form of Boltzmann equation [17] and can be approximated by:

$$\Omega_{CDM}h^2 \sim \frac{10^{-26} \text{ cm}^3/\text{s}}{\langle \sigma_{\text{ann}}v \rangle_f} \approx 0.1 \left(\frac{0.01}{\alpha} \right)^2 \left(\frac{m_\chi}{100 \text{ GeV}/c^2} \right)^2 \quad (1.1)$$

where we considered a generic form of the thermally averaged product of the WIMP-pair annihilation cross section and their relative velocity at freeze-out such that $\langle \sigma_{\text{ann}}v \rangle_f = \alpha^2/m_\chi^2$. Assuming a weakly interacting DM particle with $\alpha = 0.01$ and a mass $m_\chi = 100 \text{ GeV}/c^2$ gives the correct abundance as observed today [7]. This remarkable coincidence, often referred to as the ‘‘WIMP miracle’’, motivated a large amount of research into the possibility that DM particles, in the form of thermal WIMPs, may be part of some ‘‘new physics’’ beyond the Standard Model (BSM) with a mass scale not far from the electroweak-scale, for which there is independent strong theoretical motivation. But just how much of a miracle are thermal WIMPs? It turns out, not that much. Indeed, keeping the ratio α^2/m_χ^2 fixed to the measured relic density can be achieved for a wide ranges of WIMP effective coupling to the SM sector α , from gravitational to strong, and also m_χ , from $\sim 1 \text{ eV}/c^2$ to $\sim 120 \text{ TeV}/c^2$, consistent with the freeze-out mechanism [18, 19, 20]. Note that for the particular case of thermal fermionic WIMPs, such as massive neutrinos exhibiting EW-strength interaction with the SM sector, the particle mass must be heavier than about $4 \text{ GeV}/c^2$ to not over-close the Universe. This is the so-called Lee-Weinberg limit [21].

The neutralino, arising as the lightest supersymmetric particle, has been by far the most popular thermal WIMP DM candidate over the last decades. It is theoretically motivated, predictive in the context of low-energy SUSY models, and offers promising detection rates at both DM direct detection and collider experiments to be tested; see, *e.g.* [20, 22] for recent reviews. Other candidates that falls into the thermal WIMP category are the ones arising from the so-called ‘‘portal’’ models, in which a messenger containing one or more states mediates the SM and DM interactions which are both in their respective sectors, *i.e.* visible and dark. Though the Higgs portal has been pretty much ruled out [23] from direct detection experiments, the Dark Photon sector is a very popular class of models leading to MeV-scale DM particle candidates primarily testable at fixed target experiments and more recently at direct detection experiments exploiting the DM-electron scattering process [24, 25]. Lastly, in another scenario called asymmetric DM (ADM) [26, 27] an asymmetry between the DM particle and its antiparticle is generated in a way analogous to the mechanism of baryogenesis and modifies their freeze-out. In that case correct relic density can be obtained for DM typically in the mass range from $\sim 1 \text{ GeV}/c^2$ to \sim

1.1 The dark matter puzzle

15 GeV/c² with large annihilation cross section as (partially) asymmetric. Though the expected indirect detection rate can be highly suppressed due to today's potentially highly asymmetric abundance of χ and $\bar{\chi}$ [28], the elastic scattering rate of DM with nuclei can in some models be even larger than for usual Majorana WIMPs [29]. For this reason, ADM has been widely responsible for the recent focus on GeV/c²-scale DM from various direct detection experiments.

2) Non-thermal WIMP dark matter

If on the other hand the WIMP-SM sector interactions are very much weaker than the EW-scale, then the DM particles never reach thermal equilibrium after reheating in the early Universe and therefore never freeze out. This category of non-thermal WIMPs is called Feebly Interacting Massive Particles (FIMP) [30]. They can however still non-thermally produce the correct relic density by being generated through decays of heavier particles or from inelastic collisions from particles in the thermal plasma. This class of processes is the so-called freeze-in mechanism. Due to their highly suppressed coupling to the SM sector, their direct detection is doomed to be very challenging. However, some viable FIMPs models with masses in the sub-GeV/c² range, or even less, exist and are in principle testable via DM-electron scattering [31]. It is worth noticing that sterile neutrinos, in the keV/c² to MeV/c² mass range, are a well motivated non-thermal relic DM candidate actively searched for via astronomical x-ray experiments [32].

Last but not least, a whole class of non-thermal relics that is theoretically highly motivated and experimentally detectable is axions. The arguably most elegant solution to the strong CP problem is the introduction of a $U(1)_{\text{PQ}}$ Peccei-Quinn symmetry that is spontaneously broken at an energy scale f_a [33, 34]. The arising particle, a pseudo Nambu Goldstone boson, is the QCD axion [35, 36]. QCD axions would, hence, automatically be produced in the early Universe by the so called misalignment mechanism, when the initial phase θ_i of the $U(1)_{\text{PQ}}$ group was dynamically driven to zero during Hubble expansion and the field starts oscillating around its minimum (the amplitude of this oscillation gives the relic density of axions). The QCD axion can be easily accommodated in theories Beyond the Standard Model like supersymmetry and Grand Unified Theories, and it is a firm prediction of string theories [37]. Though the QCD axion is a highly motivated DM candidate, actively searched for by various dedicated experiments, it is out of the reach from direct detection experiments. It is however worth noticing that generic “hidden” $U(1)$ gauge fields, leading to ultra-light massive particles commonly referred to as hidden (or dark) photons that would kinetically mix with the standard model photon, could however be detectable at underground experiments with eV-scale energy threshold and searching for electron recoils [38]. These hidden photons would inevitably contribute to the cold DM density of the Universe, due to their production in the early universe, and be viable DM candidates [39, 40, 41].

3) Non-particle dark matter candidates

There have been attempts at solving the DM puzzle outside of particle physics. As discussed earlier, the vast majority of the DM is non-baryonic. Therefore astrophysical bodies in the form of baryonic MAssive COmpact Halo Objects (MACHOs) can only make up a small fraction of the DM. However primordial black holes (PBHs), black holes that may form in

the early Universe, remain a viable CDM candidate [42]. As they form before the time of primordial nucleosynthesis, PBHs are effectively non-baryonic, and if their mass is greater than $5 \times 10^{14} \text{gram} (= 3 \times 10^{-19} M_{\odot})$ their lifetime is longer than the age of the Universe. The recent discovery of gravitational waves from $\sim 10 M_{\odot}$ binary black hole (BH) mergers has led to a resurgence of interest in PBHs as a DM candidate [43, 44, 45]. Such massive PBHs are now excluded from making up all of the DM by a combination of lensing, dynamical, accretion and gravitational wave constraints. However, asteroid-mass PBHs, with $10^{17} \text{gram} \lesssim M_{\text{PBH}} \lesssim 10^{22} \text{gram}$, are challenging to detect and can still make up all of the dark matter in exotic cosmic inflation models [46]. For a recent review of the constraints on PBHs see Ref. [47].

All of the observational evidence for DM to date comes from its gravitational interactions. Therefore it is in principle possible that the observations could instead be explained by a modification of the law of gravity. Galaxy rotation curves can be explained by a phenomenological modification of Newton’s law of gravitation at low accelerations, known as Modified Newtonian Dynamics (MOND) [48]. To address cosmological observations a relativistic formalism, such as TeVeS [49], is required. These models have difficulties explaining the heights of the higher order peaks in the CMB temperature angular power [50] and are also tightly constrained by the close to simultaneous detection of gravitational waves and electromagnetic signals from a binary neutron star merger [51]. Another challenge is provided by the Bullet cluster, where gravitational weak lensing and X-ray observations show that the dominant mass component is spatially separated from the baryonic mass [52].

1.2 WIMP direct detection

If the Milky Way’s DM halo is composed of WIMPs then, assuming $m_{\chi} = 100 \text{ GeV}/c^2$, the WIMP flux on Earth is of the order of $10^5 \text{ cm}^{-2}\text{s}^{-1}$. This flux is sufficiently large that, even though the WIMPs are weakly interacting, a small but potentially measurable fraction will elastically scatter off nuclei and be detected. Direct detection has first been proposed by Goodman and Witten in 1985 [53] as a very promising way to detect dark matter. Indeed, assuming now a weak-scale-like cross section of 10^{-38} cm^2 and a 1 kg Ge target detector, one should detect about 20 events per day with a mean recoil energy of 10 keV. Such a signal would be easily detectable by most low-energy threshold detector technologies existing in the 80’s, operated in a moderately low background environment. However, almost four decades later none of the numerous direct detection experiments has observed any convincing DM signal and cross sections in the 10^{-47} cm^2 are now being explored. In order to better understand the challenge of direct detection we first briefly summarise the principles and rate calculations of direct detection in Sec. 1.2.1. The different experimental approaches and the current status of the field are discussed in Sec. 1.2.2. Eventually, in Sec. 1.2.3 we conclude by discussing the upcoming neutrino background and its implications on the future of WIMP direct detection.

1.2 WIMP direct detection

1.2.1 Direct Detection principle

Direct detection experiments search for signatures of (in)elastic scattering of WIMPs off a target nucleus [53]. The momentum transfer gives rise to a nuclear recoil which might be detectable. The discussion hereafter is inspired by the more detailed reviews [1, 17, 54].

With a virial velocity of 300 km/s, DM particles are non-relativistic such that the nuclear recoil energy is given by:

$$E_r = 2v^2 \frac{\mu}{m_N} \times \cos^2 \theta_r \quad (1.2)$$

with $\mu = m_\chi m_N / (m_\chi + m_N)$ the WIMP-nucleus reduced mass, m_N the target nucleus mass, and θ_r the WIMP-nucleus recoiling angle. From Eq. 1.2 one can easily derive that the maximum recoil energy scales as $E_r^{\max} \propto m_\chi^2$ for $m_\chi \ll m_N$ and then plateaus at $E_r^{\max} \rightarrow 2v^2 m_N$ when $m_\chi \gg m_N$. The differential scattering rate per unit detector mass is given by:

$$\frac{dR}{dE_r} = \frac{\rho_0}{m_\chi m_N} \left\langle v \frac{d\sigma_{\chi-N}}{dE_r} \right\rangle \quad (1.3)$$

where $\sigma_{\chi-N}$ corresponds to the WIMP-nucleus cross section, ρ_0 to the local dark matter density, and the brackets indicate an average over the velocities of the incoming DM. Written out in full, the differential rate is,

$$\frac{dR}{dE_r} = \frac{\rho_0 M}{m_N m_\chi} \int_{v_{\min}}^{\infty} v f(v) \frac{d\sigma_{\chi-N}}{dE_r} dv \propto \exp\left(-\frac{E_r}{E_0} \frac{4m_\chi m_N}{(m_\chi + m_N)^2}\right) F^2(E_r), \quad (1.4)$$

where M is the detector mass and $F(E_r)$ is the form factor. $f(v)$ is the DM halo normalised WIMP velocity distribution and E_0 is the WIMP's most probable kinetic energy. All velocities are defined in the detector's reference frame. v_{\min} is the minimal WIMP velocity required to induce a nuclear recoil of energy E_r . WIMPs with a velocity above the escape velocity v_{esc} have left the potential well of the Milky Way, i.e., $f(v > v_{\text{esc}}) = 0$ in the Galactic rest-frame. As shown by the right-hand term of Eq. 1.4, in the standard Maxwellian halo model the differential rate is very well approximated by a featureless falling exponential function, stressing the importance of a low-energy detector threshold to detect light DM particle candidates.

An Earth-based detector moves through the DM halo with a velocity (ϕ -component)

$$v_E = v_\odot + v_\oplus \cos(\theta) \cos[\omega(t - t_0)], \quad (1.5)$$

where $v_c = 220$ km/s is the local circular velocity, $v_\odot = v_c + 12$ km/s the motion of the Sun with respect to v_c and $v_\oplus = 30$ km/s describes the velocity of the Earth orbiting around the Sun. The inclination angle between the Earth's orbit and the galactic plane is $\theta \approx 60^\circ$. $\omega = 2\pi/T$ with a period $T = 1$ year; the phase is fixed to $t_0 = \text{June 2}$, when v_\odot and v_\oplus are parallel. This periodic modulation of v_E leads to a harder (softer) recoil spectrum in summer (winter) when v_\odot and v_\oplus are (anti-)parallel and thus producing an annually modulating DM signal $S(t)$ above a fixed detector threshold E_{low} [55, 56, 57],

$$S(t) = B(t) + S_0 + S_m \cos[\omega(t - t_0)]. \quad (1.6)$$

However, most of the signal is unmodulated (S_0) as the modulated part $S_m \sim \mathcal{O}(v_\oplus/v_c) \sim 5\%$ is small. The (potentially time-dependent) backgrounds $B(t)$ are typically much larger than S_0 ,

suggesting that large number of DM events are required to use the annual modulation signature as a proof of discovery.

Another way to exploit Eq. (1.5) to reduce backgrounds is to search for a WIMP ‘‘wind’’ from the direction in the constellation Cygnus, the point in the sky towards which the Sun is moving. The Earth’s daily rotation thus constantly changes the signal direction observed in a detector while most backgrounds are expected to be uniformly distributed (or originate from the Sun, e.g., solar neutrinos). A measurement of the track direction could distinguish a DM signal from background events [58]. This is the so-called directional detection of dark matter which, on top of genuinely identifying a DM signal, could also measure the 3-dimensional local WIMP velocity distribution related to our Galaxy’s formation history [59].

The WIMP-nucleus scattering cross section in Eq. (1.4) can be expressed as

$$\frac{d\sigma_{\chi-N}(E_r)}{dE_r} = \frac{m_N}{2v^2\mu^2} [\sigma_{\text{SI}}F_{\text{SI}}^2(E_r) + \sigma_{\text{SD}}F_{\text{SD}}^2(E_r)], \quad (1.7)$$

where the unknown interaction is usually described by a spin-independent (SI) and a spin-dependent (SD) component. The former corresponds to a scalar or vector effective 4-fermion Lagrangian, the latter has an axial-vector structure. All partial waves of the nucleons add up at small momentum transfers q and the WIMP interacts coherently with the entire nucleus. The loss of coherence at higher q is accounted for by the finite form factors F_{SI} and F_{SD} . F_{SI} is only relevant for WIMP targets with high mass numbers $A \gtrsim 100$ and at high recoil energies.

The **spin-independent (SI)** cross section is given by

$$\sigma_{\text{SI}} = \sigma_n \frac{\mu^2 (f_p Z + f_n (A - Z))^2}{\mu_n^2 f_n^2} = \sigma_n \frac{\mu^2}{\mu_n^2} A^2. \quad (1.8)$$

μ_n is the reduced mass of the WIMP-nucleon system. The WIMP-nucleus cross section σ_{SI} is converted to a WIMP-nucleon cross section σ_n to facilitate the comparison between different target nuclei. f_p and f_n are coupling constants to protons and neutrons, respectively; the second equality in Eq. (1.8) assumes $f_p = f_n$ which usually happens in Higgs dominated exchange with the sea quarks. The resulting A^2 dependence favours heavy target nuclei to search for spin-independent interactions.

Spin-dependent (SD) interactions describe the WIMP coupling to unpaired nuclear spins J [60]:

$$\frac{d\sigma_{\text{SD}}}{d|\vec{q}|^2} = \frac{8G_F^2}{\pi v^2} [a_p \langle S_p \rangle + a_n \langle S_n \rangle]^2 \frac{J+1}{J} \frac{S(|\vec{q}|)}{S(0)}. \quad (1.9)$$

\vec{q} is the momentum transfer, $\langle S_p \rangle$ and $\langle S_n \rangle$ the expectation values of the total spin operators for protons and neutrons in the target nucleus; these have to be calculated using nuclear models and thus carry some systematic uncertainty [61, 62]. The cross section depends on the spin-structure function $S(|\vec{q}|)$ and the total nuclear spin J of the target. SD-results are usually quoted assuming that WIMPs couple either only to neutrons ($a_p = 0$) or to protons ($a_n = 0$). Nuclei with an odd number of protons (e.g., ^1H , ^7Li , ^{19}F , ^{23}Na , ^{127}I) or neutrons (e.g., ^{17}O , ^{27}Al , ^{29}Si , ^{73}Ge , ^{129}Xe , ^{131}Xe , ^{183}W) can effectively probe spin-dependent WIMP-proton or WIMP-neutron interactions, respectively.

1.2 WIMP direct detection

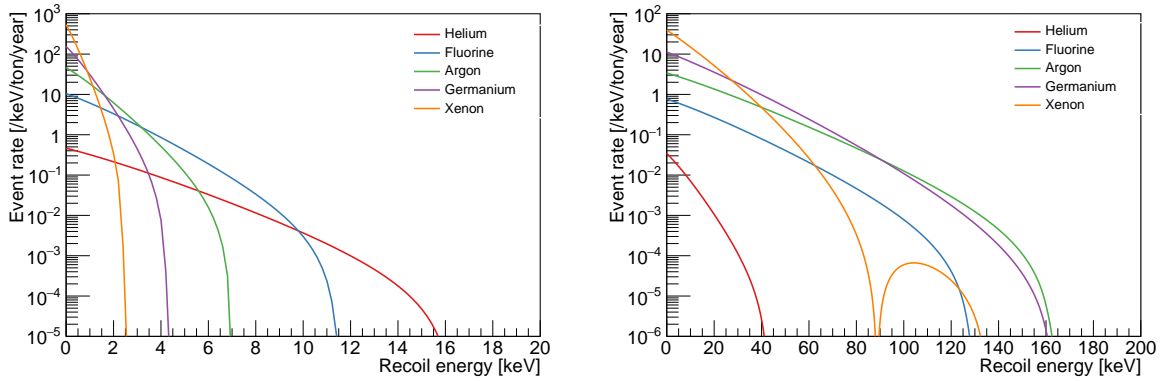


Figure 1.1: Differential event rate for various detector target materials: Helium (red), Fluorine (blue), Argon (green), Germanium (purple), and Xenon (orange), for a 5 GeV/c² (left) and a 50 GeV/c² (right) WIMP mass. The calculations have been done considering the standard halo model parameters and a SI WIMP-nucleon cross section of 10⁻⁴⁵ cm².

Going beyond the standard SI and SD interactions can be done in describing the various possible 4-point interactions by a number of relativistic and non-relativistic operators. These effective field theories (EFTs) [63, 64, 65] allow for a direct comparison of direct detection results with collider searches (when the kinematic requirements for the WIMP production are taken into account). The SI and SD interactions are mainly described by the non-relativistic EFT operators $\mathcal{O}_1 = 1_\chi 1_N$ and $\mathcal{O}_4 = \vec{S}_\chi \cdot \vec{S}_N$, respectively, however, in general any WIMP search data can be interpreted using a plethora of operators [66, 67]. Other interaction processes, such as inelastic dark matter [68], Migdal effect, WIMP-electron scattering and the detection of Axion Like Particles (ALPs) via axio-electric effect will be further discussed in Sec. 1.3 and Sec. 2.4 where they have been considered in recent EDELWEISS low-mass DM searches.

In order to conclude this section with a concrete example, we show in figure 1.1 the differential event rate as a function of the nuclear recoil energy for various targets and two different WIMP masses: 5 GeV/c² (left) and 50 GeV/c² (right). One can indeed appreciate that the expected WIMP-induced nuclear recoil spectrum is a featureless exponential with end-point energies E_r^{\max} as derived from Eq. 1.2. Few conclusions can be drawn from this figure:

- Lighter targets are kinetically considerably favored in the search for low-mass dark matter thanks to their much higher energy end-points with respect to heavier elements,
- For $\mathcal{O}(100)$ GeV/c² DM particles heavier target elements are favored both kinetically and from the A^2 coherence factor arising from the assumed SI interaction,
- With a WIMP-nucleon SI cross section of 10⁻⁴⁵ cm² and a 50 GeV/c² DM particle mass order of 1-to-100 events per ton-year are expected, depending on the considered target material, suggesting that similarly ultra-low background levels must be achieved to see the DM signal.

As one can conclude from this section, though it sounded initially extremely promising in 1985, when direct detection was first suggested by Goodman and Witten [53], four decades later the

picture has gotten significantly less trivial.

1.2.2 Experimental techniques and state of the art

In this paragraph, we briefly review the tremendous experimental challenges that are facing the current experiments, discuss their individual strategies and prospects. Based on the previous discussion about the expected WIMP signal, one can derive the following ideal dark matter detector wish list:

- Low and controlled background so that they can be subtracted
- Discrimination power between the signal and background to genuinely identify a DM signal as such
- Large exposure to get sufficient sensitivity to an hypothetical and putative DM signal
- Low energy threshold, especially if searching for low-mass DM particles.

Over the past decades, direct detection of dark matter has therefore offered an extraordinary opportunity to develop new detector technologies, and to considerably improve them². It is interesting to note that most of the existing radiation detector techniques have been considered and improved upon for the DM application: scintillating crystals, high purity Ge (HPGe) ionisation detectors, scintillating liquids, liquid and gaseous time projection chambers (TPC), bubble chambers, and of course cryogenic bolometers. The following non-exhaustive presentation of these different detector technologies is further illustrated Fig. 1.2:

Large target masses can be realised by using arrays of high-purity scintillator crystals (see Fig. 1.2 a), mainly NaI(Tl) but also CsI(Tl). The high mass numbers of I ($A = 127$) and Cs ($A = 133$) lead to a high sensitivity to spin-independent interactions. However they suffer from rather large intrinsic backgrounds and from the absence of fiducialisation and electronic recoil rejection. Facing the lack of active background rejection, the experiments thus concentrate on exploiting the annual modulation signature. The DAMA/LIBRA experiment has reported a 12.9σ -detection of a signal over a total of 20 annual cycles [69]. However, despite being the most serious DM detection claim over the past decade, it is considered highly controversial. Indeed most, if not all, experiments which have successfully demonstrated sensitivity to the DAMA/LIBRA favored DM candidate have found no signal. Even the experiments trying to reproduce DAMA/LIBRA, such as COSINE-100 [70, 71] and ANAIS-112 [72, 73] which also employ low-background NaI(Tl) crystals, are in strong tension with the DAMA/LIBRA result. Nevertheless, DAMA/LIBRA is still emulating both the theoretical and experimental side of the field and has given birth to plethora of new DM models and improved detection techniques to further investigate the origin of the observed DAMA/LIBRA signal.

Germanium and silicon semiconductor ionisation detectors are also used to search for DM-induced charge signals. Thanks to their low amount of energy needed to create an electron-hole

²As a matter of fact, based on the significant low-background detection techniques developed for DM searches, various new applications of this technology is now being considered in other field of physics, *e.g.* neutrino-less double-beta searches and coherent elastic neutrino nucleus scattering measurement

1.2 WIMP direct detection

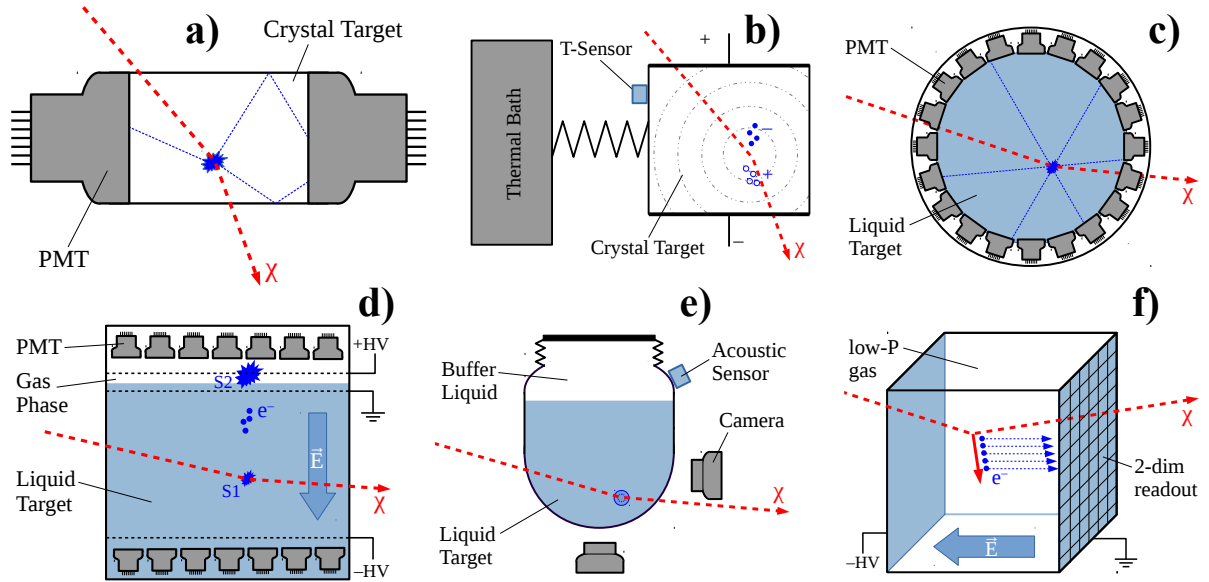


Figure 1.2: Working principle of common detector types for the direct WIMP search: (a) scintillating crystal, (b) bolometer (here with additional charge-readout), (c) single-phase and (d) dual-phase liquid noble gas detectors, (e) bubble chamber, (e) directional detector. Images adapted from [74].

pair (Ge: 2.9 eV, Si: 3.6 eV), they usually exhibit excellent ionization resolution. They however suffer from the difficulty to scale each crystal beyond a few kilograms due to the increased capacitance and degraded resolution, and from the low nuclear recoil ionization yield. The state-of-the-art experiments, such as CDEX-10 [75] and CoGENT [76], use p-type point contact HPGe crystals at the kg-scale and achieved very low thresholds down to ~ 160 eV_{ee}³ [75]. On the other hand, silicon detector such as DAMIC using charge-coupled devices (CCDs) [77], are kinetically at an advantage in using a lighter Si target but also suffer from reduced nuclear recoil ionization yield and lack of background discrimination at the lowest energies.

Crystalline cryogenic detectors (bolometers) aim at measuring the heat signals, in the form of thermal or athermal phonons, induced by a particle interaction following $\Delta T = E_r/C$ where ΔT is the corresponding temperature increase and C the heat capacity of the system (see Fig. 1.2 b). Cryogenic detectors are operated in the 10-to-50 mK range to minimize the heat capacity and the thermal fluctuation noise. Several temperature sensing techniques exist, but the most widely and mature ones are the (low-impedance) Transition Edge Sensors (TES) and neutron transmutation doped germanium (NTD-Ge) thermistors. In both cases, the heat increase is measured via a change in resistance which is either measured as a current or voltage drop at the front-end of the readout electronics. A wide variety of crystal materials can be used, but in recent years the leading materials have been: CaWO₄ in CRESST [78], Ge and Si in (Super)CDMS [79], and Ge in EDELWEISS [80]. Interestingly, a simultaneous measurement of a second observable, such as ionisation in semiconductors (Ge, Si) or scintillation in scintillating crystals (CaWO₄), allows for electronic/nuclear recoil discrimination as in both cases

³Electron equivalent energy scale

the ionization/scintillation yields vary with the recoiling particle type. Cryogenic detectors feature a precise energy measurement with almost no quenching in the heat channel, excellent energy resolution and background rejection down to energies of $\mathcal{O}(1)$ keV_{nr}⁴. The operation at mK-temperatures is challenging and expensive. Additionally, the requirement of a low-energy threshold constrains the mass of the individual detectors, limiting the reachable exposure. Cryogenic experiments have therefore progressively focused their efforts in searching for light DM candidates, usually below 10 GeV/c², as threshold then becomes more important than exposure.

The noble gases argon and xenon are excellent scintillators and can be ionized easily. In liquid state they are used to build massive, dense and compact DM targets which already exceeded the ton-scale. Interactions produce heat (undetected) and excite (X^*) and ionise (X^+) the atoms, producing in the end both light (scintillation) and charge (ionization) signals. The de-excitation time constants of the produced singlet and triplet excimer states are very similar in xenon (4 ns and 22 ns) but differ very significantly for argon (7 ns and 1.6 μ s) which allows for very efficient pulse shape discrimination in the latter [81]. Single-phase liquid noble gas detector, such as the 3200 kg argon DEAP-3600 experiment operated at SNOLAB [81], measure only the scintillation signal using a spherical target surrounded by photomultipliers, see Fig. 1.2 c. The interaction position can be reconstructed via photon timing and signal distribution with few cm-resolution. Dual-phase time projection chambers (TPC), see Fig. 1.2 d., measure the primary scintillation signal (S1) as well as the ionisation electrons as a secondary light signal (S2), following the multiplication and extraction of the ionization electrons, at the liquid-gas interface, thanks to a high electric field (~ 10 kV/cm). Both light signals are recorded using photosensors installed above and below the target allowing for the rejection of multiple scatters, reconstruction of the interaction position with mm-precision and improving of the energy resolution [82]. The partition into excitation and ionisation depends on the ionisation density and the ratio S2/S1 is used to distinguish electronic from nuclear recoils. Nowadays, dual-phase noble gas experiments are leading the field with XENON-1T [83], PANDAX-II [84], and LUX [85] (Xe-based), and DarkSide-50 [86] (Ar-based).

Bubble chamber detector use superheated liquids as target materials, see Fig. 1.2 e. By keeping their liquid at a controlled distance from the boiling point, they can choose to be sensitive to a minimal amount of deposited energy per unit of volume. This nucleation threshold is then set such that only nuclear recoil events (from α -particles, neutrons or WIMPs) will create bubbles and be detected. The detector is then almost immune to electronic recoils and the α -particles can be rejected based on the acoustics of the bubble's explosion [104]. The PICO-60 experiment, formed by a merger of the PICASSO and COUPP collaborations in 2012, operates 52 kg of C₃F₈ target with a 2.45 keV threshold and achieved the best SD WIMP-proton limit [105].

Directional detectors aim at taking advantage of the galactic dynamics to unambiguously identify the galactic origin of the DM signal. Indeed, thanks to the rotation of the Solar system around the Galactic center through the DM halo, a privileged WIMP incoming direction inducing a directional WIMP-induced signature is expected [59]. The most commonly considered approach is the use of low-pressure gaseous TPC, where the mm-scale track is reconstructed

⁴Nuclear recoil equivalent energy scale

1.2 WIMP direct detection

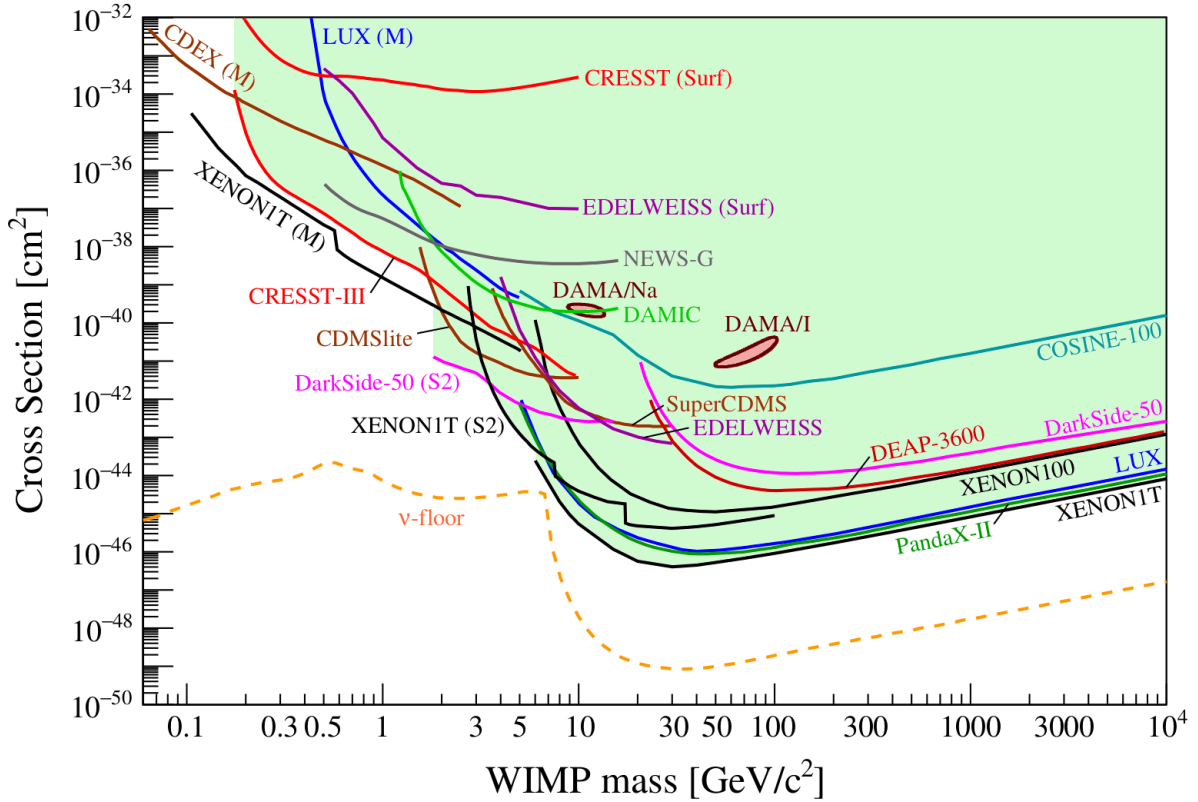


Figure 1.3: Current status of searches for spin-independent elastic WIMP-nucleus scattering assuming the standard parameters for an isothermal WIMP halo: $\rho_0 = 0.3 \text{ GeV}/c^2/\text{cm}^3$, $v_0 = 220 \text{ km/s}$, $v_{\text{esc}} = 544 \text{ km/s}$. Results labelled "M" were obtained assuming the Migdal effect [87]. Results labelled "Surf" are from experiments not operated underground. The ν -floor shown here for a Ge target is a discovery limit defined as the cross section σ_d at which a given experiment has a 90% probability to detect a WIMP with a scattering cross section $\sigma > \sigma_d$ at ≥ 3 sigma. It is computed using the assumptions and the methodology described in [88, 89], however, it has been extended to very low DM mass range by assuming an unrealistic 1 meV threshold below $0.8 \text{ GeV}/c^2$. Shown are results from CDEX [90], CDMSlite [91], COSINE-100 [70], CRESST [92, 78], DAMA/LIBRA [93] (contours from [94]), DAMIC [95], DarkSide-50 [96, 86], DEAP-3600 [81], EDELWEISS [97, 98], LUX [85, 99], NEWS-G [100], PandaX-II [84], SuperCDMS [101], XENON100 [102] and XENONIT [103, 24, 83]. Figure taken from [1].

thanks to photographic or fine-granularity track readout (see Fig. 1.2 f). The most common target gas used is CF_4 , sometimes in mixture with other quenching gases, such as: MIMAC [106], NEWAGE [107], and DMTPC [108]. The DRIFT experiment, which has pioneered the directional effort, operating a $1 \text{ m}^3 \text{ CS}_2 + \text{CF}_4 + \text{O}_2$ TPC in Boulby achieved the best SD limit from a directional experiment [109]. The CYGNUS proto-collaboration has been formed, and gathers most of the groups working on directional DM detection in the world. Their goal is to carry out R&D to determine the optimum configuration for a large target mass directional detector of up to 1000 m^3 [110].

Figure 1.3 presents the status of direct detection searches in the case of spin-independent WIMP-nucleon interaction. Above WIMP mass of $6 \text{ GeV}/c^2$, the strongest constraints come from the LXe TPCs XENON1T, LUX, and PandaX-II. XENON1T has the best sensitivity to WIMPs in this mass-range thanks to its 2.0 ton target and $1.0 \text{ ton}\times\text{year}$ exposure [103]. The results from the LAr experiments DarkSide-50 [96] (TPC, 46 kg ^{39}Ar depleted target) and DEAP-3600 [81] (single-phase, 3.6 ton target) are presently limited due to the requirement for approximately five times higher exposure than xenon (due to favourable enhancement of the cross section on xenon at low threshold), and the currently low acceptance in DEAP-3600. In the mass ranges $1.8\text{--}3.5 \text{ GeV}/c^2$ and from $3.5\text{--}6 \text{ GeV}/c^2$, the most stringent exclusion limits were placed by DarkSide-50 [86] and XENON1T [24]. Both results use only the ionisation signal to lower the threshold to $0.1 - 0.2 \text{ keVee}$. Due to their much lower sub-keV thresholds, cryogenic experiments ionisation/scintillation and phonon readout are very sensitive to low-mass WIMPs. Ge-based detectors, e.g., CDMS, improve the low-mass sensitivity by exploiting the Neganov-Trofimov-Luke effect [111] (see Sec. 1.3). Using a 24 g CaWO_4 crystal with a threshold of 30.1 eV, CRESST-III currently places the most stringent constraints from $0.16\text{--}1.8 \text{ GeV}/c^2$ [78]. Exploiting the Migdal effect [112, 87] (see Sec. 2.2) extends the reach further into the MeV/c^2 -regime. Several results using this effect were already published [99, 97] with the strongest ones being from XENON1T [83] and CDEX [90] above and below $110 \text{ MeV}/c^2$, respectively. Also shown as the brown contours is the 12.9σ DM detection claim from DAMA/LIBRA [69] which is in strong tension with the other experiments in the case of a standard SI interaction. Lastly, the orange dashed curve shown in Fig. 1.3 is the so-called “neutrino floor” which is defined as the cross section σ_d at which a given experiment has a 90% probability to detect a WIMP with a scattering cross section $\sigma > \sigma_d$ at ≥ 3 sigma. The latter will dramatically limit impact the discovery reach of future direct detection experiments [88]. This fundamental limit imposed by the cosmic neutrinos is discussed in greater details in the following section 1.2.3.

1.2.3 The neutrino background

Significant increases in WIMP sensitivity are expected in the next few years as detector target masses are increased to the ton-scale and beyond (see e.g., Ref. [1]). As anticipated in early work on direct detection, these large detectors will also be able to detect the coherent elastic neutrino-nucleus scattering (CENNS) of astrophysical neutrinos [113, 114, 115, 116]. Neutrinos are therefore the ultimate background for WIMP direct detection searches as they cannot be shielded against and produce recoils with similar rates and energy spectra [114, 115, 116, 88]. The CENNS process, well predicted within the Standard Model, was only recently observed for the first time by COHERENT in 2017 [117, 118]. It proceeds via a neutral current and has a coherence effect at low momentum transfer that approximately scales with the number of neutrons squared [119, 120, 121]. Similarly to the SI independent WIMP-nucleus interaction, at higher recoil energies, generally above a few tens of keV, the loss of coherence is described by the nuclear form factor $F(E_r)$, for which we use the standard Helm ansatz [54] – an excellent approximation at these still relatively low energies [122]. The differential cross section as a function of the nuclear recoil energy (E_r) and neutrino energy (E_ν) is given by [119, 120, 121]

$$\frac{d\sigma}{dE_r}(E_r, E_\nu) = \frac{G_F^2}{4\pi} Q_W^2 m_N \left(1 - \frac{m_N E_r}{2E_\nu^2}\right) F^2(E_r), \quad (1.10)$$

1.2 WIMP direct detection

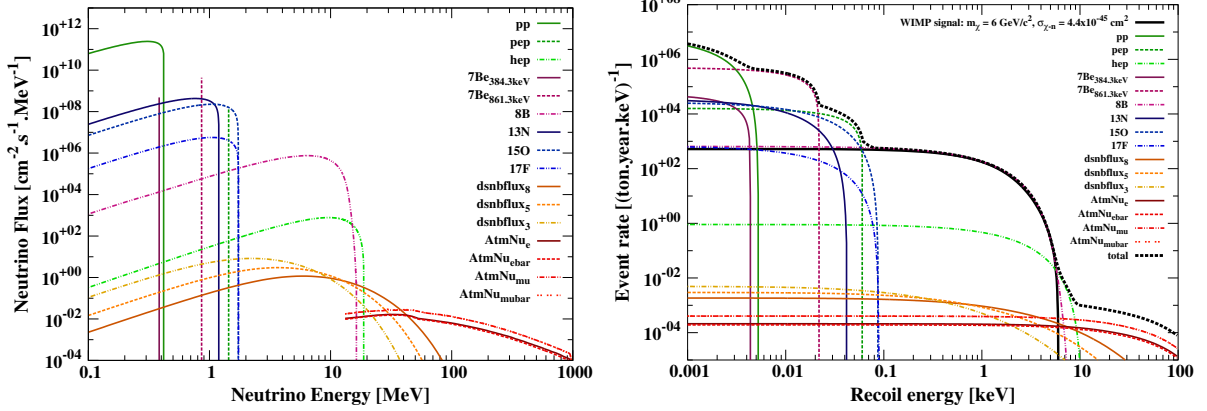


Figure 1.4: **Left:** Relevant neutrino fluxes to the background of direct dark matter detection experiments: Solar, atmospheric, and diffuse supernovae [123, 124, 125]. **Right:** Neutrino background event rates for a germanium based detector. The black dashed line corresponds to the sum of the neutrino induced nuclear recoil event rates. Also shown is the similarity between the event rate from a $6 \text{ GeV}/c^2$ WIMP with a SI cross section on the nucleon of $4.4 \times 10^{-45} \text{ cm}^2$ (black solid line) and the ${}^8\text{B}$ neutrino event rate. Figures taken from [89]

where $Q_W = A - Z - (1 - 4 \sin^2 \theta_W)Z \approx N$ is the weak hypercharge of a nucleus with mass number A and atomic number Z , G_F is the Fermi coupling constant, $\sin^2 \theta_W = 0.2312$ is the weak mixing angle [8], and N is the number of neutrons.

In figure 1.4 (left panel), we present all the neutrino fluxes that will induce relevant backgrounds to dark matter detection searches. The different neutrino sources considered in this study are the sun, which generates high fluxes of low energy neutrinos following the pp-chain [123, 126] and from the CNO cycle [127, 128], diffuse supernovae (DSNB) [125] and the interaction of cosmic rays with the atmosphere [124] which induces low fluxes of high energy neutrinos. Note that we use the standard solar model BS05(OP) and the predictions on the atmospheric and the DSNB neutrino fluxes from [124] and [125] respectively.

The different corresponding CENNS event rates are shown in Fig. 1.4 (right panel) for a Ge target. We can first notice that the highest event rates are due to the solar neutrinos and correspond to recoil energies below 6 keV. Indeed, the ${}^8\text{B}$ and *hep* neutrinos dominate the total neutrino event rate for recoil energies between 0.1 and 8 keV and above these energies, the dominant component is the atmospheric neutrinos. Also shown, as a black solid line, is the event rate from a $6 \text{ GeV}/c^2$ WIMP with a SI cross section on the nucleon of $4.4 \times 10^{-45} \text{ cm}^2$. We can already notice that for this particular set of parameters (m_χ, σ_{SI}), the WIMP event rate is very similar to the one induced by the ${}^8\text{B}$ neutrinos. As discussed in the next section, this similarity will lead to a strongly reduced discrimination power between the WIMP and the neutrino hypotheses and therefore dramatically affect the discovery potential of upcoming direct detection experiments⁵.

⁵Note that in this study we did not consider neutrino-electron scattering, even though it is predicted to provide a substantial signal in future dark matter detectors [88]. Our primary motivation for this is because the neutrino-electron spectrum is flat and is therefore easy enough to be distinguished from a WIMP signal.

1.2 WIMP direct detection

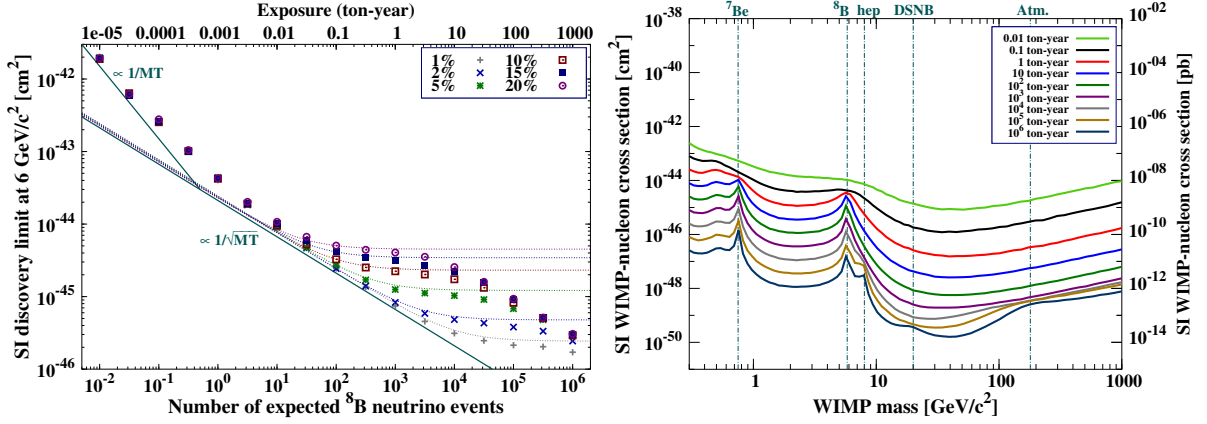


Figure 1.5: **Left:** Evolution of the discovery limit for a SI interaction as a function of the exposure for an idealized Xe experiments with perfect efficiency and a 3 eV threshold. The discovery limit is shown for a 6 GeV/c² WIMP mass for different values of the systematic uncertainty on the ⁸B flux. The second and third regions (background subtraction and saturation regime) are well described by equation 1.11 as shown by the dashed lines corresponding to the different systematic uncertainties. **Right:** Evolution of the discovery limit as a function of exposure on the WIMP mass vs SI cross section plane. These limits are computed for an idealized Xe-based experiment with no other backgrounds, 100% efficiency, and an energy threshold of 3 eV to fully map the low WIMP mass discovery limit. Features appearing on the discovery limits with increasing exposures are due to the different components of the total neutrino background, see neutrino fluxes from Fig.1.4 (left panel). Figures taken from [89].

Figure 1.5 (left panel) presents the evolution of the discovery limit for a WIMP mass of 6 GeV/c² as a function of exposure which is given in number of expected ⁸B neutrinos and ton-year on the bottom and top x-axes. Those calculations were done considering different values of the systematic uncertainties on the relevant neutrino background. From looking at Fig. 1.5, one can understand the impact of the neutrino background on the discovery potential which is worth describing in a couple of main points:

- At the lowest exposures, when the neutrino background is negligible, and if no other backgrounds are present, the discovery potential evolves as $\sim 1/MT$ where MT refers to the exposure (mass \times time) of the considered experiment.
- As soon as the experiment starts to become sensitive to the neutrino background, the discovery potential evolves as $\sim 1/\sqrt{MT}$ as we are in a Poisson background subtraction regime.
- When the exposure gets even bigger and the WIMP and neutrino signals are very similar, such as for a WIMP of 6 GeV/c² for a Xe target, the discovery potential starts to flatten out due to the systematic uncertainties. Indeed, in the extreme case where there is no discrimination power between the WIMP signal and the neutrino background, one would

1.2 WIMP direct detection

expect the discovery potential to evolve as [88]:

$$\sigma_{\text{disco}} \propto \sqrt{\frac{1 + \xi^2 N_\nu}{N_\nu}} \quad (1.11)$$

where ξ is the relative uncertainty on the relevant neutrino background and N_ν is the expected number of neutrino (CENNS) events. One can then see that the level and exposure at which the discovery potential flattens out is directly related to the level of this systematic uncertainty, as illustrated by Eq. 1.11 and shown in Fig. 1.5 (left panel). This clearly highlights the need for reducing systematic uncertainties on the neutrino fluxes and the CENNS cross section. Note that this saturation of the discovery potential can span about 2 orders of magnitude in exposure and therefore clearly represents a challenge to the development of future direct detection experiments.

- Once enough neutrino events have been accumulated (between a few thousands and a million, depending on the systematic uncertainty), one can get back to a standard Poisson background subtraction regime and therefore overcome the previously described saturation regime. This is due to the small differences in the tails of the neutrino- and WIMP-induced spectra which lead to additional discrimination power, e.g., Fig 1.4 (right panel) around 6.5 keV for the 6 GeV/c² case. However, these small differences in the induced spectra only become relevant at very high exposures and would highly depend on the detector’s energy resolution.

In Figure 1.5 (right panel) we illustrate the evolution of the discovery limit, in light of the neutrino background, as a function of the WIMP mass. We considered an idealized Xe-based experiment with a recoil energy threshold of 3 eV and perfect efficiency to map out the low and high WIMP mass range. This figure clearly shows that there are some particular WIMP mass ranges for which we expect the neutrino background to dramatically affect the discovery potential, *i.e.* going through a saturation regime. A few examples are for masses around $m_\chi = 0.8$ GeV/c², $m_\chi = 6$ GeV/c², $m_\chi = 8$ GeV/c² and above $m_\chi = 100$ GeV/c² where the WIMP signal is well mimicked by the ⁷Be, ⁸B, *hep* and the atmospheric neutrinos respectively. For WIMP masses with strong differences between the WIMP and the neutrino recoil spectra, the discovery potential evolves close to $1/\sqrt{MT}$ as one can see from Fig. 1.5 (right panel) for WIMP masses between 1 GeV/c² and 4 GeV/c² for example. This mass range is exactly what is being targeted by the high energy resolution cryogenic experiments.

In conclusion, this study suggests that the neutrino background will soon dramatically impact the DM discovery reach of upcoming eV-scale (keV-scale) energy threshold experiments with kg-year (ton-year) exposures. However, as demonstrated in figure 1.5, though there is no “rigid” neutrino induced limitation, as it depends on the exposure and the considered WIMP mass, we have defined the so-called “neutrino-floor” as the cross section σ_d at which a given experiment has a 90% probability to detect a WIMP with a scattering cross section $\sigma > \sigma_d$ at ≥ 3 sigma within three DM mass regimes corresponding to different exposure and thresholds in order to observe 1) 10,000 *pp* induced events for $10 \text{ MeV}/c^2 \leq m_\chi \leq 0.8 \text{ GeV}/c^2$, 2) 200 ⁸B induced events for $0.8 \text{ MeV}/c^2 \leq m_\chi \leq 6 \text{ GeV}/c^2$, and 3) 400 atmospheric induced events for $m_\chi \geq 6 \text{ GeV}/c^2$. Figure 1.3 presents the overall neutrino floor, computed for DM masses from

1.3 Searching for low-mass dark matter with EDELWEISS

10 MeV up to 10 TeV and a Ge target, shown as the dashed orange line [88, 89]. It is clear that next generation experiments will begin to be limited by the cosmic neutrinos, especially for WIMP masses around $6 \text{ GeV}/c^2$ where the ^8B neutrinos are expected to strongly affect their upcoming discovery potential. Eventually, it is worth emphasizing that many strategies have been investigated in order to mitigate or even by-pass this ultimate bound, such as:

Target complementarity: in [89] we have shown that combining different target materials does help significantly at reducing the impact of the neutrino background, but only in the context of spin-dependent WIMP searches,

Annual modulation: in [129] we have shown that annual modulation would help at disentangling the WIMP signal from the neutrino contribution but due to the very weak expected modulation strength, the benefit is only marginal,

Directional detection: in [129] we have shown that the most efficient strategy at mitigating the neutrino background is to measure the nuclear recoil direction. Indeed, in the case of Solar neutrino, the angular distance between the Sun and the constellation Cygnus is always comprised between 60° (February) and 120° (September), which is enough to allow clear separation between the two contributions even with angular resolutions as bad as 30° (RMS). The atmospheric and DSNB neutrinos are expected to be rather isotropic hence allowing to be well subtracted.

Despite the fact that the neutrino will dramatically impact the reach of future next generation direct detection experiments, it will also open the possibility to study cosmic neutrinos with a new approach. For instance, in a recent study we have shown that the combination of the pp and ^8B neutrino detection, respectively from elastic scattering on electrons and CENNS, will allow to test new physics scenarios in the vacuum/matter dominated transition in the Solar electron-neutrino survival probability [130]. This is of course only one of the myriad of opportunities that future direct detection experiments sensitive to cosmic neutrinos, combined with future CENNS dedicated experiments at nuclear reactors, will be able to probe in the coming decade.

1.3 Searching for low-mass dark matter with EDELWEISS

The EDELWEISS experiment has been initiated in the 90's and has completed its third phase, operated from the *Laboratoire Souterrain de Modane* (LSM), the deepest European's laboratory. With an overburden of about 4800 m.w.e the muon flux at LSM has been measured to be of $5 \text{ muons}/\text{m}^2/\text{day}$ [80]. Figure 1.6 (left panel) shows the technical drawing of the EDELWEISS setup at LSM. The dilution refrigerator hosting the bolometers is surrounded by 20 cm of lead (including 2 cm of roman lead), 50 cm of polyethylene, and a 100 m^2 active muon veto [80]. The reversed cryostat, allowing access to the bolometers from the top, can host up to 40 kg of cryogenic detectors in its 50 liter experimental volume. Based on previously acquired experience in the limiting surface backgrounds, the EDELWEISS-III experiment operated 24 FID800 cryogenic detectors. Figure 1.6 (right panel) shows a picture of a FID800 detector which are made of ultrapure germanium cylindrical crystals with a height of 4 cm, a diameter of 7 cm and a mass of 820-890 g [80]. These detectors are instrumented to perform a double heat-and-ionization measurement of signals arising from particle interactions. The double read-out is used to discriminate background-induced electron recoils (ER) from potential WIMP-induced

1.3 Searching for low-mass dark matter with EDELWEISS

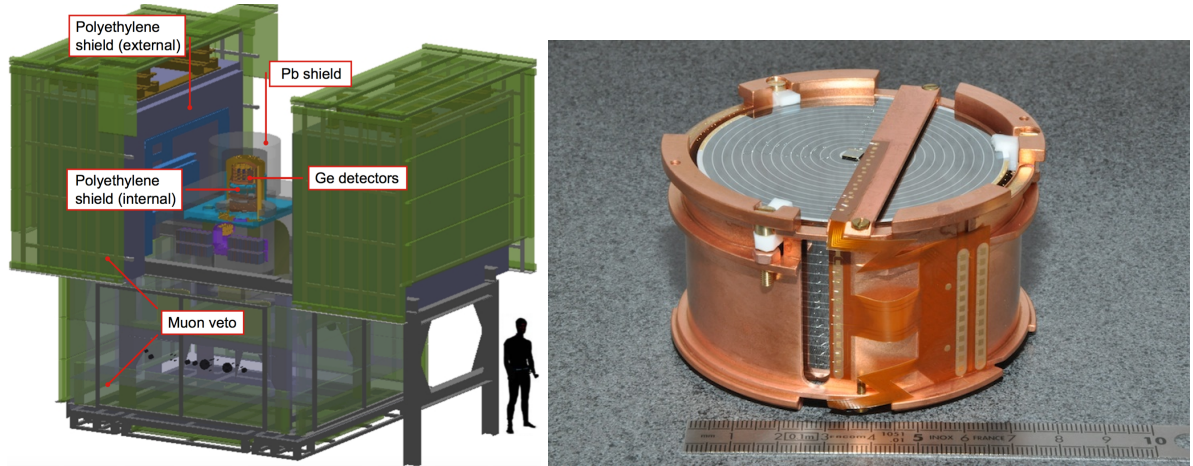


Figure 1.6: **Left:** Schematic view of the EDELWEISS-III setup showing in the center the cryostat hosting the germanium bolometers, surrounded by passive lead (Pb) and polyethylene shields and an active muon veto in order to protect the detectors from various backgrounds. **Right:** Photo of an 860-g FID detector with concentric ring electrodes covering the entire crystal surface and embedded in its copper casing held by Teflon clamps. Figures taken from [80].

nuclear recoils (NR) on an event-by-event basis.

Heat signals are measured with two Neutron Transmutation Doped (NTD) Ge sensors [80] glued at the center of the top and bottom surfaces of the crystal⁶. The resulting temperature dependence of NTD-Ge heat sensors is well described by the Shklovskii-Efrös law given by [131]:

$$\rho(T) = \rho_0 \exp(\sqrt{T_0/T}) \quad (1.12)$$

where ρ_0 depends on the intrinsic properties of Ge and of geometrical factors, and T_0 is related to the germanium doping level. As exemplified by the previous equation, the NTD resistance increases quickly with lowering the temperature. They are usually tuned to have 1-100 M Ω resistance values in the 7-20 mK temperature range. The heat pre-amplification electronics in EDELWEISS-III is based on IFN860 bi-JFETs, allowing for a differential readout, with an AC modulated current in the 500 Hz range. This differential modulation technique has been originally developed for the Archeops balloon and Planck satellite to efficiently reject both the electronics $1/f$ contribution and common-mode noise sources [80].

Ionization signals are measured thanks to the 200 nm thick Al electrodes evaporated on the whole Ge crystal, both flat and side surfaces, in the form of annular concentric rings 150 μm wide with a 2 mm pitch. The concentric electrodes are connected electrically such that all odd-numbered rings are connected to each other as well as all even-numbered rings. This leads to four groups of electrodes, *i.e.* 2 collecting and 2 surface veto electrodes, allowing an efficient discrimination between bulk and surface events. The FID800 electrode capacitance is

⁶It is worth noticing that the FID800 detectors also have a 20 mm² gold pad on the top surface used to tune the thermal leak. This is a major difference with the RED detector prototypes presented in Chap. 4 and 5 where the thermal leak is done through the NTD itself.

1.3 Searching for low-mass dark matter with EDELWEISS

about 100 pF and they are readout with a voltage pre-amplifier using IF1320-JFET. As further discussed in chapter 4, despite their low-noise application, the ionization resolution is limited from the intrinsic current noise from this JFET-based electronics.

The EDELWEISS and SuperCDMS experiments have pioneered the use of cryogenic semiconductor crystals (Ge and Si) to search for Dark Matter particles. Following a particle's interaction in the detector medium, the induced recoil (electronic or nuclear) will release its energy by creating both phonons (heat) and charge carriers (ionization). To first order⁷, the different measurable energy quantities are intertwined as follows:

$$E_{\text{ion}} = Q(E_R)E_R, \quad E_{\text{NTL}} = E_{\text{ion}}\frac{V}{\epsilon}, \quad \text{and} \quad E_{\text{heat}} = E_R + E_{\text{NTL}} = E_R \left[1 + Q(E_R)\frac{V}{\epsilon} \right] \quad (1.13)$$

where V is the voltage bias and ϵ is the average energy required for an electron recoil to produce an electron-hole pair. E_{heat} and E_{ion} stand for the heat and ionization energies, respectively. E_{NTL} is the additional Neganov-Trofimov-Luke heat energy produced by drifting the charge carriers across the crystal [134, 135]. The quenching factor $Q(E_R)$ is equal to 1 for electronic interactions by definition, whereas it is between 0 and 0.3 for nuclear recoils between 0 and 20 keV [136]. Following Eq. (1.13), two operating modes can be considered:

NR/ER discrimination mode: By operating the detector at bias voltages low enough, such that $E_{\text{NTL}} \ll E_R$ for nuclear recoils, the simultaneous measurement of heat and ionization provides an event-by-event identification of the recoil type, hence allowing a highly efficient rejection of the dominant gamma backgrounds as well as the majority of beta-backgrounds. Residual gamma- and surface beta-backgrounds are further removed using the active surface rejection, thanks to veto electrodes, of the FID detector design [80]. It is worth highlighting that, in addition to the event-by-event discrimination, the simultaneous heat and ionization energy measurements also provides a direct measurement of the true nuclear recoil energy, hence avoiding any assumptions on the ionization yield to be made.

NTL boosted mode: By operating the detector at high voltage biases (≥ 100 V), the cryogenic calorimeter is effectively turned into a charge amplifier of mean gain $(1 + Q(E_R)\frac{V}{\epsilon})$. As $E_{\text{heat}} \simeq E_{\text{ion}}$, event-by-event discrimination is no longer possible and an ionization yield model has to be assumed to convert the total heat energy into a nuclear recoil energy equivalent. It should be noted that, thanks to the much higher ionization yield of electron recoils compared to nuclear recoils, this operation mode is highly beneficial to any DM searches looking for interactions with the electrons instead of nuclei.

The EDELWEISS collaboration successfully achieved an average baseline energy resolution (RMS) of 400 eV and 200 eVee for the heat and ionization channels, respectively. Thanks to the double heat and ionization measurement, EDELWEISS has demonstrated a gamma and surface-beta rejection factors better than $< 2.5 \times 10^{-6}$ and $< 4 \times 10^{-5}$ at 90% C.L. respectively, while keeping a nuclear recoil acceptance of about 75% down to a nuclear recoil energy of 15 keV [80]. Thanks to these detector performance, the collaboration achieved leading exclusion limits on SI interactions for WIMP masses from 5 to 30 GeV/c² [98] (purple limit in Fig. 1.3), provided the first measurement of the cosmogenic activation rate of tritium in Ge

⁷We neglect here the phonon energy loss due to Frenkel defects [132, 133] and to charge trapping

1.3 Searching for low-mass dark matter with EDELWEISS

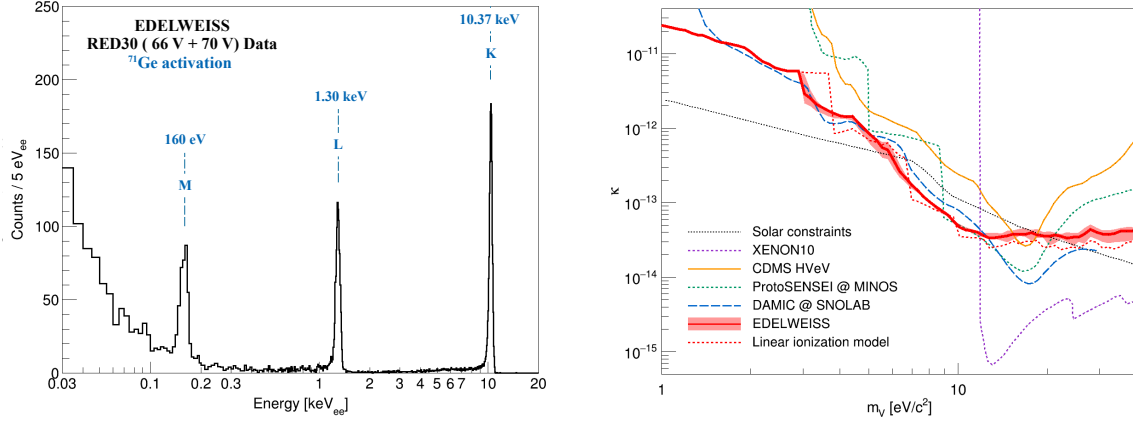


Figure 1.7: **Left:** Energy spectrum recorded with a bias of 66 V and 70 V following the ^{71}Ge activation of the RED30 detector at LSM. **Right:** 90% C.L. upper limit on the kinetic mixing κ of a dark photon. The shaded red band and dotted red line represent alternative charge distribution models. Also shown are constraints from other direct detection experiments [137, 138, 139, 140, 141], and solar constraints [142, 143]. Figures taken from [144].

above-ground [145], and derived leading limits on ALP dark matter candidates [146]. The next phase of the EDELWEISS experiment, called EDELWEISS-SubGeV, aims at probing DM particle candidates within the eV/c^2 -to- GeV/c^2 mass range by considering both DM interactions on electrons and nuclei.

In this context, the collaboration has recently demonstrated a 55 eV heat energy threshold on a 33.4 g Ge detector operated above ground leading to the most stringent above-ground limit on SI interactions above $600 \text{ MeV}/c^2$ [97] (see Chap. 2 and purple limit in Fig. 1.3). To enhance its sensitivity to DM particle masses from $500 \text{ MeV}/c^2$ to $5 \text{ GeV}/c^2$, and in synergy with RICOCHET, the collaboration is also developing new electrode designs and electronics to lower the particle discrimination threshold from $\sim 1 \text{ keV}$ to 50 eV in low voltage mode [147]. Lastly, the collaboration recently achieved an impressive 6 eVee energy threshold with a 33.6 g Ge detector operated at LSM in a high voltage mode (78 V). Figure 1.7 (left panel) shows the event energy distribution following a ^{71}Ge activation where we can clearly identify the X-ray lines from the electron-capture decays from the K/L/M shells at 10.37 keV, 1.3 keV, and 160 eV respectively. Thanks to this exquisite energy resolution, the collaboration has achieved the first Ge-based sub-100 MeV/c^2 dark matter search and the most stringent limit on Dark Photons below $\sim 10 \text{ eV}/c^2$ [144], as shown in Figure 1.7 (right panel). These first results are pathfinders to the upcoming EDELWEISS-SubGeV detector technology that will operate 30 g-scale Ge detectors both in low- and high-voltage modes for maximum sensitivity to various DM models. The CryoCube detector technology, currently being developed in the context of a precise measurement of the CENNS process at a nuclear reactor with RICOCHET (see Chap. 3 and 4), is a good candidate for the low-voltage approach. The high-voltage approach is being investigated within the SELENDIS Marie-Curie fellowship program and its follow-up CryoSEL project.

2

A light Dark Matter search from the IP2I above ground cryogenic facility

2.1 Introduction

This chapter describes the result obtained in a recent above-ground DM search performed by the EDELWEISS collaboration, called EDELWEISS-Surf, with a 33.4-g Ge detector operated from the IP2I cryogenic facility [97]. Such a search is bound to be limited by the large background induced by cosmic-ray interactions, but has the advantage of being able to probe models beyond the simple WIMP paradigm by considering relatively large values for the DM-nucleon cross sections. For sufficiently large values, each DM particle will typically interact many times in the atmosphere, Earth and shielding before reaching an underground detector. A DM particle loses energy with each interaction and may therefore arrive at the detector with insufficient energy to be observed above threshold [148, 149, 150, 151, 152, 153, 154, 155]. Above-ground searches minimize this ‘stopping’ effect in the Earth and therefore provide good sensitivity to large DM-nucleon cross sections. While most current constraints on strongly interacting massive particles (SIMPs¹) rely on a reanalysis of public data [158, 159, 160], we perform a dedicated search that fully takes into account the detailed detector response, presenting both the smallest and largest cross sections to which the experiment is sensitive.

We also present a search for WIMP-induced nuclear recoils which are accompanied by the ionization of an atomic electron [161, 162, 163]. The total energy in the nuclear recoil and ionization is typically larger than what can be deposited by elastic nuclear recoils at a given DM mass [87]. This ‘Migdal effect’ therefore allows one to probe lighter DM particles (for a fixed energy threshold) at the expense of a smaller event rate. Constraints using the Migdal effect have been reported previously for NaI crystal detectors [163] and liquid Xenon detectors [112, 99].

¹We use the term ‘SIMP’ here to refer to DM with large scattering cross sections with ordinary matter. However, we note that the term SIMP may also be used for hidden sector DM with strong self-interactions [156, 157].

2.2 EDELWEISS-Surf

Here, we present the first Migdal limit using a germanium target.

This chapter is organized as follows. In Sec. 2.2, we outline the experimental setup. In Sec. 2.3, we give details of the dark matter search, including data processing, detector calibration and data analysis. In Sec. 2.4, we present limits on weakly- and strongly-interacting DM, for both elastic nuclear recoils and the inelastic Migdal effect. The resulting exclusion regions are summarized in Fig. 2.10. Finally, we conclude in Sec. 2.5.

2.2 EDELWEISS-Surf

2.2.1 Detector

The detector prototype, called RED20, is shown in Fig 2.1. It consists of a cylindrical high-purity Ge crystal of 20 mm diameter and 20 mm height, corresponding to a total mass of 33.4-g. The thermal sensor design has been optimized for enhanced heat energy resolution. It consists of a Ge-NTD of $2 \times 2 \times 0.5$ mm³, glued on the top surface of the crystal, weakly thermally coupled to the copper housing of the detector thanks to gold wire bonds connecting its electrodes to two gold pads on a Kapton tape. With a total Ge-NTD electrode surface of 2 mm² this weak thermal link is about 2.1 nW/K which is sub-dominant with respect to the electron-phonon coupling of 6.7 nW/K ensuring that the detector properly integrates all of the heat signal [165].

The crystal is held by six PTFE clamps (three on each side) in order to ensure the mechanical constraints on all three axes of displacement and to minimize the stress due to PTFE elasticity at low temperatures. Unlike the usual EDELWEISS-III FID800 detectors [80], this detector prototype has only one heat channel and no ionization readout. Therefore, a discrimination between nuclear and electron recoils is not possible. However, as there is no electric field applied across the crystal, the detector acts as a true calorimeter measuring the deposited energy of the recoiling particle independently of its type (nuclear or electronic recoil). Quenching effects on the heat energy scale for nuclear recoils in Ge cryogenic detectors have been shown to be very small [133, 132], and are therefore neglected hereafter.

2.2.2 Experimental setup

The dark matter search has been performed in the dry dilution cryostat of the *Institut de Physique des 2 Infinis de Lyon* (IP2I) installed in a surface building with negligible overburden, see Sec. 2.4.2 and Sec. 5.1 for more details on the experimental setup briefly summarized here-

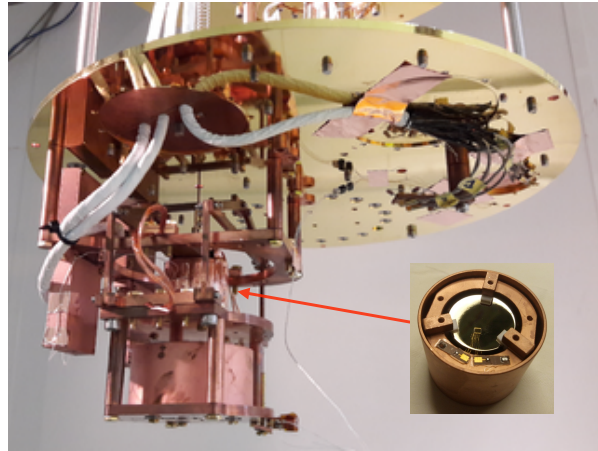


Figure 2.1: Photo of the detector tower suspended below the 10 mK stage, see Sec. 5.2 and [164]. The top detector (shown in inset) is the RED20 prototype under consideration for the DM search discussed here.

after.

The cryostat is a Hexadry-200 commercially available from Cryoconcept, which has been upgraded to reduce the vibration levels of the mixing chamber by mechanically decoupling the cold head of the pulse tube cryocooler from the dilution unit [166]. The vibrations at the detector level were further mitigated with the use of a dedicated suspended tower [164]. The latter consists in a 25 cm long elastic pendulum, attached to the 1 K stage by a Kevlar string and a stainless steel spring with an elastic constant of 240 N/m, holding the detector tower situated below the mixing chamber at 10 mK. The detector tower is thermally anchored to an intermediate holding structure, via supple copper braids, which also hosts the connectors for the detector readout. This suspended tower design reduces detector vibrations at the sub- $\mu\text{g}/\sqrt{\text{Hz}}$ level, with displacements in the order of a few nanometers (RMS) in all three axes, leading to substantial gains in energy resolutions as demonstrated in Ref. [164]. The cold and warm electronics are those described in Ref. [80], with a first Bi-FET preamplifier stage at 100 K and a second stage amplifier at 300 K.

The cryostat is surrounded by a 10 cm thick cylindrical lead shield covering a solid angle of $\sim 70\%$ of 4π around the detector. The materials used for the cryostat construction were not selected for low radioactivity, with the exception of the replacement of the standard glass fiber rods used by Cryoconcept by stainless steel ones, shown to have much less radioactive contamination. Finally, an ^{55}Fe calibration source was glued on the inner part of the detector's copper housing and facing the crystal surface opposite to the side on which is glued the Ge-NTD.

2.3 Dark Matter search

The dark matter search started two weeks after the mixing chamber reached its base temperature of 10 mK. During these first two weeks, the thermal response of the detector was studied, and its working point was optimized. The best heat energy resolution achieved was 17.7 eV (RMS), with the temperature of the suspended tower regulated at 17 mK and the Ge-NTD biased at 1 nA, leading to a steady state resistance of 3.4 M Ω . After the optimization period, it was decided to record six days of data in these conditions from May 22nd until May 27th 2018. It was decided beforehand to blind a 24-hour long data period started at 5 pm on May 26th. The remaining 5-days worth of data were then used to both tune the analysis procedure and selection cuts, and to build a data driven background model, in order to derive dark matter constraints from a blind analysis.

2.3.1 Data processing

The data acquisition used here is the same as from the EDELWEISS-III experiment located at the *Laboratoire Souterrain de Modane* [80]. In order to cancel common electronic noise sources and reduce microphonics, the voltage drop across the Ge-NTD is measured differentially and the current across it is modulated from positive to negative values, following a square wave function. A modulation frequency f_s of 400 Hz was chosen as it resulted in the best achievable signal-to-noise ratio in the experimental conditions considered here. The data are recorded continuously at this effective sampling frequency f_s , in so-called *stream mode*, such that there is no online trigger, unlike the standard EDELWEISS-III data acquisition. Instead, pulse signals

2.3 Dark Matter search

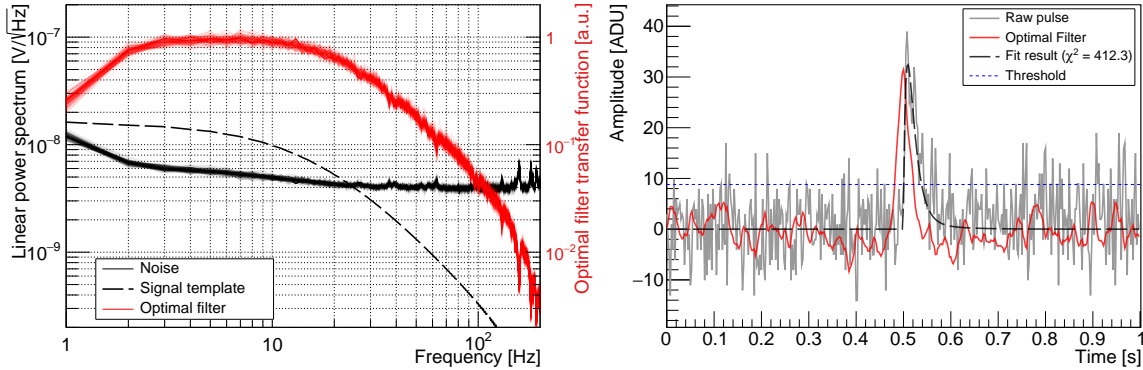


Figure 2.2: **Left:** Hourly-averaged noise Power Spectral Densities (PSD) (black curves), detector signal bandwidth (black dashed line), and resulting optimal filter transfer functions (red curves) as a function of frequency, for the six days of data acquisition. The 137 separate PSDs and transfer functions are overlaid. **Right:** Example of a 200 eV pulse: unfiltered raw trace (grey solid line) and output of the optimal filter (red solid line). The trigger level at 3σ is shown as the blue dotted line. The result of the pulse fitting procedure, with a $\chi^2/\text{ndf} = 1.03$, is shown as the black long-dashed line. Figures taken from [97].

are identified offline thanks to a dedicated signal processing pipeline, described in the following, which optimally filters the data based on the frequency dependence of the observed signal and noise. In order to avoid any noise structures at frequencies below the analysis range, from 1 Hz to 200 Hz, a second-order Butterworth numerical filter with a cut-off frequency of 2 Hz has been applied to the entire data stream before any selection of noise traces and triggers. Unless otherwise stated, the remaining part of the data processing is based on this pre-filtered data stream.

1) Noise PSD estimation

The noise Power Spectral Density (PSD) of the heat channel for an hour of recorded data is recursively determined from a random sample of 1-s time traces uniformly selected throughout the entire data stream for that hour. After an initial selection, based on their RMS dispersion, the removal of time traces containing pulses proceeds recursively by computing their individual frequency-based χ^2 with respect to the averaged PSD. The procedure stops once the mean χ^2 , from both the pre-filtered and raw data stream, from all selected time traces is compatible with the expected value of $N_s = 400$, corresponding to the number of time samples per trace. An average noise PSD is thus determined for each of the 137 hours that comprises the entire data set. These PSDs, corrected for the 2 Hz filter gain, are overlaid on Fig. 2.2 (left panel). The small dispersion shows that, despite its surface operation, the noise is very stable over the entire 6-days long run.

The PSD plateaus at a value of $4 \text{ nV}/\sqrt{\text{Hz}}$ above 20 Hz, with very little electromagnetic pickup contributions. This value is very well explained by the quadratic addition of the Johnson noise of the Ge-NTD ($1.8 \text{ nV}/\sqrt{\text{Hz}}$) and the current noise of the Bi-FET preamplifier. The slow rise

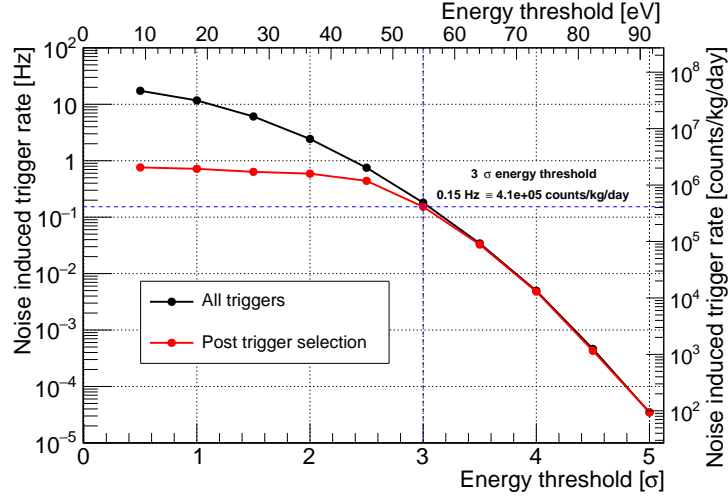


Figure 2.3: Evolution of the noise induced trigger rate (in Hz and counts/kg/day) as a function of the trigger level (in number n of σ_{OF} and eV), when considering (red) or not (black) the post-trigger selection.

in the noise level below 20 Hz, reaching a value of $6 \text{ nV}/\sqrt{\text{Hz}}$ at 2 Hz, is due to internal thermal fluctuation noise from the detector [167], see also Sec. 4.1.

2) Offline trigger

The offline trigger is based on a match filtered approach [168] designed to maximize the signal-to-noise ratio in the estimation of the signal pulse amplitude. The filter $H(f_i)$ considered hereafter is derived from the measured frequency dependence of the signal-to-noise ratio and is therefore defined as:

$$H(f_i) = h \frac{s^*(f_i)}{J(f_i)} e^{-j2\pi f_i t_M}, \quad (2.1)$$

where $s^*(f_i)$ is the complex conjugate of the signal template (shown as the black dashed line in the left panel of Fig. 2.2), $J(f_i)$ is the noise PSD in V^2/Hz (black solid lines), t_M corresponds to the time position of the pulse template maximum, and h is a normalization constant that preserves the amplitude of the pulse signal such that

$$h = \left(\sum_i \frac{|s(f_i)|^2}{J(f_i)} \right)^{-1}, \quad (2.2)$$

where f_i varies between $-f_s/2$ to $+f_s/2$. An optimally matching filter is determined from each of the recorded 137 hours. Their moduli $|H(f_i)|$ are also shown as the red solid lines in the left panel of Fig. 2.2. As one can derive from the latter, only the lowest frequencies (below 50 Hz) are relevant to recover the observed pulse amplitude. The filter from Eq. 2.1 is applied to the data using the numerical procedure described in Ref. [168]. As an example, the right panel of Fig. 2.2 shows a 200 eV event prior (grey solid line) and post (red solid line) filtering. Also shown is the best pulse fitting solution following the event processing procedure described in Sec. 3). Candidate events are identified when the filtered data exceed a given threshold level

2.3 Dark Matter search

which has been defined in terms of a fixed number n of the baseline energy resolution σ_{OF} , where $\sigma_{OF} = \sqrt{h}$.

The value of n was chosen such that the rate of noise induced triggers is significantly smaller than the rate of physical events, which is about ~ 1.3 Hz. The dependence of the rate of noise induced triggers as a function of n has been evaluated by simulating a 24-hour long stream of fake data using the observed noise PSD (see Fig. 2.2 - left panel), without injecting any signal pulses, and applying the same triggering procedure as for real data. The results from this study is shown in figure 2.3. The red and black curves respectively represent the evolution of the noise induced trigger rates with and without considering the post-trigger selection described below. We chose $n = 3$ as it resulted in an optimum between a low energy threshold and a reasonably low expected noise induced trigger rate of 0.15 Hz ($\sim 4 \times 10^5$ counts/kg/day). With the observed value of σ_{OF} of 18 eV, this corresponds to a trigger threshold of 55 eV shown as the blue dotted line in Fig. 2.2 (right panel).

The triggering procedure searches for candidate events in the filtered data stream, starting with the largest positive deviation from zero. An exclusion interval of ± 0.5 s is imposed around each pulse found, and the search is reiterated in the remaining data until no fluctuation greater than $n\sigma_{OF}$ is found. This energy ordering of the pulse finding algorithm affects the energy dependence of the triggering efficiency. For instance, the dead-time associated to the search for low-energy events is effectively greater than that associated to large pulses. A dedicated data-driven procedure, described in Sec. 2), has been developed to fully take into account these effects in the determination of the efficiency as a function of energy. The resulting trigger rate is almost constant over the six days and approximately equal to 0.58 Hz, as shown in the right panel of Fig. 2.4.

3) Event processing

Each recorded time trace, corresponding to either triggered events or noise samples, is further processed to estimate its amplitude by minimizing the following χ^2 function defined in the frequency domain as:

$$\chi^2(a, t_0) = \sum_i \frac{|\tilde{v}(f_i) - a\tilde{s}(f_i)e^{-j2\pi t_0 f_i}|^2}{J(f_i)}, \quad (2.3)$$

where $\tilde{v}(f_i)$ is the Fourier transform of the observed signal, a is the amplitude of the unit-normalized signal template s , and t_0 corresponds to the starting time of the pulse. For triggered events, the value of t_0 was allowed to vary within a 20 ms time window centered around the pulse time found by the trigger algorithm. In addition to delivering a slightly more precise estimation of the pulse amplitude a , this processing step provides a χ^2 value that quantifies the quality of the fit. This is used to reject pulses with shapes that are not consistent with the standard pulse, such as pile-ups and other categories of spurious events further detailed in Sec. 2.3.3.

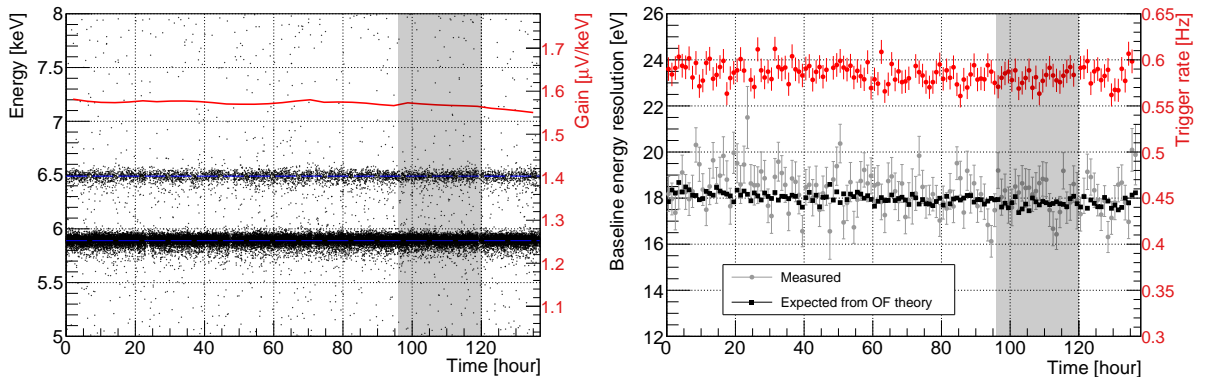


Figure 2.4: **Left:** Event energy distribution between 5 and 8 keV as a function of time. The horizontal bands at 5.90 and 6.49 keV correspond to the K_α and K_β X-ray lines, respectively, of Mn emitted by the ^{55}Fe source. The data have been corrected for the measured time-evolution of the detector gain as a function of time, shown as the red line, and corresponding to the right-hand axis. **Right:** Baseline heat energy resolution (RMS) in eV as a function of time. The grey dots are the values derived from a fit to the energy distributions of the noise event selection, and the black squares are those derived from the ratio of the signal and noise PSDs. The corresponding trigger rates in Hz are shown as red dots. Each data point corresponds to one hour. The grey shaded region in both panels corresponds to the interval of the blinded data set. Figures taken from [97].

2.3.2 Detector calibration and stability

1) Calibration

The energy calibration of the reconstructed amplitudes a was ensured by the use of a low-energy X-ray ^{55}Fe source irradiating the bottom side of the Ge crystal, opposite to the Ge-NTD heat sensor, inducing an interaction rate of ~ 0.3 Hz. The ^{55}Fe source produces two lines corresponding to the K_α and K_β lines of Mn at 5.90 keV and 6.49 keV, respectively. They are clearly visible on the left panel of Fig. 2.4, showing the calibrated energy as a function of time over the 137-hour acquisition period. The energy resolution of these peaks is 34 eV (RMS). There is sufficient statistics to calibrate each hour separately and to follow precisely any time evolution of the detector gain, defined as the voltage sensitivity per unit of deposited energy, and resolution. The red solid line on the same figure shows the variation of the heat sensor gain (in $\mu\text{V}/\text{keV}$) as a function of time deduced from the peak position. The gain fluctuations are remarkably small during the entire time period, with a mean value of $1.56 \mu\text{V}/\text{keV}$ and a maximal dispersion of $\sim 2\%$.

2) Baseline resolution stability

As mentioned in Sec. 2.3.1, the time traces used for the PSD determination, also called noise events, were also fitted with Eq. 2.3. However, in this case t_0 was arbitrarily fixed to the center of the 1-s time window, in order to estimate the amplitude distribution associated with noise

2.3 Dark Matter search

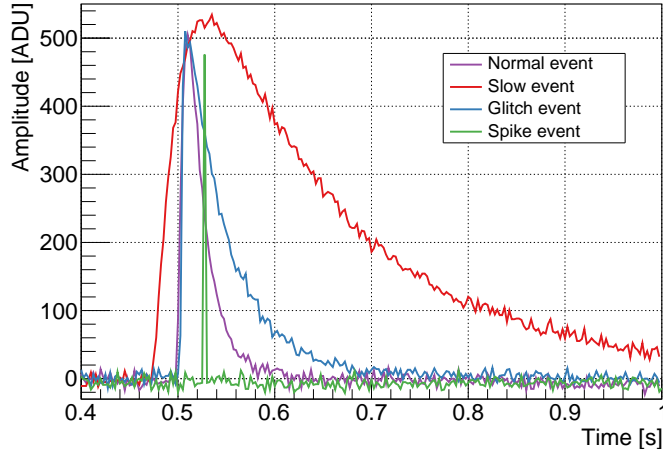


Figure 2.5: Pulse examples of the four type of events observed in the data set: *Normal* (purple), *Slow* (red), *Glitch/Fast* (blue), and *Spike* (green), which are further discussed in the main text.

events. The amplitudes are distributed according to a gaussian distribution with a standard deviation (RMS) σ that corresponds to the baseline energy resolution. This quantity, measured hour by hour, is compared to the prediction of the optimal filter resolution (σ_{OF}) on the right panel of Fig. 2.4. The good agreement between these two estimates of the energy resolution validates the assumption that the noise in each frequency bin is independent and gaussian. The average baseline energy resolution is 18 eV (RMS), with a $\sim 3\%$ overall decrease in σ_{OF} over the six days of the search. The average value of σ during the blinded data period is 17.7 eV (RMS). The stability of the noise is instrumental at maintaining an almost constant trigger rate, shown as the red dots in Fig. 2.4 (right panel), over the entire search period.

2.3.3 Data analysis

1) Selection cuts

Because of its above-ground operation and the moderate lead shield, the detector was exposed to a rather intense rate of high energy interactions in the bulk of the crystal as well as in the holding PTFE clamps and the Ge-NTD heat sensor. The pulse shape of events produced in these cases are very different. In total, we identified four types of events which are illustrated in Fig. 2.5 and further described hereafter:

Normal events: these correspond to the vast majority of observed events for which the incoming particle has interacted in the Ge crystal. They are characterized by a rise time of 6 ms and a decay time of 16 ms, as expected from our thermal model calculations [167], see Sec. 4.1.

Fast events: these are induced by incoming particles impinging the Ge-NTD heat sensor which has a non-negligible volume of 2 mm³, and from internal radioactivity of the Ge-NTD. They are characterized by a rise time of 2 ms, faster than normal events as expected, and a decay time constant of 41 ms. This longer decay time with respect to normal events could be explained by athermal phonons heating up the Au wire bonds from the weak thermal leak. This hypothesis is further strengthened by the fact that the amplitudes of these fast events are much smaller than anticipated from our theoretical calculations [167].

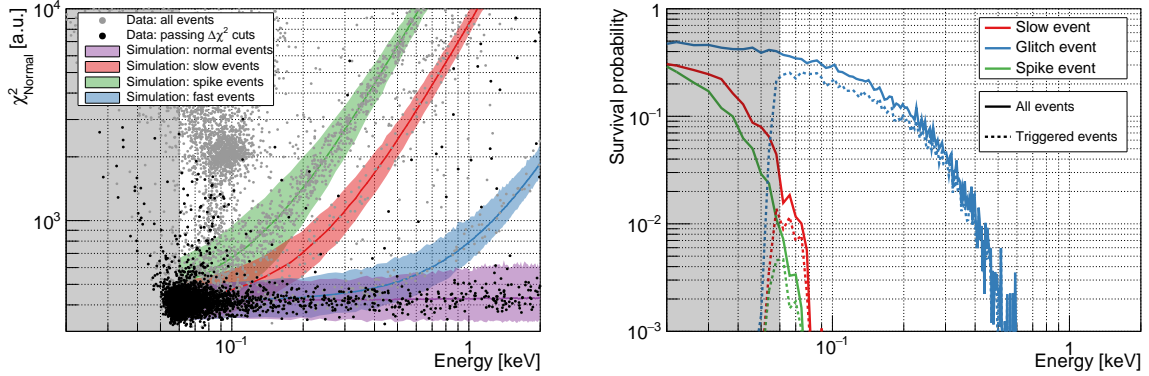


Figure 2.6: **Left:** Distribution of χ_{Normal}^2 as a function of energy for the events in the blinded data set. The events passing all $\Delta\chi^2$ cuts are shown as black dots while those rejected are shown as grey dots. The expected region where different pulse populations are expected are shown in purple (events with normal pulse shape), blue (fast pulses), red (slow pulses) and green (single-sample spikes). **Right:** Survival probability of the three type of background events: blue (glitch/fast pulses), red (slow pulses) and green (single-sample spikes), with (solid line) and without (dashed line) considering the trigger selection. Figures taken from [97].

Slow events: these could be produced by muon interactions in the holding clamps where $\mathcal{O}(1)$ MeV energy is deposited. Despite the very weak thermal coupling of these PTFE clamps to the Ge crystal, such high energy deposition can still produce some non-negligible rise in temperature of the crystal. These events are characterized by a mean rise time of 26 ms and a decay time constant of 115 ms, hence much slower than normal events. This population was later observed to be significantly reduced in detectors where the PTFE clamps have been replaced by a combination of sapphire balls with chrysocale sticks, and is almost non-existent in similar detectors operated underground at LSM.

Spike events: the data acquisition system used in this experiment (a former version of the one used by EDELWEISS-III [80]) suffers from random synchronization losses that result in occasional octal jumps in the data flow. These are well modelled by delta functions that can easily be discriminated from physical events.

To discriminate normal events from the other populations of events, including also pile-ups, cuts are performed on the goodness of fit parameter quantified by the χ_{Normal}^2 value from Eq. 2.3, where the subscript "Normal" refers to the use of the standard pulse template s in that equation. Additional pulse shape related selection cuts have been designed based on the χ^2 differences $\Delta\chi_k^2 = \chi_{\text{Normal}}^2 - \chi_k^2$, where χ_k^2 corresponds to the value calculated by replacing the standard pulse template for normal events s with the templates of the non-standard event population discussed above, *i.e.* k stands for *Fast*, *Slow* and *Spike*. All cuts were optimized on the non-blinded data set prior to un-blinding.

Figure 2.6 (left panel) shows the event distribution in the χ_{Normal}^2 versus energy plane before

2.3 Dark Matter search

and after applying the $\Delta\chi^2$ cuts (black and grey points, respectively). The colored bands, estimated from the dedicated pulse simulation discussed in Sec. 2), correspond to the 90% C.L. confidence bands for the four different types of events. Normal events are expected to have an averaged χ_{Normal}^2 value centered around $N_s = 400$ while the other event categories exhibit a quadratic divergence with increasing energy. As expected, the population of events that is the most alike to the normal ones, and therefore the hardest to reject efficiently, are the fast events. As illustrated in figure 2.6 (right panel), the combination of the various $\Delta\chi^2$ cuts and selecting events with $350 < \chi_{\text{Normal}}^2 < 450$ leads to survival probabilities of the three types of spurious events down to 10^{-2} above 60 eV for Slow and Spike events, and above 400 eV for Fast events. We note that the so-called Fast events are the hardest ones to reject due to their pulse shape similarities with the Normal ones, and if their Ge-NTD origin is confirmed then using 2 Ge-NTD could possibly improve their rejection. The additional event population observed centered at 100 eV and $\chi_{\text{Normal}}^2 \sim 2000$ corresponds to noise events where the first half of the pre-filtered time trace is affected by the tail of a previous pulse (mostly from ^{55}Fe), occurring a few hundreds of ms before the start of its 1-s time window. Note that this particular population of pile-up events, as all the other types of pile-up events that appear in the gaps between the colored bands in the left panel of Fig. 2.6 (left panel), is fully taken into account in the pulse simulation procedure described in Sec. 2), and is very well rejected by the standard χ_{Normal}^2 cut.

2) Efficiency

The trigger efficiency was evaluated using a dedicated pulse simulation where pulses are generated at random times throughout the entire real data streams. This procedure samples rigorously all possible baseline fluctuations, including those induced by tails of high-energy events, and other non-stationary behaviour, hence avoiding any possible selection-induced biases. It naturally accounts for live-time losses due to the physical event rate and comprehensively takes into account any systematic uncertainties or biases related to the processing pipeline. The following efficiency estimates, as well as the various simulated DM signals discussed in Sec. 2.4, were obtained by generating a total of 10^6 simulated events distributed over 1000 Monte Carlo iterations of injecting 1000 simulated pulses in the 24-hour long blinded data stream. This way, the simulated event rate (~ 0.01 Hz) is about two orders of magnitude lower than the real physical event rate, hence inducing negligible additional live-time losses. A full simulation of the DM signal is performed for each mass value in order to evaluate in each case the combined effect of the noise observed in the actual data stream, the trigger selection and the analysis cuts. Figure 2.7 (left panel) shows the details of the simulation of a $2 \text{ GeV}/c^2$ WIMP signal in the detector. The red long-dashed curve is the theoretical energy distribution from which are drawn the Monte Carlo sampling of the WIMP-induced recoil energies shown as the green and blue distributions before and after applying the selection cuts. Interestingly, one can see that before applying the selection cuts, a high energy tail appears in the green distribution due to pile-ups with physical events from the data stream. Also, one can appreciate that the slope of the simulated spectrum (blue histogram) is slightly harder than the theoretical one due to the energy resolution that is naturally taken into account with this approach.

To better illustrate and understand the detector performance, it is however useful to calculate an efficiency taken as the fraction of simulated events that survive all of these selection criteria, from a population of simulated events with energies uniformly distributed between 0 and 2.5

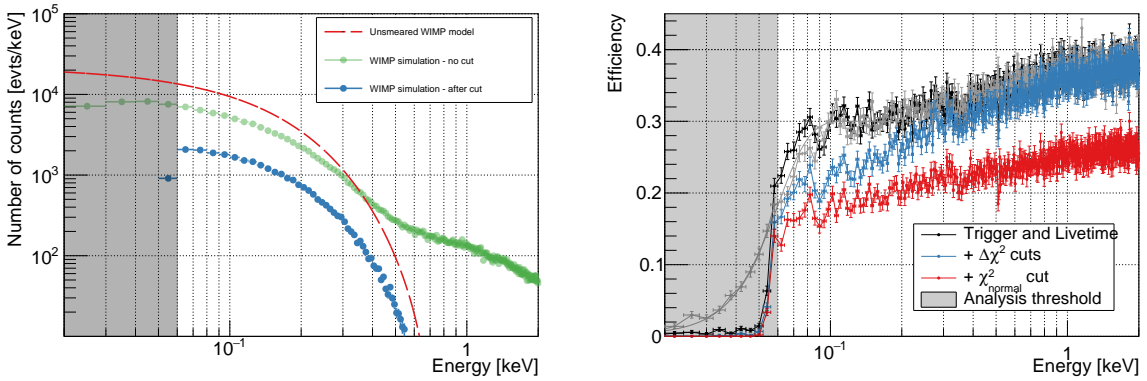


Figure 2.7: **Left:** Simulation of a $2 \text{ GeV}/c^2$ WIMP energy distribution where we show the theoretical unsmearred distribution (red long-dashed line), the resulting simulated energy distribution before (green) and after (blue) applying all the selection cuts detailed in the main text. **Right:** Signal efficiency as a function of heat energy for 10^6 simulated events injected in the data stream with energies uniformly generated between 0 and 2.5 keV, shown from 0 to 2 keV corresponding to the region of interest. Grey points: trigger plus live-time efficiency as a function of the input energy, together with a fit with an error function (grey line). Black points and line: trigger plus live-time efficiency as a function of the energy resulting from the χ^2 fit of a pulse to the data in the frequency domain. Blue points and line: the same, but after applying all $\Delta\chi^2$ cuts. Red points and line: the final efficiency obtained after applying the additional cut on χ_{Normal}^2 . In both panels, the grey area corresponds to energies below the analysis cut. Figures taken from [97].

keV. These resulting efficiencies at different stages of the trigger and analysis are shown in the right panel of Fig. 2.7. The black and grey points correspond to the variation of the combined trigger and live-time efficiency as a function of the reconstructed and input energy, respectively. The sharp rise around 55 eV of the efficiency curves expressed as a function of the reconstructed energy is due to the fact that the amplitude estimates from the triggering algorithm and the pulse processing are very similar. The rise of the efficiency as a function of the true input energy is much smoother and is well described by an error function centered at 55 eV with a dispersion of 18 eV, as anticipated from the observed baseline energy resolution and the considered 3σ trigger level. As discussed in Sec. 2.3.1, the trigger efficiency rises smoothly with energy, because of the energy ordering of the algorithm. Hence, between 0.1 and 2.0 keV, the trigger and live-time efficiency rises from 30% to almost 40%. These large dead-time losses can be expected given the size of the $\pm 0.5 \text{ s}$ exclusion time window compared to the observed trigger rate of 0.58 Hz. It has been tested that the dead time could be reduced by using shorter time traces, but at the cost of a slight deterioration of the energy resolution. As it was anticipated that this high-background DM search would not be limited by statistics, the emphasis was put on low thresholds and therefore energy resolution.

The right panel of Fig. 2.7 also shows the effect of the $\Delta\chi^2$ on the analysis efficiency. Those cuts have a significant effect on the signal below 200 eV, where all three background populations compete with the signal. Finally, the cut on the χ_{Normal}^2 value has a more uniform effect as a

2.3 Dark Matter search

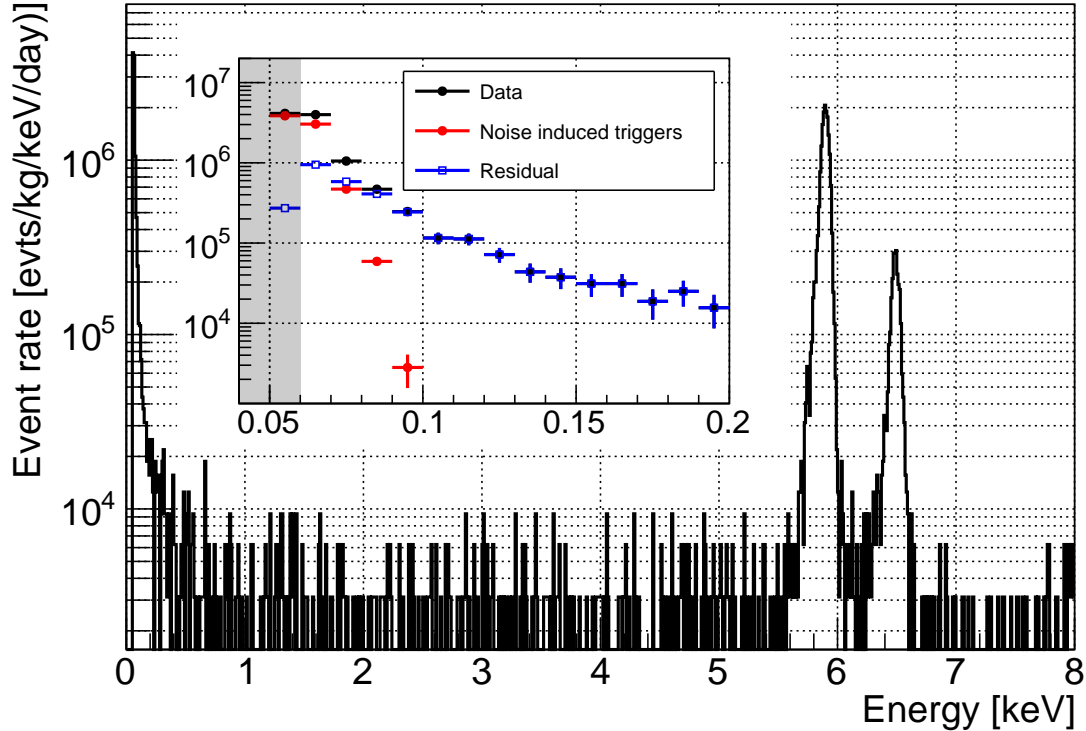


Figure 2.8: Energy spectrum recorded in the blinded day of the DM search data, after all cuts. The calibration lines from the ^{55}Fe source at 5.90 keV and 6.49 keV are clearly visible, and they exhibit an energy dispersion of 34 eV (RMS). The data are normalized in events per kilogram per day and per keV, but are not corrected for efficiency. The bin size is 10 eV. The inset shows a zoom of this distribution between 40 eV and 200 eV (black dots), as well as the energy spectrum observed in the simulated noise streams after all cuts (red dots). The blue squares are the difference between the two spectra. Figure taken from [97].

function of energy, as shown by the red points on the same figure.

3) Observed energy spectrum

The energy spectrum recorded within the blinded day of DM search data is shown in Fig. 2.8. The spectrum is dominated at high energy by the calibration source lines at 5.90 keV and 6.49 keV. A continuous and relatively flat background of $\sim 10^4$ evt/kg/keV/day is observed between 500 eV and 8 keV². The data below 500 eV, better illustrated in the inset figure, can be described approximately by an exponentially decreasing spectrum with a characteristic slope of 46.2 eV reaching 10^5 evt/kg/keV/day at 200 eV and culminating at 2×10^7 evt/kg/keV/day at the 60 eV analysis energy threshold. While the somewhat flat component of $\sim 10^4$ evt/kg/keV/day beyond a few-hundreds of eV can be explained by the superposition of the high gamma and

²The quoted background rates are corrected for the final efficiency as a function of energy (see red curve in Fig. 2.7 - right panel).

neutron environmental backgrounds, the sharp exponential rise starting below 200 eV is not yet fully explained. Dedicated studies are ongoing to better assess the origin of these events, see Sec. 5.3.4.

Finally, the inset figure also shows the contribution from the noise induced triggers (red histogram) that has been evaluated using the noise-only simulated data stream discussed in Sec. 2.3.1 and normalized using the predicted noise induced trigger rate from figure 2.3. This event population explains very well the observed spectrum below 70 eV and it has a negligible contribution to the total observed event rate above 80 eV. It should be noted that in order to derive conservative constraints on DM interactions, it was decided prior to un-blinding that this well anticipated and modeled background will not be subtracted.

2.4 Results

This section presents the limits on spin-independent interactions of DM particles with nucleons derived from the experimental spectrum of Fig. 2.8. In Sec. 2.4.1 the data are interpreted in the standard WIMP context where the signal is the kinetic energy of the nuclear recoil induced in the collision. In Sec. 2.4.2 we extend its interpretation to the case of SIMPs where Earth-shielding effects are taken into account. In Sec. 2.4.3 we consider the so-called Migdal effect where the DM-nucleus interaction is inelastic and simultaneously produces a nuclear and an electronic recoil, opening up access to an unexplored domain of cross sections for DM particles with masses well below 100 MeV/c². Finally, these results are interpreted in terms of spin-dependent interactions of DM particles in Sec. 2.4.4.

2.4.1 Weakly Interacting Spin-independent Dark Matter

The expected signal for the standard elastic DM interactions in the detector was simulated using the comprehensive pulse simulation, described in Sec. 2.3.3, that takes into account all systematic effects related to the detector response and data analysis. A total of 10⁶ fake DM-induced events were simulated for each DM mass considered. Their amplitudes were drawn from the theoretical distribution of induced nuclear recoils calculated assuming standard spin-independent interactions and using the standard astrophysical parameters for the DM velocity distribution [54]: a Maxwellian velocity distribution with an asymptotic velocity of $v_0 = 220$ km/s, and a galactic escape velocity of $v_{\text{esc}} = 544$ km/s. The local DM density at Earth position is assumed to be $\rho_0 = 0.3$ GeV/c²/cm³ and the lab velocity with respect to the DM halo is $V_{\text{lab}} = 232$ km/s. Also, the loss of coherence at high momentum is taken into account using the standard Helm form factor.

The objective of the search was to establish upper limits on the DM-nucleon cross section for each considered DM particle mass, using Poisson statistics and assuming that all events observed in a given energy interval are signal candidates. Prior to un-blinding the DM search data, the optimal energy intervals for such a purpose were determined by maximizing for each DM particle mass the signal-to-noise ratio between the simulated signals and the background model extracted from the 5 days of non-blinded data³.

³In the presence of a signal, this procedure overestimates the background and yields conservative bounds.

2.4 Results

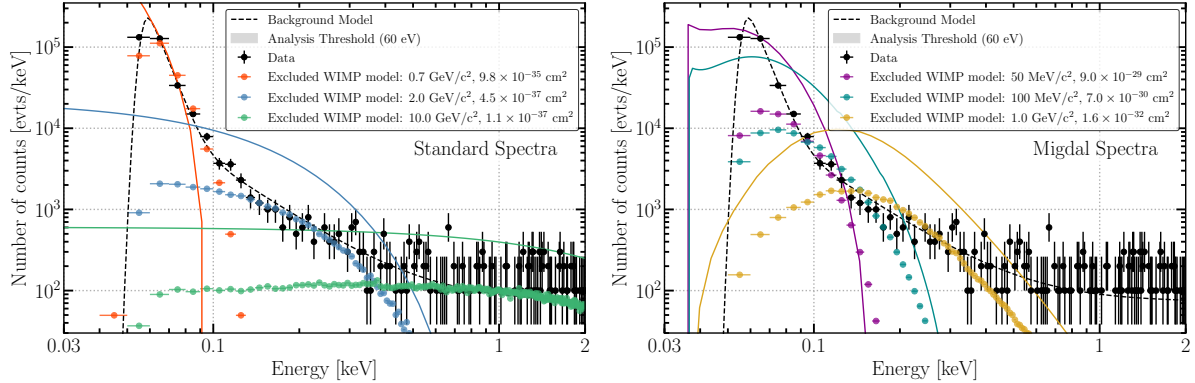


Figure 2.9: Comparison of the energy spectrum after all cuts for the blinded data set (black dots) with the background model derived from the five-day non-blinded data set (black dashed line). Also shown are the spectra for three excluded WIMP signals. The solid colored lines are the unsmeared WIMP spectra, while colored points are the simulated spectra that incorporate resolution effects and all cuts. **Left:** Standard elastic nuclear recoil spectra that are excluded for WIMPs with masses of $0.7 \text{ GeV}/c^2$ (red), $2 \text{ GeV}/c^2$ (blue) and $10 \text{ GeV}/c^2$ (green). **Right:** Inelastic Migdal spectra that are excluded for WIMPs with masses of $0.05 \text{ GeV}/c^2$ (magenta), $0.1 \text{ GeV}/c^2$ (cyan) and $1.0 \text{ GeV}/c^2$ (yellow). Figures taken from [97].

After the un-blinding, the numbers of counts in these intervals were extracted from the data shown in Fig. 2.8. In the left panel of Fig. 2.9, the derived 90% C.L. upper limits of signals for WIMPs with masses of 0.7, 2 and $10 \text{ GeV}/c^2$ are compared to the experimental data. The background model, *i.e.* the average spectrum recorded in the 5 non-blinded days, is also shown. Finally, the spin-independent WIMP-nucleon cross sections excluded at 90% C.L. as a function of the WIMP mass are shown as the solid red curve in Fig. 2.10, and compared with the other experimental results from Refs. [103, 85, 169, 170, 98, 171, 92, 172, 173, 112, 99], and the so-called neutrino floor [88, 89]. The EDELWEISS-Surf result is the most stringent, nuclear recoil based, above-ground limit on spin-independent interactions above $600 \text{ MeV}/c^2$.

2.4.2 Strongly Interacting Dark Matter

Thanks to its above-ground operation, the present DM search can probe SIMPs that would escape detection in underground experiments as the DM particles would be stopped in the rock overburden before reaching the detectors. We therefore extend the data interpretation of Sec. 2.4.1 to determine for each mass a range of excluded cross sections that take into account the absorption of the SIMP flux in the material above the detector. Overly conservative SIMP limits can be obtained by including in the analysis only those SIMPs that reach the detector without scattering [174]. Here, more stringent limits are obtained by fully taking into account the effect of scattering on the velocity distribution of the SIMP flux reaching the detector. This velocity distribution is calculated using the publicly-available `verne` code, introduced in Ref. [160]. It assumes continuous energy losses and straight-line trajectories for SIMPs travelling through the atmosphere, overburden and detector shielding [148]. Ref. [175] showed that this simplified formalism leads to constraints similar to more complete but computationally

expensive Monte Carlo simulations (e.g. [176, 177, 178, 179]).

The SIMP flux calculation takes into account the variation of the direction of the mean DM flux [59] over the course of the blinded EDELWEISS-Surf exposure (24 hours, starting 17h00 on 26th May 2018). It also accounts for the atmospheric overburden above the detector as well as shielding provided by the material in the building where the detector is located and the lead, steel and copper components in its vicinity. The dominant sources of stopping for downward-travelling particles are 20 cm (40 cm) of concrete from the ceiling (walls) and 10 cm of lead shielding which surrounds the detector in all directions, apart from an opening of around 50° above the detector. Upward-travelling particles are almost entirely stopped by the Earth.

The escape velocity from the surface of the Earth is around 11 km/s. For DM particles at such low speeds, effects such as gravitational capture [180, 181] and gravitational focusing [182] may become important. These effects are not incorporated in the flux calculation. Instead, the DM velocity distribution is conservatively set to zero below $v_{\text{cut}} = 20$ km/s when calculating SIMP bounds.

Using the signal calculated in these simulations, the same statistical procedure described in Sec. 2.4.1 is applied to derive the 90% C.L. upper bounds on the excluded cross section interval as a function of SIMP mass, resulting in the red contours shown in Fig. 2.10. The upper bound reported in this work improves upon the high-cross section reach of the CRESST 2017 surface run [92] (thin blue), as reported in Refs. [159, 160, 175]. This improvement is driven in part by the longer exposure of the EDELWEISS-Surf run, which covers a full day. This includes periods when the mean direction of the DM flux (set by the Sun’s velocity) is perpendicular to the Earth’s surface, reducing the attenuation effect of the Earth and atmosphere.

2.4.3 Migdal Search

As discussed in Sec. 2.2.1, the detector acts as a true calorimeter with equal sensitivity to the energy deposited by nuclear and electronic recoils. In this section, we consider the case where the WIMP or SIMP interaction with the target atoms induces simultaneously a nuclear recoil and the ionization of an electron. The final state comprises the two types of recoils. This is true in the case of the so-called Migdal effect, whose rate was calculated numerically in Ref. [87]. The calculations therein were performed for the case of *isolated* atoms and does not fully consider the band structure of the germanium semi-conductor which is particularly important for the valence electrons ($n = 4$).

In the absence of detailed calculations, we chose to neglect the contribution from the ionization of electrons in the $n = 4$ valence shell, as well as the much smaller contribution from excitation of electrons *into* the valence shell. The inner electrons $n \leq 2$ are too tightly bound to give an appreciable signal. Therefore, the only contribution considered here is that from the ionization of M-shell ($n = 3$) electrons. Once ionized, electrons are not free (as in Ref. [87]), but instead populate the conduction band. However, the band gap in germanium is typically much smaller than the M-shell ionization energies (~ 0.74 eV compared to 35–170 eV, respectively) and here we will also neglect this small correction. Electrons, radiation and nuclear recoils in that energy range have very short absorption lengths in germanium, and it can be considered that the detector will completely collect the energy from all contributions.

The same standard spin-independent DM-nucleus interactions are assumed as in the previous sections, and notably the ($\propto A^2$) dependence of the cross section arising from the coherent cou-

2.4 Results

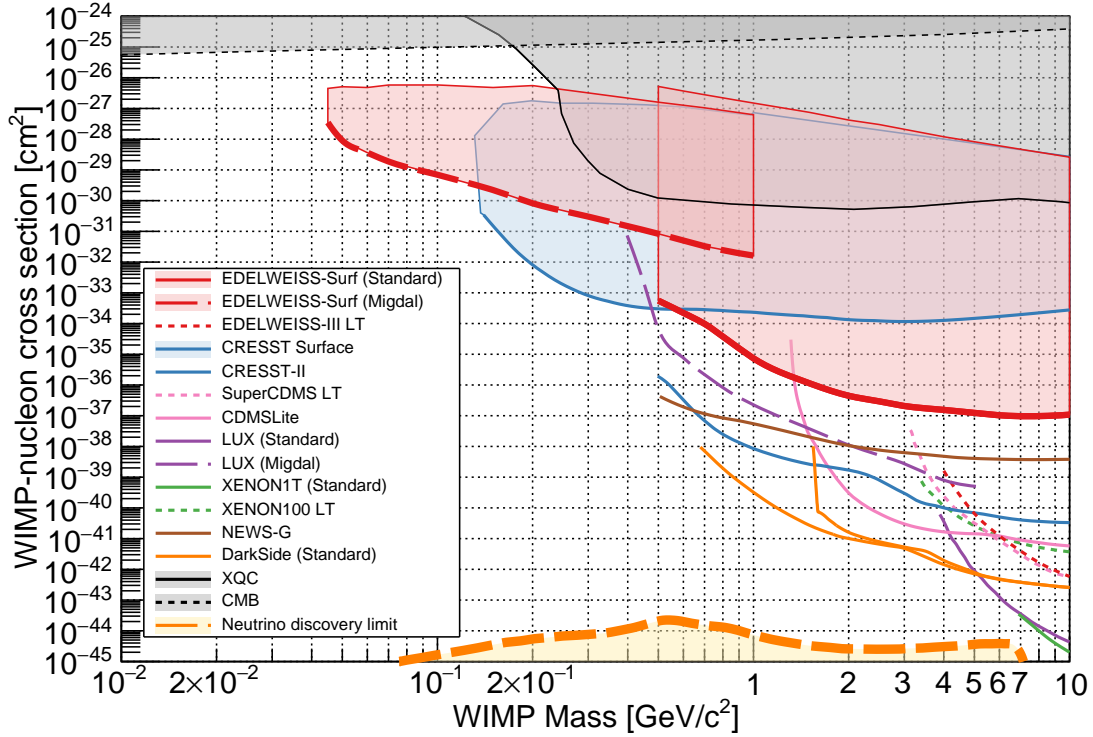


Figure 2.10: The 90% C.L. limits on the cross section for spin-independent interaction between a DM particle and a nucleon as a function of the particle mass obtained in the present work. The thick solid red line corresponds to the result from the standard WIMP analysis. The associated red contour is obtained from the SIMP analysis, taking into account the slowing of the DM particle flux through the material above the detector. The thick dashed line and its accompanying red contour is obtained in the Migdal analysis. These results are compared to those of other experiments (see legend). Other results using the Migdal effect are shown as dashed lines. The other shaded contours correspond to the SIMP analyses of the CRESST 2017 Surface Run [92, 159, 160] (blue contour), the XQC rocket [173, 179] (grey contour with full line) and the CMB [183] (grey contour with dashed line). Figure taken from [97].

pling to the whole nucleus. The Earth-shielding effects are taken into account as in Sec. 2.4.2. While the observable signal arises from inelastic Migdal events, the predominant stopping power comes from the elastic DM-nucleus collisions, and therefore only these are taken into account in the calculation of Earth-shielding effects.

The right panel of Fig. 2.9 shows the expected Migdal spectra for WIMPs with masses of 0.05, 0.1 and 1.0 GeV/c^2 corresponding to the respective interaction cross section values excluded at 90% C.L. The comparison with the standard signal in the left panel for WIMPs with considerably larger masses clearly shows how the Migdal effect greatly enhances the sensitivity to very light WIMPs, albeit for significantly larger cross section values.

The resulting 90% C.L. exclusion region is shown in Fig. 2.10, bounded from below by the thick dashed red line. The constraints weaken rapidly for WIMPs with masses below 100 MeV/c^2 .

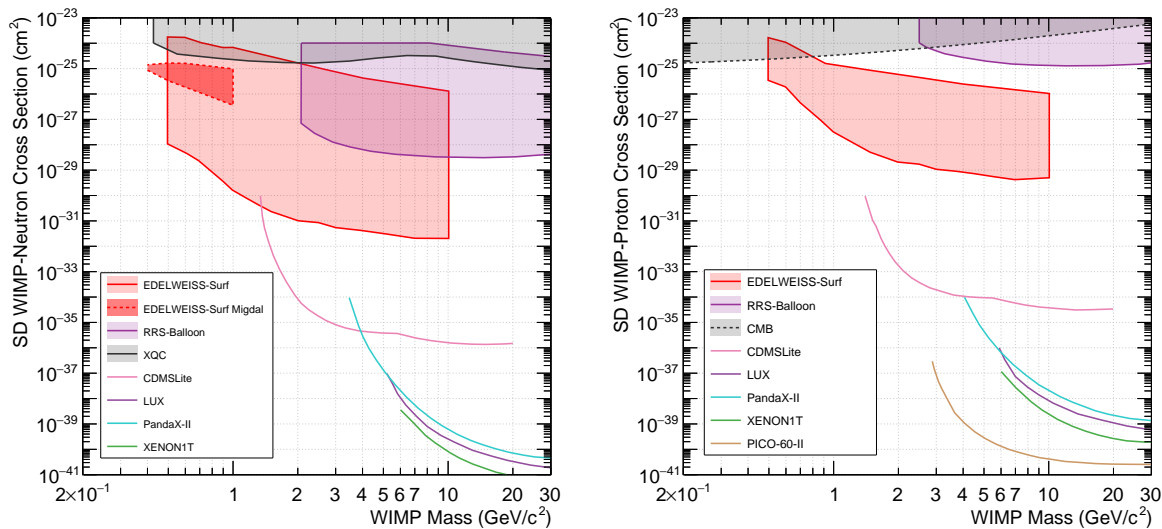


Figure 2.11: The 90% C.L. limits on the cross section for spin-dependent interactions assuming a dark matter coupling only to neutrons (left panel) and to protons (right panel) as a function of the particle mass obtained in the present work. The thick red lines and contours correspond to the presented surface dark matter search taking into account Earth-shielding effects and the so-called Migdal effect (dashed line) which is only relevant for the neutron SD coupling. These results are compared to those of other direct detection experiments shown as solid lines: LUX [184] (purple), XENON1T [185] (green), PICO-60-II [105] (brown), CDMSLite [169] (pink), and PANDAX-II [186] (blue). The other shaded contours correspond to the SIMP analyses from the XQC rocket [173, 179, 174] (black solid line), the RRS balloon experiment [174], and the CMB [183] (grey contour with dashed line). Figures taken from [97].

For lighter WIMPs, the peak in the expected Migdal signal spectrum overlaps in large part with the observed rapid rise of the data below 100 eV. Nevertheless, limits are obtained for WIMP masses as low as 45 MeV/c². Below this, the large cross sections required to give an observable signal lead to substantial stopping effects in the atmosphere and shielding, meaning that no constraints can be obtained anymore.

2.4.4 Spin-dependent Interactions

In this last section we present our result in the context of a spin-dependent coupling between the dark matter particle and the nucleus. The isotope ⁷³Ge (with a natural abundance of 7.73%) is the only stable germanium isotope with non-zero nuclear spin ($J = 9/2$), hence providing sensitivity to spin-dependent (SD) WIMP-nucleus interactions. For the spin expectation values, we assume $\langle S_p \rangle = 0.031$ and $\langle S_n \rangle = 0.439$ [187], with the larger $\langle S_n \rangle$ value coming from a single unpaired neutron. For the spin-structure functions, we take the average of the values reported in Table V of Ref. [187] which includes both 1- and 2-body currents.

We account for Earth-scattering effects, including only the SD scattering of the dark matter particles with nitrogen-14 in the atmosphere, which is the dominant source of stopping for surface-based SD searches [174]. Nitrogen-14 has nuclear spin $J = 1$ and we assume equal proton and

2.5 Conclusion and outlook

neutron spin contents $\langle S_p \rangle = \langle S_n \rangle = 1$. The results, presented as 90% C.L. excluded regions and limits, are shown in Fig. 2.11 for DM-neutron and DM-proton SD couplings on the left and right panels respectively. Our results, shown as red lines and contours, are compared to those of other direct detection experiments shown as solid lines: LUX [184] (purple), XENON1T [185] (green), PICO-60-II [105] (brown), CDMSLite [169] (pink), and PANDAX-II [186] (blue). The other shaded contours correspond to the SIMP analyses from the XQC rocket [173, 179, 174] (black solid line), the RRS balloon experiment [174], and the CMB [183] (grey contour with dashed line).

The EDELWEISS-Surf results are exploring new parameter space of the SD couplings, on both neutrons and protons, for dark matter masses ranging from 500 MeV/c² to 1.3 GeV/c² considering the standard DM induced nuclear recoil signal. The Migdal effect, producing both a nuclear recoil and an ionised electron, extends our lower DM mass bound down to 400 MeV/c² only in the SD-neutron case because of the dominating Earth-shielding effects happening at such high cross sections. In the case of WIMP-proton SD interactions, we obtain no limit from the Migdal effect due to the strong Earth-shielding effects at such high cross sections. Indeed, the combination of the small proton spin content of ⁷³Ge and the low ionization probability means that the scattering rate in this case is extremely small, hence requiring a large cross section to be detectable (around 10⁻²⁴ cm² at 1 GeV/c²). However, at such large cross sections, atmospheric stopping is too strong for a DM particle to reach our detector. We also note that at low masses $\mathcal{O}(500)$ MeV/c² both the Migdal WIMP-neutron and the standard WIMP-proton constraints are affected by Earth-stopping effects at both the upper and lower parts of the excluded regions.

2.5 Conclusion and outlook

2.5.1 On the direct detection of light dark matter

We have searched for dark matter particles with masses between 45 MeV/c² and 10 GeV/c² using a 33.4-g germanium detector operated at the IP2I surface lab, and thus relevant in the search for Strongly Interacting Massive Particles (SIMPs). The energy deposits were measured using a Ge-NTD thermal sensor with a 17.7 eV (RMS) heat energy resolution leading to a 60 eV analysis threshold. This performance, combined with the nearly completely stationary behavior of the detector, led to the achievement of the first limit for the spin-independent interaction of sub-GeV WIMPs based on a germanium target. The experiment provides the most stringent, nuclear recoil based, above-ground limit on spin-independent interactions above 600 MeV/c². The search results were also interpreted in the context of SIMPs, taking into account the screening effect of the atmosphere and material surrounding the detector. The lower part of the excluded region for SIMPs corresponds to the previously mentioned WIMP limit and represent the most stringent constraint for masses above 600 MeV/c². The upper part of the excluded region is limited by Earth-shielding effects: it probes the largest SIMP-nucleon cross sections of any direct detection experiment, excluding a value of 10⁻²⁷ cm² for a 1 GeV/c² WIMP⁴. There are a number of complementary constraints on SIMP DM, including searches for DM annihilation to neutrinos [188]; anomalous heating of the Earth [181, 189]; heating of Galactic gas clouds

⁴Note that CDMS-II provides the strongest SIMP constraints for DM masses above around 10⁸ GeV/c² [158, 160].

[190, 191]; and DM-cosmic ray interactions [192]. These typically require additional assumptions about the properties of the DM particle, while the current constraints depend only on its large scattering cross section with nuclei and its interactions near the Earth.

The dark matter search has also been extended to interactions via the Migdal effect, resulting in the exclusion for the first time of particles with masses between 45 and 150 MeV/c² with cross sections ranging from 10⁻²⁹ to 10⁻²⁶ cm². These limits also take fully into account the modeling of Earth-shielding effects essential for obtaining accurate constraints for such large cross section values.

Finally, interpreted in terms of spin-dependent interactions with protons or neutrons, these results exclude new regions of the parameter space below masses of 1.3 GeV/c². In this case, atmospheric stopping is significant and has a strong effect on the derived exclusion limits, in particular for WIMP-proton interactions and the Migdal effect.

2.5.2 On the future RICOCHET experiment at ILL

Eventually, this level of detector performance, achieved in an above-ground laboratory with a 30 g-scale massive bolometer, is also very promising in the context of the future RICOCHET experiment aiming for a low-energy and high precision measurement of the Coherent Elastic Neutrino-Nucleus Scattering (CENNS) process at ILL (see Chapter 3).

Figure 2.12 (left panel) shows how the observed EDELWEISS-Surf energy spectrum (black) compares with the expected CENNS induced nuclear recoil energy distributions from neutrino fluxes corresponding to three different sites:

Strong source - $2.4 \times 10^{13} \nu/\text{cm}^2/\text{s}$ - 15 meters away from the reactor core of KNPP (green),

Medium source - $1.2 \times 10^{12} \nu/\text{cm}^2/\text{s}$ - 8 meters away from the ILL reactor core (orange),

Weak source - $5 \times 10^{10} \nu/\text{cm}^2/\text{s}$ - 400 meters away from the Chooz reactor cores (red),

From this figure one can conclude that: 1) the energy threshold achieved with this 33.4 g Ge detector is sufficiently low to probe the low-energy end of the CENNS signal, 2) kg-scale detector array made of tens of such detectors is feasible, and 3) the RICOCHET background level at ILL needs to be at least 3-to-4 orders of magnitude lower than the one observed at IP2I to ensure a high significance detection of the CENNS process.

It is worth noticing that there is a tremendous similarity between the direct detection of WIMP dark matter and the neutrino detection via the CENNS process, which both produces low-energy nuclear recoils. As a matter of fact, the nuclear recoil energy spectrum induced by the CENNS detection of reactor neutrinos is almost identical to the one induced by a $\sim 2.7 \text{ GeV}/c^2$ WIMP. The cross section for both processes being coherent, *i.e.* scaling with the number of neutron squared, allows to establish a target independent correspondence between the neutrino flux and a $2.7 \text{ GeV}/c^2$ WIMP cross-section. For instance, we found that the expected CENNS signal 8 meters away from the ILL reactor core is equivalent to the one expected from a $2.7 \text{ GeV}/c^2$ WIMP with a $2 \times 10^{-40} \text{ cm}^2$ spin-independent cross section.

Figure 2.12 (right panel) shows the WIMP-equivalent models to the three neutrino fluxes discussed above: KNPP (triangle), ILL (circle), and Double Chooz near site (cross); as well as the state of the art of both underground (solid lines) and above-ground (dashed lines) low-mass direct detection exclusion limits. First, one can see that next generation CENNS experiments, that will be considering neutrino fluxes of the order of the ones discussed here, will need to

2.5 Conclusion and outlook

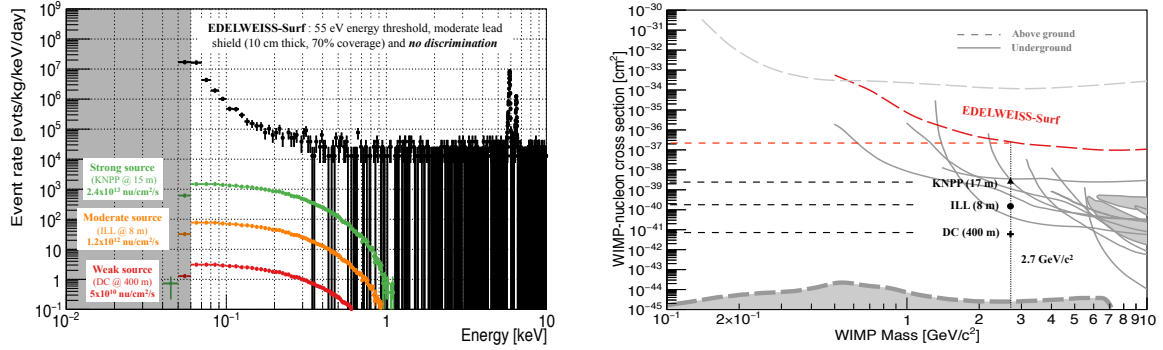


Figure 2.12: **Left:** EDELWEISS-Surf observed energy distribution (black) compared to simulated CENNS signals assuming three different reactor neutrino fluxes and sites: 15 m away from KNPP (green), 8 m away from ILL (orange), and 400 meters away from the two Chooz reactor cores (red). **Right:** State of the art of low-mass WIMP direct detection limits from both underground (solid lines) and above ground (dashed lines) experiments. Also shown are the WIMP equivalent models to the three CENNS neutrino signals shown on left panel.

have sensitivities at least comparable to the leading underground low-mass DM experiments (CRESST, EDELWEISS, SuperCDMS) while being at the surface. This result clearly highlights the tremendous challenge that future CENNS experiments are facing in order to achieve their ambitious goals. Second, this study suggests that the future RICOCHET experiment, that aims at detecting CENNS from the ILL reactor (see chapter 3), has to improve upon the EDELWEISS-Surf sensitivity by more than 3 orders of magnitude to achieve its scientific goals. In order to do so, the collaboration will benefit from 1) a much improved shielding including lead, polyethylene, a muon veto, and a ~ 15 m.w.e overburden, 2) particle identification down to ~ 100 eV, and 3) the possibility to subtract reactor independent backgrounds thanks to the ON/OFF CENNS signal modulation.

3

The future RICOCHET low-energy neutrino observatory

3.1 Introduction

Neutrinos continue to be a source of scientific wonder and discovery in nuclear physics, particle physics, and cosmology. Although much has been learned about the properties of neutrinos, much still pleads for more experimental investigation. What is the scale and structure of neutrino masses? Are neutrinos their own antiparticle? Even a question as simple as whether there are more than three types of neutrinos is the source of serious scientific debate. The answers to these questions are not simply for their own sake; they have significant ramifications as to how we construct the Standard Model (SM) of particle physics and could be the gateway for an entirely new physics paradigm. Over the last decades, various experimental efforts based on a host of techniques and neutrino sources have led to two major conclusions: i) neutrinos have a mass, and ii) they have significant mixing with each other. Therefore, starting from almost no knowledge about the neutrino sector twenty years ago, we have built a robust, simple, three-flavor paradigm which successfully describes most of the data. However, despite these major breakthroughs, further experimental investigations based on new experimental techniques and unexplored neutrino processes are still dramatically needed to go beyond the SM which, as we know from precision cosmology and particle physics, has to be extended.

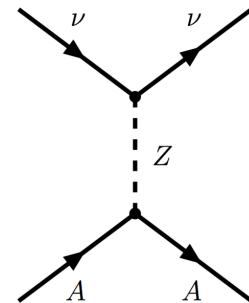


Figure 3.1: Feynman diagram of the CENNS process as predicted by the SM [119].

The measurement of Coherent Elastic Neutrino-Nucleus Scattering (CENNS) has been a holy grail in neutrino physics since its prediction almost 40 years ago [119] — see Fig. 3.1. This elastic scattering process, inducing sub-keV nuclear recoils, proceeds via the neutral weak cur-

3.2 Experimental state of the art

rent and benefits from a coherent enhancement proportional to the square of the number of neutrons (see Eq. 1.10), suggesting that even a kg-scale experiment will observe a sizable neutrino signal. This opens the possibility to probe the neutrino sector with orders of magnitude smaller experiments than current and planned kiloton-scale ones with a new approach. The full coherence condition, when the wavelength of the scattering is longer than the size of the nucleus, is guaranteed for nearly all nuclear targets when neutrino energies are below ~ 10 MeV. Such neutrinos are produced in copious amounts in the Sun, and at nuclear power and research reactors.

The search for physics beyond the Standard Model with CENNS requires to measure with the highest level of precision the lowest energy range of the induced nuclear recoils, as most new physics signatures induce energy spectral distortions in the sub-100 eV region. By providing a percentage-level precision CENNS measurement down to $\mathcal{O}(10)$ eV, thanks to next generation cryogenic bolometers with unprecedented low-energy threshold and background rejection capabilities, the RICOCHET collaboration proposes to go far beyond simply completing the Standard Model picture by testing various exotic physics scenarios. These include for instance the existence of sterile neutrinos and of new mediators, that could be related to the long lasting Dark Matter (DM) problem, and the possibility of Non Standard Interactions (NSI) that would dramatically affect our understanding of the electroweak sector.

3.2 Experimental state of the art

Thanks to its exceptionally rich science program, CENNS has led to significant worldwide experimental efforts, over the last decades, with several ongoing and planned dedicated experiments based on a host of techniques. Most of these experiments are, or will be, located at nuclear reactor sites producing low-energy neutrinos (~ 3 MeV): CONNIE using Si-based CCDs [193]; TEXONO [194], NuGEN [195], and CONUS [196] using ionization-based Ge semiconductors; and MINER [197], NuCLEUS [198], and RICOCHET [199] using cryogenic detectors. Only the COHERENT experiment [117, 118] is looking at higher neutrino energies (~ 30 MeV) as produced by the Spallation Neutron Source (SNS) in Oak Ridge.

3.2.1 The first CENNS detection

In August 2017, the COHERENT experiment has reported the first CENNS detection at the 6.7-sigma level [117]. This first result was based only on their CsI[Na] detectors exposed to ~ 30 MeV neutrinos, cumulating a total target mass of 14.6 kg, with an energy threshold of ~ 4.25 keV. Figure 3.2 displays the first CENNS observation done by the COHERENT collaboration, derived from 15 months of accumulated live-time data. The results are given as the residuals between the observed signals in the CsI[Na] detectors before proton-on-target (POT) triggers, and those taking place immediately after. They observe a high-significance (6.7-sigma) excess in the second population of signals, visible in both the energy spectrum (given in number of photoelectrons) (top panel), and of signal-arrival times (bottom panel). The timing information provided by the pulsed proton-beam, producing pulsed neutrinos, provides an unambiguous CENNS signature. With an energy threshold of 5 photoelectrons, corresponding to a ~ 4.25 keV nuclear

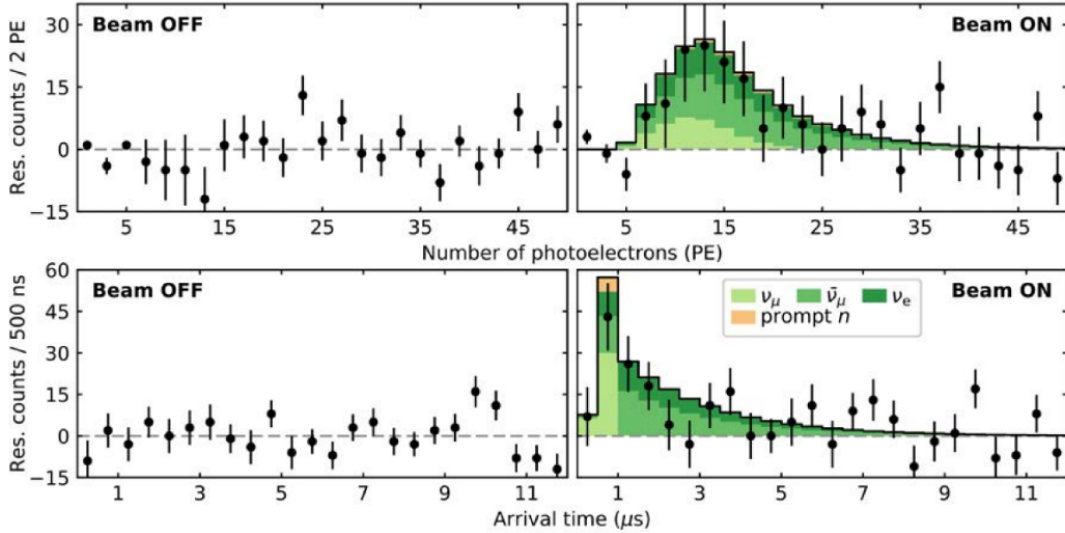


Figure 3.2: First observation of Coherent Elastic Neutrino-Nucleus Scattering. Shown are residual differences (data points) between CsI[Na] signals in the $12 \mu\text{s}$ following POT triggers, and those in a $12 \mu\text{s}$ window before, as a function of their energy in number of photoelectrons detected (top panel), and of event arrival time onset of scintillation (bottom panel). These residuals are shown for 153.5 live-days of SNS inactivity (“Beam OFF”) and 308.1 live-days of neutrino production (“Beam ON”), over which 7.48 GWhr of energy (1.76×10^{23} protons) was delivered to the mercury target. Figure from [117].

recoil energy threshold [117], the COHERENT collaboration has observed a clean sample of 134 ± 22 CENNS events. Due to the nature of the SNS neutrino source, three neutrino flavors are emitted: electron-neutrino, muon-neutrino and muon-anti-neutrino, with roughly equal contributions to the total observed CENNS signal. In addition to their CsI[Na] detectors, the COHERENT collaboration intends to pursue investigating this newly observed neutrino detection mechanism using additional detector technologies such as: ~ 1 -ton LAr detector, a 2-ton NaI[Tl] detector array, and a p-type point contact high-purity germanium detector [117]. In March 2020, the COHERENT collaboration has also confirmed a first CENNS detection with their LAr detector at the 3σ level [118].

Even though this first detection has only limited sensitivity to new physics, as most new physics signatures will arise in the sub-100 eV region, COHERENT has proven the existence of this new neutrino detection channel that opens the door to a myriad of new scientific opportunities that we wish to explore with RICOCHET at ILL.

3.2.2 Ongoing and planned cryogenic CENNS experiments

We hereafter focus only on cryogenic detector based experiments as they are uniquely well suited to probe the CENNS process at the lowest energies, *i.e.* in the $\mathcal{O}(10)$ eV energy-range, where new physics signatures are expected to arise (see Sec. 3.5). Indeed, the overwhelming advantage of bolometers, compared to any other detection techniques, is that the deposited energy from a neutrino-nucleus interaction is fully sensed, therefore they act as true calorimeters

3.3 The RICOCHET experiment at ILL

with almost no quenching effects. Based on this unique characteristic, MINER, NuCLEUS and RICOCHET are new CENNS bolometer-based experiments being developed in the wake of the long experience of cryogenic direct dark matter detection experiments CDMS, CRESST and EDELWEISS respectively. We give hereafter a brief description of MINER and NuCLEUS, as RICOCHET will be further detailed in the next section:

- **MINER** is a cryogenic bolometer-based experiment that is located at the 1 MW thermal power research reactor from the Mitchell Institute in Texas [197]. The experiment will use Si and Ge bolometers with a total target mass of 10 kg combined with a projected energy threshold of about 100 eV with no background discrimination. The great originality of this project is that the reactor core is movable such that the distance between the core and the detectors can vary from 2 to 10 meters. This is perfectly well suited to study the existence of sterile neutrinos with meter-scale oscillations. Their first commissioning run, expected to start in 2020, should pave the way to their future high-precision measurement phase in the coming years.
- **NuCLEUS** is a gram-to-kg scale planned cryogenic bolometer-based experiment that will be deployed at the Chooz power plant, 80 meters away from the two 4.25 GWth reactor cores [200]. It will use a combination of CaWO_4 and Al_2O_3 detectors with an assembly of vetoing detectors to provide fiducialization and therefore reject both internal and external backgrounds [198]. The NuCLEUS strategy is to focus primarily on lowering the energy threshold, at the cost of drastically reducing the size of the individual bolometers ($\sim 0.5/0.8$ g). They are therefore planning to go with two phases of 10 g and 1 kg, that should start in 2022 and 2024 respectively, to reach a high precision measurement.

3.3 The RICOCHET experiment at ILL

RICOCHET is a France, USA and Russia wide collaboration accounting for about 50 physicists, engineers and technicians. The objective of the RICOCHET experiment is to provide a low-energy and high precision measurement of CENNS to search for new physics in the electroweak sector. To achieve its ambitious scientific goal, the RICOCHET experiment will fulfill the following criteria:

1. **Cryogenic detector performance:** Low energy threshold (~ 50 eV) combined with high gamma background rejection (10^3) and a kg-scale payload to achieve high CENNS statistics (~ 15 events/day)
2. **Nuclear reactor site requirements:** Large ($\phi \sim 10^{12} \text{ cm}^{-2}\text{s}^{-1}$) and well controlled neutrino flux ($\delta\phi/\phi \sim 3\%$) well shielded against environmental irradiations (i.e. reactogenic and cosmogenic backgrounds)
3. **Experimental setup specifications:** Achieve a low noise environment (electronics and vibrations) with low background levels (few events/kg/day) and compatible with nuclear safety regulations

We hereafter detail the three above mentioned objectives and the related RICOCHET strategy to achieve them in order to reach a high sensitivity to physics beyond the standard model.

3.3.1 The cryogenic detectors

The RICOCHET detectors are designed to provide the first percentage precision CENNS measurement in the sub-100 eV energy region to search for new physics in the electroweak sector. The key feature of the RICOCHET program, compared to other planned or ongoing CENNS projects (see Section 3.2), is to aim for a kg-scale experiment with unparalleled background rejection capabilities down to the demonstrated 50 eV energy threshold [97]. The background rejection, based on particle identification, will be done thanks to the simultaneous heat and ionization measurements and pulse shape discrimination in semi- and super-conducting detectors respectively. This way, the largely dominating electromagnetic background (gammas, betas, low-energy X-rays), producing electronic recoils (ER) in the target medium, can be unambiguously discriminated from the CENNS-induced nuclear recoils (NR). Based on our targeted detector performance, particle identification should lead to a 2- and 5-sigma separation between the NR and ER event populations at 50 and 140 eV recoil energies, respectively. Assuming a flat 95% acceptance, this leads to an unprecedented CENNS-spectrum-averaged electromagnetic background rejection of about 10^3 , see Sec. 4.3.2. Only the neutrons, also producing nuclear recoils, cannot be discriminated from the CENNS signals and are therefore considered to be the ultimate background (especially if correlated with the reactor activity). Another objective, is to combine two monolithic targets (Ge and Zn) and cryogenic detector techniques to benefit from both target complementarity and reduced systematics in the quest of new physics. To that end, the collaboration is developing two arrays of highly-performing cryogenic bolometers, namely the CryoCube (Ge) and the Q-Array (Zn). The RICOCHET cryogenic detector assembly will be suspended below the inner shielding with its dedicated cryogenic suspension system [164], and cold front end electronics [147]. It consists of a total array of 36 bolometers of about 30 g each, leading to a total payload of ~ 1.3 kg, and divided among the two sub-arrays:

- **The CryoCube** consists of an array of 27 single 30-g Ge highly performing cryogenic detectors individually equipped with a Ge-NTD heat sensor and aluminum electrodes for the ionization readout, see Chap. 4. We have recently demonstrated a 55 eV energy threshold on a 33.4g Ge bolometer operated above-ground [97], and reached similar performance with 5 additional bolometers since then (see Sec.5.3.1). Now that the heat energy threshold has been established and reproduced numerous times, we are focusing on the ionization readout electronics in order to provide the required resolution and resulting background discrimination power, see Sec. 5.3.5.
- **The Q-array** consists of an array of 9 superconducting 30-gram Zn cubes. The motivation for using superconducting detectors is that they may offer the unique possibility to provide a low-energy threshold and particle identification simultaneously with a single heat readout channel per detector. Each unit will be read out by a transition-edge sensor and the signal feed into a microwave resonant SQUID array (uMUX), allowing the sig-

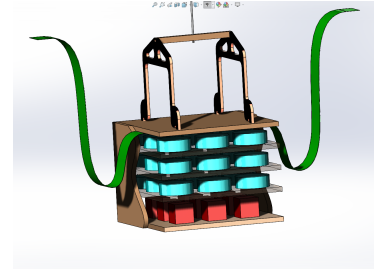


Figure 3.3: RICOCHET cryogenic detector assembly – the CryoCube with its 27 Ge crystals (blue) and the Q-Array with its 9 Zn crystals (red) – suspended below the inner shielding.

3.3 The RICOCHET experiment at ILL

nals from multiple detectors to be read out by a single feed line, paving the way to future tens of kilogram payloads with this multiplexed technology.

3.3.2 The ILL-H7 nuclear reactor site

In the past couple of years, the collaboration has explored various potential nuclear sites, namely the MIT-R [201] and the near hall of the Double Chooz experiment [202] for which the science potential was found to be too low. In February 2019, the RICOCHET collaboration has submitted a Letter of Intent to the ILL directorate to perform a comprehensive study about the feasibility of deploying the RICOCHET experiment at the H7 experimental site (see Fig. 3.4), where the STEREO neutrino experiment is currently running and will be decommissioned by 2021. Following the neutron background and floor vibration characterizations (see Sec. 3.7), and the sensitivity studies detailed hereafter, the RICOCHET collaboration has decided to focus its efforts on integrating the ILL-H7 site. In May 2020, following the project evaluation in a public call for proposals, the collaboration has been granted the official support from the ILL scientific council to deploy the RICOCHET experiment at the ILL-H7 site.

The H7 site starts at about 8 m from the ILL reactor core that provides a nominal nuclear power of 57.8 MW, leading to a neutrino flux at the RICOCHET detectors of $1.4 \times 10^{12} \text{ cm}^{-2} \text{ s}^{-1}$. The reactor is operated in cycles of typically 50 days' duration with reactor-off periods sufficiently long to measure reactor-independent backgrounds, such as internal radioactivity or cosmogenic induced backgrounds, with good statistics. The available space is about 3 m wide, 6 m long and 3.5 m high. It is located below a water channel (see Fig. 3.4) providing about 15 m water equivalent (m.w.e.) against cosmic radiation. It is not fed by a neutron beam and is well-shielded against irradiation from the reactor and neighboring instruments (IN20 and D19). The site is well-characterized in terms of backgrounds, and the operation of the STEREO neutrino experiment at this site has been successfully demonstrated [203].

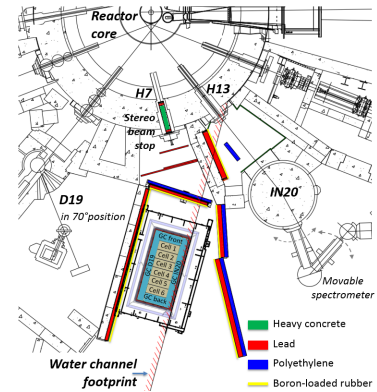


Figure 3.4: Top view of the STEREO experiment at the ILL-H7 site, about 8 meters away from the 57.8 MW reactor core. The light red hatched line shows the footprint of the water channel.

3.3.3 Preliminary experimental setup

Thanks to the high CENNS cross section, RICOCHET will be a compact neutrino experiment with a total detector payload of about one kilogram. Due to its use of cryogenic detectors running at ~ 10 mK and its need to mitigate the environmental backgrounds, the future RICOCHET experiment will need the operation of a dry dilution refrigerator surrounded by both lead and polyethylene shields. Figure 3.5 shows a preliminary drawing of the future RICOCHET experiment deployed at the ILL-H7 experimental site. The cryostat (to be delivered at IP2I in early-2021) is composed of a dilution unit with several stages (50 K, 4 K, 1 K, 100 mK, and 10 mK) as shown on the right panel of Figure 3.5. The detectors will be suspended below the mixing chamber, underneath the inner shielding layers, thanks to a dedicated cryogenic suspension system [164]. To minimize the stray capacitance from the cabling, the cold front-end electronics

3.3 The RICOCHET experiment at ILL

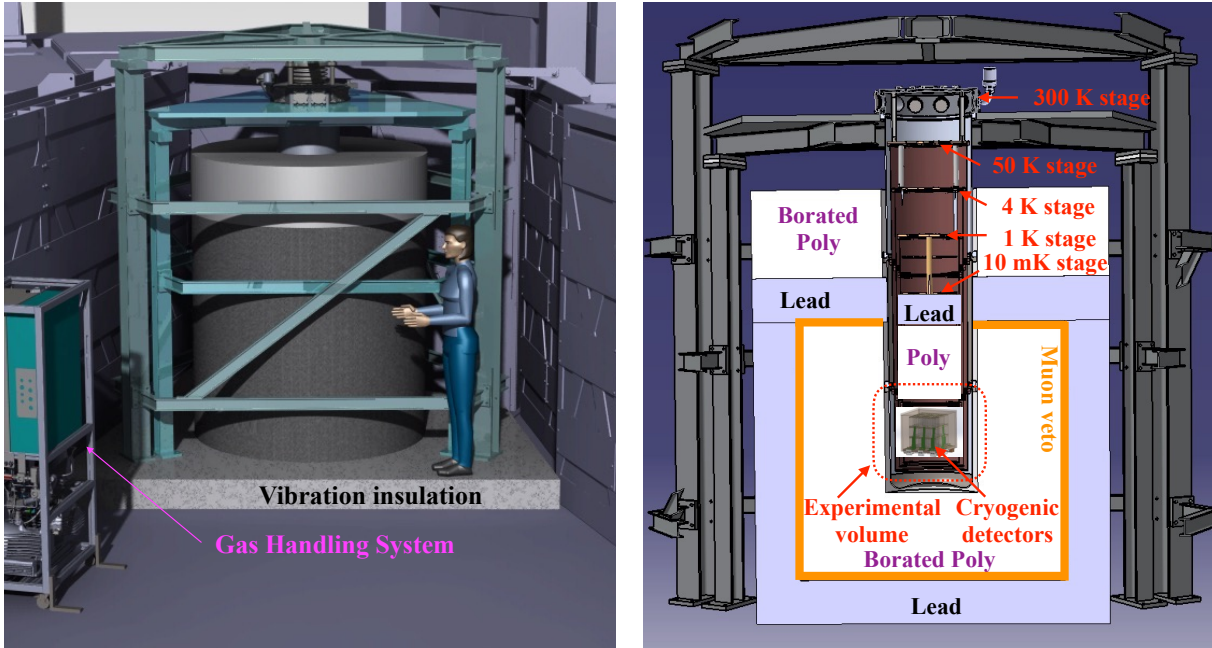


Figure 3.5: **Left:** Future RICOCHET experimental setup, illustrating the cryostat held by a double-frame, its movable lead and polyethylene shields and its gas handling system. For clarity, the tubing from the GHS and the cryostat is not shown. **Right:** Open view of the RICOCHET setup where the dilution refrigerator, the internal shields, the muon-veto, and the experimental volume hosting the detectors and the cold electronics are shown. The double frame has a mass of 1.5 tons, the lead 22 tons and the PE 3 tons, all previous masses are subject to changes depending of the final design.

will be thermally anchored at 1 K and mounted between the detectors and the inner polyethylene shielding. Eventually, the warm electronics, containing the bias DACs, signal preamplifiers and digitizers will be mounted directly on the 300 K flange. Based on the excellent noise performance achieved in the EDELWEISS-III experiment [80], we chose to use optical fibers to send the digitized signals to the data acquisition system. Eventually, even though the site provides a muon flux attenuation of about 4 thanks to the water channel, an active muon-veto will be inserted within the RICOCHET shielding (see Sec. 3.4 for a more detailed discussion). The whole setup will be mounted on a dedicated vibration insulated floor to mitigate ambient vibrations, arising from the reactor operation, that were found to be potentially too large at high frequencies (see Sec. 3.7).

3.3.4 RICOCHET CENNS sensitivity

Figure 3.6 presents the expected signal and targeted background event rates as a function of the recoil (kinetic) energy expected for the RICOCHET experiment installed at 8 meters from the ILL reactor core. The blue solid line is the CENNS event rate as predicted by the Standard Model. For the sake of illustrating new physics signatures detailed in Sec. 3.5, the dot-dashed and dashed purple lines are from adding a 1 MeV Z' boson, with a coupling strength

3.4 Shielding optimization and expected backgrounds

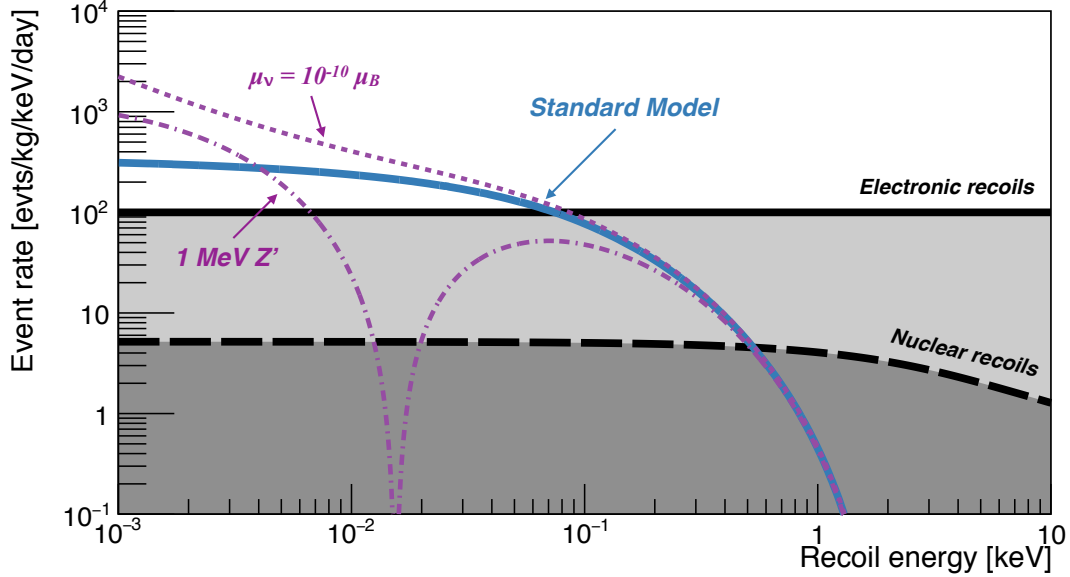


Figure 3.6: Expected event rate and targeted background levels as a function of the recoil energy for the RICOCHET experiment deployed at 8 meters from the ILL reactor core. The blue solid line is the standard model predicted CENNS event rate while the dot-dashed and dashed blue lines are respectively from adding a 1 MeV Z' boson and a NMM of $\mu_\nu = 10^{-10} \mu_B$. The black solid and long-dashed lines represent the electronic and nuclear recoil background populations respectively. Figure adapted from [204].

$g_{Z'} = 10^{-5}$, and a Neutrino-Magnetic Moment of $\mu_\nu = 10^{-10} \mu_B$, respectively. Also shown are the total background expected before (solid line) and after (long dashed line) the electromagnetic background rejection. We then expect to observe ~ 15.5 CENNS events/kg/day between 50 eV and 1 keV and a total background rate of ~ 100 events/kg/day and ~ 5 events/kg/day before and after background discrimination. With a signal-to-noise ratio of $S/B \sim 3$, we expect to reach a $5\text{-}\sigma$ CENNS detection after only a couple of days and a percentage-level precision measurement after one year of reactor ON data, *i.e.* two years on site, if the signal systematics can be controlled at a few percent-level (see Sec. 3.6) and the targeted background levels achieved.

3.4 Shielding optimization and expected backgrounds

In order to optimize the RICOCHET shielding design and estimate the resulting background level, a wealth of Geant4 simulations have been done. The latter were performed considering the three dominating sources of background emitting both high energy gammas and fast neutrons:

3.4 Shielding optimization and expected backgrounds

Reactogenic background: the reactor and the neighbouring experiments (IN20 and D19) produce an important flux of high energy gammas, fast and thermal neutrons. Against such backgrounds an important mass of layered passive shielding is mandatory; polyethylene is utilised to thermalize fast neutrons, boron doping captures thermal neutrons and lead mitigates the gamma flux. The simulations of the reactogenic gamma background have relied upon the earlier HPGe gamma measurements by the STEREO collaboration [203] at the H7 site, while neighbouring experiments were running. Reactogenic neutrons have been simulated with the energy spectrum of the neutrons leaving the steel cap of the H7 line, as computed by the STEREO collaboration by way of MCNP simulations [203]; these neutrons have a maximum energy of 6 MeV. Simulations of the fast neutrons from H13 are in preparation. Note that even though reactogenic neutron flux is expected to be large, thanks to their relatively low maximum energy of about 10 MeV, they are expected to be highly efficiently stopped with the use of an appropriate shielding design.

Cosmogenic background: cosmic ray showers generate many high energy particles, especially high energy muons, neutrons and gammas. Muons are known to produce secondary fast neutrons by spallation inside shielding material like lead. A water channel above the H7 site adds up to 15 m.w.e of overburden, providing a valuable attenuation of the muon flux by a factor of almost four. This configuration makes the H7 site attractive for RICOCHET. Although cosmogenic backgrounds can be estimated during reactor OFF periods and subtracted from the reactor ON data, this subtraction is feasible only if the signal to background ratio is high enough. In addition, a muon-veto will also be used to reject events correlated with muons. The CRY library has been used to generate cosmic showers above the ILL containment building and particle propagation has been carried out by Geant4 through the ILL building into the STEREO casemate, as previously done for the STEREO experiment. The flux of all the particles entering the casemate over the course of five actual days has subsequently served as the input of the RICOCHET simulation. As a first validation, the background rates measured by the Giove [205] and CONUS [196] experiments have been reproduced, within a factor of two to three (which could be explained by the oversimplified Giove and CONUS geometry considered), by our cosmic RICOCHET simulation.

Radiogenic background: the materials surrounding the detectors are naturally affected by primordial radioactive elements, among them the ^{238}U and ^{232}Th chains that produce gammas, betas and alphas; the latter generate neutrons via (α, n) reactions. Materials close to the detector ought to be chosen carefully and their radiopurity measured with a dedicated HPGe detector in the Laboratoire Souterrain de Modane [80]. This radiogenic background is currently under investigation, combining ongoing material screening measurement and Geant4 simulations.

The preliminary RICOCHET shielding design is presented in Fig. 3.7 (left panel). It will be divided into two parts: a cold inner shielding inside the RICOCHET cryostat, directly above the detectors, and an outer cylindrical shielding surrounding the sides and the bottom of the cryostat. The inner (outer) shielding will be composed of 1) a 8.5 (20) cm thick outer layer of lead to mitigate the gamma flux, and 2) a 21 (40) cm thick inner layer of 3%-borated polyethylene to thermalize and capture fast neutrons. Additionally, a third (external) layer of polyethylene on top of the outer lead layer and ~ 8 mm thick polyethylene layers mounted on each thermal screens will be used to reduce neutron spallation in the lead shielding and further improve the shielding tightness, respectively. Lastly, muon induced gamma and neutron backgrounds will

3.4 Shielding optimization and expected backgrounds

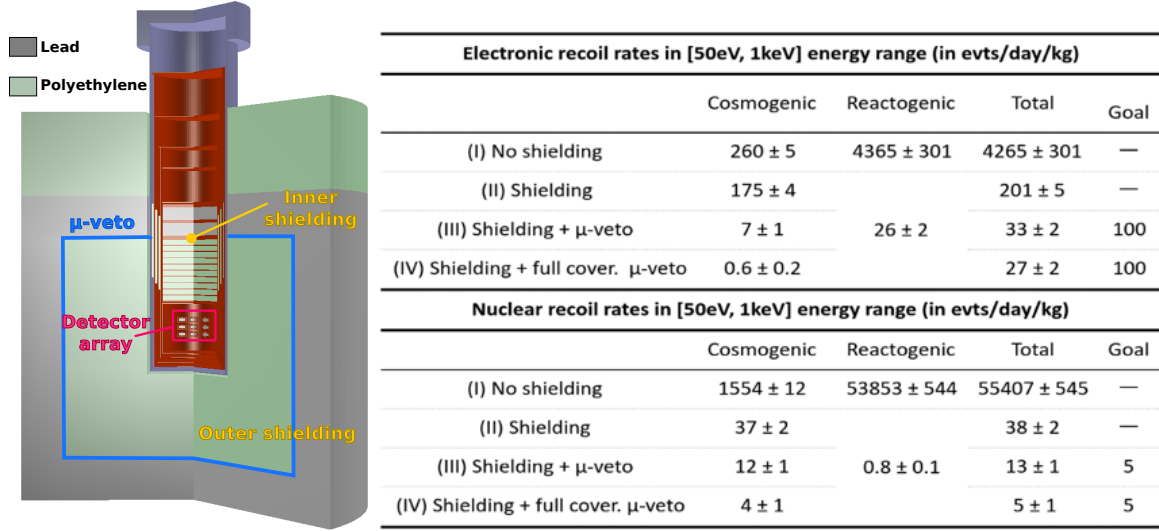


Figure 3.7: **Left:** Preliminary shielding design of the RICOCHET experiment at ILL-H7 considered in the Geant4 simulations. **Right:** Simulated background rates inside the cryogenic detector array for various shielding design scenarios, when only one bolometer has triggered. Scenario (III) corresponds to our preliminary shielding design illustrated on the left panel. The muon-veto (blue) has been modelled assuming a perfect muon tagging efficiency.

be further reduced thanks to a surrounding muon-veto allowing to reject events in temporal coincidence with muons going through the experimental setup. The muon-veto is planned to be inserted inside the outer layer of lead in order to avoid spurious triggers induced by harmless gamma rays which are produced in copious amounts at ILL. Though the exact depth to which the muon veto should be inserted in the lead is still under investigation (see Sec. 4.3), we will consider here the case where it is right between the outer layers of lead and polyethylene (shown as the blue line in Fig. 3.7 – left panel).

Resulting rates for both electronic and nuclear recoil backgrounds from cosmogenic and reactogenic origins, and under different shielding configurations, are presented and compared to our targeted background levels in Fig. 3.7 (right panel). We found that while the total electronic background is well below our targeted level, the neutron one is about three times larger, implying an expected $S/B \sim 1$. We see that our dominating source of nuclear recoil background is from the muon induced neutrons, and by comparing the results from configurations (III) and (IV) we can conclude that a full muon-veto coverage might be essential if 1) the spurious gamma induced trigger rate is low enough and 2) the induced dead time is reasonable. With an expected 150 Hz muon-veto trigger rate, and a demonstrated $\sim 100\mu\text{s}$ timing resolution for the Ge cryogenic detectors (see Sec. 4.3.1 and 5.3.3), thanks to the fast ionization signal, we anticipate a dead-time between 9% and 14% while dividing the muon-induced gamma and neutron backgrounds by about 25 and 3, respectively (compared to config. II). Further reducing these backgrounds by factors of 300 and 9 for ER and NR respectively, could be done with a full-coverage muon-veto (config. IV), by positioning the muon-veto on the outside surface of the lead layer and operating veto panels inside the cryostat (which has to be demonstrated first). Note that this would lead to a still manageable 350 Hz muon-induced trigger rate resulting in

3.5 Searching for new physics with RICOCHET

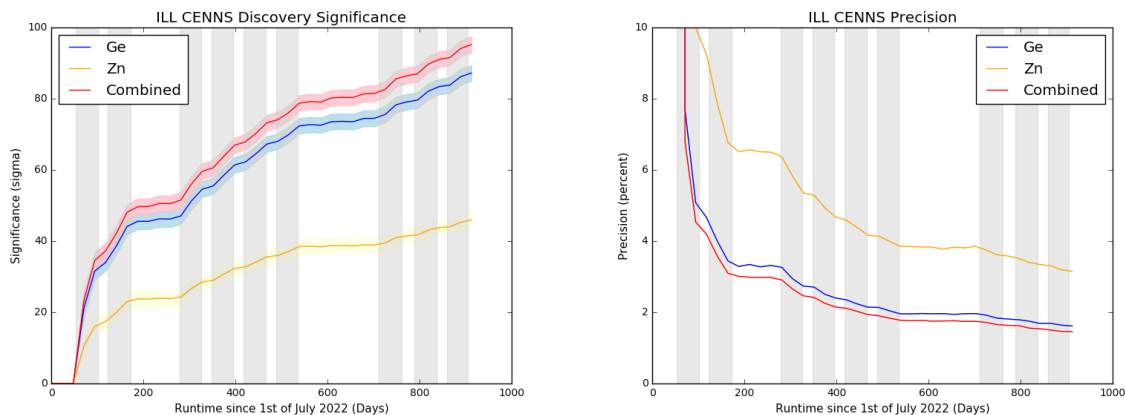


Figure 3.8: CENNS discovery significance (**left**) and precision (**right**) as a function of exposure. Median significance and precision (and 95% confidence level bands) for the discovery of CENNS using Ge (blue), Zn (yellow), and the combination of the two (red). Grey regions indicate time periods when the reactor is on.

a 20-30% dead-time. Eventually, it is worth noticing that the expected CENNS signal is found to be 20 times larger than the particularly damaging correlated reactogenic NR background of 0.8 events/day/kg.

Studies are still ongoing to finalize the shielding design to further reduce the expected neutron background to reach our targeted $S/B = 3$. Different solutions are currently being investigated: 1) add more polyethylene inside the cryostat at warmer stages, and 2) use cryogenic veto detectors, encapsulating the Ge and Zn detector arrays, made of CsI or Ge that can easily be scaled to sufficiently large payloads and be fast enough by reading out the scintillation light or the ionization signals respectively. We are confident that following these improvements, we will be able to achieve our targeted background levels.

3.5 Searching for new physics with RICOCHET

The following projected discovery reach and exclusion limits are computed using a frequentist profile likelihood analysis where we assumed 5% systematic uncertainties on all backgrounds, and a 70% detection efficiency mostly due to the deadtime loss from the muon-veto. Note that we purposely did not consider any systematics on the signal, which would obviously affect the ultimate achievable CENNS precision measurement, and are discussed in detail in Sec. 3.6. Figure 3.8 presents the CENNS discovery significance (left panel) and the CENNS precision measurement (right panel) as a function of time assuming RICOCHET science data taking starting on the 1st of July 2022. As one can see, a 5- σ significance detection is reachable in only a couple of days with both detector technologies. After the first reactor cycle (of about ~ 50 days) we should reach a $\sim 30\text{-}\sigma$ significance and a corresponding 5% CENNS precision measurement, where we should start being sensitive to possible exotic physics scenario. After 9 reactor cycles, *i.e.* two years and a half onsite, we will reach the targeted $\sim 1\%$ precision measurement (not

3.5 Searching for new physics with RICOCHET

including signal systematics), that will lead to orders of magnitude improved sensitivities to various new physics scenarios compared to existing experiments. Note that even with our current background estimates, based on our preliminary Geant4 simulations (see Table in Fig. 3.7), we still expect to reach a $\sim 2\%$ precision measurement after one year of reactor ON data.

With such a low-energy and high-precision measurement of the CENNS process, RICOCHET will be uniquely positioned to probe new physics in the electroweak sector. We hereafter discuss projected sensitivities to some exotic scenarios further detailed in our recent work [204]:

The Neutrino-Magnetic Moment (NMM): as neutrinos oscillate, they must have a non-vanishing mass and sufficiently large mixing with each other. In the case of a Dirac neutrino, the minimal extension of the standard model leads to a small but nonzero neutrino magnetic moment of about $10^{-19} \mu_B$ (Bohr magneton). This theoretical limit is orders of magnitude below the most stringent ground-based limit from GEMMA $\mu_\nu < 2.9 \times 10^{-11} \mu_B$ (90% C.L.) [206]. However, in some more general extensions, including new physics at the TeV-scale, the NMM can be as high as $10^{-15} \mu_B$ and $10^{-12} \mu_B$ for Dirac and Majorana neutrinos respectively [207]. Therefore, the observation of an anomalously large NMM, inducing sub-100 eV CENNS spectral distortions, would unambiguously lead to two major conclusions: 1) there is new physics, and 2) neutrinos are Majorana fermions; which will have tremendous implications on the global neutrino physics program. Our goal is to provide a competitive CENNS-based NMM limit down to $\mu_\nu \sim 10^{-11} \mu_B$ (90% C.L.).

Searching for new massive mediators: the Coherent Elastic Neutrino-Nucleus Scattering is done through the exchange of the Standard Model Z boson. Plausible extensions of the SM suggest the presence of an additional vector mediator boson [208], that couples both to the neutrinos and the quarks, called Z' . The latter could therefore interfere with the standard CENNS process and modify the observed effective weak nuclear hyper-charge. Fig. 3.9 (left panel) presents the anticipated 90% C.L. upper limit on the Z' coupling that we aim to achieve with the RICOCHET experiment. Unlike fixed target (APEX [209]) or collider-style (LHC di-electron searches [210, 211]) experiments, CENNS-based experiments have the unique possibility to scan any Z' masses. As the constraint on the Z' coupling evolves as $(\text{exposure})^{1/4}$ if not background limited, the RICOCHET's key feature is its sub-100 eV energy threshold combined with its significant background rejection. Eventually, we see that within a year, RICOCHET will improve by about two orders of magnitude over the current COHERENT result [117].

Searching for Non Standard Interactions (NSI): new physics that is specific to neutrino-nucleon interaction is currently quite poorly constrained, and is motivated in some beyond-SM scenarios [214]. In the context of a model-independent effective field theory, the Lagrangian describing the neutrino-nucleon interaction leads to NSI operators which can either enhance or suppress the CENNS event rate. Fig. 3.9 (right panel) shows the 90% C.L. allowed regions derived from several particle physics experiments including CHARM [213], LHC mono-jet searches [212], the recent COHERENT result [117], and RICOCHET's anticipated sensitivity. The RICOCHET result is shown as: Ge only (blue), Zn only (orange), and Ge + Zn combined (red). Due to the interference between the couplings, CENNS constraints lead to two allowed regions (not visible for COHERENT as they overlap). We can therefore appreciate the comple-

3.5 Searching for new physics with RICOCHET

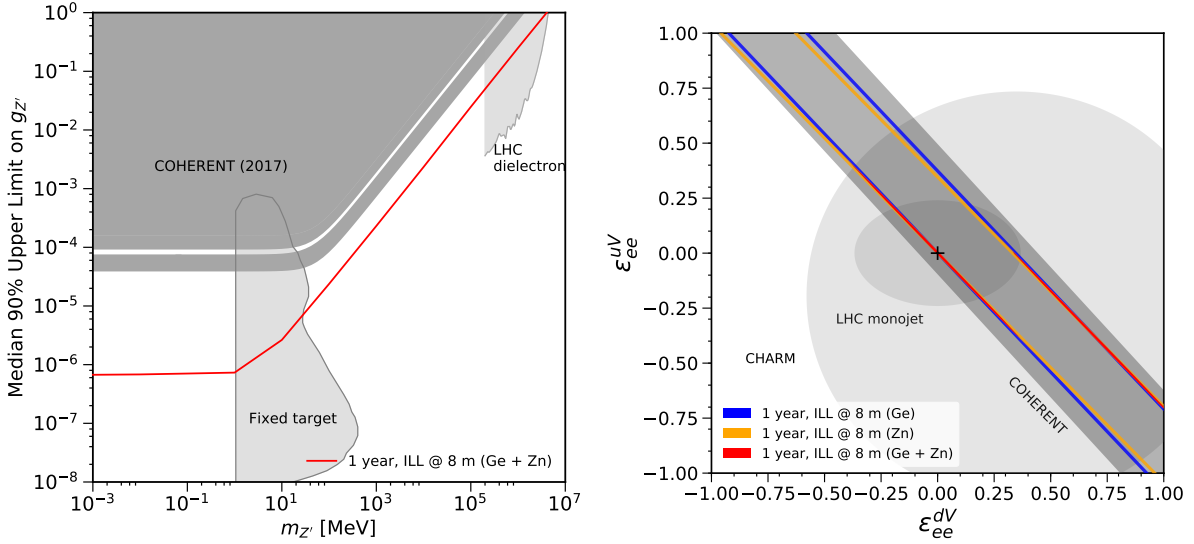


Figure 3.9: Projected sensitivities of the RICOCHET experiment, located at 8 m from the ILL reactor core, to new physics searches in the low-energy CENNS sector where a 50 eV energy threshold and a flat electromagnetic background rejection power of 10^3 was assumed. **Left:** constraints on Z' searches where we have assumed unified coupling to the quarks. The results are shown as 90% C.L. upper limits on the Z' coupling. Also presented are current leading constraints from the APEX fixed target experiment [209], LHC di-electron searches [210, 211], and COHERENT [117]. **Right:** constraints on Non-Standard neutrino-quark Interactions in the neutrino-electron sector. Results are shown as 90% C.L. allowed regions. Also shown are current experimental constraints from LHC mono-jet searches [212], CHARM [213], and COHERENT [117]. The cross represents the Standard Model. Figures adapted from [204].

mentarity between these two targets which breaks the degeneracy along the up- and down-quark neutrino-electron couplings. Such neutral current NSI constraints, as expected from RICOCHET, will be mandatory to future long-baseline experiments exploring the neutrino mass hierarchy, such as DUNE [215]. After only one year of data taking, our goal is to improve current NSI constraints by about two orders of magnitude.

A precise CENNS measurement will also allow to test the existence of sterile neutrinos. For the typical sterile neutrino masses required to explain the LSND anomaly [216] ($\Delta m_{41}^2 \sim 1$ eV), and for typical neutrino energies from nuclear reactors of 3 MeV, the wavelength of active-to-sterile oscillations is of a few meters. Therefore, to be competitive, such a search has to be done few meters away from a compact nuclear reactor in order to observe with sufficient significance the spectral distortions and change in normalizations induced by the existence of a sterile neutrino. Thanks to the compact ILL reactor core, RICOCHET should also lead to competitive sensitivities to eV/c^2 -scale sterile neutrinos with a new and complementary approach from ongoing experiments. To that end, combined analyses between STEREO and RICOCHET, both operated at the ILL-H7 site but using two different neutrino detection mechanism, could be highly valuable.

3.6 Signal systematics

As we are aiming for a percentage-level precision measurement of the CENNS process, it is pivotal to properly anticipate and mitigate possible sources of signal systematics. We hereafter list three different sources of systematics that could potentially limit the ultimately achievable precision of the low-energy CENNS measurement from the RICOCHET experiment at ILL.

3.6.1 Anti-neutrino reactor flux predictions

Accurate prediction of the reactor anti-neutrino flux and the resulting CENNS rate is important for precision measurements of new physics. Table 3.1 shows the predicted uncertainties on parameters that affect the CENNS rate prediction. The thermal power P_{th} and distance to the core [203] have previously been measured for the ILL reactor site. The energy released per fission has been calculated with an uncertainty of 0.2% to 0.5% for fission isotopes in a commercial PWR reactor, with an uncertainty of 0.2% for ^{235}U [217]. This uncertainty may vary for the ILL reactor, but a value around 0.3% can be expected. Uncertainties on the fission fractions α_i will be of order 1% on ^{235}U and 5-10% on other fission isotopes, since ^{235}U will be the dominant fission isotope. Uncertainties of 10% on α_i will lead to small uncertainties around 1% on the total rate, due to similarities in rate and shape of the four fission isotope spectra, as seen in analysis of IBD measurements [218].

Prediction of the fission spectra S_i must be performed differently for the portions of the spectra above and below the inverse beta decay threshold of 1.8 MeV. Above 1.8 MeV the neutrino flux can be constrained by converting IBD measurements from other experiments to constraints on the flux. In particular, RICOCHET would be able to use data from the STEREO experiment to constrain the ILL reactor flux in this region. Typical uncertainties from such conversion are 2-3% [218]. Below 1.8 MeV there are currently no measurements of the neutrino flux from reactors, meaning that the flux must be predicted by using summation calculations of the spectra from the decay products of fission isotopes in the reactor. Summation calculations can be performed by coupling the output of the spectrum calculation tool BESTIOLE with evaluated cumulative fission yields [219]. The uncertainties on such summation calculations have not previously been calculated, but are expected to have larger values around 5-10%.

The resulting uncertainty on the total CENNS rate from the uncertainties on fission spectra

	Uncertainty on Parameter	Approximate Uncertainty on CENNS Rate
P_{th}	1.4 %	1.4%
Distance	0.3%	0.6%
E/fission	~ 0.3 %	~ 0.3 %
α_i	$\leq 1\%$ ^{235}U $\approx 5\text{-}10\%$ ^{239}Pu , ^{241}Pu	$\ll 0.5\%$
S_i	Conversion: 2-3%	2-3%
	Summation: 5-10%	
σ_k	0.5% (θ_W)	

Table 3.1: Expected systematics on the CENNS rate.

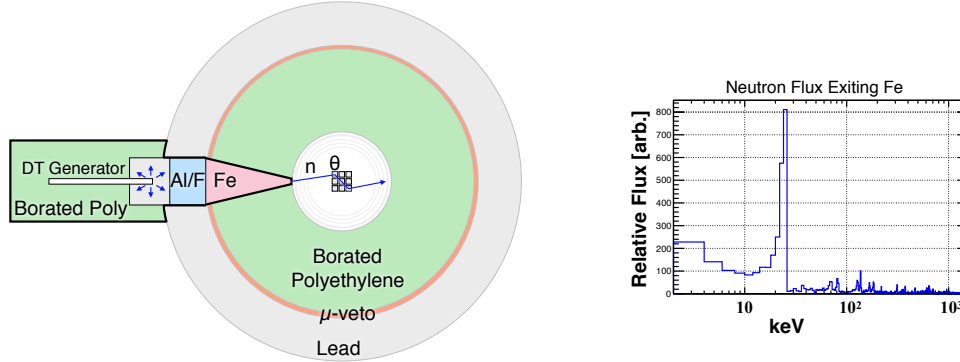


Figure 3.10: **Left:** The *in situ* neutron calibration source consists of a DT neutron generator (14.2 MeV), followed by several stages of moderating and filtering materials: ~ 10 cm of Pb, ~ 20 cm of an Al/F mixture, and finally ~ 40 cm Fe for the final filtering to 24.4 keV. These moderating/filtering materials are inserted in a special port formed by removing a portion of the polyethylene and Pb shielding. The DT generator is surrounded by B-doped polyethylene to reduce human exposure. The most interesting event topology is a double scatter spread between two detectors, with the angle θ defining the energy of the first scatter. **Right:** A Geant4 simulation of the neutron flux leaving the end of the Pb/Al/F/Fe assembly shows the high purity of the monoenergetic 24.4 keV flux.

S_i is energy dependent, meaning that they must be combined together with the CENNS cross section σ_k of the target isotope. The total uncertainty on the CENNS rate is then derived from convolving the covariance matrix of the fission spectra with the CENNS cross section. For neutrinos above 1.8 MeV, leading to a maximum recoil energy of ~ 100 eV, a 2-3% uncertainty on S_i will result in approximately a 2-3% uncertainty on the total CENNS rate with a 50 eV energy threshold. For neutrino energies below 1.8 MeV, where much larger uncertainties of 5-10% are expected, the resulting uncertainty on the total CENNS rate are actually anticipated to be in the sub-% regime. Indeed, despite 69% of the neutrino flux having energies below 1.8 MeV, the small CENNS cross section at low energies means that a small portion of the total CENNS rate will come from low energy neutrinos. As a matter of fact, even if a CENNS measurement could be performed with no threshold, only 17% of the total rate would come from neutrinos below 1.8 MeV, and a 10% uncertainty on the summation calculation would only contribute to a 1.7% uncertainty to the total rate. In our case, where RICOCHET will be operating with a 50 eV energy threshold, a 10% uncertainty on the summation calculation would only contribute 0.2% uncertainty to the total CENNS rate. This indicates that even though the uncertainty on the low energy flux is large, it will not be the dominant contributor to the total CENNS rate uncertainty.

In summary, with RICOCHET deployed at the ILL-H7 site, we anticipate a total CENNS rate systematic uncertainty of about 3%, mostly arising from the fission spectra conversion (>1.8 MeV neutrino) and the reactor thermal power uncertainties.

3.6.2 Low-energy nuclear recoil energy calibration

Understanding the response of our detectors to both electron and nuclear recoils is paramount for the RICOCHET experiment as we both need to 1) discriminate between backgrounds and

3.6 Signal systematics

signal, and 2) accurately recover the true kinetic energy of the CENNS induced nuclear recoil at extremely low energies. To that end, the UMass RICOCHET group is developing a highly innovative low-energy, mono-energetic, and pulsed neutron calibration source that will be encapsulated in the RICOCHET shielding (see Fig. 3.10 – left panel). The latter is based on the use of a DT pulsed neutron generator followed by several stages of moderating and filtering materials to eventually produce 24.4 keV neutrons that will induce Ge and Zn nuclear recoils from 0 to 1.2 keV, hence fully covering the CENNS energy region.

These moderating/filtering materials will be inserted in a special port formed by removing a portion of the RICOCHET shielding. It is worth noticing that Fe has been used by many groups in the past to filter neutrons to this quasi-monoenergetic state, taking advantage of a narrow anti-resonant feature in the ^{56}Fe neutron scattering cross section [220, 221]. It is however novel to pair that Fe-based filter with the moderated flux of a DT neutron generator, but this pairing is appropriate in the RICOCHET case given that a low calibration flux is in fact desired, and given that a pulsed calibration source is advantageous in reducing backgrounds to the calibration. Figure 3.10 (right panel) shows the neutron flux leaving the end of the moderating/filtering material assembly, demonstrating the high purity of the mono-energetic 24.4 keV flux. Additionally, thanks to the pulsed nature of this neutron source, refined calibration using neutron double-scatter between two detector elements from the detector array will allow to precisely recover the true scattering energy on an event-by-event basis. Thanks to the cryogenic detector array topology, 10-to-45 degree scattering angle, corresponding to recoil energies in the range of 10-200 eV, will be accessible.

Eventually, thanks to this dedicated low-energy and mono-energetic pulsed neutron source, *in-situ* calibration will be possible on a regular basis to track any gain dispersion and ensure a highly robust nuclear recoil energy calibration over the CENNS energy region of RICOCHET.

3.6.3 In-situ neutron background monitoring

One last important source of systematics arises from the neutron induced nuclear recoils in the energy range of interest for CENNS studies, which cannot be discriminated based on the Ge/Zn particle identification capabilities. We therefore need to properly evaluate and statistically subtract this low-energy neutron background component from the observed energy distribution to accurately extract the neutrino signal. To do so, one needs to be able to precisely evaluate the expected number of neutron events, and their low-energy distribution, in the Ge and Zn detectors, thanks to an *in-situ* and independent fast neutron spectroscopy measurement.

Lithiated bolometers are the most promising detectors for this concern, since the Q value of the neutron capture reaction on ^6Li (4.78 MeV) is well above the natural gamma background ending at 2.6 MeV (^{208}Tl line), and that the simultaneous heat and scintillation measurements can ensure a background free fast neutron monitoring. Two main bolometric targets incorporating lithium nuclei have been studied up to now: LiF and LMO (Li_2MoO_4) by the ROSEBUD [222] and LUMINEU [223] collaborations respectively. Based on their previous studies, it has been demonstrated that such bolometers can achieve energy resolutions at the capture peak of 4.78 MeV of a few keV [223], suggesting that fast neutron spectroscopy is feasible for neutron energies relevant to the region of interest for CENNS. Indeed, the minimum neutron energies required to produce Ge or Zn nuclear recoils of 50 eV and 1 keV are 1 and 20 keV respectively. An array of a few $\mathcal{O}(100)\text{g}$ scintillating lithiated bolometers is under consideration for an in-

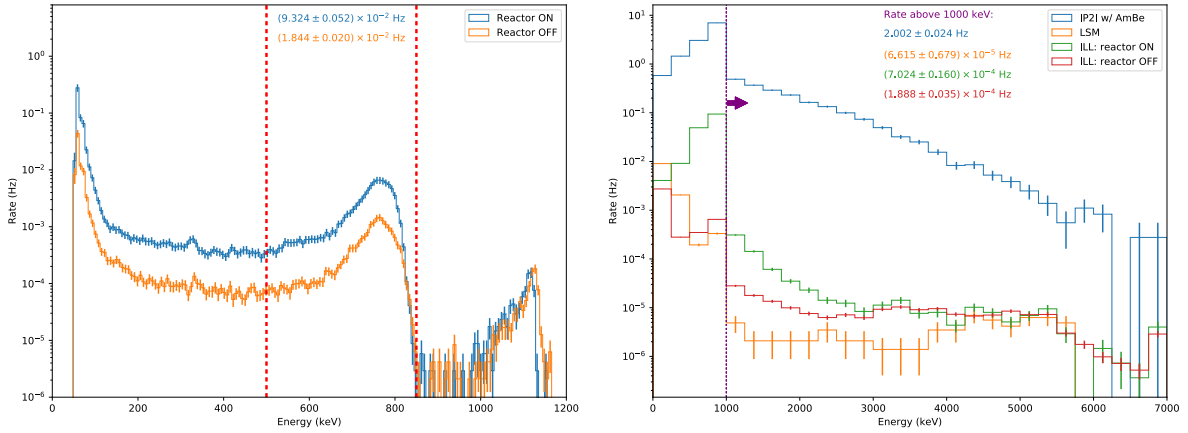


Figure 3.11: Energy distribution as observed by the ILL (**left**) and the JINR (**right**) detectors during reactor ON and OFF periods at the ILL-H7 site. For the JINR detector, we also show data taken at LSM and at IP2I with the detector exposed to an AmBe neutron source.

situ monitoring of the fast neutron background of RICOCHET at ILL. Calibration measurements, combined with Geant4 simulations, are currently under investigation to 1) demonstrate the performance and the interest of such an *in-situ* neutron monitoring technique, and 2) optimize its integration with the Ge and Zn detector array if proven to be efficient.

3.7 Characterization of the ILL site

Starting in February 2019, the RICOCHET collaboration has been working on characterizing the ILL-H7 site in order to validate the possible operation of the future RICOCHET experiment. We hereafter describe the resulting onsite neutron and vibration measurements, which combined to previous gamma and muon onsite measurements done by the STEREO collaboration, led the RICOCHET collaboration to consider deploying its experiment at the ILL-H7 site which was then granted by the ILL scientific council in May 2020.

3.7.1 The neutron background

As RICOCHET plans on being at only ~ 8 meters from the reactor core, the reactogenic neutron background will play a crucial role in the experiment. Fast neutron scatterings are able to mimic the expected CENNS signals, in producing low-energy nuclear recoils that cannot be discriminated thanks to particle identification. Moreover, even thermal neutrons could be a problem through secondary reactions. Indeed some γ s, after (n,γ) reactions, are highly energetic and have therefore large enough penetration power to be the source of further (γ,n) reactions, or even produce elastic scatterings on Ge nuclei [224]. Though coherent photon-nucleus scattering cross sections is negligible for nuclear recoils above 50 eV, it is worth noticing that kinetically a 5 MeV gammas can produce nuclear recoils up to ~ 200 eV.

In RICOCHET the neutron problem is being addressed by: 1) Preliminary on-site neutron measurements, thus realistic Geant4 calculations of the shield can be performed (see Sec. 3.4); 2)

3.7 Characterization of the ILL site

On-site neutron monitoring during the RICOCHET experiment will be done thanks to adjacent He-3 detectors; 3) Monitoring of fast neutrons producing nuclear recoils beyond the CENNS region of interest (>2 keV) in both Ge and Zn detectors with particle identification capabilities; 4) *in-situ*, i.e. within the RICOCHET cryostat, monitoring of fast neutrons will be achieved thanks to lithiated bolometers, if proven to be suitable (see Sec. 3.6). Lastly, it is worth emphasizing that neutrons reaching the cryogenic detectors can be further rejected from event multiplicity in several detectors. This has been proven to be very efficient in large arrays of Ge detectors such as the EDELWEISS experiment [80]. During the fall of 2019, fast neutron measurements have been performed within the STEREO casemate, more precisely between the STEREO detector and its front wall (closest to the reactor). To that end, two ^3He Proportional Counters (PC) were used simultaneously though operated in different modes:

Fast neutron moderation: the so-called ILL detector was inserted inside a thick (20 cm) polyethylene shield further surrounded by a few cm thick B_4C layer acting as a thermal neutron catcher. In such a configuration, this PC was maximally sensitive to few MeV ambient neutrons. The fast neutron flux is then assessed by computing the capture rate between 400 keV to 800 keV (where low-ionizing events from muons and gammas are negligible [201]). Figure 3.11 (left panel) shows the observed energy distribution with the ILL detector during the reactor ON and OFF periods, where we measured a fast neutron capture rate 4 times larger during the ON period.

Fast neutron spectroscopy: The so-called JINR detector is an ultra low background proportional counter (low alpha background), with large dynamic range, and excellent intrinsic energy resolution. It was therefore used in a “capture on flight” mode with no moderator, but was only surrounded by B_4C neutron catcher to avoid pile ups of thermal neutron captures. This way, for events with energies beyond the capture line at 764 keV, the neutron energy can be derived thanks to $E_{\text{neutron}} = E_{\text{measured}} - 764$ keV. However, it should be noted that contributions from fast neutron elastic scattering are also expected beyond the capture line. The fast neutron flux, and information about its energy spectrum, is then assessed by counting the rate of events between 1 MeV and 6 MeV. Figure 3.11 (right panel) shows the observed energy distribution with the JINR detector during the reactor ON and OFF periods, as well as when operated at the LSM to estimate the remaining alpha contribution. A neutron flux excess during the reactor ON period is clearly observed, especially at low energies, suggesting the detection of few MeV reactogenic neutrons. It is however worth noticing that we observe no excess of neutrons with energies ≥ 3 MeV, while we have clearly demonstrated sensitivity of this detector to neutrons with energies up to 6 MeV thanks to an AmBe neutron calibration done at IP2I.

Figure 3.12 shows the fast neutron rates as measured by the two ^3He PC described above, with the ILL (moderation) and JINR (spectroscopy) setups on the x- and y-axes respectively. We observe an excellent correlation between these two fast neutron monitoring approaches which gives us great confidence in the validity of our measurements, done both at ILL (reactor ON/OFF) and IP2I (with/without an AmBe neutron source). It should be noted that the ultra-low alpha background (producing events with energies below 5 MeV at a rate of 6.6×10^{-5} Hz) in the JINR detector has been characterized at the Laboratoire Souterrain de Modane and was properly taken into account in the interpretation of our results (see Fig. 3.12) which conclusions

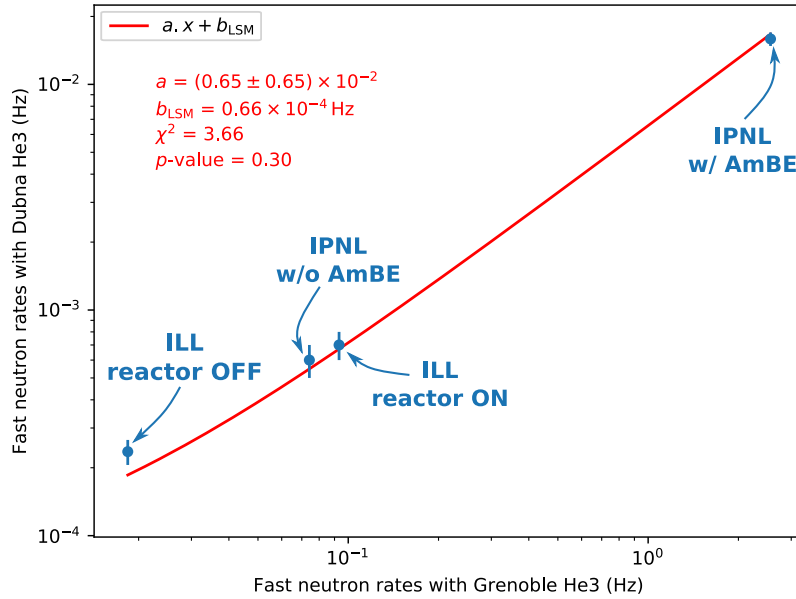


Figure 3.12: Correlation between the fast neutron measurements from the ILL (x-axis) and JINR (y-axis) ³He PC, realised at the ILL-H7 site and at IP2I.

are the following:

- The fast neutron flux at ILL is 5 times larger reactor ON than reactor OFF
- The fast neutron flux between reactor ON and the IP2I lab (inside the lead shield), with no calibration sources, is about 25% higher

Interestingly, the low-energy neutron background at IP2I has been previously measured with our RED80 prototype Ge bolometer (see Sec. 5.3.4) and shown to be about 10^4 events/keV/kg/day (DRU) at 2 keV. This suggests that a similar low-energy neutron background should be observed with our Ge bolometers at the ILL reactor ON assuming no shielding surrounding the RICOCHET cryostat. This is indeed confirmed by the Geant4 simulations, as discussed in Sec. 3.4, where the total (reactogenic + cosmogenic) NR rate between 50 eV and 1 keV is expected to be about 5×10^4 events/kg/day with no shielding. Moreover, this suggests that the RICOCHET shielding has to be designed to reach attenuation levels of 10^3 -to- 10^4 to reach our physics goals. According to our Geant4 simulations (see Sec. 3.4), including both cosmogenic and reactogenic contributions to the neutron background, reaching such attenuation factor seems feasible as the final NR rate expected with our preliminary shielding design is of 5 (13) events/kg/day with (without) a full coverage muon-veto. As a matter of fact, it is worth noticing that as reactogenic neutrons have energies lower than 10 MeV, they are easier to shield against compared to cosmogenic ones which can have energies up to few GeV. This further highlight the great advantage of the ILL-H7 site, where the STEREO experiment is currently running, thanks to its artificial overburden of about 15 m.w.e from the water channel.

Nowadays, additional studies combining measurements at both ILL (after STEREO decommissioning), IP2I and LSM with the JINR detector (which has neutron spectroscopy capabilities)

3.7 Characterization of the ILL site

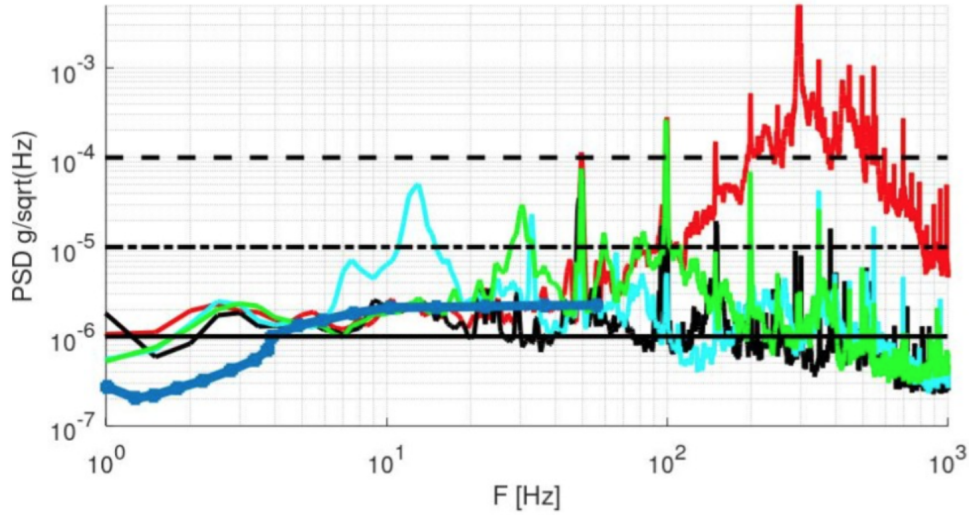


Figure 3.13: Compilation of vibration measurements realised at ILL in the STEREO casemate (red – with no insulation, green and cyan – with two different thicknesses of vibration insulation), at the IP2I with no insulation (black), and compared to a seismic model (blue).

with Geant4 simulations are being performed in order to further refine our fast neutron models and improve our background estimations and shielding design.

3.7.2 Vibration levels

Due to the high sensitivity of cryogenic detectors to environmental vibrations, it is of paramount importance to make sure that the vibration levels at ILL are either low enough or can be efficiently mitigated to ensure a proper operation of the RICOCHET experiment. We therefore performed vibration measurements at different places, within the STEREO experiment perimeter, in the H7 site at ILL. Following the procedure described in [166], we used a PCB39B04 high sensitivity, low intrinsic noise, one-axis accelerometer. The latter was mounted within a cylindrical vacuum chamber of a total mass of about 1 kg. A compilation of the vibration measurements, expressed as acceleration power spectral densities given in $g/\sqrt{\text{Hz}}$, is shown in Figure 3.13. We then compare measurements performed with the accelerometer disposed directly onto the concrete floor (red) to the ones obtained with two different thicknesses of visco-elastic vibration insulator (green and cyan). For the sake of completeness, we also compare these ILL results to the ones obtained at IP2I with no insulation (black), and to the theoretical ultimate vibration level predicted by seismic models (dark blue). We can conclude that without insulation, the vibration level at ILL is similar to the one observed at IP2I up to ~ 50 Hz and then becomes two orders of magnitude larger with a maximum at about 300 Hz. Such vibration levels, though beyond the detector bandwidth (≤ 50 Hz), can produce dramatic microphonic noises or even produce parasitic heat loads on the detectors due to internal frictions. Thanks to the use of visco-elastic materials used as insulators, we were able to show that vibration levels comparable to the ones observed in Lyon are reachable. Furthermore, the GRANIT [225] and GAMS [226] experiments, also requiring low vibration levels, are operating successfully

at ILL. We are therefore confident that a suitable vibration mitigation system, such as floating deck or passive/active dampers (see Figure 3.5 for illustration), could be specifically designed to achieve the RICOCHET requirements.

3.8 Conclusion and perspectives

The RICOCHET collaboration aims at building a low-energy reactor neutrino observatory and provide a high-precision CENNS measurement down to the sub-100 eV energy range in order to search for new physics in the electroweak sector. These include for instance the existence of sterile neutrinos and of new mediators, that could be related to the Dark Matter problem, and the possibility of Non Standard Interactions that would have tremendous implications on the global neutrino physics program. The first key feature of the RICOCHET program, compared to other planned or ongoing CENNS projects, is to aim for a kg-scale experiment with unparalleled background rejection, thanks to particle identification, down to the $\mathcal{O}(10)$ eV energy threshold. The latter will allow to both properly understand and model the observed background and reject both known and unknown backgrounds in a yet to be explored energy region. The second key feature is to combine several targets and cryogenic detector techniques to benefit from target complementarity in the quest of new physics searches, and further alleviate possible detection technique related systematics.

After demonstrating its science potential, and with the approval from the ILL scientific committee, the RICOCHET collaboration will deploy its experiment at the ILL-H7 site by 2022-2023. After about 2 years of onsite operations, hence by 2025, the collaboration expects to achieve a few-percent precision measurement of the CENNS process, *i.e.* at the level of the anticipated systematic uncertainties mostly arising from the neutrino flux predictions, down to the demonstrated 50 eV energy threshold. Such timeline happens to be quite similar to other low-threshold CENNS experiments with the exception that only RICOCHET plans on having a single kg-scale phase to reach such high precision measurement, hence significantly mitigating the risks of delays from phase upgrades.

Though the RICOCHET program is primarily motivated by the enormous potential impact of a low-energy precision measurement of the CENNS process in the quest of new physics searches in the neutrino sector, it will also have major repercussions in other fields:

Probing the dark sector: As demonstrated in [88], the CENNS interaction of cosmic neutrinos will soon become the ultimate background to upcoming ton-scale direct dark matter experiments. One way to mitigate this irreducible background is to reduce the systematic uncertainties on the CENNS cross-section and use several monolithic targets [89], see Sec. 1.2.3. Additionally, thanks to its low-energy threshold, RICOCHET will considerably extend the dark matter searches to the MeV/c²-to-GeV/c² mass-scale, and be competitive with the ongoing CRESST, EDELWEISS and SuperCDMS experiments.

Nuclear reactor monitoring: thanks to its very low 50 eV nuclear recoil energy threshold, RICOCHET will be sensitive to neutrino energies down to ~ 1 MeV, which is almost two times lower than the Inverse Beta Decay (on free proton) neutrino energy threshold of 1.8 MeV. Therefore, as a by-product of this research program, RICOCHET will be able to provide insightful

3.8 Conclusion and perspectives

information regarding the low-energy neutrino spectrum and related nuclear physics processes that take place inside nuclear reactor cores. Lastly, RICOCHET will pave the way to the next generation of nuclear reactor monitoring dedicated experiments with a movable and significantly more compact technology than current ton-scale neutrino detectors, able to study the non-proliferation of nuclear fuels and weapons.

Cryogenic detector technology driver: in order to provide such a high-precision CENNS measurement at low-energies, the RICOCHET collaboration is developing two highly innovative cryogenic detector technologies: the CryoCube and the Q-Array. While the latter could be scaled-up to much larger payloads of $\mathcal{O}(10)$ kg, thanks to its built-in multiplexed readout, the CryoCube would be significantly harder to expand. To that end, we recently started investigating the use of multiplexed kinetic inductance detectors (mKID), with 30-g scale Si crystals and deported feedlines, as a possible $\mathcal{O}(10 - 100)$ kg-scale payload technology for next generation CENNS and/or dark matter experiments [227].

4

CryoCube design optimization and expected CENNS sensitivity with RICOCHET

The CryoCube detector, and its front-end HEMT-based electronics, are funded thanks to the ERC-CENNS starting grant and are meant to be deployed within the future RICOCHET low-energy neutrino observatory (see Chap. 3). They are being designed to provide a percentage precision CENNS measurement in the sub-100 eV energy region to search for new physics in the electroweak sector. Therefore, they have to fulfill the following specifications:

1. **Energy thresholds in the $\mathcal{O}(10)$ eV range**, as the discovery potential scales exponentially with lowering the energy threshold;
2. **Significant background rejection** combined with a low-radioactivity environment, as the experiment's sensitivity increases with the signal-to-noise ratio;
3. **Total target mass of about one kilogram** to have significant sensitivity to putative new physics signatures.
4. **Timing resolution in the $\mathcal{O}(100)$ μs** , in order to reject muon-induced backgrounds from above ground operation while keeping a high enough CENNS signal sensitivity
5. **Accommodation of several monolithic target materials**, as most new physics signatures, such as Non Standard Interactions, depend on the target's nuclear properties.

To achieve these technological goals, the CryoCube will consist of an array of 27 Ge-crystal bolometers of about 30 g each. Each of these individual Ge detector will be able to achieve particle identification thanks to the double heat/ionization measurement, and achieve sub-100 eV threshold thanks to optimized NTD-Ge sensors. Depending on future results, the Ge-crystals could be replaced by other semiconducting target materials such as Si, or even be used with superconducting materials such as Zn that may also exhibit particle identification capabilities

4.1 Electro-thermal model and heat resolution optimization

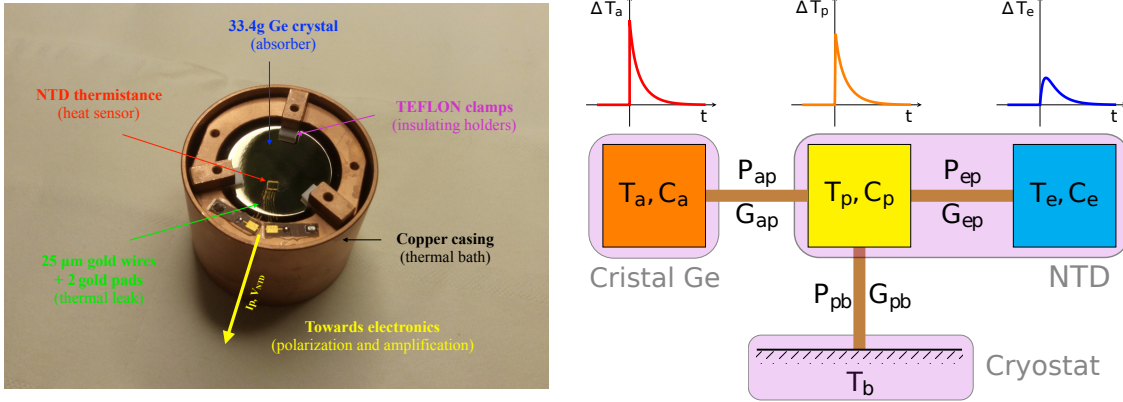


Figure 4.1: **Left:** Picture of the RED20 detector prototype where all the relevant components related to its thermal modelization are labeled. **Right:** Simplified block diagram of the thermal modelization of the RED20 detector (*Courtesy of D. Misiak*).

thanks to pulse shape discrimination. Eventually, the crystals will be packed together in a $3 \times 3 \times 3$ topology and encapsulated in radio-pure infrared-tight copper box suspended below the inner shielding with its dedicated cryogenic suspension system [164], and cold front end electronics [147]. In the two first sections, we will describe how the heat and ionization channels of the individual CryoCube Ge detectors are being modeled and optimized in order to achieve the targeted performance required for the RICOCHET experiment. Eventually, the last section is dedicated to the estimation, under a large number of scenarios, of the CENNS discovery potential of the CryoCube detector technology at ILL within the forthcoming RICOCHET experiment.

4.1 Electro-thermal model and heat resolution optimization

We hereafter present the modelisation of our heat sensors which eventually will help us at optimizing our detectors and further improve their performance. It should be noted that this thermal model formalism has first been applied to characterize the EDELWEISS FID800 detectors using a data driven approach and which has resulted in the following publication [167], and follows the work from my PhD student D. Misiak [228].

A photo of the RED20 detector and its corresponding simplified thermal block diagram are presented in Fig. 4.1. The RED20 detector, similarly to all the RED detectors presented in Sec. 5.3, are equipped with a single NTD heat sensor connected to gold pads on the copper casing thanks to gold wire-bonds. By doing so, we ensure both the electrical contact of the NTD to the readout electronics and its weak thermal coupling to the bath (cryostat) of temperature T_b . The block diagram then describes 3 heat capacities: the absorber (33.4 g Ge crystal), and the electron and phonon systems of the NTD. Note that for the sake of simplicity of this brief introduction to thermal modeling, we hereafter neglect the contribution of the thermal clamps to both the thermal leak and to the overall heat capacity which will be further discussed later on. We have considered here that the glue spots, the wire-bonds and gold pads (for the thermal leak) have negligible heat capacities. All these blocks are then characterized by a heat capac-

4.1 Electro-thermal model and heat resolution optimization

ity C and a corresponding temperature T and are connected to each other via thermal links characterized by different conductances G . Eventually, the NTD thermistance is connected to a voltage preamplifier and is polarized to a current bias I_p obtained from applying a constant voltage through a high-impedance load resistor R_L mounted in serie with the NTD with a corresponding C_c cabling capacity. Following [229, 228], such a thermal system is characterized by a set of non linear differential equations describing the heat flow between the different baths and their coupling to the electronic readout through its bias voltage V_b and resulting Joule heating $P_J = V^2/R$:

$$\begin{aligned}
 C_a \frac{dT_a}{dt} &= g_{glue} S_{NTD} (T_p^{n_g} - T_a^{n_g}) \\
 C_p \frac{dT_p}{dt} &= -g_{glue} S_{NTD} (T_p^{n_g} - T_a^{n_g}) + V_{NTD} g_{ep} (T_e^n - T_p^n) - g_k S_{Au} (T_p^{n_k} - T_b^{n_k}) \\
 C_e \frac{dT_e}{dt} &= \frac{V^2}{R(T_e)} - V_{NTD} g_{ep} (T_e^n - T_p^n) \\
 C_c \frac{dV}{dt} &= \frac{V_b - V}{R_L} - \frac{V}{R(T_e)}
 \end{aligned} \tag{4.1}$$

where V and R are the NTD voltage and resistance. The latter depends on the electron bath temperature T_e following the Shklovskii-Efrös law: $R(T_e) = R_0 \exp(\sqrt{T_0/T_e})$ where R_0 depends on the intrinsic properties of Ge and of geometrical factors, and T_0 is related to the germanium doping level [131]. The various n indices correspond to the power law of the different heat conductances. V_{NTD} and g_{ep} are the volumes and electron-phonon coupling constants of the NTD. S_{NTD} and g_{glue} are the NTD surface, *i.e.* the gluing surface, and the glue coupling constant. S_{Au} and g_k are the surface of the gold NTD electrodes and the Kapitza conductance characterizing the thermal leak¹. From Eq. 4.1, one can fully describe the detector response in all three regimes of interest: 1) the steady state when everything is in equilibrium, 2) the time domain where we can simulate pulses arising from particle interaction, and 3) the frequency domain which is used to study the noise power spectral densities and related energy and timing resolutions.

4.1.1 Steady state

By solving Eq. 4.1 assuming $d\phi_i/dt = 0$ with $\phi = \{T_a, T_p, T_e, V\}$, we can derive the steady state solutions ($\bar{\phi}_i$) of the detector. By studying the evolution of the measured voltage \bar{V} as function of the polarization current $I_p = V_b/(R_L + R(T_e))$, one can have access to the various thermal conductances, as well as the R_0 and T_0 constant characterizing the NTD thermistance [167, 228]. Only the heat capacities and the complex impedance of the system are not accessible in this case as the latter are only accessible in the time and frequency domain response of the detector [167, 228].

4.1.2 Time domain

In order to derive the detector response in the time domain, one can either solve Eq. 4.1 numerically, *e.g.* with ODEINT from PYTHON, or analytically within the context of first order

¹All the parameters are given later in Table 4.1

4.1 Electro-thermal model and heat resolution optimization

perturbation theory. The latter implies that the time dependent solution of our system can be expressed in the form $\phi(t) = \bar{\phi} + \delta\phi(t)$ where $\bar{\phi}$ corresponds to the steady state and $\delta\phi(t)$ to the first order perturbation [228, 230, 165]. By Taylor expanding to first order all of the non-linear power transfer terms such as: $P_{ij} \approx \bar{P}_{ij} + \left. \frac{\partial P_{ij}}{\partial \phi_i} \right|_{\bar{\phi}_i} \delta\phi_i + \left. \frac{\partial P_{ij}}{\partial \phi_j} \right|_{\bar{\phi}_j} \delta\phi_j$, one can rewrite Eq. 4.1 as:

$$\begin{aligned}
 \frac{d\delta T_a}{dt} &= -\frac{G_{ap}^a}{C_a} \delta T_a + \frac{G_{ap}^p}{C_a} \delta T_p \\
 \frac{d\delta T_p}{dt} &= \frac{G_{ap}^a}{C_p} \delta T_a - \frac{G_{ap}^p + G_{ep}^p + G_{pb}^p}{C_p} \delta T_p + \frac{G_{ep}^e}{C_p} \delta T_e \\
 \frac{d\delta T_e}{dt} &= \frac{G_{ep}^p}{C_e} \delta T_p - \frac{1}{C_e} \left(G_{ep}^e + \frac{\bar{V}^2}{R(\bar{T}_e)^2} \left. \frac{dR}{dT_e} \right|_{\bar{T}_e} \right) \delta T_e + \frac{2}{C_e} \frac{\bar{V}}{R(\bar{T}_e)} \delta V \\
 \frac{d\delta V}{dt} &= \frac{1}{C_c} \frac{\bar{V}}{R(\bar{T}_e)^2} \left. \frac{dR}{dT_e} \right|_{\bar{T}_e} \delta T_e - \frac{1}{C_c} \left(\frac{1}{R_L} + \frac{1}{R(\bar{T}_e)} \right) \delta V
 \end{aligned} \tag{4.2}$$

with the following linearized conductivities in units of [W/K] given by :

- glue crystal-NTD (G_{ap}): $G_{ap}^{a,p} = n_g g_{glue} S_{NTD} \bar{T}_{a,p}^{n_g-1}$
- electron-phonon coupling (G_{ep}): $G_{ep}^{e,p} = n_g g_{ep} V_{NTD} \bar{T}_{e,p}^{n-1}$
- gold wires thermal leak (G_{pb}): $G_{pb}^p = n_k g_k S_{Au} \bar{T}_p^{n_k-1}$

Eventually, using linear algebra Eq. 4.2 can be re-written in the form of a first order differential equation such as:

$$\frac{d\delta\phi}{dt} = -\mathbf{M}\delta\phi + \mathbf{F}(t - t_0) \tag{4.3}$$

where $\mathbf{F}(t - t_0)$ represents any kind of external power in the system (*e.g.* particle interaction, external radiation, ...), and \mathbf{M} is the matrix describing the electro-thermal couplings between the different elements derived from the linearized set of equations given by :

$$\mathbf{M} = \begin{pmatrix} \frac{G_{ap}^a}{C_a} & -\frac{G_{ap}^p}{C_a} & 0 & 0 \\ -\frac{G_{ap}^a}{C_p} & \frac{G_{ap}^p + G_{ep}^p + G_{pb}^p}{C_p} & -\frac{G_{ep}^e}{C_p} & 0 \\ 0 & -\frac{G_{ep}^p}{C_e} & \frac{1}{C_e} \left(G_{ep}^e + \frac{\bar{V}^2}{R(\bar{T}_e)^2} \left. \frac{dR}{dT_e} \right|_{\bar{T}_e} \right) & -\frac{2}{C_e} \frac{\bar{V}}{R(\bar{T}_e)} \\ 0 & 0 & -\frac{1}{C_c} \frac{\bar{V}}{R(\bar{T}_e)^2} \left. \frac{dR}{dT_e} \right|_{\bar{T}_e} & \frac{1}{C_c} \left(\frac{1}{R_L} + \frac{1}{R(\bar{T}_e)} \right) \end{pmatrix} \tag{4.4}$$

The general solution of Eq. 4.3 is a linear combination of $N = 4$ exponential functions characterized by different time constants $\tau_i = 1/\lambda_i$, where λ_i are the eigenvalues of the matrix \mathbf{M} and may have a rather complicated form (see Eq. 4.4). One can easily demonstrate that the time dependent solution for each element ϕ_i of the state vector is given by:

$$\delta\phi_j = \sum_i P_{ij} A_i e^{-t/\tau_i} \tag{4.5}$$

where P_{ij} corresponds to the basis formed by the eigenvectors satisfying the following conditions $\mathbf{M} = \mathbf{P}\mathbf{D}\mathbf{P}^{-1}$, with \mathbf{D} the diagonal matrix of \mathbf{M} . \mathbf{A} is a vector of normalization constants to be determined thanks to the initial conditions by solving $\mathbf{A} = \mathbf{P}^{-1}\phi(0)$.

4.1.3 Frequency domain

Thanks to the time domain description of our electro-thermal modelisation of our detector previously described, we can investigate the detector's response in the frequency domain where the noise sources are more easily characterized via their power spectral densities (PSD) referred to the input of the voltage preamplifier. To do so, we take the Fourier Transform of the previous equation 4.3 where we additionally multiply each term from the left with the diagonal capacitance matrix \mathbf{C} as,

$$\mathbf{C}(i\omega + \mathbf{M})\delta\tilde{\phi}(\omega) = \mathbf{Z}(\omega)\delta\tilde{\phi}(\omega) = \mathbf{C}\tilde{\mathbf{F}}(\omega) \quad \text{with} \quad \mathbf{C} = \{C_a, C_p, C_e, C_c\} \quad (4.6)$$

where we have introduced the complex electro-thermal impedance matrix Z containing all the couplings and their frequency dependence given by [228]:

$$Z(\omega)\delta\tilde{\phi}(\omega) = \begin{pmatrix} \frac{1}{a} & -g & 0 & 0 \\ -b & \frac{1}{c} & -h & 0 \\ 0 & -d & \frac{1}{e} - k & -l \\ 0 & 0 & -f & Z_{eq}^{-1} \end{pmatrix} \begin{pmatrix} \delta\tilde{T}_a \\ \delta\tilde{T}_p \\ \delta\tilde{T}_e \\ \delta\tilde{V} \end{pmatrix} = \begin{pmatrix} W - \tilde{P}_{ap} \\ \tilde{P}_{ap} + \tilde{P}_{ep} + \tilde{P}_{bp} \\ -\tilde{P}_{ep} \\ \tilde{I} \end{pmatrix} = C\tilde{F}(\omega) \quad (4.7)$$

where the red terms refer to the various noise sources discussed below and W is the injected power into the system following a particle interaction in the absorber. The \mathbf{Z} matrix coefficients are identified from Eq. 4.4 and defined as²:

$$\begin{aligned} a &= (iC_a\omega + G_{ap}^a)^{-1} & g &= G_{ap}^p \\ b &= G_{ap}^a & h &= G_{ep}^e \\ c &= (iC_p\omega + G_{ap}^p + G_{ep}^p + G_{pb}^p)^{-1} & k &= -\frac{(dR/dT)V^2}{R^2} \\ d &= G_{ep}^p & \ell &= \frac{2V}{R} \\ e &= (iC_e\omega + G_{ep}^e)^{-1} & Z_{eq} &= \left(\frac{1}{R_L} + \frac{1}{R(T_e)} + i\omega C_c \right)^{-1} \\ f &= \frac{(dR/dT)V}{R^2} \end{aligned} \quad (4.8)$$

Eventually the contributions to the different temperature fluctuations and voltage output from the various noise sources (and signal) can easily be computed following: $\delta\tilde{\phi}(\omega) = \mathbf{Z}^{-1}(\omega)\tilde{\mathbf{F}}(\omega)$.

Before computing the expected noise contributions to the output voltage, and the resulting energy resolution, we first need to evaluate the signal sensitivity of the detector $s_V(\omega)$ to a particle interaction in the absorber. Assuming that all of the particle energy is released under the form of phonons thermalizing within the Ge crystal absorber, we can define $s_V(\omega) = Z_{va}^{-1}\hat{p}(\omega)$ where $\hat{p}(\omega)$ is the Fourier transform of the signal power injected from the particle interaction W . In the approximation that the energy is released instantaneously in the absorber we have $\hat{p}(\omega) = 1$.

²Note that the expressions of the various coefficients have been chosen to be compatible with a standard block diagram formalism, see [229, 228] for more details

4.1 Electro-thermal model and heat resolution optimization

Note that this formalism can easily be extended to cases where the deposited energy gets released in different elements (absorber, sensor, ...) simultaneously and with some possible thermalization time constants, see [167, 228]. This latter case is usually relevant when the sensor is sensitive to athermal phonons which have the ability to get thermalized in other elements than the main absorber³. For instance, if we assume that a fraction ϵ of the phonons is thermalized directly within the electron system of the NTD, the expression of the sensitivity then becomes:

$$s_V(\omega) = [\epsilon Z_{ve}^{-1} + (1 - \epsilon) Z_{va}^{-1}] \hat{p}(\omega) \quad (4.9)$$

Note that the sensitivity $s_V(\omega)$ is in units of [V/W].

The total noise power spectral density referenced to the output voltage of the preamplifier $S_{V,tot}$ is computed in summing quadratically all sources of noise, assuming that they are uncorrelated. We expect three distinct sources of noise: 1) thermal fluctuation noise (TFN), 2) current noise from the preamplifier and the resistors, and 3) voltage noise from the preamplifier.

Thermal fluctuation noise arise at each thermal link (G_{ij}) from the temperature differences between the detector elements so that the total TFN contribution referenced at the output voltage can be expressed as [229, 230]:

$$S_{V,TFN} = 2k_B \left[\sum_{(i,j)}^{(e,p),(a,p),(p,b)} (T_i^2 + T_j^2) G_{ij} |Z_{vi}^{-1} - Z_{vj}^{-1}|^2 \right] \quad [V^2/Hz] \quad (4.10)$$

The total current noise, coming from the preamplifier i_n and the Johnson noise contributions from the NTD thermistance $R(\bar{T}_e)$ and the load resistor R_L heat sunk at T_{RL} is:

$$S_{V,i} = \left[i_n^2 + 4k_B \left(\frac{\bar{T}_e}{R(\bar{T}_e)} + \frac{T_{RL}}{R_L} \right) \right] |Z_{vv}^{-1}|^2 \quad [V^2/Hz] \quad (4.11)$$

Finally, the last noise contribution comes from the voltage noise of the preamplifier e_n which is directly referenced to the voltage output as it is independent of the impedance such that:

$$S_{V,e} = e_n^2 \quad [V^2/Hz] \quad (4.12)$$

Now that both the noise power spectral density and the signal sensitivity are defined, we can compute the Noise Equivalent Power (NEP). The latter corresponds to the amount of thermal noise in the absorber (if only a thermal phonon contribution is assumed) that would produce an identical amount of voltage noise in the NTD. The NEP is defined as [230, 229, 165],

$$\text{NEP}^2(\omega) = \frac{S_{V,tot}}{|\hat{s}_V|^2} \quad [W^2/Hz] \quad (4.13)$$

Interestingly, one can see that the NEP is basically related to the amount of noise that seats inside of the bandwidth of the sensor and we can therefore intuitively realize that it is closely related to the energy resolution of the system. Indeed, the latter is defined as [230, 229, 165],

$$\sigma_E^2 = \left(\int_0^\infty \frac{d\omega}{2\pi} \frac{4}{|\text{NEP}(\omega)|^2} \right)^{-1} \quad [J^2] \quad (4.14)$$

³Note that we are currently investigating the possibility of athermal contributions to our observed signal and ‘‘phonon leaks’’ through the TEFLON clamps, which can be both easily modeled within this formalism, see [228].

4.1 Electro-thermal model and heat resolution optimization

Note that with real data, the lower and upper integration bounds are set by the length of the time window considered and the Nyquist frequency, defined as half of the sampling frequency, respectively.

4.1.4 Results and discussion

Figure 4.2 shows the spectral analysis of the electro-thermal RED20 detector response with the input parameters listed in Table 4.1. All of the heat capacities are taken from literature [229] (and reference therein), while the heat conductances (g_{ep} and g_k) and the NTD parameters, R_0 and T_0 , values are extracted from comparing our IV data with our theoretical predictions [228]. We can see for instance that the NTD is properly sensing the heat deposited in the absorber as $G_{pb} \ll G_{ep}$ and that electronics bandwidth is larger than the sensor one as $\tau_{elec.} \ll \tau_{ep}$. This RED20 detector design, which we now use for all our detector prototype, resulted from extensive scans of these tuning design parameters confronted with our data collected at both Modane and IP2I [167, 228]. It should however be noted that while our model predicts the stationary states (IV data) very well, we still have some discrepancies in the pulse shapes, both in terms of time constants and height (also called sensitivity). This suggests that the model described here (see Fig. 4.1) is oversimplified and that our detectors should be better described with a more complex structure. My student D. Misiak has investigated more extended models to improve our understanding of our detector response and to further optimize them [228]. These investigations include for instance the existence of 1) athermal phonons ($\epsilon \neq 0$), and 2) additional parasitic heat capacities with non negligible thermal coupling to the crystal and to the bath (e.g. TEFLON clamps). To provide a more comprehensive understanding of our simulated RED20 and its expected performance, we consider in Table 4.1 the case of a pure thermal signal ($\epsilon = 0$), and a mixture of both thermal and athermal signals with $\epsilon = 0.43$ which matches the observed sensitivity of RED20 at both 17 mK with $I_p = 1$ nA ($1.8 \mu\text{V}/\text{keV}$), and 13 mK with $I_p = 0.2$ nA ($5 \mu\text{V}/\text{keV}$) – see Sec. 5.3.1. Note that the possible contribution of athermal phonons to our observed signal could also explain why the measured time constants are a few times smaller than the ones predicted (see Table 4.1 and Sec. 2.3.3), implying that our detectors are faster than expected from this overly simplified thermal model. It is for these reasons of possible athermal phonon sensitivity that we glue the NTD directly onto the Ge crystal, and not on the electrodes (see Sec. 4.2) as was previously the case with the FID800 detectors in EDELWEISS [80].

From Fig. 4.2 we see that the FET induced voltage e_n and current i_n noises are dominating the total noise PSD at low (2 Hz) and high (20 Hz) frequencies. This is highly mitigated with the use of the HEMT-based electronics for which the induced noise only dominates over the other sources of noise below 1 Hz (e_n) and beyond 100 Hz (i_n). Note how all sources of noise and signal are further filtered when going from a FET- to a HEMT-based electronics. This is due to the five times larger input capacitance of the HEMT with respect to the JFET. The electronic noise put aside, from high to low frequencies, we see that the dominating thermal sources of noise are: the NTD Johnson noise (red) down to ~ 7 Hz, then followed by the electron-phonon and phonon-bath TFN down to ~ 0.7 Hz and below, respectively. It is worth noticing that the filtering of the Johnson noise at the lowest frequencies is due to the so-called electro-thermal feedbacks which allows the damping of the fluctuations back into the absorber, hence mitigating

4.1 Electro-thermal model and heat resolution optimization

Component	Value	Notes
Bath		
Temperature	13 mK	
Absorber	Ge	
Volume	$\pi \times 2^2/4 \times 2 = 6.3 \text{ cm}^3$	33.4 g
Heat capacity	$C_a = 5.97 \times 10^{-11} \text{ J/K}$	$C_a = 2.7 \times 10^{-6} \bar{T}_a^3 \text{ J/K/cm}^3$
NTD	Ge	
Surface (S_{NTD})	$2 \times 2 = 4 \text{ mm}^2$	
Thickness	0.45 mm	
Volume (V_{NTD})	1.8 mm^3	
Surface electrodes (S_{Au})	$2 \times (0.15 \times 2) = 0.6 \text{ mm}^2$	
R_0 / T_0	0.96 Ω / 4.52 K	$\bar{R}(\bar{T}_e) = R_0 e^{\sqrt{T_0/\bar{T}_e}}$
Heat capacity (phonon)	$C_p = 1.71 \times 10^{-14} \text{ J/K}$	$C_p = 2.7 \times 10^{-6} \bar{T}_p^3 \text{ J/K/cm}^3$
Heat capacity (electron)	$C_e = 3.17 \times 10^{-11} \text{ J/K}$	$C_e = 1.1 \times 10^{-6} \bar{T}_e \text{ J/K/cm}^3$
Conductivities		
Electron-Phonon (NTD)	$G_{ep}^e \approx G_{ep}^p = 1.12 \text{ nW/K}$	$g_{ep} = 100 \text{ W/K}^6/\text{cm}^3$
Phonon (NTD-Abs.)	$G_{pa}^a = G_{pa}^p = 55.9 \text{ nW/K}$	$g_{glue} = 1.4 \times 10^{-4} \text{ W/K}^{3.5}/\text{mm}^2$
Phonon (Abs-Bath)	$G_{pb} = 0.42 \text{ nW/K}$	$g_k = 5 \times 10^{-5} \text{ W/K}^4/\text{mm}^2$
Equilibrium state $\phi(0)$		
NTD-electron	$\bar{T}_e = 15.9 \text{ mK}$	
NTD-phonon	$\bar{T}_p = 15.2 \text{ mK}$	
Absorber	$\bar{T}_a = 15.2 \text{ mK}$	
Voltage	$\bar{V} = 3.82 \text{ mV}$	$\bar{V} = V_b \bar{R} / (R_L + \bar{R})$
Electronic considerations		
Voltage bias	$V_b = 0.2 \text{ V}$	$I_p = V_b / (R_L + \bar{R}) \approx 0.2 \text{ nA}$
Load resistor	$R_L = 1 \text{ G}\Omega$	$T_{R_L} = 13 \text{ mK}$
NTD Resistance	$\bar{R} = 19.48 \text{ M}\Omega$	$\bar{R} = R(\bar{T}_e)$
IF1320-JFET ($C_{tot} = 50 \text{ pF}$)	$e_n^2 = e_a^2 + e_b^2/f$ $i_n^2 = i_a^2 + i_b^2 \times f$	$\{e_a, e_b\} = \{0.5, 7.3\} \text{ nV}/\sqrt{\text{Hz}}$ $\{i_a, i_b\} = \{18, 50\} \text{ aA}/\sqrt{\text{Hz}}$
200pF-HEMT ($C_{tot} = 250 \text{ pF}$)	$e_n^2 = e_a^2 + e_b^2/f$ $i_n^2 = i_a^2 + i_b^2 \times f$	$\{e_a, e_b\} = \{0.18, 5.2\} \text{ nV}/\sqrt{\text{Hz}}$ $\{i_a, i_b\} = \{8.2 \times 10^{-4}, 21\} \text{ aA}/\sqrt{\text{Hz}}$
Time constants of the system		driven by :
1st eigenvalue	$\tau_1 = 0.3 \mu\text{s}$	$\tau_{ap} = C_p / G_{ap} = 0.3 \mu\text{s}$
2nd eigenvalue	$\tau_2 = 118.7 \text{ ms}$	$\tau_{ab} = C_a / (G_{pb} \parallel G_{ap}) = 143.2 \text{ ms}$
3rd eigenvalue	$\tau_3 = 16.4 \text{ ms}$	$\tau_{ep} = C_e / G_{ep} = 28.2 \text{ ms}$
4th eigenvalue (FET)	$\tau_4 = 979 \mu\text{s}$	$\tau_{elec.} = \bar{R} C_c = 974 \mu\text{s}$
4th eigenvalue (HEMT)	$\tau_4 = 5.7 \text{ ms}$	$\tau_{elec.} = \bar{R} C_c = 5 \text{ ms}$
Energy resolutions (RMS)	$\epsilon = 0 \mid (\epsilon = 0.43, \tau_p = 6 \text{ ms})$	$\epsilon \neq 0$ to match observations (Sec. 5.3)
Sensitivity [$\mu\text{V}/\text{keV}$]	$s_V = 1.8 \mid s_V = 5$	Pulse height in time domain (with FET)
FET (DC)	$\sigma_E = 10.7 \text{ eV} \mid \sigma_E = 7.6 \text{ eV}$	
HEMT (DC)	$\sigma_E = 9.0 \text{ eV} \mid \sigma_E = 6.3 \text{ eV}$	
FET (AC)	$\sigma_E = 13.2 \text{ eV} \mid \sigma_E = 9.9 \text{ eV}$	400 Hz modulation
No elec. noise	$\sigma_E = 6.5 \text{ eV} \mid \sigma_E = 4.8 \text{ eV}$	Only TFN + Johnson noise
Theoretical limit	$\sigma_E = 1.7 \text{ eV}$	$\sigma_E = \sqrt{k_B \bar{T}_a^2 C_a}$

Table 4.1: Characteristics of the thermal model simulation shown in Fig. 4.2.

4.1 Electro-thermal model and heat resolution optimization

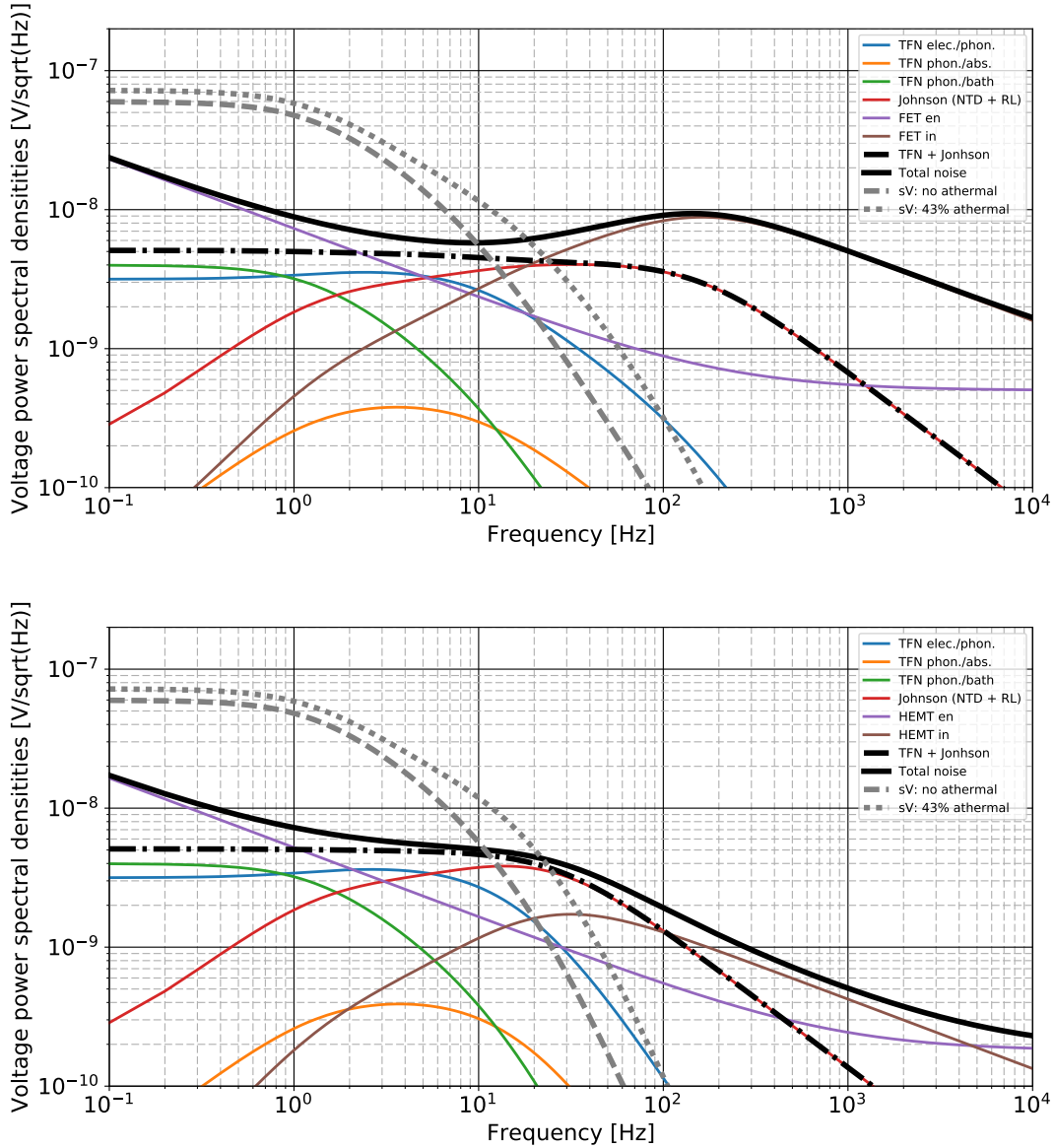


Figure 4.2: Spectral analysis of a 33.4 g Ge detector equipped with a single NTD and connected to the a 100 K JFET-based (top panel) and a 1 K HEMT-based (bottom panel) preamplifier with the input parameters listed in Table 4.1. The total noise power spectral density with (without) the electronic induced noise is shown as the black solid (black solid dotted) line. Also shown are the various noise contributions (colored solid lines) as well as the signal sensitivities $|s_V|$ considering (or not) some athermal contribution as the gray dotted (dashed) line.

their impact on the output voltage. Note that this electro-thermal feedback is also the reason why our detectors are stable when current biased. Unlike with usual low-impedance TES [165], the dominating source of noise in a well designed NTD-based detector is its intrinsic Johnson noise and not its electron-phonon TFN. As a matter of fact, in the case of NTD the TFN are roughly at the level of the Johnson noise, hence only marginally contributing to the total noise at the lowest frequencies.

4.2 Electrostatic simulation and electrode optimization

Eventually, thanks to Eq. 4.14 we can compute the expected energy resolutions considering various cases as detailed in Table 4.1. We hereafter summarize the most relevant results:

- Energy resolutions in the 10 eV (RMS) range, with or without athermal contribution, seems to be achievable with and without considering the electronics induced noises, and either performing a strict DC or a modulated AC measurement. The latter is being used in our current EDELWEISS electronics as it allows to remove the e_n component at the lowest frequencies by folding back and whitening the noise level at its modulation frequency. However, when the contribution of i_n becomes significant, *i.e.* when \bar{R} is larger than about 10 M Ω , the AC modulation achieves worst noise levels than the DC mode. Note that in using this AC electronics in similar conditions than the simulations described in Tab. 4.1, we have already achieved a 17.7 eV (RMS) resolution with RED20.
- In switching from our current AC modulated FET-based to our future DC HEMT-based electronics, we expect to improve our baseline energy resolution by about 40%. Despite of its larger input capacitance, thanks to its much lower high-frequency current noise (i_n) we even expect to improve our timing resolution with the HEMT preamplifiers (see Sec. 5.3.5).

4.2 Electrostatic simulation and electrode optimization

In this section, we present the modeling of the ionization response of our Ge detectors and how thanks to an optimized design of the electrode scheme we can achieve 20 eV (RMS) ionization resolution combined with excellent charge collection efficiency, surface background rejection and large fiducial volume. Eventually, at the end of this section we describe and present the expected performance of our two detector design candidates, PL38 and FID38, which will be studied soon in order to select the best one for the CryoCube array. This section follows the work from my PhD student D. Misiak [228].

4.2.1 Basics of the ionization signal

The behavior of the charge signal in our Ge crystals depends crucially on several aspects of the semiconductor properties. Ge has a band gap (0.74 eV), meaning that electrons must gain a fixed energy threshold before they can leave the localized valence band and move freely in the conduction band. At finite temperature, the probability that an energy state is occupied is given by the Fermi-Dirac distribution, and some charge carriers in the tail of the distribution will populate the conduction band. At 10 mK however, the charge carriers are essentially “frozen out”, meaning that there are no electrons in the conduction band and the crystal behaves as an insulator. When energy is deposited in the detector, electrons and holes can be excited into the conduction band (so-called ionization process). Charge carriers are randomly populated into conduction band states by ionizing radiation with a mean energy, that has been measured, of 2.96 eV/*leh*-pair, which is greater than the size of the band gap.

Once charges are produced, they propagate under the influence of the electric field towards the collecting electrodes. The Shockley-Ramo theorem [231, 232] states that the image charge Q_k

4.2 Electrostatic simulation and electrode optimization

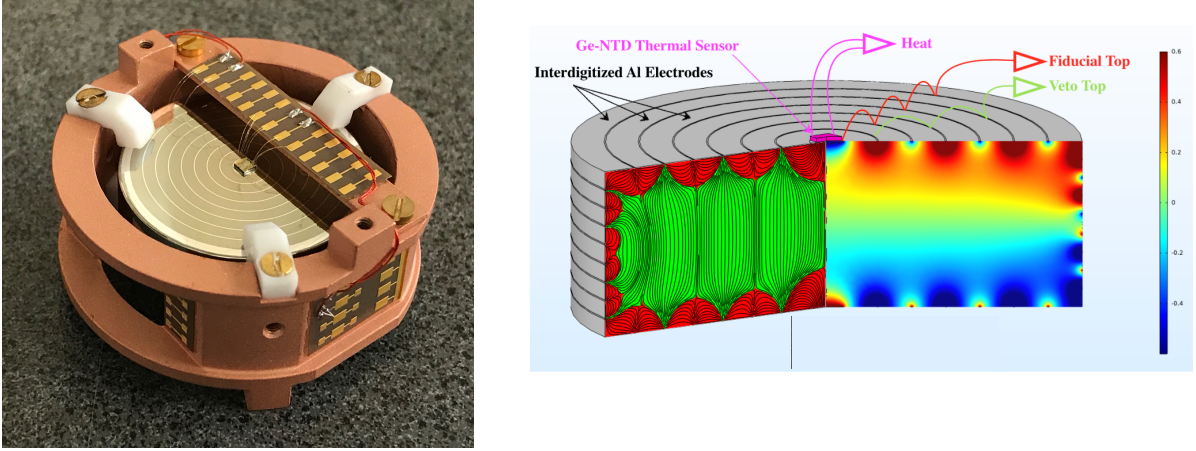


Figure 4.3: **Left:** Photo of a FID38 detector prototype where we can see the electrode rings, its NTD at the center, and the TEFLON clamps holding the crystal. **Right:** Corresponding schematic and COMSOL simulation of the FID38 detector design where we show the fiducial (green) and surface (red) volumes arising from the interleaved polarization of the veto and fiducial electrodes.

induced on an electrode k by N pairs created at an initial position $\vec{r}_{q,i}^n$ and moving to a final position $\vec{r}_{q,f}^n$ is given by,

$$Q_k = e \sum_{n=1}^N [\Phi_k(\vec{r}_{e,f}^n) - \Phi_k(\vec{r}_{h,f}^n)] \quad (4.15)$$

where Φ_k corresponds to the weighted potential, also called Ramo potential, of the k -electrode. The latter is computed without any charges in the detector volume, and by setting the k electrode to 1 V and all the other electrodes to the ground. Note that $\Phi_k(\vec{r}_{q,f}) = 1$ if $\vec{r}_{q,f} \in k$ -electrode, and $\Phi_k(\vec{r}_{q,f}) = 0$ otherwise. If however, the charges are trapped, such that $\vec{r}_{q,f}$ does not belong to any of the electrodes, then a fractional charge signals will be emitted on all electrodes [233]. Due to their high drift velocities of $\sim 2 \times 10^4$ cm/s for an electric field of 1 V/cm [234], as planned for the CryoCube Ge detectors, the image current on each electrodes will last for only about 20 μ s. As we are aiming for few tens of kHz sampling frequency with our new HEMT-based electronics, to first order, the induced charge signals can then be considered as instantaneous. The collection of charges \vec{Q} at the N electrodes is translated into voltage variations \vec{V} with respect to the ground following:

$$\vec{V} = C^{-1} \vec{Q} \quad (4.16)$$

where C is the Maxwell capacitance matrix which can be expressed in terms of mutual capacitance C_{ij}^m as:

$$C = \begin{pmatrix} C_{11} & C_{12} & \cdots & C_{1N} \\ C_{21} & C_{22} & \cdots & C_{2N} \\ \vdots & \vdots & \ddots & \vdots \\ C_{N1} & C_{N2} & \cdots & C_{NN} \end{pmatrix} = \begin{pmatrix} \sum_{j=1}^N C_{1j}^m & -C_{12}^m & \cdots & -C_{1N}^m \\ -C_{21}^m & \sum_{j=1}^N C_{2j}^m & \cdots & -C_{2N}^m \\ \vdots & \vdots & \ddots & \vdots \\ -C_{N1}^m & -C_{N2}^m & \cdots & \sum_{j=1}^N C_{Nj}^m \end{pmatrix} \quad (4.17)$$

4.2 Electrostatic simulation and electrode optimization

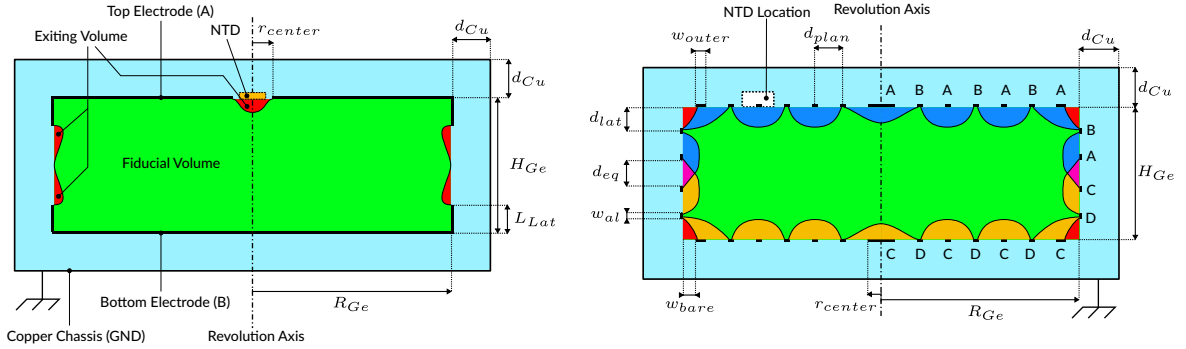


Figure 4.4: Detailed PL38 (**left**) and FID38 (**right**) detector design schematics exhibiting all of the various relevant design parameters and charge collection zones: fiducial (green), corner (red), equatorial (pink), top veto (blue), and bottom veto (yellow). The parameter values are all given in Tab. 4.2. Figure taken from [228].

The diagonal terms of the Maxwell capacitance matrix C_{ii} corresponds to the self-capacitance of the electrode i and can be understood as its capacitance to the ground if all other electrodes are grounded. The C_{ii}^m and C_{ij}^m corresponds to the capacitance of electrode i with respect to the ground and with the other electrodes $j \neq i$, respectively. Note that in formal electronic calculations, only the mutual capacitance terms are relevant, see Sec. 4.2.3.

4.2.2 Electrode design optimization for FID38 and PL38

In this paragraph, we briefly describe the general principle of the electrode design optimization methodology. For the sake of concreteness, we will exemplify the following discussion with the case of the FID38 detector design, and later present the results for both CryoCube detector design candidates: the FID38 and the PL38.

Figure 4.3 shows a photo of a 38 g Ge Fully Interdigitated Design (FID38) detector (left panel) and its corresponding COMSOL simulation (right panel) showing both the resulting field lines (left side) and 2-dimensional electric potential (right side). Within this design, ring-like aluminum electrodes are deposited on each surfaces of the Ge crystal (top, bottom, and side). The fabrication of these charge collection electrodes is done thanks to the evaporation of thin films of Aluminum that can be patterned to an optimized design using photo-lithography and shadow mask techniques [235]. The electrodes are then connected together into 4 groups: top veto (A), top fiducial (B), bottom veto (C), and bottom fiducial (D). A different potential is applied to each group of electrodes in order to create a complex electric field near the Ge surface allowing the fiducialization of the detector volume. This strategy, first experimentally demonstrated by the EDELWEISS collaboration [80], allows to reject events interacting at the detector's surface (red zone), *e.g.* beta electrons, alphas, and low-energy x-rays, with a high efficiency while keeping a significant fiducial volume (green zone).

As can be understood from Figure 4.3 such surface event rejection strategy comes with three possible drawbacks: 1) reduced fiducial volume, 2) low-electric field in the bulk possibly degrading the charge collection efficiency, and 3) large capacitances, due to the proximity of some

4.2 Electrostatic simulation and electrode optimization

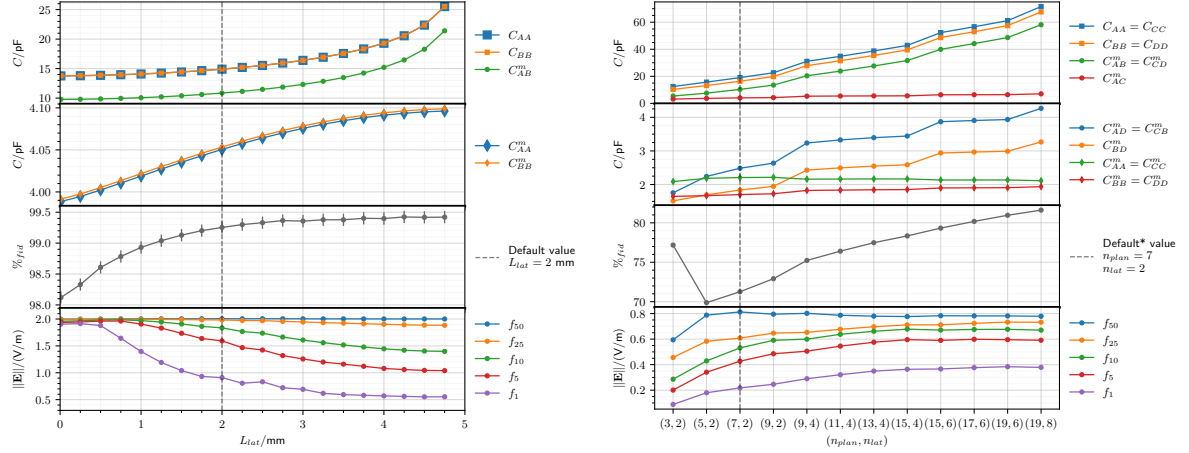


Figure 4.5: Scans over the corner length L_{lat} for the PL38 design (**left**), and over the number of lateral n_{lat} and planar electrodes n_{plan} for the FID38 design (**right**). Shown are: the Maxwell and mutual capacitance terms (two top panels), the percentage of fiducial volume (third panel), and some percentiles of the electric field magnitude distribution (fourth panel). The default values are represented by the vertical dashed lines at $L_{lat} = 2$ mm, $n_{lat} = 2$, and $n_{plan} = 7$. Figures taken from [228].

of the electrodes to each other, which will result in degraded energy resolutions. As an FID-like design is specifically well suited when dominated by surface backgrounds, as was the case for the EDELWEISS-III experiment searching for $10 \text{ GeV}/c^2$ dark matter candidates, an alternative “Planar” PL38 design solution is also proposed. The PL38 design should lead to much improved charge collection efficiency and fiducial volume, but at the cost of not being able to reject surface events. The choice between these two designs illustrated in Fig. 4.4 will ultimately be RICOCHET background dependent, and are therefore both investigated for the time being.

The electrode design optimization, performed by my student D. Misiak, was done thanks to the COMSOL software using the Multiphysics and AC/DC modules. The combination of both allows to perform the required electrostatic simulations and the computation of the Maxwell capacitance matrix. The PL38 and FID38 are characterized by 5 and 11 parameters respectively, hence resulting in computationally intensive high dimensional scans [228]. For the sake of illustration we hereafter only discuss the optimization of the PL38 corner length L_{lat} , and both of the FID38 number of lateral n_{lat} and planar n_{plan} electrodes illustrated in Figure 4.5 – left and right panels, respectively.

PL38 - L_{lat} : From the two top panels, describing the mutual and Maxwell capacitance terms, one can see that these capacitances all increase with the corner length. This is easily explained by the increased surface area of the two electrodes distant from each other by 1 cm and to the ground Cu casing by 3 mm. As a matter of fact, we see that the mutual C_{AB}^m term increases very rapidly when L_{lat} gets close to 5 mm, as the two electrodes are almost touching each other at the equator. From the third panel, we see that the fiducial volume increases slightly with L_{lat} , but it is however bounded between 98% and 99.3%. This suggests that the PL38 design benefits from a very large fiducial volume which is only weakly dependent on the corner length. Even-

4.2 Electrostatic simulation and electrode optimization

Parameter	Symbol	Value
Common PL38 & FID38		
Ge crystal Height	H_{Ge}	10 mm
Ge crystal Radius	R_{Ge}	15 mm
Distance between crystal and copper chassis	d_{Cu}	3 mm
Electrode Thickness	h_{Al}	50 nm
Main Voltage Bias	V_{bias}	2 V
Symmetric factor of the voltage bias	S_{bias}	0.5
PL38 specifics		
Radius of the central NTD hole	r_{center}	1.5 mm
Corner length	L_{lat}	2 mm
FID38 specifics		
Electrode Width	w_{Al}	80 μ m
Radius of the innermost planar electrode	r_{center}	0.25 mm
Width of bare Ge crystal on corners	w_{bare}	0.3 mm
Width of the outermost veto electrode	w_{outer}	0.08 mm
Number of planar electrodes	n_{plan}	7
Number of lateral electrodes	n_{lat}	2
Interdistance of Planar electrodes	d_{plan}	1.98 mm
Interdistance of Lateral electrodes	d_{lat}	2.40 mm
Equatorial distance	d_{eq}	2 mm
Ratio Veto/Main voltage bias	R_{veto}	-0.25

Table 4.2: Parameter values taken from [228] of the PL38 and FID38 detector design shown in Fig. 4.4

tually, the bottom and fourth panel shows the distribution of the electric field norm within the detector volume. As the corner length increases, we expect to create low-electric field zones in the corners, which may be responsible for poor charge collection (see Fig. 4.4 – left panel). For our selected value of $L_{lat} = 2$ mm, we see that about 1% of the detector volume has an electric field intensity lower than 1 V/cm (for a bias voltage of $V_{bias} = 2$ V), which is high enough to ensure an almost perfect and ideal charge collection of charges. Additionally, we expect a fiducial volume of about 99.3% and self electrode capacitance values below 20 pF, as required for a better than 20 eVee (RMS) resolution with HEMT, see Sec. 5.3.5.

FID38 - (n_{plan} & n_{lat}): As the number of electrodes (n_{plan} and n_{lat}) increases, we see that all the capacitance terms increase. As for the previous case, this is well explained by the increased total electrode surface area, but most importantly by how close the electrodes are to each other when adding more and more electrodes. As a matter of fact, only the first three (n_{plan} , n_{lat}) combinations offer the possibility to reach self capacitance values lower than 20 pF. On the other hand, as we increase the number of electrodes, we see that both the fiducial volume and the electric field norm distribution increase. The ultimate choice ($n_{plan} = 7$ & $n_{lat} = 2$) was then done by maximizing both the fiducial volume and the electric field conditions while maintaining $C_{ii} \leq 20$ pF. We then expect a fiducial volume of about 71% and only 10% of the detector volume to exhibit an electric field intensity lower than 0.5 V/cm, where we have evidence from RED80 studies that charge collection starts to become degraded (see Sec. 5.3.2).

Eventually, we give in Table 4.2 the optimized electrode design parameters for both the PL38 and FID38 configurations, and the resulting Maxwell capacitance matrices in pF below [228],

$$C_{\text{PL38}} = \begin{pmatrix} 14.92 & -10.86 \\ -10.86 & 14.92 \end{pmatrix} \quad C_{\text{FID38}} = \begin{pmatrix} 18.25 & -10.19 & -4.02 & -2.58 \\ -10.19 & 15.94 & -2.58 & -1.98 \\ -4.02 & -2.58 & 18.25 & -10.19 \\ -2.58 & -1.98 & -10.19 & 15.94 \end{pmatrix} \quad (4.18)$$

4.2.3 Results and discussion

In order to properly assess the overall ionization performance of our detector design, we need to compute the expected resolutions. To do so, we consider a simplified, though comprehensive enough to capture all leading effects, electronic circuit dedicated to reading out a PL38 detector, as shown in Figure 4.6. The capacitors in blue correspond to the mutual capacitance terms from Eq. 4.18, and the violet current sources $+i_q$ and $-i_q$ correspond to the collection of a bulk event generating charges of opposite signs at both electrodes: $\vec{Q}_{\text{bulk}} = \{+q, -q\}$. The various sources of noise are shown in red: the load resistor Johnson noise e_{R_L} , and the intrinsic HEMT/FET voltage e_n and current i_n ones.

Before heading towards the signal and noise analysis of this readout electronics, it is worth discussing the implications of dealing with capacitance matrices when more than one electrode is considered. Let's assume that all the components, except from the mutual capacitance terms, are removed from the circuit shown in Figure 4.6. In such a case, one can demonstrate that the

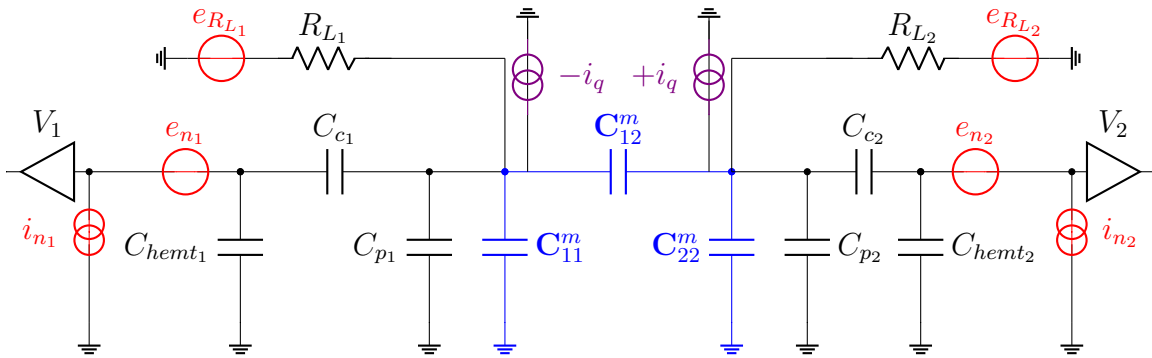


Figure 4.6: Circuit diagram of the HEMT/FET-based readout electronics reading out the two PL38 electrodes shown as $V1$ and $V2$. In blue are the mutual capacitance terms C_{ij}^m derived from the COMSOL simulations and given in Eq. 4.18. The noise sources are represented in red: the load resistor Johnson noise (e_{R_L}), and the intrinsic HEMT/FET voltage (e_n) and current (i_n) noises. In violet are the equivalent current sources following the collection of a bulk event, *i.e.* where the electrons and holes are collected at both electrodes. We chose: $R_{L1,2} = 10 \text{ G}\Omega$ and $T_{R_L} = 10 \text{ mK}$, $C_{c1,2} = 2 \text{ nF}$, and $C_{p1,2} = 5/125 \text{ pF}$ (HEMT/JFET).

4.2 Electrostatic simulation and electrode optimization

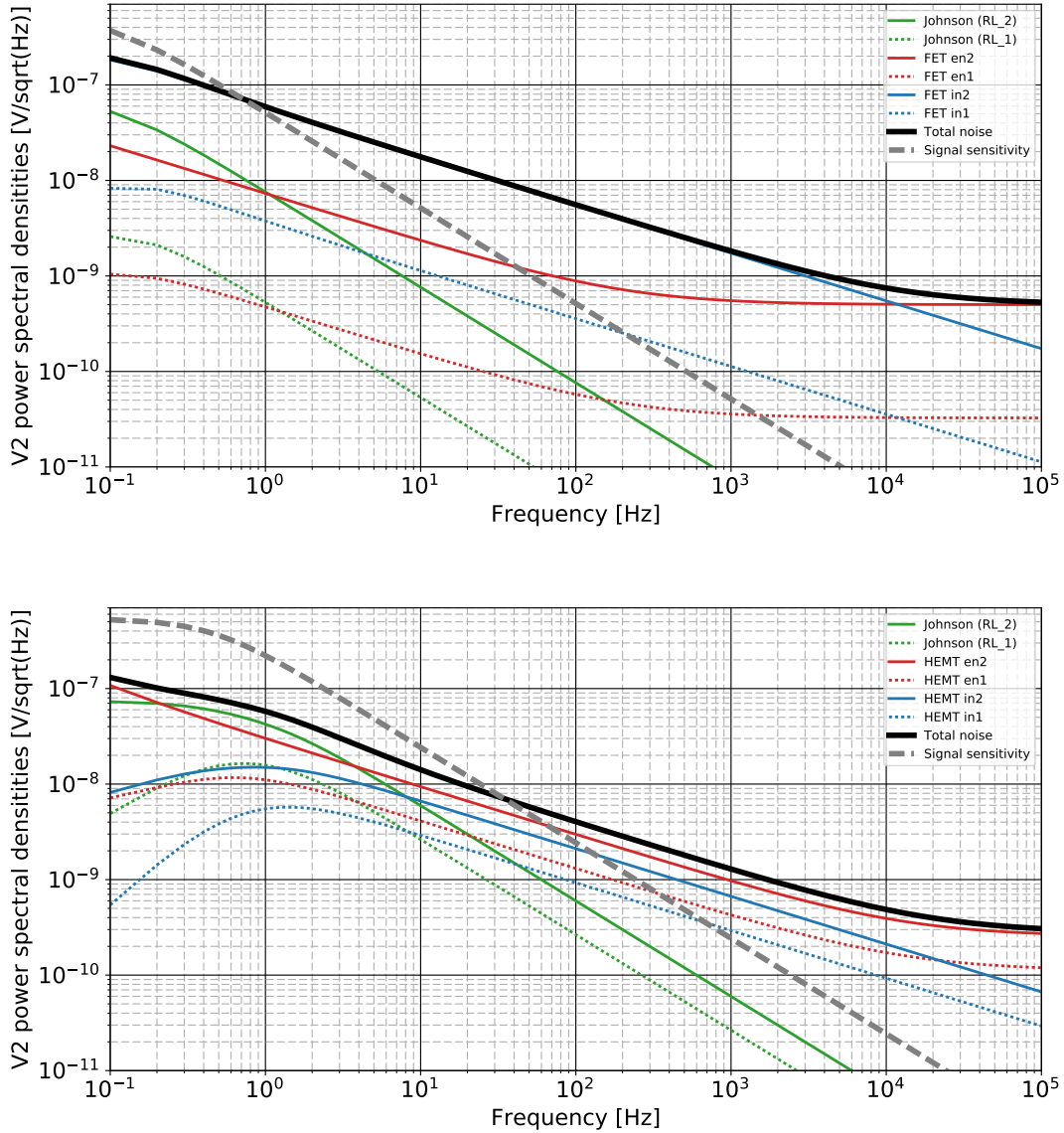


Figure 4.7: Spectral analysis of channel-2 from the PL38 detector design connected to our currently used JFET-based (top panel) and upcoming HEMT-based (bottom panel) electronics. In both cases, we considered the same electronic diagram as shown in Fig. 4.6. The total noise and signal sensitivity power spectral densities are shown as the black solid line and the grey dashed line respectively. Also shown are the various noise contributions from the V2 (V1) channel as the solid (dotted) colored lines.

output voltage V_2 is equal to:

$$V_2 = I_q Z_{eq}^{tot} = I_q [Z_{eq}^{+i_q} - Z_{eq}^{-i_q}] = I_q \frac{Z_{C_{11}^m} Z_{C_{12}^m}}{Z_{C_{11}^m} + Z_{C_{22}^m} + Z_{C_{12}^m}} \approx \frac{I_q}{26 \text{ pF}} \quad (4.19)$$

Interestingly, one can see that the equivalent capacitance of 26 pF is significantly larger than one could have expected from naively assuming the Maxwell self-capacitance $C_{22} = 14.92 \text{ pF}$

4.2 Electrostatic simulation and electrode optimization

General performance	PL38	FID38	Comments
ER/NR discrimination	YES	YES	heat & ion
Surface event rejection	NO	YES	betas, low-energy x-rays, alphas
Fiducial volume	99.2%	70%	
f_1	0.9 V/cm	0.2 V/cm	$V_{bias} = 2 \text{ V} \ \& \ H_{Ge} = 1 \text{ cm}$
f_5	1.6 V/cm	0.4 V/cm	$V_{bias} = 2 \text{ V} \ \& \ H_{Ge} = 1 \text{ cm}$
f_{10}	1.8 V/cm	0.5 V/cm	$V_{bias} = 2 \text{ V} \ \& \ H_{Ge} = 1 \text{ cm}$
FET-based resolutions			
IF1320-JFET			$\{e_a, e_b\} = \{0.5, 7.3\} \text{ nV}/\sqrt{\text{Hz}}$ $\{i_a, i_b\} = \{18, 50\} \text{ aA}/\sqrt{\text{Hz}}$ $C_{FET_i} = 15 \text{ pF}, C_{p_i} = 125 \text{ pF}$
Fiducial electrodes $\sigma_{B,D}$	178.6 eV	179.8 eV	[1 Hz, 50 kHz]
Fiducial electrodes $\sigma_{B,D}^{\text{ind}}$	165.9 eV	166.1 eV	[1 Hz, 50 kHz] other electrodes shorted
Fiducial electrodes $\sigma_{B,D}^{200 \text{ Hz}}$	253 eV	254.9 eV	[2 Hz, 200 Hz] identical to current data
Veto electrodes $\sigma_{A,C}$	-	180.0 eV	[1 Hz, 50 kHz]
Veto electrodes $\sigma_{A,C}^{\text{ind}}$	-	166.5 eV	[1 Hz, 50 kHz] other electrodes shorted
Veto electrodes $\sigma_{A,C}^{200 \text{ Hz}}$	-	255.2 eV	[1 Hz, 200 Hz] identical to current data
Fiducial resolution σ_{bulk}	126.2 eV	127.1 eV	$= \sigma_{B,D}/\sqrt{2}$ if uncorrelated noise
Veto resolution σ_{veto}	-	180.0 eV	$= \sigma_{A,C}$
HEMT-based resolutions			
HEMT-5pF			$\{e_a, e_b, e_c\} = \{0.256, 29.65, 5.34\} \text{ nV}/\sqrt{\text{Hz}}$ $\{i_a, i_b\} = \{4 \times 10^{-5}, 2.6\} \text{ aA}/\sqrt{\text{Hz}}$ $C_{HEMT_i} = 4.6 \text{ pF}, C_{p_i} = 5 \text{ pF}$
Fiducial electrodes $\sigma_{B,D}$	28.3 eV	28.5 eV	[1 Hz, 50 kHz]
Fiducial electrodes $\sigma_{B,D}^{\text{ind}}$	16.9 eV	17.4 eV	[1 Hz, 50 kHz] other electrodes shorted
Veto electrodes $\sigma_{A,C}$	-	32.5 eV	[1 Hz, 50 kHz]
Veto electrodes $\sigma_{A,C}^{\text{ind}}$	-	18.5 eV	[1 Hz, 50 kHz] other electrodes shorted
Fiducial resolution σ_{bulk}	20.0 eV	20.1 eV	$= \sigma_{B,D}/\sqrt{2}$ if uncorrelated noise
Veto resolution σ_{veto}	-	32.5 eV	$= \sigma_{A,C}$

Table 4.3: Expected performance of the PL38 and FID38 detector design shown in Fig. 4.4 of the electrode⁴. This is explained by the fact that the total voltage at each electrode is affected by the collection from both opposite charges at each electrodes. This is particularly true as long as mutual capacitance between the electrodes C_{12}^m is of the same order of magnitude than the capacitance of each electrodes to the ground C_{ii}^m . Note that this effect was however never observed using our current EDELWEISS-III electronics. But this is easily explained from the fact that the cabling capacitance C_{cp} is very large, *i.e.* about 100 pF, such that $C_{12}^m \ll C_{cp} + C_{ii}^m$. Alternatively, if one sets the electrode 1 to the ground by shorting it with a wire, then a similar calculation would lead to $V_2 = I_q/(C_{12}^m + C_{22}^m) = I_q/C_{22}$ where C_{22} is now the self capacitance of the second electrode, as expected by definition.

We now focus on the frequency domain analysis in order to extract the expected energy res-

⁴Note that a similar result is obtained by using instead the Maxwell capacitance matrix formalism given in Eq. 4.16, where we can easily identify: $Z_{eq}^{+i_q} = C_{11}/(C_{11}C_{22} - C_{12}^2)$ and $Z_{eq}^{-i_q} = -C_{12}/(C_{11}C_{22} - C_{12}^2)$.

4.3 Expected CryoCube CENNS sensitivity

olutions. By performing various successive Thevenin-Norton transformations of the diagram shown in Fig. 4.6, we were able to reference both the signal (shown in violet) and the different noise sources (shown in red) to the output voltage V_2 , reading out electrode-2. The resulting frequency domain analysis, shown as power spectral densities referenced to the output voltage V_2 , are shown in Figure 4.7. The “bulk” signal sensitivity is shown as the grey dashed line, while the various noise sources from the readout channel 1 (2) are shown in colored dotted (solid) lines, and the total noise PSD is shown as the black solid line. The top and bottom panels show the expected readout performance with a IF1320-JFET, as currently used in the EDELWEISS-III electronics, and a 5pF-HEMT as planned for the CryoCube ionization readout electronics, see Sec. 5.3.5. The resulting ionization resolutions, as well as a summary of the PL38 and FID38 design performance, are given in Table 4.3. As one can see, the FET-based performance are heavily limited by the large total capacitance of the system (signal sensitivity lower than with the HEMT), and by the intrinsic IF1320-FET current noise. One may naively think that bringing the FET-based electronics few centimeters away from the detector, to reduce the cabling capacitance significantly, might be enough to dramatically improve the FET-based resolutions. This is in fact not true for the two following reasons:

1. JFET do not operate properly below 100 K and cryogenics-wise it is rather impossible to have a thermally anchored 100 K electronics connected to bolometers heat sunk at 10 mK few centimeters away.
2. Even if one successfully achieve a few-pF cabling capacitance between the JFET and the bolometers, lowering C_p would only make the current noise i_n even stronger as less filtered. As a matter of fact, assuming a FET-based readout with $C_p = 5$ pF, we found an estimated energy resolution of 214.6 eV.

It is therefore obvious that JFET-based preamplifiers will never allow us to reach our targeted ~ 20 eV ionization resolution. Low-impedance (5 pF) HEMT on the other hand offer 1) a dramatically reduced intrinsic current noise and 2) a low-capacitance cabling possibility as they can work down to 1 K where they only dissipate tens of μW , which is compatible with our fridge cooling power (see Sec. 5.3.5). HEMT are therefore an excellent candidate for our CryoCube readout, and as illustrated in Table 4.3, with both the PL38 and FID38, we expect to reach a fiducial ionization resolution for “bulk events” down to 20 eV, hence achieving our goal.

Eventually, one can notice that the expected energy resolution is worse when all electrodes are floating, *i.e.* being readout, than when all but one are shorted to the ground. This comes back to the previous discussion about the larger equivalent capacitance due to the collection of charges of opposite signs at each electrodes. Also, and as shown in Fig. 4.7 in comparing the dotted and solid lines from the various noise sources, reading out more than one electrode allow for noise sources to impact all channels. In the case of the PL38, noise sources from channel-1 contribute to about 8% to the expected resolution of channel-2.

4.3 Expected CryoCube CENNS sensitivity

In the previous sections, we presented both the modeling of the ionization and heat channels and their respective expected energy resolutions. Based on these previous results, we will now

4.3 Expected CryoCube CENNS sensitivity

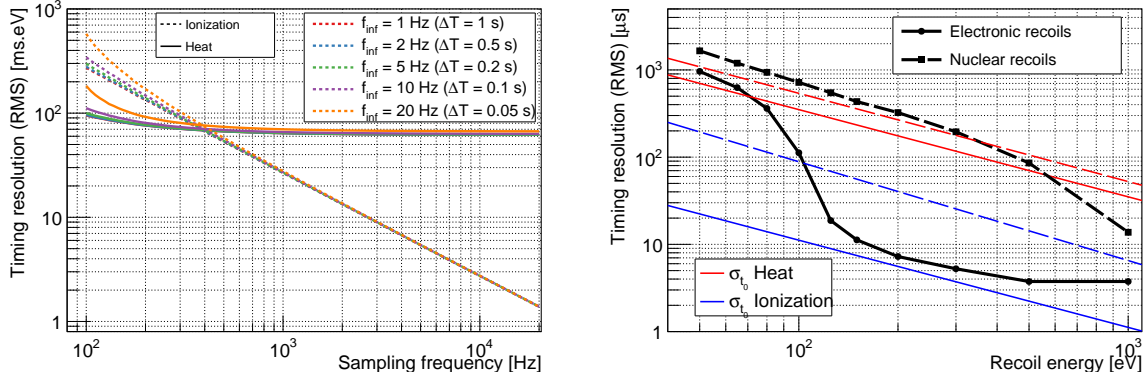


Figure 4.8: **Left:** Timing resolution as a function of the sampling frequency for the heat and ionization channels shown as the solid and dotted lines respectively, and for varying time windows ranging from 1 s (red) to 50 ms (orange). **Right:** Combined (heat + ionization) timing resolutions for electronic (solid line) and nuclear (dashed line) recoils as a function of the recoil energy. The dashed and solid red and blue lines refer to the theoretical predictions of the timing resolution for the heat and ionization channels respectively for both electronic and nuclear recoils. These results were obtained using the NEPAL pulse simulation and processing pipeline considering the Lindhard quenching factor with a 2 V voltage bias, and a 20 kHz sampling frequency.

discuss the overall performance of the CryoCube detector array in the context of the future RICOCHET experiment at ILL, see Chap. 3.

4.3.1 Timing resolution and muon-veto coincidence

One important aspect of our detector performance is the timing resolution. Indeed, as RICOCHET will be located above ground, with only a moderate muon flux attenuation, the muon induced neutrons and gammas are expected to contribute significantly to the total background (see Sec. 3.4). In order to reduce this background, the use of a muon-veto in order to tag any recoils in coincidence with a passing by muon is mandatory. With an anticipated muon trigger rate in the veto of about 150 Hz or 350 Hz depending on its final design, one can easily assess that timing resolutions of the order of hundreds of μs may be required to provide an efficient muon-induced background reduction combined with a minimal loss in detector lifetime.

The theoretical timing resolution σ_{t_0} is computed as follows:

$$\sigma_{t_0}^2 = \left(\hat{E}^2 \int_0^\infty \frac{d\omega}{2\pi} \frac{4\omega^2 |\hat{s}_V|^2}{S_{V,tot}} \right)^{-1} \quad [J^2 \cdot s^2] \quad (4.20)$$

where \hat{E} is the amplitude/energy estimator of the pulse, hence suggesting that the timing resolution scales inversely with the event energy. As one can see, the expression of the timing resolution is very similar to the one from the energy resolution (see Eq. 4.14), where more weight is given to the high frequency response of the detector.

Figure 4.8 (left panel) shows the evolution of the heat and ionization timing resolutions as a function of the sampling frequency and for varying length of time windows, ranging from 1 s

4.3 Expected CryoCube CENNS sensitivity

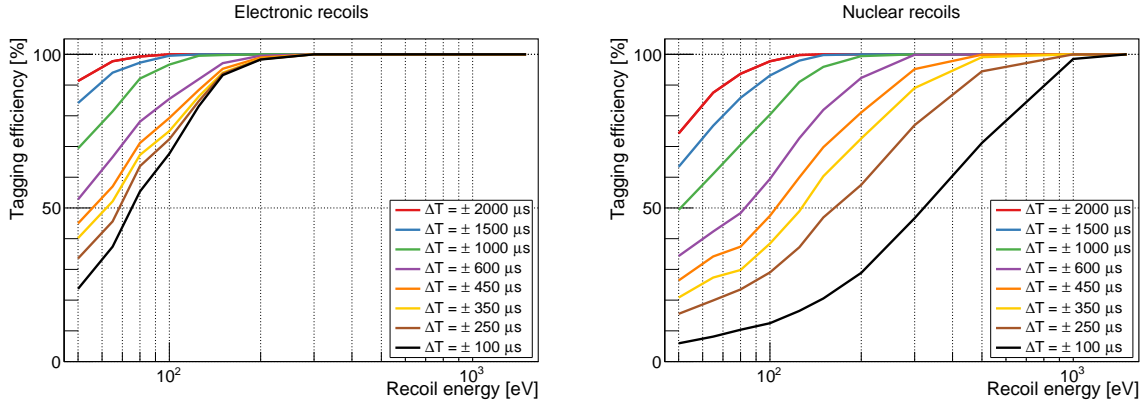


Figure 4.9: Tagging efficiency as a function of recoil energy for electronic (**left**) and nuclear (**right**) recoils, with varying lengths of time windows ranging from 2 ms (red) to 100 μs (black).

down to 50 ms. These results were obtained using the noise predictions from the thermal and ionization models, combined with the HEMT-based electronics, discussed in Sec. 5.3.5. Due to the remaining uncertainties on the exact thermal model predictions of the signal sensitivity, we hereafter opted for a fully data driven approach by considering the measured one from the RED80 detector (see Sec. 5.3). Indeed, as discussed earlier, our observed signal bandwidth is about 4 times larger than our thermal model predictions when no athermal component is considered. From figure 4.8 (left panel) we see that while for the heat-based timing resolution there is no need to consider sampling frequencies beyond 1 kHz, the ionization-based timing resolution on the other hand linearly improves with increasing the sampling frequency. This explains why the CryoCube readout electronics is being designed to work at 100 kHz even though working at 20 kHz has been demonstrated to be enough for our purpose.

Figure 4.8 (right panel) shows the combined (heat + ionization) timing resolution for both electronic (solid line) and nuclear (dashed line) recoils as a function of the recoil energy. These results were obtained using the NEPAL pulse simulation and processing pipeline, where we injected events, characterized by 1 heat pulse and 2 ionization pulses, in simulated streams with the corresponding noise PSD as given by the previously described electro-thermal and ionization models. Once generated, these streams were then processed by the full NEPAL processing pipeline, as for real data, and time shift (between the reconstructed and the input t_0) distributions were drawn to further extract the expected timing resolutions. These simulations consider a PL38-like detector, a 2 V bias voltage and the Lindhard ionization quenching factor. The combined timing resolution for both the electronic and nuclear recoils are compared to the individual theoretical heat- and ionization-based timing resolutions. This way one can see that the electronic recoils, thanks to their large ionization yield, benefit strongly from the fast ionization response starting at about 100 eV⁵. However, this boost of the combined timing resolution due to the fast ionization response only starts at around 500 eV for nuclear recoils due to their lower ionization yield. This suggests that the fast ionization readout will considerably improve the tagging efficiency of muon-induced gammas, but only moderately of muon-induced neutrons

⁵Note that the saturation of the combined timing resolution at about 4 μs is due to the limited numerical precision of the NEPAL processing, which can be further refined if needed, but at the cost computational time.

4.3 Expected CryoCube CENNS sensitivity

below 500 eV.

This is indeed what is observed in Fig. 4.9 where we show the muon tagging efficiency as a function of the recoil energy for both electronic (left panel) and nuclear (right panel) recoils, and for varying length of coincidence time-windows (ΔT_{coinc}). These results were obtained from the previously discussed NEPAL-based – pulse simulation and processing – time shift distributions at varying energies and for the two types of recoils. Note that this complex but rigorous Monte Carlo pulse simulation approach is mandatory as the combination of both the ionization and heat channels is highly non-trivial, as it depends on the frequency domain behavior of the combined χ^2 minimization, which is highly non-gaussian at the lowest energies. From Fig. 4.9 we see that for a given coincidence time-window size, the tagging efficiency for electronic recoils is indeed vastly superior than for nuclear recoils. Also, we see that by increasing the size of the coincidence window, we increase the tagging efficiency, but this comes with the cost of a reduced livetime which can be computed as follows:

$$\epsilon_{\text{Veto}}(\Delta T_{\text{coinc}}, R_{\mu}) = \exp(-2\Delta T_{\text{coinc}} \times R_{\mu}) \quad (4.21)$$

where R_{μ} is the muon-veto trigger rate. Eventually, one can compute the expected event rates for cosmogenic, reactogenic and radiogenic backgrounds, as well as for the CENNS signal, for any coincidence time window ΔT_{coinc} following:

$$\left. \frac{dR}{dE_r} \right|_{\Delta T_{\text{coinc}}}^{\text{cosmo}} = \left[\left. \frac{dR}{dE_r} \right|_{\text{Veto}}^{\text{cosmo}} + \left(\left. \frac{dR}{dE_r} \right|_{\text{NoVeto}}^{\text{cosmo}} - \left. \frac{dR}{dE_r} \right|_{\text{Veto}}^{\text{cosmo}} \right) \times (1 - \epsilon_{\text{tag}}(E_r | \Delta T_{\text{coinc}})) \right] \times \epsilon_{\text{Veto}} \quad (4.22)$$

$$\left. \frac{dR}{dE_r} \right|_{\Delta T_{\text{coinc}}}^{\text{reacto., radio., heat only, CENNS}} = \left. \frac{dR}{dE_r} \right|_{\text{reacto., radio., heat only, CENNS}} \times \epsilon_{\text{Veto}} \quad (4.23)$$

where the “cosmo” event rate with the subscript “Veto” and “NoVeto” refer to the case where an ideal muon veto, *i.e.* with no livetime loss and 100% efficiency, is considered or not respectively. Figure 4.10 shows the expected differential event rates for the CENNS signal (green) and of the various backgrounds: gammas (red), neutrons (blue), and heat only (violet). The blue and red shaded areas also show the span of the cosmogenic induced ER and NR backgrounds covered by the “Veto” and “NoVeto” event rates, considering the two veto configurations III and IV discussed in Sec. 3.4. Table 4.4 gives all the background and detector modeling parameters used hereafter. Note that with respect to the background assumptions discussed in Sec. 3.4 we added a radiogenic ER component of 50 evt/kg/day/keV and a Heat Only component corresponding to what has been observed with RED20 and RED30 (see Sec. 5.3.4). As one can see from figure 4.10, considering a time coincidence window of $\Delta T_{\text{coinc}} = 350 \mu\text{s}$ allows to fully benefit from the muon veto background suppression, for energies above ~ 300 eV, for both configurations while keeping a reasonable 80-90% signal efficiency. Note that this value of $\Delta T_{\text{coinc}} = 350 \mu\text{s}$ is not necessarily an optimal choice and its optimization will be discussed in the next section. Lastly, one can see that following this muon-veto background suppression, the CENNS signal is still overwhelmed by the remaining reactogenic and radiogenic backgrounds, as well as by the hypothetical and strong heat only background. An additional way to further mitigate these backgrounds is therefore mandatory to provide a highly significant CENNS detection with the CryoCube detector at ILL.

4.3 Expected CryoCube CENNS sensitivity

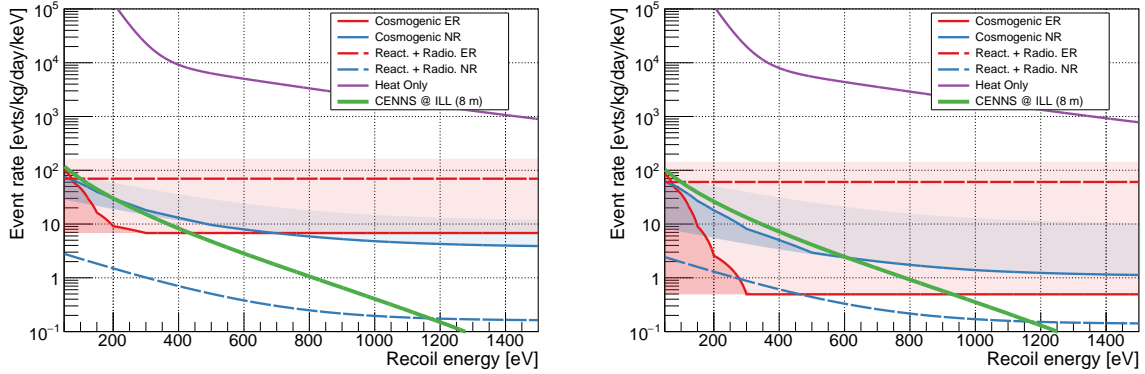


Figure 4.10: Differential event rates of the CENNS signal (green) and of the various background components: cosmogenic ER (solid red) and NR (blue solid), reactogenic plus radiogenic ER (dashed red) and NR (dashed blue), and Heat Only (violet). The blue and red shaded areas illustrate the span of the cosmogenic NR and ER backgrounds related to the muon veto application or not, considering the muon veto configuration III (**left**) and IV (**right**) from Sec. 3.5. For both panels, we considered $\Delta T_{\text{coinc}} = 350 \mu\text{s}$ leading to $\epsilon_{\text{Veto}} = 0.9$ and 0.78 for configurations III and IV respectively.

4.3.2 Heat Vs Ionization based particle identification

In this section, we investigate the use and interest of the particle identification capability from the CryoCube detector technology. To do so, we will consider a PL38 like detector design, which has been extensively discussed in the previous sections, with its expected performance and background model parameters summarized in Tab. 4.4.

Figure 4.11 shows the resulting simulation of 350 days of reactor ON data at ILL, corresponding to about 7 cycles distributed over about 2 years. The top panel shows the distribution of all observed events in the ionization (E_{ion}) versus heat (E_{heat}) plane where the CENNS signal, the total gamma and neutron backgrounds are shown in green, red and blue respectively. One can see that some of the events are reconstructed with reduced ionization energies, this is due to incomplete charge collection arising from low-voltage zones of the detector where charge trapping can arise. We considered a 1% probability of incomplete charge collection based on the results from the PL38 detector simulations. We also show the $\pm 2\sigma$ nuclear recoil (NR) band (orange dashed lines) and an optimized ionization threshold (not visible here) that we use in the following to select nuclear recoil candidates. The heat energy distribution of such nuclear recoil candidates are shown in the bottom panel of Figure 4.11 as the solid line histograms. As one can see, thanks to this NR selection cut, the CENNS signal is now well above the electromagnetic background over the entire energy range from 50 eV to 1.5 keV. As a matter of fact, the remaining dominating background is the neutrons, from both cosmogenic and reactogenic origins. The CENNS detection significance Z can easily be computed, ignoring the background and signal related systematics, using the standard significance expression:

$$Z = \frac{S}{\sqrt{S+B}} \quad (4.24)$$

where S and B are the total number of CENNS and background events passing the NR selection

4.3 Expected CryoCube CENNS sensitivity

Background model	dR/dEr	rate in [50 eV, 1 keV] [evt/kg/day]	Comments (a and c in DRU, e in eV)
Radio. gam.	c	47.5	c = 50
Radio. neut.		$<10^{-3}$	Negligible
Reacto. gam.	c	26	c = 27.4
Reacto. neut.	$c + ae^{-Er/e}$	0.8	{c, a, e} = {0.177, 3.66, 221.7}
Cosmo. gam. (no veto)	c_g	175	$c_g = 184$
Cosmo. gam. (veto III)	c'_g	7.2	$c'_g = c_g/24.21$
Cosmo. gam. (veto IV)	c''_g	0.6	$c''_g = c_g/292$
Cosmo. neut. (no veto)	$c_n + a_n e^{-Er/e_n}$	37	{c _n , a _n , e _n } = {12.6, 101, 305.8}
Cosmo. neut. (veto III)	$c'_n + a'_n e^{-Er/e_n}$	12	{c' _n , a' _n } = {c _n , a _n }/3.09
Cosmo. neut. (veto IV)	$c''_n + a''_n e^{-Er/e_n}$	4	{c'' _n , a'' _n } = {c _n , a _n }/9.26
Heat Only	$\sum_{1,2,3} a_i e^{-Er/e_i}$	1.64×10^5	{a _i } = {10 ⁷ , 1.92 × 10 ⁴ , 382.7} {e _i } = {46.25, 462, 3413}
CENNS	Eq. 1.10	15.5	8 m from 57.8 MW ILL reactor
Detector model			
Heat resolution	10 eV	CryoCube mass	1 kg
Ionization resolution	20 eV	Trigger efficiency	100% starting at 50 eV
Incomplete Q collec.	1%	Muon trig. config III	150 Hz
Voltage bias	2 V	Muon trig. config IV	350 Hz

Table 4.4: Parameter values of both the background and the detector models. Note that the background models, including the muon veto configurations, are the ones discussed in Sec. 3.4, except for the Heat Only (HO) and the radiogenics which have been added for this study.

4.3 Expected CryoCube CENNS sensitivity

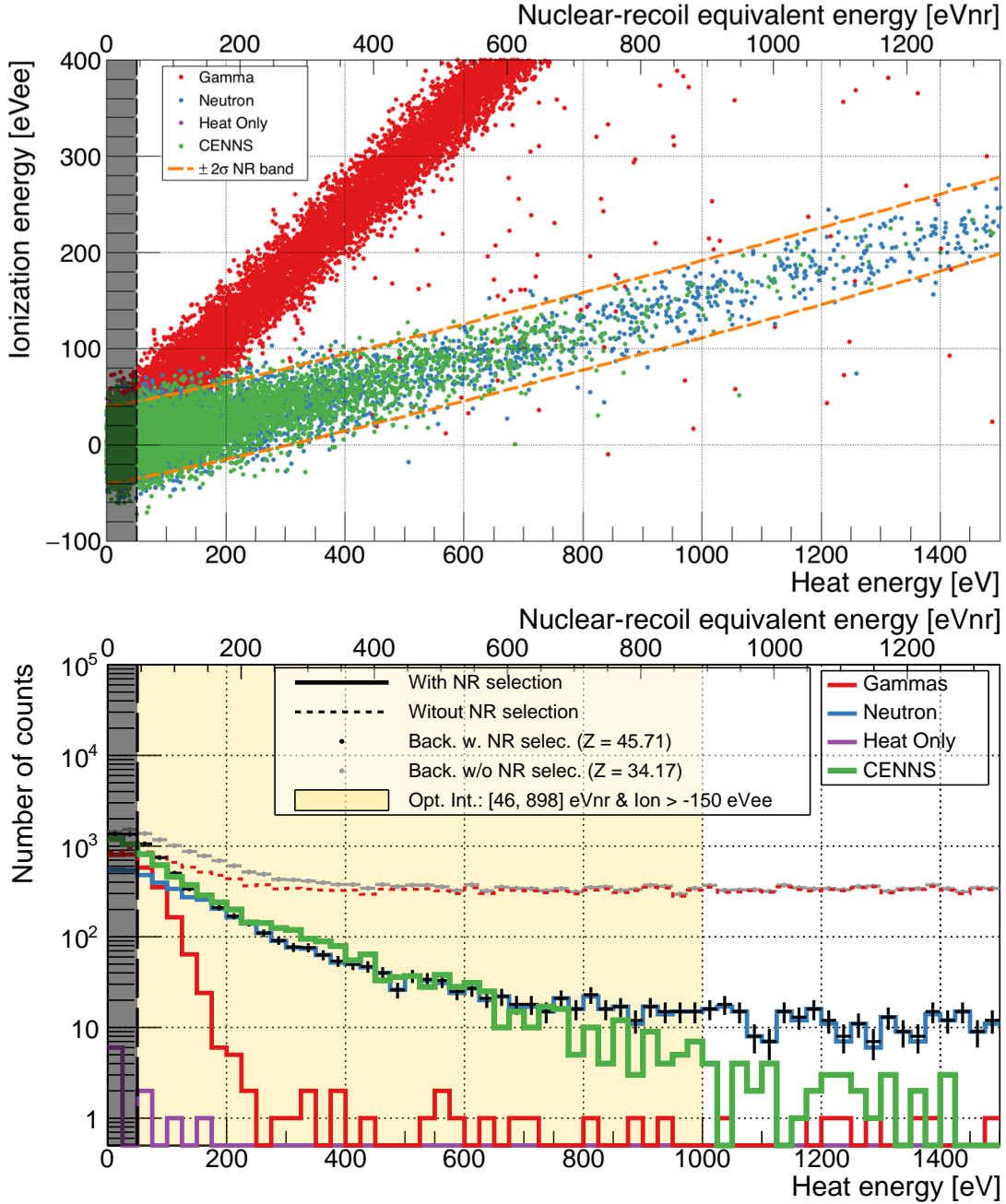


Figure 4.11: **Top:** Simulated event distribution on the ionization vs heat plane where the CENNS signal, the gamma, the neutron and the hypothetical heat only backgrounds are shown as green, red, blue and violet dots respectively. The nuclear recoil candidates are selected from the $\pm 2\sigma$ nuclear recoil (NR) band (orange dashed lines) and an optimized ionization threshold (horizontal black dashed line). **Bottom:** Corresponding heat energy distributions with (with-out) the NR selection as solid (dashed) lines or dots. The yellow area illustrates the optimal energy interval. In both panels, the black filled region illustrates the 50 eV heat energy threshold. We considered here the standard simulation parameters described in Table 4.4 with a HO rate reduced by 10^7 and the muon veto from configuration IV with $\Delta T_{\text{coinc}} = 350 \mu\text{s}$.

cut and in an optimal energy range⁶ (shown as the yellow area in bottom panel of Fig. 4.11).

⁶The optimized energy range has been derived from maximizing Z while scanning over a $\pm 6\sigma_{E_{\text{ion}}}$ fiducial

4.3 Expected CryoCube CENNS sensitivity

As a matter of fact, we find that within these conditions, the expected significance is $Z = 45.71/\sqrt{350/50} \sigma = 17.3 \sigma$ after only 50 days, *i.e.* one reactor cycle. This result is very similar to what has been found in Sec. 3.5 with a likelihood approach and an idealized flat 10^{-3} ER/NR discrimination over the entire energy range. This result suggests that, if the considered background assumptions can be met, the CryoCube detector design and technology is well suited for a low-energy and high precision CENNS detection with RICOCHET at ILL.

4.3.3 The hypothetical Heat Only background

In recent years, as cryogenic detector experiments successfully lowered their energy threshold in the sub-keV region, a strong and yet-to-be-explained low-energy background component has been observed. This result is roughly independent of the target material used, the heat sensor technology considered, and from operating the detectors above or underground. This is a major issue, discussed in more details in Sec. 5.3.4, which may very well limit the sensitivity of upcoming low-energy threshold cryogenic experiments to CENNS and dark matter searches in the next years if not solved⁷. In RED20 (operated at IP2I) and RED30 (operated at LSM) we observed a multi-component exponential rise with slopes of 46 eV, 460 eV, and 3.4 keV and as high as 10^6 DRU at 100 eV, which we attribute to this so-called Heat Only events, meaning they do not ionize the crystal⁸ (see Sec. 5.3.4). This latter observation was indeed confirmed with the RED30 detector operated underground from which we observed that the shape of this strong background rise at low-energy was independent of the voltage bias [144]. Note that we saw about one order of magnitude variations of this background, among our detectors and over time, but consider here the highest observed rate to derive conservative sensitivity estimates.

Figure 4.12 now shows the impact of this hypothetical Heat Only (HO) background on our expected CENNS sensitivity. As one can see, thanks to their non-ionizing properties, they can still be discriminated from the CENNS induced nuclear recoils. However, due to the proximity of the ionization yields from the CENNS-induced nuclear recoil ($Q \sim 0.1$) and the one from the HO ($Q = 0$), the discrimination is not as efficient as against the gamma-induced electronic recoils ($Q = 1$). As a matter of fact, one can intuitively appreciate that applying a fiducial ionization threshold on top of the NR band selection as we do will indeed be beneficial in improving our NR candidate selection's signal-to-noise ratio. Bottom panel of fig. 4.12 shows the event energy distributions passing our NR candidate selection (NR band + fiducial ionization threshold) and the resulting optimal heat energy interval leading to an estimated CENNS significance after one reactor cycle of $Z = 4.4 \sigma$. Based on this very simplistic cut-based analysis approach, this result suggests that HO as observed today in our detectors would: 1) reduce the overall detection significance by about a factor of 4, and 2) increase our CENNS analysis effective threshold from 50 eVnr up to ~ 270 eVnr, hence by a factor about 5. As a matter of fact, Fig. 4.13 shows the evolution of the resulting heat energy distributions as a function of the heat only background magnitude. One can see that the lower bound of the optimal interval gets shifted towards lower energies as the HO background is reduced (from the top left panel

ionization threshold and all possible combinations of lower and upper heat energy bounds.

⁷Note that more and more people are investigating the possibility of a dark matter origin of this unexplained signal [236]

⁸Note that despite of their higher energy thresholds, FID800 detectors from EDELWEISS operated at LSM had already observed the 3.4 keV component of this HO background [98]

4.3 Expected CryoCube CENNS sensitivity

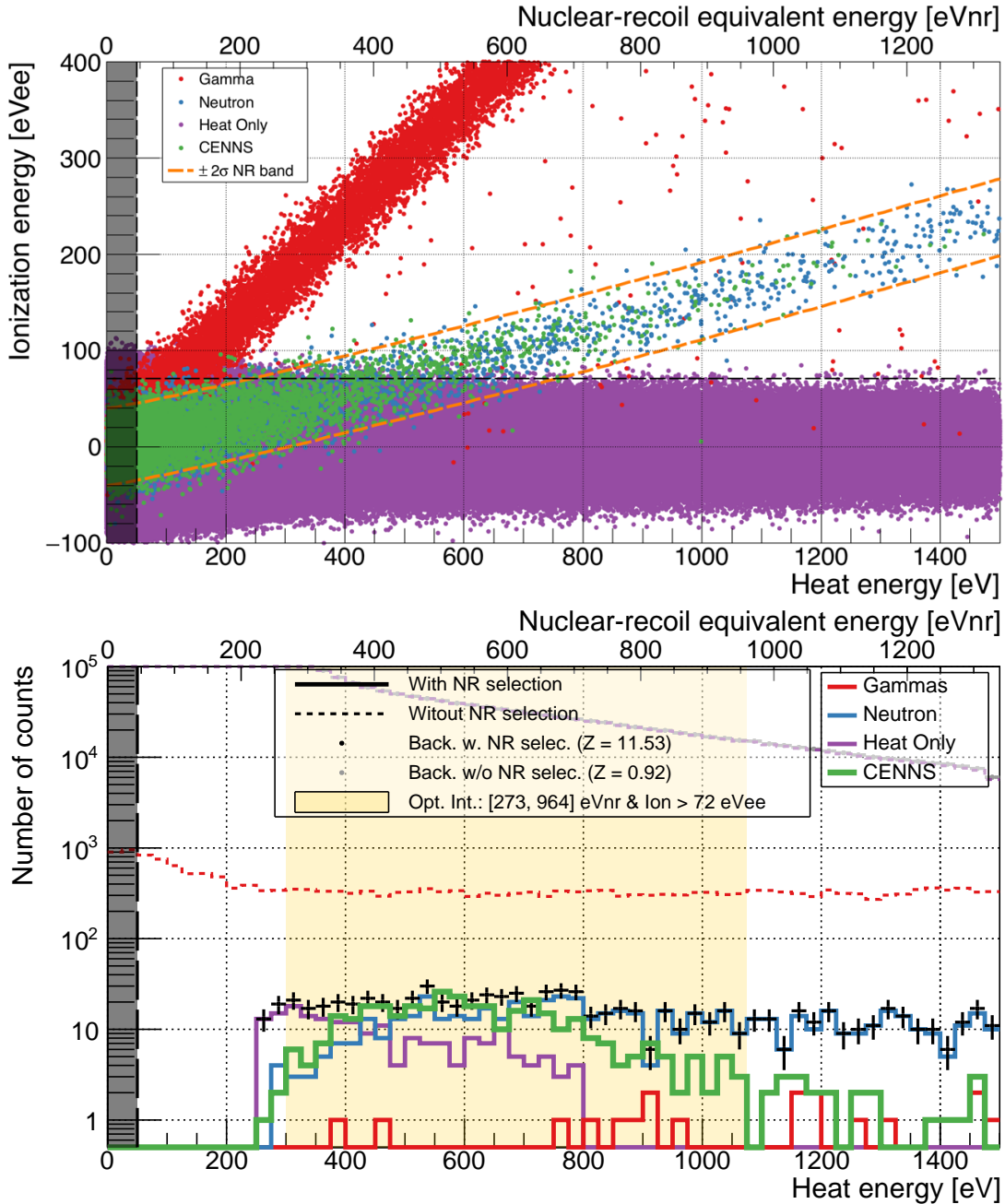


Figure 4.12: **Top:** Simulated event distribution on the ionization vs heat plane where the CENNS signal, the gamma, the neutron and the hypothetical heat only backgrounds are shown as green, red, blue and violet dots respectively. The nuclear recoil candidates are selected from the $\pm 2\sigma$ nuclear recoil (NR) band (orange dashed lines) and an optimized ionization threshold (horizontal black dashed line). **Bottom:** Corresponding heat energy distributions with (with-out) the NR selection as solid (dashed) lines or dots. The yellow area illustrates the optimal energy interval. In both panels, the black filled region illustrates the 50 eV heat energy threshold. We considered here the standard simulation parameters described in Table 4.4 with HO rate as observed in RED30, and the muon veto from configuration IV with $\Delta T_{\text{coinc}} = 350 \mu\text{s}$.

to the bottom right one). Actually, we found that every one order of magnitude reduction of

4.3 Expected CryoCube CENNS sensitivity

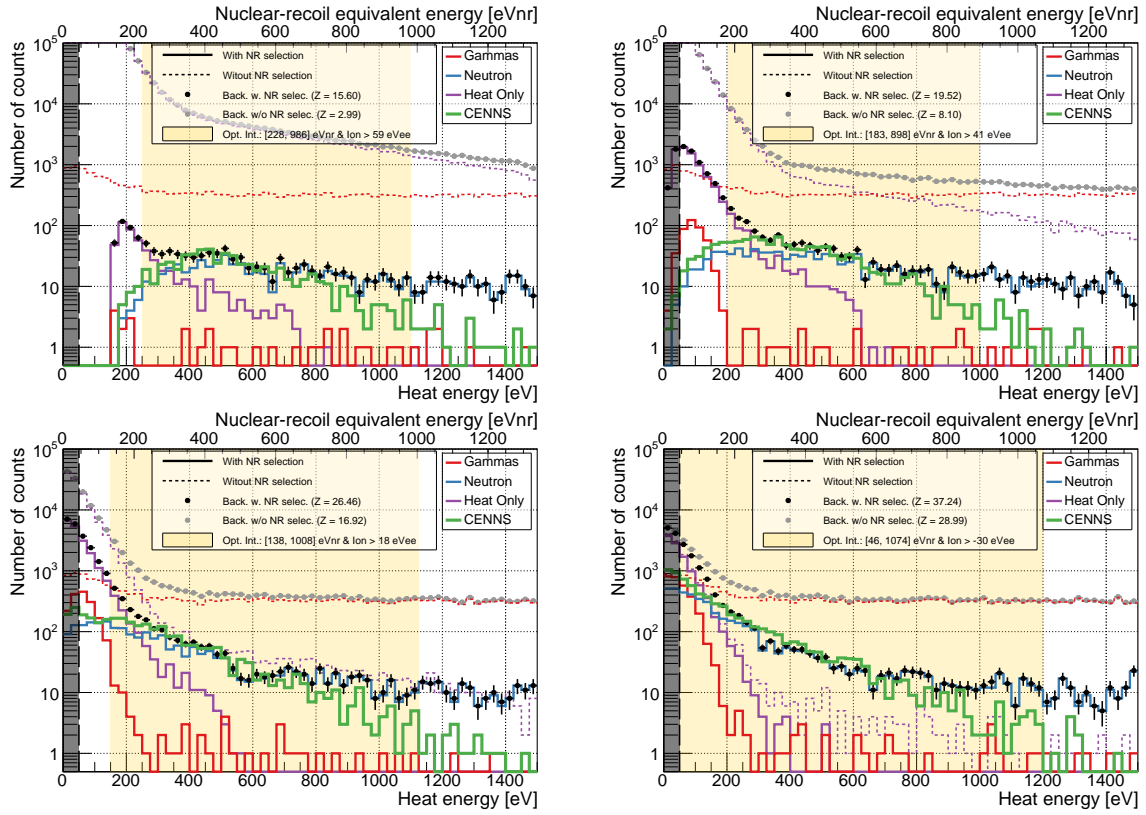


Figure 4.13: Simulated heat energy distributions with the same background and detector model parameters as given in Tab. 4.4 with varying HO background reduction factors of 10 (top left), 100 (top right), 1000 (bottom left), and 10000 (bottom right).

the HO background leads to an effective CENNS recoil energy threshold reduced by 50 eVnr until reaching its ultimate 50 eVnr threshold from the heat channel for a HO background reduction of 10^4 . Note that without particle identification the impact of the heat only background on the CENNS discovery significance, and its effective threshold, would be so dramatic that it would prevent any sensible detection if not reduced by at least 3 orders of magnitude. This clearly highlights: 1) the outstanding interest of particle identification when exploring new energy ranges where unexpected backgrounds may arise, and 2) that our ability to measure and study precisely the CENNS energy spectrum at the lowest energies is not limited by our detector energy threshold but by this hypothetical and unexplained strong low-energy background that is currently under investigations.

4.3.4 The muon veto cut optimization

For now we have always considered a muon veto coincidence time window of $\Delta T_{\text{coinc}} = 350 \mu\text{s}$. We discuss here how this value was optimized and how it depends on the underlying background and detector assumptions. Figure 4.14 shows the evolution of the CENNS detection significance when the HO background is (not) taken into account on the left (right) panel, and for both muon veto configurations III and IV. We also compare the case where we consider (solid line) or not (dashed line) the NR candidate selection cut. These curves, especially when we consider the NR selection, exhibit a maximum for values between $\Delta T_{\text{coinc}} = 200 \mu\text{s}$ and $\Delta T_{\text{coinc}} = 1 \text{ ms}$. At

4.3 Expected CryoCube CENNS sensitivity

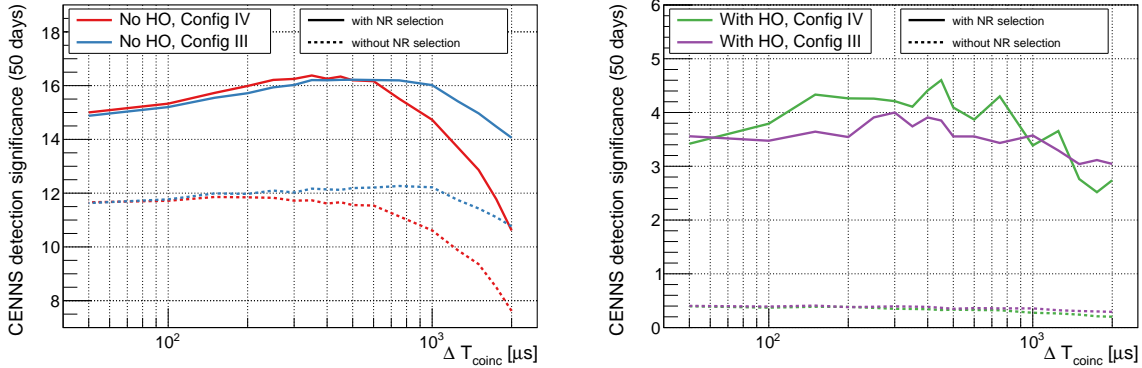


Figure 4.14: Evolution of the CENNS detection significance as a function of the muon veto coincidence time window ΔT_{coinc} without (with) taking into account the heat only background on the **left** (**right**) panel, and for the muon veto configuration III and IV. The solid (dashed) lines are with (without) considering the nuclear recoil selection cut. Note that the “with HO” case has been computed with 10 times less statistics for computational time reasons, hence the larger statistical fluctuations.

the lowest ΔT_{coinc} values the significance goes down because the cosmogenic background contamination becomes too high, and at the highest ΔT_{coinc} values the significance also goes down due to the increasing livetime loss. As already suggested earlier, adding the HO background decreases dramatically the overall significance by a factor of about 4, but also more strongly favors the use of the configuration IV muon veto. This is easily explained by the fact that the HO background puts more pressure on lowering the remaining neutron backgrounds which is lower in configuration IV than III by a factor of 3. This neutron background reduction overcomes the $\sim 10\%$ additional livetime loss. This result therefore suggests that if the HO background is as strong as what has been observed in RED30 and other detectors, then it may be better to go with the muon veto configuration IV which encapsulates the whole RICOCHET shielding.

4.3.5 CryoCube sensitivity study: results and discussion

In this final section dedicated to the estimation of the CryoCube CENNS sensitivity with RICOCHET at ILL, we perform a multi-dimensional scan of the most relevant parameters that are: the HO background reduction factor, the ionization resolution, the muon veto configuration, and the voltage bias. Figure. 4.15 shows the CENNS discovery significance as a function of the HO background reduction factor for the three different muon veto configurations, and four different ionization resolutions. The ionization resolution is indeed a key parameter in discriminating the heat only background, on top of the gammas. As one can see, for large HO rate (small reduction factors) the significance is indeed much larger with $\sigma_{E_{\text{ion}}} = 10$ eVee than 30 eVee, by about a factor 3 to 4. We can also observe that the impact of the muon veto configuration is significantly more important for large HO background contamination than when this background is negligible or even non-existent. As a matter of fact, for large HO background reduction factors, we see that the CENNS significance is almost independent of both the ionization resolution and the muon veto configurations (except if no muon veto at all is considered). Eventually this study highlights the importance of achieving the best possible ionization resolution while still

4.3 Expected CryoCube CENNS sensitivity

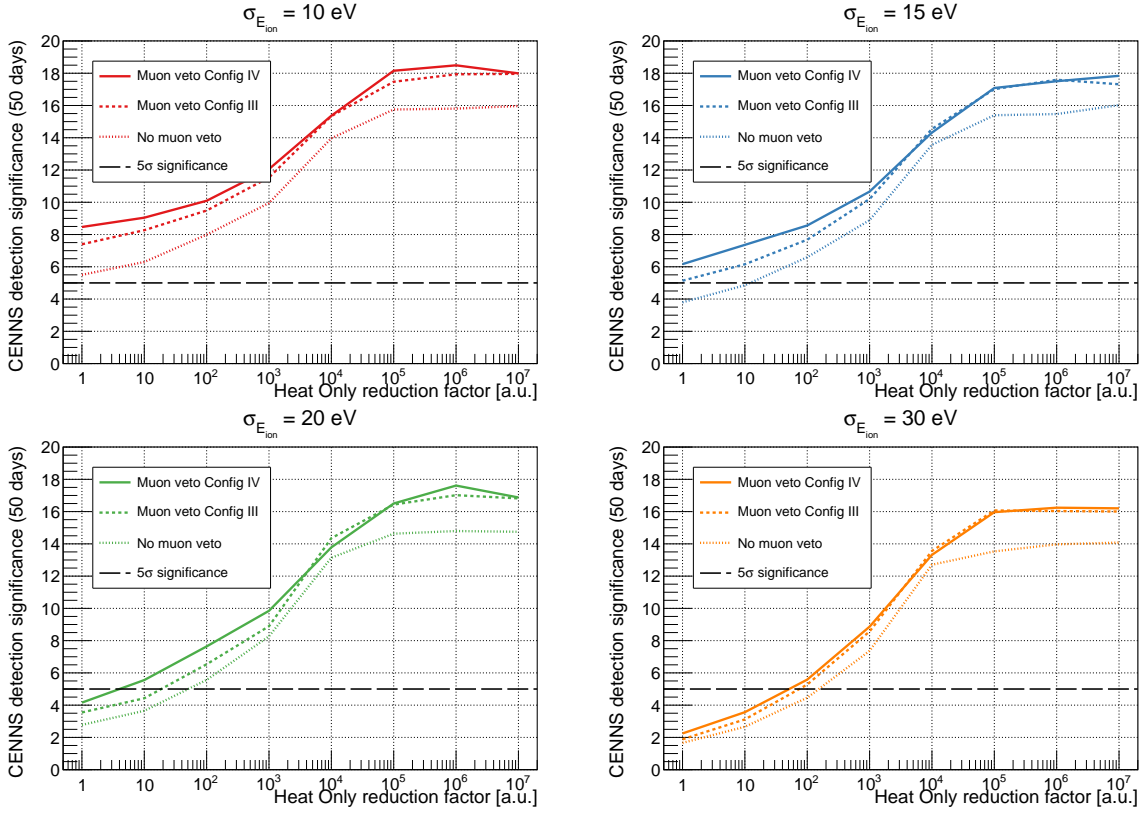


Figure 4.15: Evolution of the CENNS detection significance as a function of the HO background reduction factor ranging from 1 (no reduction) to 10^7 (almost complete reduction) for three different muon veto configurations: config. IV (solid), config. III (dashed), and no muon veto (dotted). These results are given for four different ionization resolutions $\sigma_{E_{\text{ion}}} = 10 \text{ eVee}$ (red - **top left**), 15 eVee (blue - **top right**), 20 eVee (green - **bottom left**), and 30 eVee (orange - **bottom right**).

suggesting that our planned 20 eVee (RMS) resolution is enough to reach our targeted 4-to-6 σ CENNS detection significance after one reactor cycle, even in the worst HO background conditions, *i.e.* with reduction factors from 1-to-10.

Finally, as a last study, we address the impact of the voltage bias on the CENNS detection significance. Figure 4.16 shows the CENNS discovery significance as a function of the voltage bias for the three muon veto configurations, a HO background rate reduced by 10, and with or without considering the NR candidate selection cut. We also show as the grey shaded area the voltage bias range of our upcoming HEMT-based electronics ranging from 0 to 20 V. As one can see, the significance remains constant or increases with the voltage bias depending on whether we consider or not the NR selection. This is easily explained with the following arguments and by looking at the right panel of Fig. 4.16 that shows the re-scaled heat energy event distribution in the case of a 100 V voltage bias:

- As the voltage increases, the total heat energy gets boosted thanks to the increased Luke Neganov contribution which is non-zero for any recoiling particle with non-null ionization yields. This boost in heat energy tends to lower the effective recoil energy threshold.

4.3 Expected CryoCube CENNS sensitivity

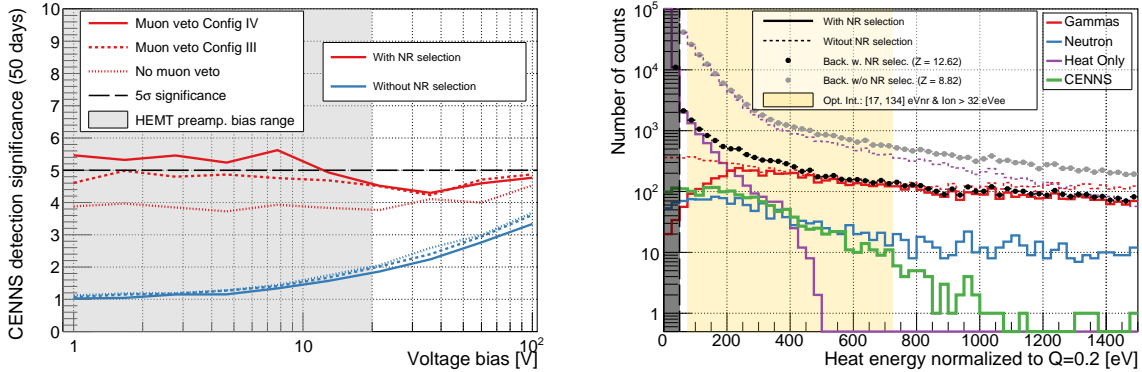


Figure 4.16: **Left:** Evolution of the CENNS detection significance as a function of the voltage bias for all three muon veto configurations, considering or not the NR selection cut, and a heat only rate divided by 10. **Right:** Simulated energy distributions corresponding to the case of a 100 V voltage bias and the muon veto configuration IV. Note that the x-axis units have been changed to a $Q = 0.2$ re-scaled heat energy in order to ease the illustration at various voltages and keep the analysis unchanged.

At 100 V, we expect our 50 eV heat energy threshold to correspond to ~ 10 eVnr nuclear recoil energy threshold, hence improving the CENNS energy threshold by about 5 with respect to $V_{bias} = 2$ V.

- As the heat only are non-ionizing they do not benefit from any Luke Neganov gain as the voltage increases. Therefore the discrimination between the HO and the CENNS signal improves as both distributions grow apart as the voltage increases.
- As the gamma induced electronic recoils have a large ionization yield, their energy distribution gets significantly expanded to higher heat energies, such that over the same [50, 1500] eV heat energy range, the gamma background gets reduced by $1 + V_{bias}/w_{eh} \approx 34.8$. This can be seen by looking at the red dashed histogram from Fig. 4.16 (right panel).
- Lastly, as the heat channel gets amplified, the timing resolution associated to a given nuclear recoil energy gets significantly improved under high voltages, hence leading to a more efficient muon-veto cosmogenic background rejection.

For all these reasons the significance increases steadily when no particle identification is used (blue lines), but does not improve when, on the contrary, particle identification is considered (red lines) as the loss of discrimination dominates over these positive effects. This clearly justifies our choice of working at low-voltage in order to fully exploit our heat/ionisation measurement background discrimination capability. Note that these observations are of course highly dependent on the background assumptions suggesting that it may still be worthwhile investigating the use of larger voltages bearing in mind the following difficulties and drawbacks of such high-voltage approaches:

- The gain on the CENNS discovery reach when working at higher voltages is totally dependent on the ionization yield of nuclear recoils which has yet to be precisely measured below 1 keVnr. It is also highly dependent on the expected background model: magnitude, type of recoil, and shape.

- Past results from the EDELWEISS and SuperCDMS experiments have shown that working at high voltages brings additional difficulties which are not to be neglected: leakage currents, infrared radiation producing additional low-energy backgrounds, stability of the crystal operation and charge collection.
- Recently we tested some high voltage detectors in Lyon and found that the high muon rate from above ground operation imposes some very strong constraints on the achievable high voltage biases. Indeed, the few MeV energy deposition following a muon interaction in a cm thick Ge crystal every ~ 10 s gets boosted up to GeV-scale energy depositions which are setting the detectors in unstable operation conditions. This could be solved in using smaller crystals leading to either a significantly smaller payload or a similar one but with a much larger number of crystals, adding more complexity.
- Lastly, the strong correlation between the ionization and heat energies when working at high voltage forbids the possibility to study the various backgrounds thanks to particle identification. As a matter of fact it has always been very difficult in dark matter search experiments to perform likelihood-based analysis due to the lack of possibility to model the backgrounds at low-energy precisely. This is something that should not be taken lightly as most, if not all, CENNS projections (including ours) use likelihood-based analysis methods where the backgrounds are well modeled and subtracted.

Based on these results, and the various and delicate uncertainties discussed above, we can conclude that the low-voltage strategy, including the ultra-low noise HEMT-based readout, is the best way forward. However, despite of the challenges of working at higher voltage biases, one could still benefit from the complementarity of using different data sets, at various voltage biases, in further improving the background modeling and further optimize the overall CENNS discovery potential. This is the reason why our upcoming HEMT-based electronics will be able to deliver voltage biases as high as 20 V, allowing us to investigate this valuable complementarity only possible with cryogenic semiconductors such as Ge and Si.

4.4 Conclusion

In this chapter, we have introduced two optimized detector designs, with two different strategies. The PL38 favors the CENNS signal efficiency with respect to the background rejection (especially of surface events), while the FID38 does the opposite. The resulting expected performance are summarized in Table 4.4. What one can conclude from this table is that, thanks to the currently being developed HEMT-based electronics, both designs have a clear path at achieving a 10 eV (RMS) heat energy resolution combined with a 20 eVee (RMS) fiducial ionization resolution. Based on these expected performance, we assessed the CryoCube CENNS discovery potential once integrated in the RICOCHET experiment at ILL. We found that a baseline scenario without heat only events should lead to a 17.3σ CENNS detection significance after only one reactor cycle, ultimately leading to a percentage-level precision measurement of the CENNS process down to the 50 eVnr energy threshold after one year of reactor ON data.

When we include this hypothetical and overwhelming heat only background (HO), with the worst rate observed from our detectors, thanks to particle identification we found that the significance drops only by a factor of about 4 after one reactor cycle. Note that even in this scenario,

4.4 Conclusion

a 7-to-9% precision measurement would still be achievable after 7 reactor cycles, *i.e.* after two years at ILL. It is worth noticing that thanks to particle identification, the overall signal-to-noise ratio in the CENNS region of interest is improved by almost four orders of magnitude. Additionally, we found that as these heat only background tends to induce a higher energy threshold, where timing resolution gets better, the configuration IV muon veto is therefore favored over the configuration III despite of its higher muon trigger rate of 350 Hz. Though we have demonstrated that this HO background is manageable, and should not prevent us from achieving a high-precision CENNS measurement, it is being actively investigated to both understand and efficiently mitigate it.

Lastly, we demonstrated that in light of our current background model the low-voltage approach allowing for particle identification is to be favored with respect to the high-voltage alternative. However, and as discussed above, the complementarity between these two approaches could be very instructive in further improving our background modeling. To that end, our upcoming HEMT-based readout electronics will be able to deliver up to 20 V voltage bias in order to exploit this potentially interesting and unique capability of the Ge cryogenic detector technology. Eventually, it is worth advertising that a more detailed multivariate analysis approach, including different sources of systematics, reactor ON-OFF data, and the detector response is ongoing to further assess the final CryoCube CENNS discovery potential.

5

Ongoing CryoCube detector R&D

5.1 The IP2I cryogenic facility

The IP2I cryogenic facility is located in the basement of the IP2I Haefely building. The overburden has been roughly estimated to be about 1.5 m.w.e. The total surface area of the facility is about a 100 m² and encompasses the main cryogenic lab (80 m²), a technical room for pumps and gas handling system (6 m²), an ISO-5 clean room for detector mounting (9 m²), and a room hosting a chemical bench also related to detector fabrication (5 m²).

The dry dilution cryostat shown on the left panel of Figure 5.1 is a Hexadry-200 from CryoConcept operated with a CRYOMECH PT-410. The particularity of this cryostat is that the first two stages (50K and 4K) are thermally coupled to the highly vibrating pulse-tube cold head thanks to low-pressure gas exchangers (HexagasTM), hence avoiding any mechanical contact and vibration propagation to the dilution unit. In 2016, one year after its delivery to IP2I, the cold head has been mechanically anchored to the ceiling hence providing two independent and maximally decoupled frames, one for the dilution unit (hosting the detectors) and one for the cold-head. In doing so, we demonstrated a reduction of the vibration levels by about two orders of magnitude between 0.5 Hz and 20 Hz, hence achieving world-leading vibration levels in a dry cryostat of few- $\mu g/\sqrt{\text{Hz}}$ below 20-Hz [166]. The impact on our detectors has been tremendous. Indeed, before the decoupling, due to the high vibration levels, the detectors were not able to operate due to the significant vibration-induced frictional heat power dissipation. As discussed in section 5.2, despite this successful and mandatory first decoupling, with the improvement of our detector sensitivity and resolution, a second vibration mitigation system at the mixing chamber level, where the detectors are installed, had to be implemented.

The cryostat is surrounded by a 10 cm thick lead shield of about 2 tons in order to reduce the environmental gamma background. We found a reduction of about a factor of 10 in the triggering rate of our detectors in doing so. There is no lead shield inside the cryostat, which then only provides a 70% solid angle coverage. As further detailed in Sec. 5.3.4 we have recently characterized the neutron and gamma backgrounds of our setup down to 1 keV.

5.1 The IP2I cryogenic facility



Figure 5.1: **Left:** Photo of the cryogenic lab, where the dry dilution cryostat (opened) and its lead shield are clearly visible. On the left side are the computers controlling the cryostat, and on the right side are the detector readout and DAQ. **Right:** Photo of the ISO-5 clean room hosting a wire bonder (right side) and a die bonder (left).

By early 2021, our cryogenic lab will be hosting the RICOCHET cryostat for a little over one year in order to be fully commissioned prior to its deployment at ILL. The commissioning phase includes: validation of the cabling (noise and thermal performance), the cold front-end electronics, the cool down of the inner shielding layers (lead and polyethylene), the demonstration of the CryoCube detector array performance (threshold, particle identification capability and livetime), and the DAQ and monitoring pipelines.

Our recently setup clean room hosts a wire bonder from Kulicke & Soffa, and a die bonder from JFP (see right panel of Fig. 5.1). The wire bonder, performing wedge bonding with a deep access is equipped with both gold and aluminium wires of $25\ \mu\text{m}$ diameter with their associated titanium and tungsten needles. Being in a superconducting state at low temperatures, the aluminium is used generally for the ionization electrodes and any other electrical connections that does not require thermal connection. Alternatively, gold wire bonds are used for both electrical and thermal connections, and are used to connect the NTDs (see Sec. 4.1 for more details on the thermal model). The die bonder is used to glue small chips such as micro resistors or NTD on electronic boards or on the Ge crystals. It operates a needle of $100\ \mu\text{m}$ diameter connected to a pump to hold the few- mm^2 chips in order to perform a precise and controlled gluing. It is also equipped with a system of cameras in order to monitor the gluing process, usually performed with AW106 epoxy¹.

On the data processing side, a dedicated pipeline called NEPAL, has been developed in order to ensure high quality data processing. The NEPAL pipeline is based on optimal filter processing algorithms, working in the frequency domain, and can process any type of cryogenic bolometers. Once the processing is done at the CC-IN2P3, monitoring plots are transferred automatically to a monitoring website allowing us to follow the performance and behavior of the detectors as a function of time.

¹It should be noted that even though detector mounting and fabrication is only recently possible at IP2I, all of the bolometers discussed hereafter were fabricated by our collaborators at IJCLab, CEA Saclay, and Institut Néel.

5.2 Vibration mitigation and cryogenic suspension

Dry Dilution Refrigerators (DDR) are a convenient alternative to Wet Dilution Refrigerators (WDR) in terms of low-cost and ease of operation. They have a high level of automation and avoid the consumption of liquid helium while providing a similar low temperature environment as the one obtained with WDR. The cool-down process of the two first stages within DDR is ensured by the technology of pulse-tube cryocoolers. However, the mechanical vibrations they induce can drastically affect the performance of cryogenic detectors. This effect has been reported by several cryogenic experiments using such bolometers [237, 238, 166]. With the significant improvement in heat energy resolution and sensitivity, we found that the cold-head decoupling discussed in Sec. 5.1 was not enough to ensure optimal operation of our new generation of detectors. More precisely, we found that the large radial stiffness of the edge-welded below connecting the cold-head to the dilution unit still allows for some vibration propagation down to our detectors, hence calling for an additional and cryogenic vibration mitigation strategy.

Several approaches have been considered to mitigate vibrations in dry dilution refrigerators: CUORICINO [239, 240], CUORE and its 988 TeO₂ detector array [241, 242], and more recently the LUMINEU and CUPID-Mo collaborations with their three springs detector towers each hosting three to four crystals in the EDELWEISS cryostat in Modane [223]. The CUORE experiment has implemented a different strategy. A Y-Beam (with three connecting points) at 300 K, isolated from the cryostat through *Minus-K* suspensions, supports the whole 988 TeO₂ detector array. Despite the use of three CRYOMECH PT415 pulse tubes, they report keV-scale detector energy resolutions [241, 242]. Other implementations of passive decoupling systems on DDR, with a large panel of physics applications, can be found in [243, 238].

In this published work [164], we demonstrate the vibration mitigation efficiency of a suspended tower based on a ~ 25 cm long elastic-pendulum. The motivation of this choice, discussed in the next section, is to reduce the number of vibration modes and to have a high attenuation along both vertical and radial directions. Later on, we compare both the vibration levels and the detector noise performance obtained on the mixing chamber and on the suspended tower.

5.2.1 An elastic-pendulum based cryogenic suspended tower

As discussed above, the main focus is to mitigate the transmission of both vertical and radial vibrations, with a particular emphasis on the radial modes as these are less efficiently damped from our pulse-tube cold head decoupling [166].

Our proposed solution is to mount the detectors onto an elastic pendulum. The 3-D dynamical description of the elastic-pendulum can be divided into two pseudo-independent equations in the approximation of small perturbations. The natural frequency for vertical modes is then given by:

$$f_{0,\text{vertical}} = \frac{1}{2\pi} \cdot \sqrt{\frac{k}{M}} \equiv \frac{1}{2\pi} \cdot \sqrt{\frac{g}{(l_{\text{eq}} - l_0)}}, \quad (5.1)$$

where M corresponds to the total mass of the suspended tower, k , l_0 , and l_{eq} are the elastic constant, the rest length, and the length at equilibrium of the spring, respectively. The natural

5.2 Vibration mitigation and cryogenic suspension

frequency for radial oscillations of the pendulum, which are related to its total length l_{tot} , is given by:

$$f_{0, \text{radial}} = \frac{1}{2\pi} \cdot \sqrt{\frac{g}{l_{\text{tot}}}}. \quad (5.2)$$

From these approximations, we can estimate the theoretical resonance frequency of the elastic pendulum depending on the spring constant, the pendulum length and the total mass of the detector assembly. Interestingly, one can notice that: 1) as $l_{\text{tot}} \geq (l_{\text{eq}} - l_0)$, the natural frequency in the radial direction is necessarily lower than in the vertical direction, and 2) the vertical resonance frequency can either be expressed of k and M simultaneously or by its elongation length alone.

As already mentioned, thanks to the use of a single spring holding system, we avoid any transverse momentum related natural frequencies which could populate the vibration spectrum at high frequencies. Therefore, in this case, we expect the suspended tower to have a transfer function response under the form of a 2nd order low-pass filter with a single resonance frequency in both directions $i = \{\text{vertical, radial}\}$:

$$H(\omega_i) = \frac{\omega_{0,i}^2}{\omega_{0,i}^2 - \omega_i^2}, \quad (5.3)$$

where $\omega_{0,i}$ is the natural pulsation of the suspended tower, with $\omega_{0,i} = 2\pi \cdot f_{0,i}$. Two main arguments motivate a low-pass filter suspended tower design: 1) the heat signal bandwidth of the tested detectors has a roll-off frequency around ~ 40 Hz, and 2) the natural frequency of the pulse-tube cryocooler is at 1.4 Hz. Therefore, the natural frequencies of the suspended tower in both vertical and radial directions have been tuned to be as low as possible in order to attenuate all vibrations above 1.4 Hz. According to Eq. 5.1, a vertical resonance frequency of 1 Hz requires a spring elongation of at least $(l_{\text{eq}} - l_0) \geq 25$ cm. Following Eq. 5.2, a total pendulum length of at least 25 cm results in a radial frequency below 1 Hz.

The challenge then comes from accommodating with the constraints imposed by the cryostat geometry. As the distance between the mixing chamber plate and the inner thermal screen is only of about 20 cm, the pendulum had to be attached to the still plate and not directly to the mixing chamber. As shown in Figure 5.2 (left panel), the holding strategy is carried out in three steps: 1) a wire is fixed below the still plate (1 K) and running through the 100 mK stage ; 2) a stainless steel spring is attached to the wire between the 100 mK stage and the MC ; 3) the suspended tower is connected to the spring via a copper wire through the MC plate. For the wire at the still plate, both nylon and Kevlar were used. Note that the elastic constant k of the spring has to be carefully chosen, taking into account the total mass of the detector assembly, as its elongation is constrained by the ~ 18 cm distance between the 100 mK stage and the MC. With this approach, the total pendulum length l_{tot} from the still plate to the center of mass of the detector assembly, can be equal to 25 cm.

The detector tower is shown in the right panel of Fig. 5.2. This module can host two cryogenic detectors (RED2 and RED10 here) and has a total height of 13 cm. During the installation, before attaching the spring, the tower is firmly held by a copper frame screwed under the MC

5.2 Vibration mitigation and cryogenic suspension

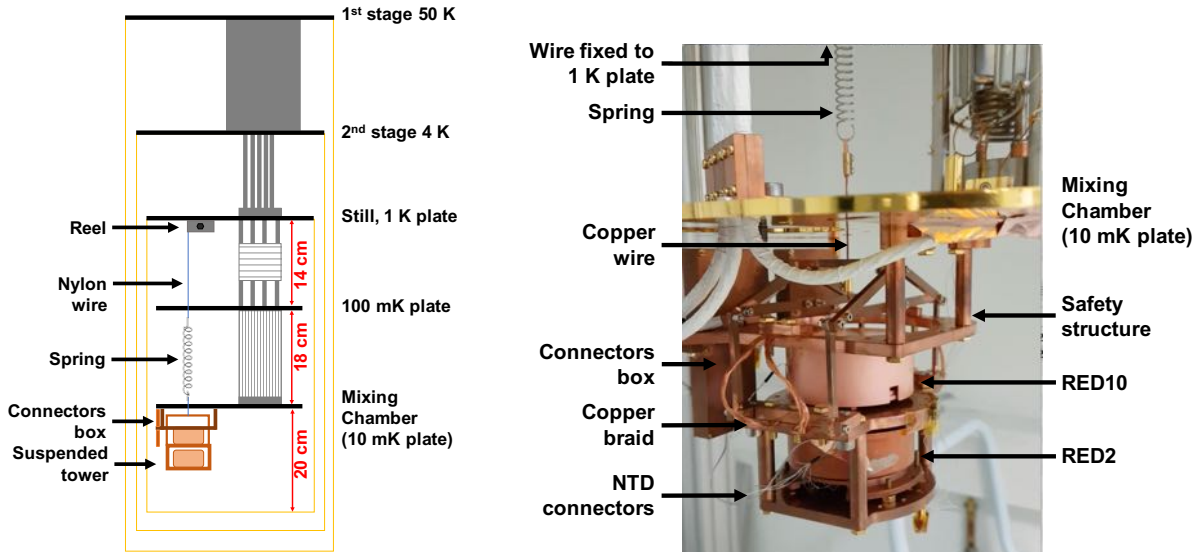


Figure 5.2: **Left:** Schematic of the suspended tower design and integration in the cryostat with a nylon wire ($l \approx 19$ cm) and a stainless steel spring ($k = 240$ N/m, $l_0 = 3.4$ cm). **Right:** Suspended tower prototype hosting here two detectors (RED2 and RED10) considered for this study. Figures taken from [164].

plate. This structure remains as a safety structure during cool-down and operation in case the wire should break. Connector boxes are placed close to the detector on the external side of the safety structure. They are used to connect the sensors of the detectors to the readout electronics at the warmer stages. Both the suspended tower and the safety structure are made of clean CuC_2 copper. During operation, the suspended tower is floating and its thermalization is realized by four 10 cm long ultra-supple flat copper braids linking the safety structure and the tower.

A thick (~ 2 mm diameter) 5 cm long copper wire connects the top of the tower to the spring passing through the MC plate to ensure the thermalization of the stainless steel spring. Indeed, test with less conductive wires have shown that the steel spring remains warm enough to emit infrared radiation damaging our detector performance.

5.2.2 Characterization of the vibration levels

The vibration measurement method and apparatus used in this work is similar to the one described in our previous work [166]. The set-up is composed of a high sensitivity seismic accelerometer from *PCB Piezotronics*. We used the high sensitivity accelerometer *PCB-393B05* which has a gain of 10 V/g and an intrinsic noise limit of $[0.5-0.07]$ g/ $\sqrt{\text{Hz}}$ within [1-1000] Hz frequency range.² This accelerometer is connected to a *PCB-480E09* signal conditioner with an anti-tribo-electric coaxial cable tightly fixed to the cryostat frame to avoid parasitic noise from the stress or vibrations of the cable. The connection between the inside and the outside of the cryostat is ensured thanks to leak-tight feedthrough. The data is digitized using a 16-bit National Instrument DAQ-6218 and processed off-line.

²The manufacturer indicates a possible 5% uncertainty on the accelerometer sensitivity.

5.2 Vibration mitigation and cryogenic suspension

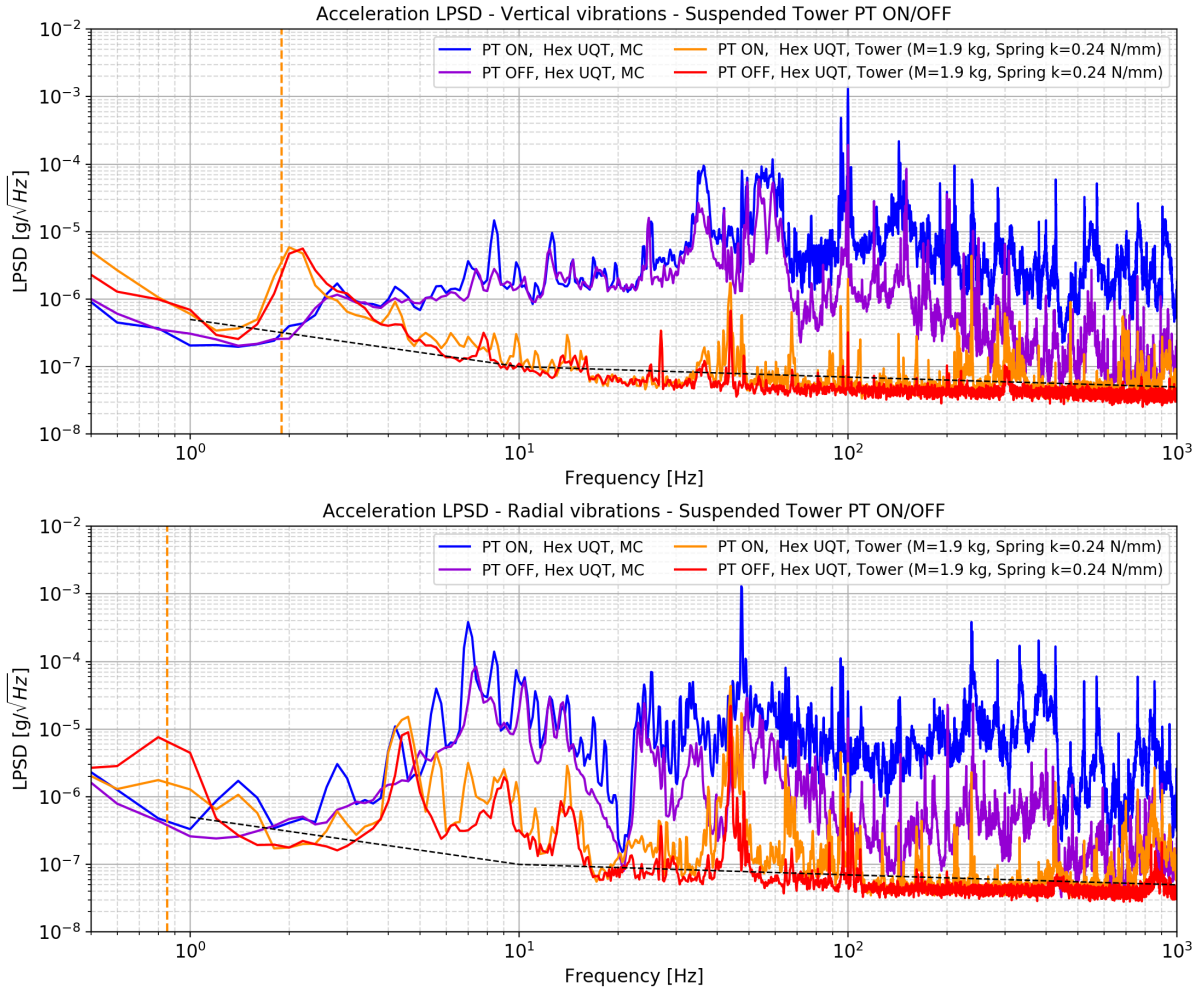


Figure 5.3: Comparison of the vertical (**top**) and radial (**bottom**) vibration levels of the MC plate and the suspended tower in both PT ON and OFF configurations. The dashed black line is the accelerometer sensitivity, and the orange vertical dashed lines represent the position of the natural frequencies of the suspended tower derived from Eqs. 5.1 and 5.2. Figures taken from [164].

As in [166], all vibration measurements are performed at room temperature.³ The accelerometer is fixed below the MC stage of the cryostat, and then below the bottom stage of the suspended tower thanks to a U-shaped workpiece allowing to mount the accelerometer along either the radial or the vertical direction. The output signal of the accelerometer is sampled at 10 kHz, well beyond the signal bandwidth of the accelerometer of 1 kHz. The vibration level is obtained from a Fast Fourier Transform (FFT) analysis using Hanning windowing over 5 s time windows. Figure 5.3 shows the impact of the pulse-tube cryocooler on the acceleration power spectra, expressed in units of $g/\sqrt{\text{Hz}}$, by comparing measurements PT ON and OFF. The mixing chamber vibration levels shown as the blue (PT ON) and purple (PT OFF) solid lines are compared to the

³The variation between 300 K and 4 K, for stainless steel and copper, which are the main materials used for the rigid structures of the DDR units, of the elastic constant k and Young's modulus E values is expected to be small [244].

5.2 Vibration mitigation and cryogenic suspension

ones obtained with the suspended tower shown as the orange (PT ON) and red (PT OFF) solid lines. The main differences observed between these two PT configurations are coming from few pick-up lines which are mostly at high frequencies and arise from acoustic perturbations originating from: e.g. the noise of the rotary valve, the audible whistling noise from the high-pressure gas going through the corrugated pipes and flex hoses. At low frequencies (< 40 Hz), in the detector bandwidth, the impact of the PT is clearly negligible on the suspended tower. As a matter of fact, by comparing the “mixing chamber” PT OFF case (purple solid line) to the “suspended tower” PT ON case (orange solid line), one can further conclude that the suspended tower is not only efficient at reducing the PT-induced noises but also most of the whole setup-related vibrations from the building, the cryostat holding structure, and so on. We can therefore conclude from this result that vibration-wise, our detectors are largely insensitive to their surrounding environment, suggesting that they should run in optimal conditions.

5.2.3 Cryogenic detector performance improvement

Eventually, we discuss hereafter the overall noise and energy resolution performance achieved with the two RED10 and RED2 200 gram Ge bolometers installed in the suspended tower. Both detectors exhibit similar sensitivities of about 50-100 nV/keV at around 18 mK and are massive enough to sense putative displacements and vibrations.

The NTDs are polarized at their optimal current bias and the heat signals (*i.e.* the voltage across the NTDs) are read-out continuously in the form of streams. The latter are then further processed offline to estimate the noise power spectra with a similar procedure as described in Sec. 2.3.1 to remove events. Figure 5.4 shows the PSDs obtained for RED2 (top and middle panels) and RED10 (bottom panel) on the mixing chamber (MC) as dashed lines, and on the suspended tower as solid lines. Also shown are the 1 V normalized heat signal template in the frequency domain and the theoretical noise calculations based on a full electro-thermal modeling of the detectors (see Sec. 4.1). We show as blue (PT-ON) and green (PT-OFF) lines when the NTD are polarized, *i.e.* the sensor is activated, and for completeness we also show measurements with the NTDs not polarized (red curve), to estimate the effect of the vibrations on the cabling, such as microphonics.

From comparing the various voltage PSD presented in Figure 5.4, we can extract a few major conclusions regarding the effectiveness of the suspended tower at mitigating the vibration-induced noise on bolometers. Note that our discussion will mostly focus on the frequency range of interest, from 1 Hz to 40 Hz, as it corresponds to the detector signal bandwidth (as illustrated from the gray solid lines). The first obvious comparison is between the cases where the detectors are optimally polarized (blue curves) and either on the mixing chamber (dashed lines) or on the suspended tower (solid lines). For each of the three NTDs presented in Figure 5.4, the PSD at the lowest frequencies are reduced by one to two orders of magnitude. Furthermore, we observe that the noise levels obtained PT ON and with the NTD optimally polarized (blue solid lines) are almost identical to the case where the NTDs are not polarized and the pulse-tube OFF (red dashed lines), suggesting that we are limited by both the electronics and the intrinsic thermal noise from the detector, and not by the vibrations when the detectors are mounted on the tower. This is confirmed by the fact that the resulting noise levels are very close to the theoretical expectations illustrated by the black solid lines.

5.2 Vibration mitigation and cryogenic suspension

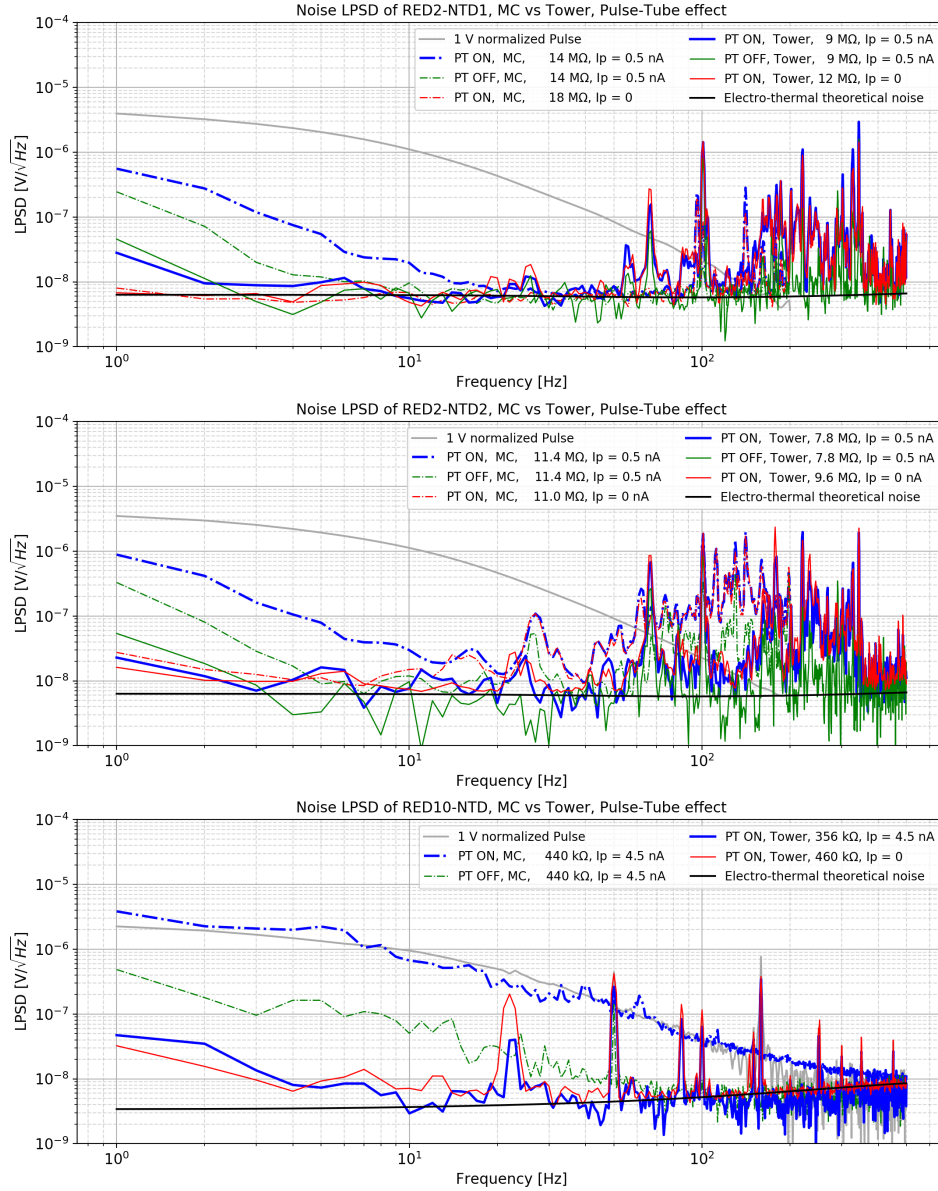


Figure 5.4: Noise power spectra density for NTD1 (**top**) and NTD2 (**middle**) thermal sensors of RED2 and the NTD of RED10 (**bottom**) mounted on the MC plate (dashed lines) and on the suspended tower (solid lines). Measurements were performed at optimal NTD polarization currents with PT ON and PT OFF at 16 mK. The black solid line refers to the expected noise level derived from the electro-thermal model described in Sec. 4.1, while the grey solid line shows the unit normalized pulse template illustrating the signal bandwidth. Figures taken from [164].

Interestingly, we do not see on any of the three NTDs a 1.8 Hz pick-up noise as was potentially suggested from the vertical acceleration measurements shown as the red (PT OFF) and orange (PT ON) solid lines from Figure 5.3. This is a major observation as it suggests that such frequency vibrations within the detector bandwidth do not limit the detector performance.

5.3 Overview of recent experimental results

Finally, one can derive from Figure 5.4 that the noise PSD obtained with the NTDs optimally polarized on the suspended tower with PT ON (blue solid lines) are below the ones obtained with the detectors running on the mixing chamber with the PT OFF (green dashed lines). This major results indicates that not only the suspended tower damps very efficiently the vibration-induced noise from the pulse-tube cryocooler, but makes the detectors insensitive to any residual vibrations from the surrounding environment of the experiment, *e.g.* building and pumps. Note that this conclusion was already suggested from the vibration measurements shown in Figure 5.3.

At the time of this work, many of the calibration sources and techniques were not yet in place. The RED2 and RED10 detectors were then calibrated using the ~ 18 MeV muon pic. By doing so, we found that RED2 went from a 1.6 keV (RMS) resolution (combining both NTDs) and RED10 from 14 keV when installed on the mixing chamber, to a 250 eV and 400 eV (RMS) energy resolution when installed in the suspended tower, respectively⁴. Based on these two detector prototypes, this result suggests that the suspended tower allows for an improvement of the energy resolution between one-to-two orders of magnitude, depending on their susceptibility to vibrations.

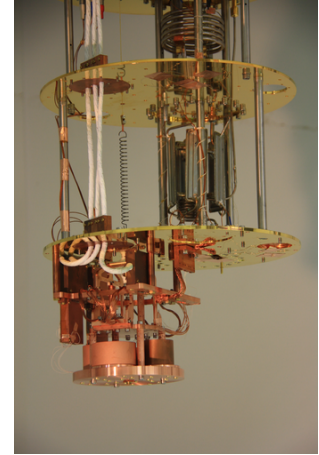


Figure 5.5: New suspended detector tower being commissioned.

Following the publication of this work [164] we found similar improvement factors, between a factor of a few up to one order of magnitude, on all of our most recent and sensitive detector prototypes discussed in the next section, Sec. 5.3. Based on this success we are now commissioning a new suspended tower shown in Fig. 5.5 that can host up to 5 RED detectors, for a total payload of about 200 g of Ge bolometers. Nowadays, our detectors are no longer limited by vibrations, but only by the intrinsic JFET-based electronic noise limiting us from reaching the ultimate thermal fluctuation noise floor, see Sec. 4.1. Though a similar elastic pendulum approach would not be feasible in the RICOCHET cryostat for the CryoCube, a slightly different three-spring pendulum approach is currently being investigated for optimal operation of the CryoCube detector at ILL.

5.3 Overview of recent experimental results

In this section we briefly review the main and most relevant recent experimental results to the CryoCube detector array design and performance. In Sec. 5.3.1 we first review the achieved heat energy resolution and discuss how we optimized the mass of our single Ge crystal from the CryoCube array. In Sec. 5.3.2 we present the ionization resolution and the charge collection experimental characterization methodology exemplified with our recent RED80 detector prototype. In Sec. 5.3.3 we discuss how, with three different methods, we can reliably estimate the timing resolution of our detectors at the lowest energies. In Sec. 5.3.4 we present our

⁴Note that since this work, tremendous progress have been made on the low-noise cold cabling, the processing tools, and the low-energy calibration, such that RED10 actually achieved 50 eV (RMS) heat energy resolution later on, see Sec. 5.3.1

5.3 Overview of recent experimental results

Name	T [mK]	I_p [nA]	\bar{R} [M Ω]	Freq. [Hz]	Sens. [μ V/keV]	Res. [eV]	Stream
RED10 - 200 g	14	1.5	3.5	400	0.86	50.0	sd27g000
RED20 - 33.4 g	17	1	3.4	400	1.6	17.7	se26g000
	14	0.5	8	200	2.5	18.2	uf15l002
	13	0.2	22.9	50	4.7	16.5	uf18l003
RED30 - 33.4 g	15	0.75	3.5	400	1.1	25.3	si26g001
RED50 - 33.4 g	14	2	2.4	400	1.2	24.2	tc12l000
RED60 - 33.4 g	14	1.5	3.3	400	1.1	25.1	tc12l000
RED70 - 33.4 g	13	1.7	3.5	400	1.3	18.1	tj18l011
RED80 - 37.6 g	16	1	3.9	400	0.4	124.8	tg27l000
RED90 - 37.6 g	13	1.2	8	200	1.7	33.2	ug20l002
RED100 - 37.6 g	13	1.6	8	200	1.6	26.8	ug20l002

Table 5.1: Summary of the heat channel performance of the nine RED detectors tested over the last two years at IP2I. These measurements were all done using the JFET-based EDELWEISS electronics, either in the suspended tower PT-ON, or mounted directly on the mixing chamber but with PT-OFF. The energy calibrations were done using a ^{55}Fe source (5.89 keV and 6.49 keV X-rays) or the internal K/L/M shell EC-decays, respectively at 10.37 keV, 1.3 keV and 160 eV, following a ^{71}Ge neutron activation of the Ge crystal. The data were all processed using the NEPAL processing pipeline.

data-driven IP2I background model based on observed energy spectra from 5 RED detectors operated at IP2I, including one with particle identification capabilities, and a sixth one operated in Modane. Lastly, in Sec. 5.3.5 we present our HEMT model, motivating our choice for the use of future HEMT-based preamplifiers for our heat and ionization readouts, and first noise power spectral densities measured at IP2I in our newly developed HEMT characterization bench.

5.3.1 Heat energy resolution and detector mass optimization

As mentioned in Sec. 4.1 where we presented a simplified electro-thermal model of our RED detectors, initiated within the EDELWEISS collaboration in 2015, we are aiming for a 10 eV heat energy resolution for each of the 38 g Ge individual bolometers of the CryoCube.

Table 5.1 gives a comprehensive summary of the heat channel performance of all the RED detectors that have been tested in our cryogenic test facility at IP2I. We give hereafter a few observations that can be inferred from this table:

An averaged resolution of 22 eV on 33.4 g crystals: Based on the five 33.4 g detectors, we achieved an averaged 22 eV (RMS) heat energy resolution. This resolution is 70% higher than our thermal model predictions considering the JFET-based electronic noise with a 400 Hz modulation frequency (13.2 eV). This can be explained by some variance in the signal sensitivity which depends on the NTD characteristics and some additional noise at low-frequency. At $\sim 3\text{ M}\Omega$ impedance, excess noise can be explained by some residual vibrations inducing microphonic noise and/or some additional thermal fluctuation noise. The latter hypothesis is indeed strongly supported by our measurements exhibiting some time varying noise contribution that decays slowly over time, see Sec. 2.3.2. The TEFLON clamps are an ideal candidate for such a source of noise due to their plastic nature which makes their thermalization much slower than the copper and germanium materials from the detectors.

5.3 Overview of recent experimental results

Microphonic issues with 37.6 g crystals: The 37.6 g detectors have achieved a 30 eV (RMS) heat energy resolution without considering RED80 which had poor microphonic performance due to a sub-optimal holding design. Indeed, all 37.6 g Ge crystal were initially mounted with only TEFLON clamps in a newly designed holder. However, we found that none of them were achieving good resolution due to microphonics. By switching the top TEFLON clamp with sapphire balls held with bronze/chrysocale sticks, we were able to very efficiently fix this issue. However, we still see some residual microphonic noise. We are therefore designing a new detector holder for these crystals which are the ones that will be used for the CryoCube. Note that RED80 did not benefit from this new holding strategy which came after it was unmounted, hence its significantly worse energy resolution.

NTD gluing on bare Ge surface: RED80 is the only detector that had its NTD glued directly on top of one of its aluminium electrode and as one can see, its signal sensitivity of $0.4 \mu\text{V}/\text{keV}$ is significantly lower than what we observed with the other RED detectors. This, combined with additional observations from the FID800 EDELWEISS detectors [80], suggests that the electrode may be preventing the athermal phonons to reach directly the NTD, hence lowering the overall signal sensitivity. Based on these observations, the PL38 and FID38 from the CryoCube will have their NTD glued directly on the Ge surface and be held with an optimized clamping strategy.

Working at higher impedance for maximum sensitivity: As one can see from Tab. 5.1 most of the data were taken in temperature and polarization current conditions such that the NTD impedance was around $4 \text{ M}\Omega$. This is due to the fact that for larger impedance, the JFET current noise (i_n) starts to affect our noise performance significantly, see Sec. 4.1. Therefore, as one can see from the RED20 data, though the sensitivity increases significantly when working at higher impedance the resolution does not improve. With the much lower current noise from the upcoming HEMT-based electronics we want to fully benefit from this increase in sensitivity at high impedance and improve by a factor of about 2 our energy resolution (see Sec. 5.3.5).

Figure 5.6 (left panel) compares the observed energy resolutions from the RED detector serie (blue) given in Tab. 5.1, and the targeted CryoCube performance (blue star), with the ones achieved by various cryogenic experiments: SuperCDMS 600 g Ge crystals (purple) [101], CDMS R&D recent above-ground results using Si 1 and 10 g crystals (yellow) [245, 246], CRESST 300 g and 24 g CaWO_4 crystals (orange) [247, 78], EDELWEISS-III 860 g Ge crystals (red) [80], and NuCLEUS 0.5 g Al_2O_3 crystal (brown) [92]. As one can see, the RED detectors have among the best resolution-to-mass yield despite being operated at the surface where the high flux of cosmic rays makes the operation of ultra-sensitive detectors difficult. For instance the highly sensitive 24 g CRESST crystal had a 38.1 eV (RMS) [248] heat energy resolution when operated at the surface before reaching its impressive 4.6 eV (RMS) resolution at LNGS [78]. Figure 5.6 (left panel) also shows two possible scaling laws of the energy resolution with the crystal mass. The dark grey one, proportional to the crystal mass, is motivated by the assumption of a purely thermal signal. The light grey one, where the resolution scales with $M^{1/2}$ is however motivated by our observations from the RED detector serie at 33.4 g, 37.6 g, 200 g, and 860 g, and suggests again a non-purely thermal origin of the signal. Interestingly, under similar considerations of an athermal signal depending on the detector geometry, the target detector from the NuCLEUS experiment are expected to exhibit a scaling law of their energy resolution as $M^{2/3}$ [249], which would then grow faster with the detector mass compared to our

5.3 Overview of recent experimental results

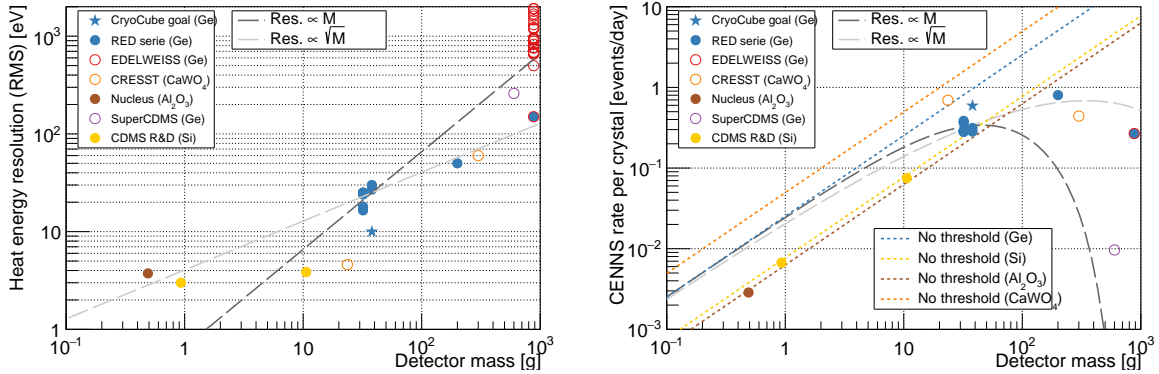


Figure 5.6: **Left:** State of the art of heat energy resolution achieved by several experiments and groups as a function of the cryogenic detector mass. The filled and empty circles correspond respectively to above- and under-ground measurements. Note that the blue filled circle outlined in red is a RED-like detector of 860 g operated in Modane in the EDELWEISS setup. The dashed dark and light grey lines represent two different scaling laws of the energy resolution with the detector mass. **Right:** Same as left panel but now presented as the CENNS event rate per crystal (in events/day) as a function of the cryogenic detector mass. The CENNS rate has been computed considering a reactor neutrino flux of 10^{12} neutrino/cm²/s and a common threshold definition of $5\sigma_E$. The thin dotted lines correspond to the expected CENNS event rate considering a 0 eV energy threshold for the four relevant target materials discussed here.

NTD-based technology.

One pivotal parameter in the CryoCube design is the mass of the individual Ge detectors from the array. To that end, figure 5.6 (right panel) shows the similar state of the art of cryogenic detector performance as shown in the left panel, but now shown as the expected CENNS event rate per crystal as a function of the detector mass. To perform these calculations, a reactor neutrino flux of 10^{12} neutrino/cm²/s and a common threshold definition of $5\sigma_E$ have been considered⁵. Taken at face value, this figure suggests that thanks to their 30 g-scale mass and 20 eV (RMS) resolution, combined with the use of a heavy Ge target element, the individual RED detectors have proven to be expecting the highest expected CENNS event rate of 0.3 events/day (0.6 events/day as per the CryoCube expected 10 eV resolution). From the scaling laws, one can see that we could have envisioned higher masses, up to a ~ 300 gram crystals to improve by a factor 2.5 the expected CENNS rate per crystal. However, our goal is not only to have the largest CENNS rate, but also the highest sensitivity to many new physics signals that may predominantly arise in the lower end of the CENNS induced recoil energy spectrum. As a matter of fact, the departure from the blue dotted line illustrates the loss in sensitivity to the lowest CENNS recoil energies. Interestingly, one can see that the Si-based CDMS R&D and the Al₂O₃ Nucleus prototypes would almost fully sense the CENNS process at the lowest energies ensuring optimal sensitivity to new physics scenarios appearing at low energy. Similarly, we see that the Ge-based CryoCube detector will be probing a similar fraction of the low-energy CENNS

⁵Note that thanks to their small bandwidth, for our NTD-based RED detector prototypes a $3\sigma_E$ threshold can be considered and still achieve similar noise induced trigger rates as from the faster TES-based detectors with a $5\sigma_E$ threshold. However, for the sake of a fair comparison, we use a $5\sigma_E$ threshold definition for all technologies.

5.3 Overview of recent experimental results

spectra as a ~ 20 eV energy threshold CaWO_4 detector due its more constraining kinematics associated with the use of the heavy W target element. Though ensuring a high CENNS rate per crystal is of pivotal importance to avoid the use of very large detector arrays to guarantee a high CENNS significance detection, and to possibly increase the signal-to-noise ratio per crystal, it is not the only mass-tuning parameter to be taken into account. Indeed, larger crystals come with larger heat capacities, which in turn leads to slower detectors. As CENNS experiments are operated at the surface with small-to-negligible overburden, the cosmic-induced backgrounds are expected to be overwhelming. In order to efficiently reject a significant fraction of this cosmogenic background, CENNS experiments use muon-veto to be used in anti-coincidence with the target cryogenic detectors. Due to their $\mathcal{O}(100)$ Hz muon-induced trigger rate, fast enough detectors are required to minimize the muon-veto induced livetime loss. In our case, thanks to the use of the additional fast ionization channel, we have shown that the timing resolution expected with our 30 g-scale Ge detector should be enough to ensure a highly efficient muon-induced background rejection, especially for gammas, see Sec. 4.3.1.

5.3.2 Ionization channel experimental characterization and performance

Following the selection of the Ge crystal geometry (diameter = 30 mm, height = 10 mm) for the CryoCube detector array, significant mechanical adjustments of the aluminium evaporator at Orsay (IJCLab) had to be done to perform a precise and efficient electrode deposition with these new crystal dimensions. Figure 5.7 shows the photo (left panel) and the design schematic (right panel) of the first heat+ionization RED80 detector prototype. RED80 was designed to have an hybrid electrode scheme with planar electrodes on the top and bottom surfaces (as in PL38) and of ring electrodes on the side (as in FID38) to validate the aluminium evaporation and lithography techniques. The NTD is glued on the top electrode and is thermally anchored to the cryostat thanks to the use of gold wirebonds, following the RED detector thermal design specifications. Based on its electrode topology and COMSOL simulations, RED80 is expected to exhibit a 80.75% fiducial volume and a 5% low electric field region (in the corner) subject to charge trapping [228].

Regarding the ionization channel resolutions, all channels exhibit energy resolutions between 252.6 eVee (RMS) and 275.2 eVee (RMS) which is in perfect agreement with our resolution predictions of 254.9 eVee with this JFET-based electronics and a sampling frequency of 400 Hz (see Sec. 4.2.3). The fiducial ionization resolution was found to be $\sigma_{bulk} = 188.9 \pm 18$ eVee (RMS), which is compatible with the 180.2 eVee resolution expected from our predictions assuming uncorrelated noise. It is worth highlighting that we observed similar ionization resolutions with other detector prototypes, and that these performance were not impacted by the vibration levels. The fact that the resolutions were found to be similar for all channels and for varying detector prototypes having different capacitance is very well explained by the fact that we are dominated by the large cabling capacitance which has been measured to be of $C_p = 125 \pm 9$ pF [228]. Due to this dominating cabling capacitance we observed a small 4-to-5% cross talk among the different ionization channels which are easily corrected for using the Maxwell capacitance formalism detailed in D. Misiak thesis [228].

After having discussed the ionization resolutions, we now focus on the experimental determination of the RED80 charge collection efficiency and fiducial volume, which are key characteristics of our detector performance. In order to do so, prior to mounting the detectors in our

5.3 Overview of recent experimental results

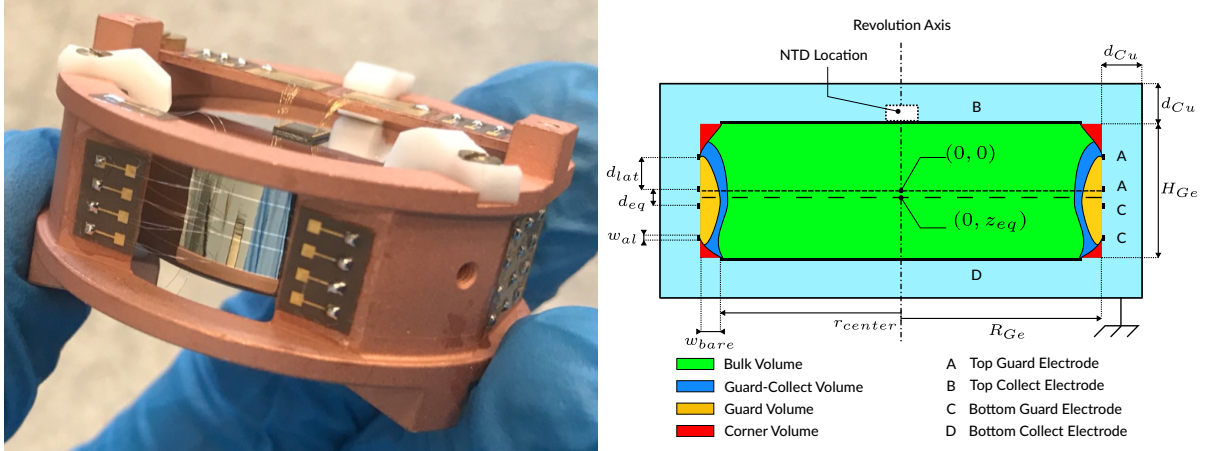


Figure 5.7: Photo of the RED80 detector prototype (**left**) and its simplified schematic (**right**). RED80 is a $H_{Ge} = 10$ mm and $R_{Ge} = 15$ mm 37.6 g Ge crystal with planar fiducial electrodes on the top and bottom surfaces (B and D) and veto electrodes on the side (A and C). Based on its electrode topology and COMSOL simulations, RED80 is expected to exhibit a 80.75% fiducial volume (green) and a 5% low electric field volume in the corner (red) subject to charge trapping. The self-capacitance of each electrodes are estimated to be between 14 pF and 18 pF. Figure taken from [228].

cryostat, we expose them to an AmBe source emitting 6×10^5 neutron per seconds for 24 hours in a dedicated shield in order to activate them. Indeed, the ^{71}Ge activation from neutron capture will lead to electron-capture decays from the K/L/M shells producing X-ray lines with summed energies of 10.37 keV, 1.3 keV, and 160 eV respectively. On top of being monoenergetic, these lines are uniformly distributed through out the entire detector volume, hence allowing the precise study and measurement of the fiducial and veto volumes of the detectors. Note that after a 24 hours activation of our 37.6 g Ge crystal we get about 1 Bq of K-shell decays. The L- and M-shell decay lines have rates 10 and 100 times lower respectively than the K-shell one. Figure 5.8 (left panel) shows the event distributions in the total ionisation energy versus heat energy plane. The grey dots show all the events passing the quality cut selection (χ^2 , offset, and good data periods) while the red and blue dots show the K-shell 10.37 keV events with complete and incomplete charge collection. Indeed, operating at a 2 V voltage bias implies that events with full charge collection will entirely benefit from the Luke Neganov amplification leading to a total heat energy $E_c = 10.37 \times (1 + 2/2.96) = 17.37$ keV. On the other hand, events with no charge collection, *i.e.* no ionization signal on any electrode and no Neganov-Luke heat contribution, will exhibit a total heat energy $E_c = 10.37$ keV. Note that the 1.3 keV L-shell line is also clearly visible though the 160 eV M-shell line is in the noise blob due to the poor heat energy resolution of this detector for the reasons explained in the previous section.

Figure 5.8 (right panel) shows the results of the charge collection study and characterization as a function of the voltage bias, always considering $V_A = V_B$ and $V_C = V_D$ in a so-called “planar mode”, done by my student D. Misiak. The purple dots correspond to the fraction of K-shell events with incomplete charge collection, *i.e.* suffering from charge trapping at either the surfaces or in the bulk of the crystal. As expected, the fraction of incomplete charge collection decreases drastically towards high voltage bias thanks to higher electric field mini-

5.3 Overview of recent experimental results

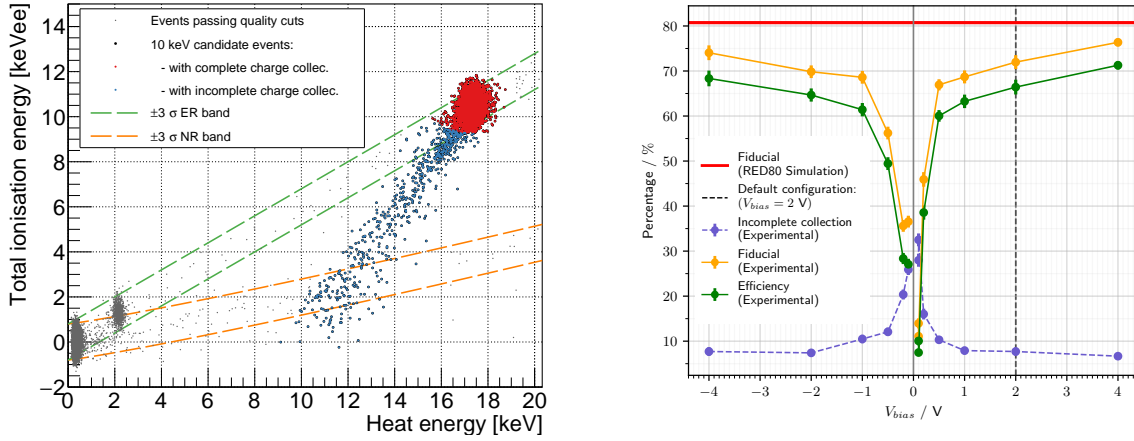


Figure 5.8: **Left:** Event distribution in the total ionisation energy, defined as $(Ei_A + Ei_B + Ei_C + Ei_D)/2$, versus heat energy from a “background” data taking period with a 2 V voltage bias (tg181005). The events shown in grey are passing all the data quality selection cuts, while the black ones are 10.37 keV candidate events with the red (blue) ones exhibiting a complete (incomplete) charge collection. For illustration we also show the $\pm 2\sigma$ ER and NR bands in green and orange dashed lines respectively. **Right:** Measurement of the fraction of: incomplete charge collection (purple), fiducial volume (orange), and combined fiducial and collection efficiency (green), as a function of the voltage bias. The vertical dashed line at 2 V corresponds to the bias voltage used in our neutron calibration and background characterization discussed in Sec. 5.3.4. Figure taken from [228].

mizing the trapping probability. At our baseline 2 V voltage bias we found this fraction to be of $8.0 \pm 0.3\%$. This can be explained by the sum of the 5% “corner volume” (shown in red in Fig. 5.7), exhibiting a low electric field, and some fraction of 7% “guard volume” (shown in orange in Fig. 5.7) where charges can be subject to trapping at the surface. Note that the PL38 design has a “corner volume” of $<1\%$ and minimal Ge bare surface to maximize the charge collection efficiency. Also shown in figure 5.8 (right panel) are the measurements of fiducial volume (orange) and the overall charge collection efficiency (green). The latter is defined as the combination of the fiducial volume and requiring a complete charge collection. The fiducial volume is estimated from the K-shell events exhibiting a full charge collection (red) and by requiring that no veto electrodes (A or C) see a signal 2σ beyond their baseline noise. The measurement of the overall charge collection efficiency is similar to the fiducial one except that it accounts for the efficiency loss from requiring to have simultaneously a full charge collection. The latter is what needs to be considered when estimating the CENNS signal efficiency. As one can see from Fig. 5.8, both the fiducial volume and overall collection efficiency increase with the magnitude of the voltage bias. This is easily explained by the reduced trapping probability discussed before, and the fact that the electron drift gets more and more aligned with the electric field lines at higher voltages. Though we did not work at higher voltages than ± 4 V due to electronics limitations, we can appreciate that our theoretical estimation of the fiducial volume (80.25%) is somewhat compatible with our observations at the highest voltages. Note that for the PL38 and FID38 designs we anticipate, from COMSOL simulations, fiducial volumes of

5.3 Overview of recent experimental results

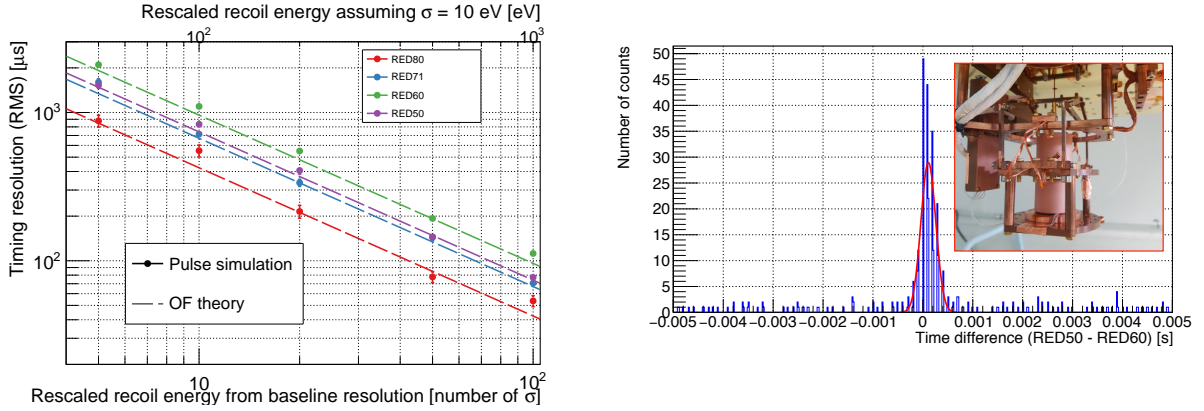


Figure 5.9: **Left:** Timing resolution estimated from optimal filter theory (dashed line), considering the observed noise PSD and measured signal sensitivity, and from pulse simulation (dots), for four different detectors: RED80 (red), RED70 (blue), RED60 (green), and RED50 (purple). **Right:** Time difference from pulses onset between RED50 and RED60 operated simultaneously in the same two-detector suspended tower (see inset). This result was obtained from 63 hours of background data (stream: tc011001), and by selecting events passing the quality cuts and with energies between 500 eV and 10 keV but excluding the ones between 5 keV and 7 keV because of the ^{55}Fe calibration source. Only about 200 events were found in coincidence, *i.e.* within ± 1 ms, with a timing dispersion dispersion of $\sigma_{t_0}^{\text{coinc}} = 150 \mu\text{s}$ (red Gaussian distribution).

99.2% and 70% respectively, see Tab. 4.3.

This compatibility between our theoretical predictions and experimental measurements of both our fiducial volumes and charge collection efficiencies is quite remarkable and gives us confidence in both our experimental and theoretical methodologies at optimizing the ionization performance. The experimental investigations of the two CryoCube candidate designs, PL38 and FID38, will start by the end of 2020 in order to assess their true performance.

5.3.3 Timing resolution

As discussed in Sec. 4.3.1 timing resolution is also a key parameter from our overall detector performance characterization in order to 1) ensure a highly efficient muon-induced background rejection with the muon-veto, 2) fully benefit from the low-energy pulsed DT calibration source in coincidence, and 3) reject backgrounds from event multiplicity among the 27 detectors from the CryoCube array. In the following, we discuss how we estimate the timing resolutions of our detectors with three different approaches.

Figure 5.9 (left panel) shows the timing resolution of four different RED detectors as a function of their re-scaled energies in number of standard deviations from their baseline resolution (bottom x-axis) and re-scaled assuming our targeted energy resolution of 10 eV (top x-axis). For instance, based on its ~ 25 eV heat energy resolution, this figure shows that RED60 has a timing resolution of $100 \mu\text{s}$ at 2.5 keV (100σ). This re-scaling based on the energy resolution allows to extrapolate the resulting timing resolutions to our targeted 10 eV (RMS) heat

5.3 Overview of recent experimental results

energy resolution assuming that the shape of both the signal bandwidth and the noise PSD are conserved. First of all, we can conclude from this figure that both the optimal filter theory, considering the measured signal sensitivity in the frequency domain and noise PSD, and the pulse simulation approaches give similar results. This is an excellent cross check of the NEPAL processing pipeline and gives us confidence in our extracted timing resolutions. Interestingly, we can see that at 5σ (or equivalently 50 eV if $\sigma_E = 10$ eV) the averaged timing resolution from these four RED detectors is of 1.52 ± 0.4 ms which is consistent with the ~ 1 ms predicted CryoCube timing performance considering only the heat channel (see red dashed line in Fig. 4.8).

A third and obvious way of estimating our timing resolution is via a direct measurement. Figure 5.9 (right panel) shows a first attempt at measuring the timing resolution of the RED50 and RED60 detectors that were operated simultaneously in our cryogenic suspended tower (see inset photo). This measurement, shown as the distribution in time difference between adjacent pulse onsets from RED50 and RED60, was performed after 63 hours of background data taking. Both detectors were running in very stable conditions with variations of the energy resolution less than 5% over the entire run. The distribution shown has been derived from selecting only events passing the quality cuts and having energies between 500 eV and 10 keV for both detectors. Due to the presence of the ^{55}Fe calibration source, we excluded the [5, 7] keV energy range from the analysis. We found a total of about 200 events in coincidence, *i.e.* within 1 ms from each other, with a mean energy of 2.1 keV and a timing dispersion (RMS) of about $\sigma_{t_0}^{\text{coinc}} = 150 \mu\text{s}$ (see red Gaussian fit). With 25 eV (RMS) baseline energy resolution, figure 5.9 (left) suggests that we should expect a timing resolution for RED50 and RED60 of about $110 \pm 5 \mu\text{s}$ and $73 \pm 5 \mu\text{s}$ respectively, which combined leads to $\sim 132 \pm 7 \mu\text{s}$ which is consistent with the $150 \mu\text{s}$ dispersion from the measured distribution. Though this validation is extremely valuable, measuring the timing resolution directly with background data and two 30 g-scale detectors is highly inefficient (~ 200 events in 63 hours !). Based on the tremendous importance of properly characterizing the timing resolution of our detectors, we are currently setting up a dedicated calibration method using optical fibers that will emit pulsed and controlled infrared photons from a laser source. This in turn will allow us to measure properly and very efficiently our timing resolution as a function of the deposited energy. It is worth mentioning that these infrared photon calibration and optical fiber design will also be useful to calibrate our detector and neutralize them.

5.3.4 IP2I background characterization

As discussed before, thanks to its particle identification capability the CryoCube Ge detector will be able to reject with a high efficiency the electromagnetic backgrounds, arising from beta-electrons, gammas, and low-energy X-rays, inducing electronic recoils. However, the additional benefit of particle identification also lies in its ability to describe and understand the observed backgrounds. This is particularly important when exploring new low-energy regime where unknown backgrounds may arise. Additionally, being able to characterize and model the backgrounds will ultimately be pivotal in establishing trustworthy likelihood-based analyses of upcoming CENNS data that will be required to reach our targeted precision measurement and test various exotic physics models, see Sec. 3.5. As an illustration of this particle identification capability we propose here to characterize and build a background model associated

5.3 Overview of recent experimental results

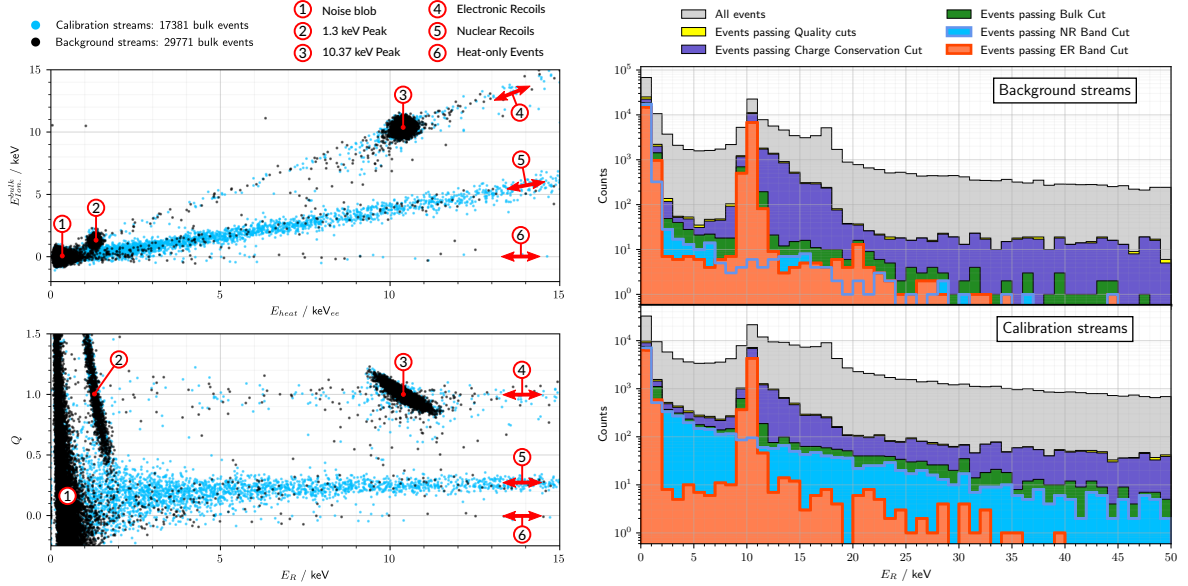


Figure 5.10: **Left:** Comparison of the observed event distributions with RED80 in the fiducial ionisation vs heat energy (top) and ionization yield vs recoil energy (bottom), with (blue) and without (black) the AmBe neutron source 4.5 m from the cryostat. **Right:** Recoil energy distribution of the observed events passing the different selection cuts with (bottom) and without (top) the AmBe neutron calibration source. Nuclear and electronic recoils, passing all the quality selection cuts, are shown as the cyan and orange histograms respectively. Figures taken from [228].

to our IP2I cryogenic facility. To do so, we first discuss our recent neutron calibration and neutron/gamma background measurements with RED80 and then compile the observed background energy spectra from 5 different RED detectors, including RED30 operated at LSM in the ultra-low background EDELWEISS setup [144].

Figure 5.10 (left panel) compares the observed event distributions following a cumulated 52.9 hours of background data (black dots) and a cumulated 76 hours of neutron calibration (blue dots). These event distributions are shown in the fiducial ionization against heat energy (top panel) and ionization yield against recoil energy (bottom panel). We can clearly see the K- and L-shell lines at respectively 10.37 keV and 1.3 keV and three types of populations: heat only, electronic recoils (to which belong the K/L lines), and nuclear recoils. The presence of the latter is considerably magnified during the neutron calibration where a strong population of events with an ionization yield of about $Q \approx 0.2$ is clearly visible. The neutron calibration was done with an AmBe source emitting a 6×10^5 neutron/s and placed 4.5 m away from the cryostat (with the Pb shield still in place). Right panel of Fig. 5.10 shows the resulting recoil energy distributions of both data sets, background measurement (top) and neutron calibration (bottom), following the successive application of selection cuts. The nuclear and electronic recoil candidates are shown as the cyan and orange histograms respectively. Here again, one can clearly appreciate the significant increase in the nuclear recoil population when the AmBe source is deployed, while the electronic recoil population stays roughly constant. It should be noted that

5.3 Overview of recent experimental results

10 cm of lead bricks were positioned in front of the AmBe source in order to maximize the attenuation of the emitted high energy gammas. After correcting for the selection cut efficiencies, the detector livetime and correcting for the event leakages at low energies, my student D. Misiak has been able to measure the neutron and gamma backgrounds in our cryostat to be of $(1.3 \pm 0.3) \times 10^4$ event/kg/keV/day and $(3 \pm 0.6) \times 10^3$ event/kg/keV/day between 2 and 3 keV [228]. As this was our first attempt at performing such analysis above-ground, we ended up with a rather large systematic uncertainties of about 20% due to the lack of statistics from the data but also from the pulse simulation data sets, used to estimate the analysis efficiencies [228]. We plan on doing this measurement with the future FID38 and PL38 with an improved set up: lower neutron activation of the Ge crystal, smaller processing time windows, longer acquisition times, and an improved pulse simulation approach.

Eventually, in figure 5.11 we show a compilation of all our low-energy background measurements achieved with various RED detectors operated at IP2I: RED20 (red), RED50 (blue), RED60 (green), RED70 (purple), and RED80 (orange dashed/solid lines corresponding to ER/NR), and RED30 (yellow) operated in Modane at 78 V. Additionally, we show as black dashed and solid lines/contours, the Geant4/CRY estimations of ER and NR cosmogenic backgrounds expected in our IP2I setup considering the ~ 2 ton lead shield with an approximate 70% solid angle coverage. There are a few conclusions that can be inferred from this background compilation measurements that we discuss hereafter:

A consistent low-energy background measurement: All RED detectors converge towards a similar low-energy background level of about 4,000 DRU at 10 keV and 20,000 DRU at 1 keV with a strong rise at the lowest energies further discussed below. This is particularly interesting because they were all operated and analysed in different conditions. For instance, the calibration methods were not always the same: ^{55}Fe for RED20, RED50, and RED60, and ^{71}Ge activation for RED80 and RED70, the length of the time traces were also different varying from 2 to 0.5 s, and the resolutions also had some dispersion (see Tab. 5.1). Lastly, note that some of the measurements here were done with low statistics, such as RED50, RED60 and RED70, with less than a 24 hours of exposition time.

A dominating neutron background below 5 keV: Thanks to the RED80 particle identification capability, though it was limited to roughly 2 keV due to the JFET-based electronics limitations, we were able to identify the origin of our observed rise in our background level starting at ~ 5 keV. Indeed, we found that the environmental neutron background starts to become important at these energies and actually dominates the gamma background by about a factor 4-to-5 at 2 keV. Interestingly, this measurement and observation is supported by our cosmogenic background simulation suggesting that the neutron background is indeed expected to dominate significantly over the gamma background at low-energies. Note however that a $\sim 20\%$ systematic uncertainties should be attributed to these simulation results based on the uncertainties on the exact geometry of the IP2I building. In addition, it should be noted that the ambient radiogenic component is not simulated here. The latter is expected to be mostly producing gammas, from the U/K/Th chains from the surrounding concrete and cryostat materials, which are only partly shielded thanks to our 70% coverage 10 cm thick lead shield.

A strong sub-keV background component: As one can see from this background measurement compilation, all detectors indicate the presence of a strong background component arising at the lowest energies. Unfortunately, due to the ~ 190 eV fiducial ionization energy achievable

5.3 Overview of recent experimental results

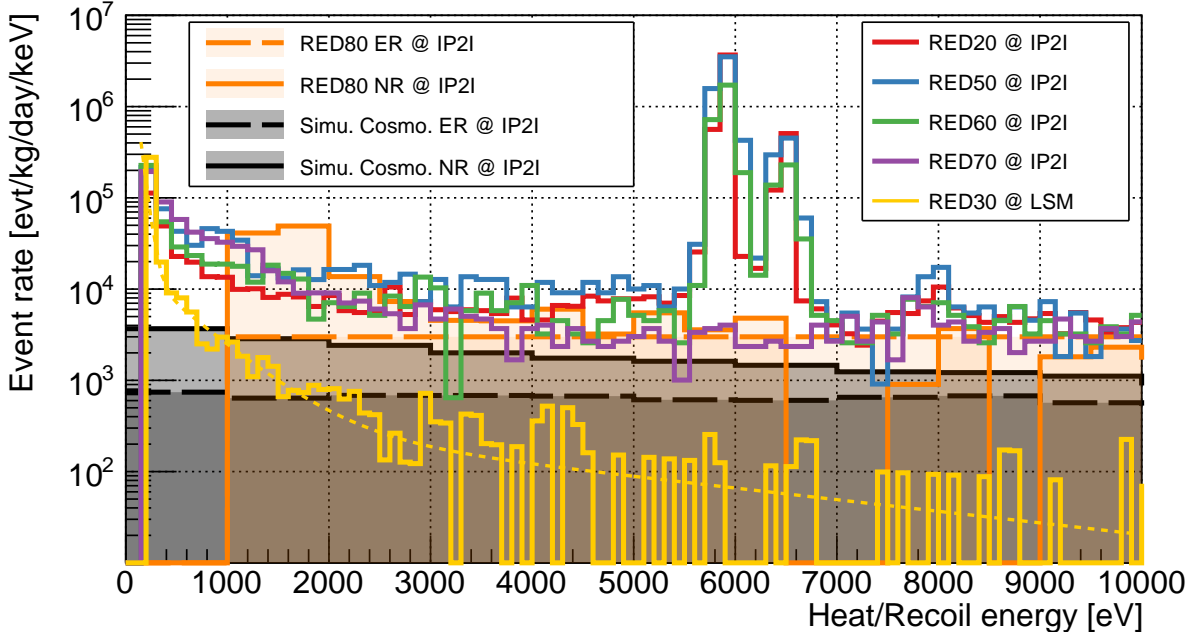


Figure 5.11: Compilation of background energy distributions measured with various RED detectors operated at IP2I: RED20 (red), RED50 (blue), RED60 (green), RED70 (purple), and RED80 (orange dashed/solid for ER/NR), within the ultra-low background environment from the EDELWEISS setup at LSM (with RED30 (yellow)), compared with cosmogenic Geant4/CRY-based simulations of our cryogenic facility (black dashed/solid for ER/NR).

with our current electronics, we can't further investigate the origin of these events below 1 keV. However, we recently operated a RED detector in Modane equipped with grid electrodes, allowing for a direct NTD contact with the Ge surface, to further investigate the topology of these events. RED30 was then operated at different voltage biases from 0 V up to 78 V in order to study the difference in the low-energy spectrum shape. Indeed, in the presence of non-zero ionization associated with these events, we would have expected the shape to become shallower by increasing the voltage. On the contrary, we saw no evidence of change of slope with the voltage bias. Though indirect and likely not sufficient to state that all these events are non-ionizing, this ensemble of measurements suggests that at least a dominating fraction of these events have $Q = 0$, hence their "Heat Only" name. The RED30 spectrum measured at 78 V is shown in figure 5.11 as the yellow histogram and the yellow dashed line is the HO background model used in our previous CryoCube sensitivity studies (see Sec. 4.3). Its level, which seems independent of the operating facility reaches 10^6 DRU at 100 eV and 10^5 DRU at 200 eV, and is our leading background component below 1 keV. This yet-to-be-explained background represents a tremendous threat to many ongoing and upcoming low-threshold Dark Matter and CENNS experiments as it may very well overwhelm the putative targeted signals. Indeed, the RED detectors are far from being the only ones suffering from it as similar background levels of 10^8 DRU at 20 eV and of 10^6 DRU at 100 eV have been observed by the NuCLEUS-0.5g Al_2O_3 [92] and CDMS-10g Si [246] detector prototypes. Within EDELWEISS, active techniques to reject this background are being investigated and depending on their efficiency, they could be added to the

future CryoCube detectors. It is worth noticing that this new background has been observed by many cryogenic experiments over the globe, using different sensing techniques and at different cryogenic facilities, ever since all these groups and teams have been able to lower sufficiently their detector thresholds. This suggests two important facts: 1) maybe this background is actually a signal from some kind of dark radiations [236], 2) it highlights the pivotal benefit of particle identification when exploring new energy ranges. Indeed, in the CryoCube case we expect to fully reject this HO background, thanks to the 20 eVee (RMS) resolution ionization channel, at about 250 eV (see Sec. 4.3). Of course if this background is not mitigated beforehand we would lose a significant fraction of the CENNS signal, damaging the new physics reach of RICOCHET, but we won't be totally blinded.

5.3.5 Low-noise HEMT-based electronics

As it has been said multiple times throughout this document, our ionization (and to a lower extent heat) energy resolution is limited by the intrinsic noise of the Si-JFET transistors commonly used for high impedance amplifiers. As further discussed below, High Electron Mobility Transistor (HEMT) as uniquely produced by the CNRS/C2N, are an excellent alternative to the Si-JFET. HEMTs are based on a 2-Dimensional Electron Gas (2DEG) realized in a Al-GaAs/GaAs hetero-structure with a high purity material interface [250]. As the Fermi level of the 2DEG is within the conduction band, unlike Si-JFETs whose conducting channel freezes out at low temperature, the 2DEG of the HEMT is formed even at 0 K [250]. Therefore, the HEMT can be placed much closer to the 10 mK detectors as they do not require any external heating and dissipate significantly less power $\mathcal{O}(10) \mu\text{W}$ than Si-JFET $\mathcal{O}(1) \text{mW}$. Closer proximity to the detector reduces the two dominant performance limitations of amplifiers for high impedance sensors, *e.g* NTD and electrodes, which are: stray capacitance and microphonics susceptibility.

The CNRS/C2N produces high-impedance dedicated HEMT with five different geometries, determined by the gate lengths and widths, with the following input capacitance C_{gs} of 230 pF, 100 pF, 30 pF, 5 pF, and 2 pF. Figure 5.12 (left and middle panels) presents the characterization of the noise performance, in terms of voltage (e_n) and current (i_n) noise, of these 5 HEMT geometries done at C2N. Each of these measurements were done with a fixed 100 μW dissipation power ($I_{ds} = 1 \text{mA}$, $V_{ds} = 100 \text{mV}$) at 4.2 K. Voltage noises are compared to the very best commercially available Si-JFET from InterFET which can have noise as low as 0.3-2 nV/ $\sqrt{\text{Hz}}$ down to 1 Hz depending on their input capacitance. As seen in Fig. 5.12, HEMTs from CNRS/C2N exhibit better or similar white noise performance to comparable Si-JFETs from Interfet, although the 1/f knee occurs at higher frequency. For all gate geometries, the voltage noise is well-fit by a $1/\sqrt{f}$ term and a white noise term as in previous work [251, 252]. The noise magnitude varies as $\sqrt{C_{gs}}$.

Typical HEMTs suffer from poor 1/f noise up to several MHz. In this regard, the voltage noise performance of the CNRS/C2N HEMTs is greatly improved. For high impedance sensors (*i.e.* ionization), however, the main advantage comes from their ultra-low current noise. The current noise contribution of Si-JFETs is often considered negligible, however Fig. 5.12 clearly shows that the noise contribution is actually comparable to its white noise for input impedance above 10 M Ω . This also confirms the results from Sec. 4.2.3 where we presented the expected ionization performance of a PL38 detector design with a JFET-based electronics and where the

5.3 Overview of recent experimental results

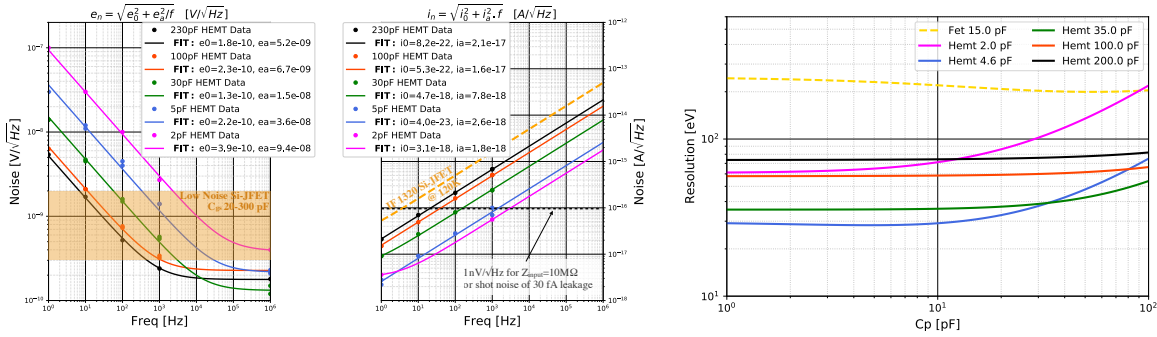


Figure 5.12: **Left and middle:** Voltage and current noise of the 5 HEMT geometries studied at 4.2 K and 100 μ W at C2N [251]. Brown area illustrates the best voltage noise achieved by Si-JFET. Current noise of the IF1320 from InterFET studied at 120 K (data from [80]) is also plotted for comparison. Black dashed line at 10^{-16} A/ \sqrt{Hz} is equivalent to the shot noise induced by a 30 fA leakage current and would give a 1 nV/ \sqrt{Hz} voltage noise for a 10 M Ω input impedance. **Right:** Evolution of the ionization resolution with the cabling capacitance for the 5 HEMT geometries and the IF1320 Si-JFET from InterFET for comparison. We assumed a PL38 detector design, with the two electrodes floating, and the readout scheme from Fig. 4.6. Figures taken from [147].

current noise was found to be the limiting factor.

Figure 5.12 (right panel) shows the evolution of the resolution for one of the two PL38 ionization channel as a function of the cabling capacitance. We considered here the same electronic scheme as presented in Fig. 4.6 with a 10 G Ω bias resistor heat sunk at 10 mK. This figure clearly suggests that the 5-pF input capacitance HEMT is our optimal choice to reach the lowest ionization resolution. The latter is found to be about 27 eVee (RMS) per channel, with 5 pF cabling capacitance, leading to a \sim 20 eVee (RMS) fiducial ionization resolution from combing the two ionization channels together. Similarly than for the ionization readout, we found that 200-pF HEMT are the optimal choice for the heat NTD-based readout, as they offer the best compromise between voltage and current noise, when operated at around 20 M Ω (see Sec. 4.1).

With the beginning of J.-B. Filippini’s thesis in 2019, under the supervision of A. Juillard, a dedicated HEMT characterization bench at IP2I has been developed. Its goal is threefold: 1) to be able to reproduce the ultra-low noise performance as performed by the C2N and confirm their voltage and current noise HEMT measurements, 2) study the HEMT behavior at lower temperatures, *i.e.* down to 1 K as feasible in a dilution cryostat, and 3) develop some first heat and ionization HEMT-based preamplifier prototypes. Figure 5.13 shows some noise PSD measurements for 4 5-pF HEMT (left panel) and 2 200-pF HEMT (right panel). These measurements are also compared with the corresponding HEMT models extracted from the C2N measurements shown in Fig. 5.12 (left panel). As one can derive from these results, we find an excellent agreement between our measurements and the ones performed by the C2N. It seems also that the HEMT under consideration here are slightly less noisier than suggested by the C2N measurements which were done on other similar HEMTs. This suggests that there is some dispersion in the noise performance of each HEMT and that characterizing them all before their

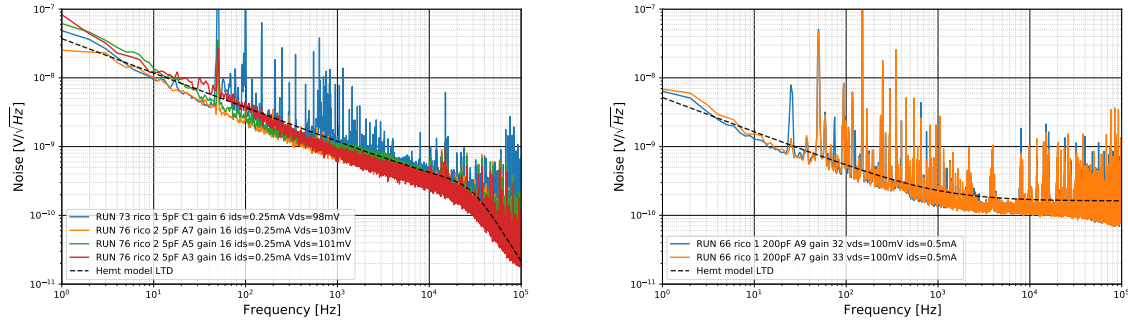


Figure 5.13: Compilation of noise PSD measurements with various 5-pF (**left**) and 200-pF (**right**) HEMT done at IP2I in our dedicated test bench. All measurements were performed at 1 K, with a 50 Ω input resistor, a 1 k Ω resistor on the drain, and a SR5184 amplifier (gain of 1000) followed by a SR560 amplifier and filter (low-pass at 30 kHz - only for the 5-pF HEMT) acquired by a NI6218 digitizer. In both panels, the black dashed line represent the 5- and 200-pF HEMT voltage noise model from Fig. 5.12 (left panel). *Courtesy of J.-B. Filippini.*

integration in the CryoCube electronics might be highly beneficial in only selecting the best ones. To that end, we recently developed a fully automated 10 channels HEMT test bench which will allow us to “cherry pick” the best ones in order to reach the best possible energy resolutions.

Nowadays, the French side of the RICOCHET collaboration has gathered a team of about 6 engineers from Institut Néel, IP2I and LPSC working on designing these future low-noise HEMT-based heat and ionization preamplifiers to readout the 150 channels from the CryoCube detector array.

5.4 Conclusions

Over the past few years, considerable efforts have been dedicated in improving the cryogenic test facility that started in 2015 with the acquisition of the CryoConcept cryostat thanks to the LabEx LIO. Our detector prototypes are now operated in optimal conditions, *i.e.* in an ultra-low vibration and noise environment with low energy calibration sources and with efficient data processing and monitoring pipelines. We achieved an averaged 22 eV (RMS) heat energy resolution on five bolometers with hints that it may be further improved with a dedicated HEMT readout characterized by a much lower intrinsic current noise. We have also developed an experimental procedure to characterize the ionization performance, *i.e.* resolutions and charge collection, of our newly designed PL38 and FID38 detector prototypes. Using three different approaches, we found an averaged timing resolution of about 1 ms at $5\sigma_E$ as was theoretically predicted from our electro-thermal model. Based on all these results, we were able to derive a first complete IP2I background model which will help us at calibrating our RICOCHET simulations and optimize our upcoming RICOCHET at IP2I setup. Our low-energy understanding of the observed background clearly shows that it is for now limited by our ~ 200 eVee (RMS) fiducial ionization resolution achieved with the JFET electronics, especially in studying the low-energy rise (so-called heat only). To that end, the development of our next generation low-noise HEMT-based

5.4 Conclusions

electronics is our top priority and first results from our dedicated HEMT characterization bench are promising.

Bibliography

- [1] J. Billard et al., *Direct Detection of Dark Matter – APPEC Committee Report*, [arXiv:2104.07634](#).
- [2] G. Bertone and D. Hooper, *History of dark matter*, *Rev. Mod. Phys.* **90** (2018), no. 4 045002, [[arXiv:1605.04909](#)].
- [3] F. Zwicky, *On the Masses of Nebulae and of Clusters of Nebulae*, *Astrophys. J.* **86** (1937) 217–246.
- [4] A. H. Gonzalez, S. Sivanandam, A. I. Zabludoff, and D. Zaritsky, *Galaxy Cluster Baryon Fractions Revisited*, *Astrophys. J.* **778** (2013) 14, [[arXiv:1309.3565](#)].
- [5] J. A. Tyson, G. P. Kochanski, and I. P. Dell’Antonio, *Detailed mass map of CL0024+1654 from strong lensing*, *Astrophys. J.* **498** (1998) L107, [[astro-ph/9801193](#)].
- [6] J. A. Holtzman, *Microwave background anisotropies and large scale structure in universes with cold dark matter, baryons, radiation, and massive and massless neutrinos*, *Astrophys. J. Suppl.* **71** (1989) 1–24.
- [7] **Planck** Collaboration, N. Aghanim et al., *Planck 2018 results. VI. Cosmological parameters*, *Astron. Astrophys.* **641** (2020) A6, [[arXiv:1807.06209](#)].
- [8] **Particle Data Group** Collaboration, M. Tanabashi et al., *Review of Particle Physics*, *Phys. Rev.* **D98** (2018), no. 3 030001.
- [9] J. I. Read, *The Local Dark Matter Density*, *J. Phys.* **G41** (2014) 063101, [[arXiv:1404.1938](#)].
- [10] Y. Sofue, *Rotation Curve of the Milky Way and the Dark Matter Density*, *arXiv e-prints* (Apr., 2020) arXiv:2004.11688, [[arXiv:2004.11688](#)].
- [11] V. Springel, C. S. Frenk, and S. D. M. White, *The large-scale structure of the Universe*, *Nature* **440** (2006) 1137, [[astro-ph/0604561](#)].
- [12] V. Iršič et al., *New Constraints on the free-streaming of warm dark matter from intermediate and small scale Lyman- α forest data*, *Phys. Rev. D* **96** (2017), no. 2 023522, [[arXiv:1702.01764](#)].

- [13] M. Viel, J. Lesgourgues, M. G. Haehnelt, S. Matarrese, and A. Riotto, *Constraining warm dark matter candidates including sterile neutrinos and light gravitinos with WMAP and the Lyman-alpha forest*, *Phys. Rev. D* **71** (2005) 063534, [[astro-ph/0501562](#)].
- [14] S. Tulin and H.-B. Yu, *Dark Matter Self-interactions and Small Scale Structure*, *Phys. Rept.* **730** (2018) 1–57, [[arXiv:1705.02358](#)].
- [15] B. Audren, J. Lesgourgues, G. Mangano, P. D. Serpico, and T. Tram, *Strongest model-independent bound on the lifetime of Dark Matter*, *JCAP* **1412** (2014) 028, [[arXiv:1407.2418](#)].
- [16] M. Safarzadeh and D. N. Spergel, *Ultra-light Dark Matter is Incompatible with the Milky Way's Dwarf Satellites*, [arXiv:1906.11848](#).
- [17] M. Lisanti, *Lectures on Dark Matter Physics*, in *Theoretical Advanced Study Institute in Elementary Particle Physics: New Frontiers in Fields and Strings*, pp. 399–446, 2017. [arXiv:1603.03797](#).
- [18] J. L. Feng and J. Kumar, *The WIMPlless Miracle: Dark-Matter Particles without Weak-Scale Masses or Weak Interactions*, *Phys. Rev. Lett.* **101** (2008) 231301, [[arXiv:0803.4196](#)].
- [19] S. Profumo, *Astrophysical Probes of Dark Matter*, in *Proceedings, Theoretical Advanced Study Institute in Elementary Particle Physics: Searching for New Physics at Small and Large Scales (TASI 2012): Boulder, Colorado, June 4-29, 2012*, pp. 143–189, 2013. [arXiv:1301.0952](#).
- [20] H. Baer, K.-Y. Choi, J. E. Kim, and L. Roszkowski, *Dark matter production in the early Universe: beyond the thermal WIMP paradigm*, *Phys. Rept.* **555** (2015) 1–60, [[arXiv:1407.0017](#)].
- [21] E. W. Kolb and M. S. Turner, *The Early Universe*, *Front. Phys.* **69** (1990) 1–547.
- [22] L. Roszkowski, E. M. Sessolo, and S. Trojanowski, *WIMP dark matter candidates and searches â current status and future prospects*, *Rept. Prog. Phys.* **81** (2018), no. 6 066201, [[arXiv:1707.06277](#)].
- [23] G. Arcadi, A. Djouadi, and M. Raidal, *Dark Matter through the Higgs portal*, *Phys. Rept.* **842** (2020) 1–180, [[arXiv:1903.03616](#)].
- [24] **XENON** Collaboration, E. Aprile et al., *Light Dark Matter Search with Ionization Signals in XENON1T*, *Phys. Rev. Lett.* **123** (2019), no. 25 251801, [[arXiv:1907.11485](#)].
- [25] **SENSEI** Collaboration, L. Barak et al., *SENSEI: Direct-Detection Results on sub-GeV Dark Matter from a New Skipper-CCD*, [arXiv:2004.11378](#).
- [26] M. L. Graesser, I. M. Shoemaker, and L. Vecchi, *Asymmetric WIMP dark matter*, *JHEP* **10** (2011) 110, [[arXiv:1103.2771](#)].

- [27] H. Iminniyaz, M. Drees, and X. Chen, *Relic Abundance of Asymmetric Dark Matter*, *JCAP* **1107** (2011) 003, [[arXiv:1104.5548](#)].
- [28] K. Petraki and R. R. Volkas, *Review of asymmetric dark matter*, *Int. J. Mod. Phys. A* **28** (2013) 1330028, [[arXiv:1305.4939](#)].
- [29] K. M. Zurek, *Asymmetric Dark Matter: Theories, Signatures, and Constraints*, *Phys. Rept.* **537** (2014) 91–121, [[arXiv:1308.0338](#)].
- [30] L. J. Hall, K. Jedamzik, J. March-Russell, and S. M. West, *Freeze-In Production of FIMP Dark Matter*, *JHEP* **1003** (2010) 080, [[arXiv:0911.1120](#)].
- [31] N. Bernal, M. Heikinheimo, T. Tenkanen, K. Tuominen, and V. Vaskonen, *The Dawn of FIMP Dark Matter: A Review of Models and Constraints*, *Int. J. Mod. Phys. A* **32** (2017), no. 27 1730023, [[arXiv:1706.07442](#)].
- [32] A. Boyarsky, M. Drewes, T. Lasserre, S. Mertens, and O. Ruchayskiy, *Sterile Neutrino Dark Matter*, *Prog. Part. Nucl. Phys.* **104** (2019) 1–45, [[arXiv:1807.07938](#)].
- [33] R. D. Peccei and H. R. Quinn, *CP conservation in the presence of pseudoparticles*, *Phys. Rev. Lett.* **38** (Jun, 1977) 1440–1443.
- [34] R. D. Peccei and H. R. Quinn, *Constraints imposed by CP conservation in the presence of pseudoparticles*, *Phys. Rev. D* **16** (Sep, 1977) 1791–1797.
- [35] S. Weinberg, *A new light boson?*, *Phys. Rev. Lett.* **40** (Jan, 1978) 223–226.
- [36] F. Wilczek, *Problem of strong p and t invariance in the presence of instantons*, *Phys. Rev. Lett.* **40** (Jan, 1978) 279–282.
- [37] P. Svrcek and E. Witten, *Axions In String Theory*, *JHEP* **06** (2006) 051, [[hep-th/0605206](#)].
- [38] M. Goodsell, J. Jaeckel, J. Redondo, and A. Ringwald, *Naturally Light Hidden Photons in LARGE Volume String Compactifications*, *JHEP* **11** (2009) 027, [[arXiv:0909.0515](#)].
- [39] J. Preskill, M. B. Wise, and F. Wilczek, *Cosmology of the invisible axion*, *Physics Letters B* **120** (1983), no. 1 127 – 132.
- [40] L. Abbott and P. Sikivie, *A cosmological bound on the invisible axion*, *Physics Letters B* **120** (1983), no. 1 133 – 136.
- [41] M. Dine and W. Fischler, *The not-so-harmless axion*, *Physics Letters B* **120** (1983), no. 1 137 – 141.
- [42] G. F. Chapline, *Cosmological effects of primordial black holes*, *Nature* **253** (1975), no. 5489 251–252.
- [43] S. Bird et al., *Did LIGO detect dark matter?*, *Phys. Rev. Lett.* **116** (2016), no. 20 201301, [[arXiv:1603.00464](#)].

- [44] M. Sasaki, T. Suyama, T. Tanaka, and S. Yokoyama, *Primordial Black Hole Scenario for the Gravitational-Wave Event GW150914*, *Phys. Rev. Lett.* **117** (2016), no. 6 061101, [[arXiv:1603.08338](#)]. [erratum: *Phys. Rev. Lett.* 121,no.5,059901(2018)].
- [45] B. Carr, F. Kuhnel, and M. Sandstad, *Primordial Black Holes as Dark Matter*, *Phys. Rev.* **D94** (2016), no. 8 083504, [[arXiv:1607.06077](#)].
- [46] M. Sasaki, T. Suyama, T. Tanaka, and S. Yokoyama, *Primordial black holes—perspectives in gravitational wave astronomy*, *Class. Quant. Grav.* **35** (2018), no. 6 063001, [[arXiv:1801.05235](#)].
- [47] B. Carr, K. Kohri, Y. Sendouda, and J. Yokoyama, *Constraints on Primordial Black Holes*, [arXiv:2002.12778](#).
- [48] M. Milgrom, *A Modification of the Newtonian dynamics as a possible alternative to the hidden mass hypothesis*, *Astrophys. J.* **270** (1983) 365–370.
- [49] J. D. Bekenstein, *Relativistic gravitation theory for the MOND paradigm*, *Phys. Rev.* **D70** (2004) 083509, [[astro-ph/0403694](#)]. [Erratum: *Phys. Rev.* D71,069901(2005)].
- [50] C. Skordis, D. F. Mota, P. G. Ferreira, and C. Boehm, *Large Scale Structure in Bekenstein’s theory of relativistic Modified Newtonian Dynamics*, *Phys. Rev. Lett.* **96** (2006) 011301, [[astro-ph/0505519](#)].
- [51] S. Boran, S. Desai, E. O. Kahya, and R. P. Woodard, *GW170817 Falsifies Dark Matter Emulators*, *Phys. Rev.* **D97** (2018), no. 4 041501, [[arXiv:1710.06168](#)].
- [52] D. Clowe, A. Gonzalez, and M. Markevitch, *Weak lensing mass reconstruction of the interacting cluster 1E0657-558: Direct evidence for the existence of dark matter*, *Astrophys. J.* **604** (2004) 596–603, [[astro-ph/0312273](#)].
- [53] M. W. Goodman and E. Witten, *Detectability of Certain Dark Matter Candidates*, *Phys. Rev.* **D31** (1985) 3059. [,325(1984)].
- [54] J. D. Lewin and P. F. Smith, *Review of mathematics, numerical factors, and corrections for dark matter experiments based on elastic nuclear recoil*, *Astropart. Phys.* **6** (1996) 87–112.
- [55] A. K. Drukier, K. Freese, and D. N. Spergel, *Detecting Cold Dark Matter Candidates*, *Phys. Rev.* **D33** (1986) 3495–3508.
- [56] K. Freese et al., *Signal modulation in cold-dark-matter detection*, *Phys. Rev. D* **37** (1988) 3388.
- [57] K. Freese et al., *Colloquium: Annual modulation of dark matter*, *Rev. Mod. Phys.* **85** (2013) 1561, [[arXiv:1209.3339](#)].
- [58] D. N. Spergel, *The Motion of the Earth and the Detection of Wimps*, *Phys. Rev.* **D37** (1988) 1353.

- [59] F. Mayet et al., *A review of the discovery reach of directional Dark Matter detection*, *Phys. Rept.* **627** (2016) 1–49, [[arXiv:1602.03781](#)].
- [60] J. Engel, S. Pittel, and P. Vogel, *Nuclear physics of dark matter detection*, *Int. J. Mod. Phys.* **E1** (1992) 1–37.
- [61] P. Toivanen, M. Kortelainen, J. Suhonen, and J. Toivanen, *Large-scale shell-model calculations of elastic and inelastic scattering rates of lightest supersymmetric particles (LSP) on I-127, Xe-129, Xe-131, and Cs-133 nuclei*, *Phys. Rev.* **C79** (2009) 044302.
- [62] J. Menendez, D. Gazit, and A. Schwenk, *Spin-dependent WIMP scattering off nuclei*, *Phys. Rev.* **D86** (2012) 103511, [[arXiv:1208.1094](#)].
- [63] J. Fan, M. Reece, and L.-T. Wang, *Non-relativistic effective theory of dark matter direct detection*, *JCAP* **1011** (2010) 042, [[arXiv:1008.1591](#)].
- [64] A. L. Fitzpatrick et al., *The Effective Field Theory of Dark Matter Direct Detection*, *JCAP* **1302** (2013) 004, [[arXiv:1203.3542](#)].
- [65] M. Hoferichter, P. Klos, J. Menendez, and A. Schwenk, *Analysis strategies for general spin-independent WIMP-nucleus scattering*, *Phys. Rev.* **D94** (2016), no. 6 063505, [[arXiv:1605.08043](#)].
- [66] **XENON** Collaboration, E. Aprile et al., *Effective field theory search for high-energy nuclear recoils using the XENON100 dark matter detector*, *Phys. Rev.* **D96** (2017), no. 4 042004, [[arXiv:1705.02614](#)].
- [67] **CRESST** Collaboration, G. Angloher et al., *Limits on Dark Matter Effective Field Theory Parameters with CRESST-II*, *Eur. Phys. J.* **C79** (2019), no. 1 43, [[arXiv:1809.03753](#)].
- [68] D. Tucker-Smith and N. Weiner, *Inelastic dark matter*, *Phys. Rev.* **D64** (2001) 043502, [[hep-ph/0101138](#)].
- [69] **DAMA** Collaboration, R. Bernabei et al., *First Model Independent Results from DAMA/LIBRA Phase2*, *Universe* **4** (2018), no. 11 116, [[arXiv:1805.10486](#)]. [Nucl. Phys. Atom. Energy19,no.4,307(2018)].
- [70] **COSINE** Collaboration, G. Adhikari et al., *An experiment to search for dark matter interactions using sodium iodide detectors*, *Nature* **564** (2018) 83, [[1906.01791](#)].
- [71] **COSINE** Collaboration, G. Adhikari et al., *Search for a Dark Matter-Induced Annual Modulation Signal in NaI(Tl) with the COSINE-100 Experiment*, *Phys. Rev. Lett.* **123** (2019) 031302, [[arXiv:1903.10098](#)].
- [72] **ANAIS** Collaboration, J. Amaré et al., *First Results on Dark Matter Annual Modulation from the ANAIS-112 Experiment*, *Phys. Rev. Lett.* **123** (2019) 031301, [[arXiv:1903.03973](#)].

- [73] **ANAIS** Collaboration, M. L. Sarsa et al., *ANAIS-112 status: two years results on annual modulation*, *J. Phys.: Conf. Ser.* **1468** (2020) 012014, [[arXiv:1910.13365](#)].
- [74] M. Schumann, *Direct Detection of WIMP Dark Matter: Concepts and Status*, *J. Phys.* **G46** (2019), no. 10 103003, [[arXiv:1903.03026](#)].
- [75] **CDEX** Collaboration, H. Jiang et al., *Limits on Light Weakly Interacting Massive Particles from the First 102.8 kg \times day Data of the CDEX-10 Experiment*, *Phys. Rev. Lett.* **120** (2018), no. 24 241301, [[arXiv:1802.09016](#)].
- [76] **CoGeNT** Collaboration, C. E. Aalseth et al., *CoGeNT: A Search for Low-Mass Dark Matter using p-type Point Contact Germanium Detectors*, *Phys. Rev. D* **88** (2013) 012002, [[arXiv:1208.5737](#)].
- [77] **DAMIC** Collaboration, A. Aguilar-Arevalo et al., *Results on low-mass weakly interacting massive particles from a 11 kg d target exposure of DAMIC at SNOLAB*, [arXiv:2007.15622](#).
- [78] **CRESST** Collaboration, A. H. Abdelhameed et al., *First results from the CRESST-III low-mass dark matter program*, *Phys. Rev.* **D100** (2019), no. 10 102002, [[arXiv:1904.00498](#)].
- [79] **SuperCDMS** Collaboration, R. Agnese et al., *Demonstration of Surface Electron Rejection with Interleaved Germanium Detectors for Dark Matter Searches*, *Appl. Phys. Lett.* **103** (2013) 164105, [[arXiv:1305.2405](#)].
- [80] **EDELWEISS** Collaboration, E. Armengaud et al., *Performance of the EDELWEISS-III experiment for direct dark matter searches*, *JINST* **12** (2017), no. 08 P08010, [[arXiv:1706.01070](#)].
- [81] **DEAP-3600** Collaboration, R. Ajaj et al., *Search for dark matter with a 231-day exposure of liquid argon using DEAP-3600 at SNOLAB*, *Phys. Rev. D* **100** (July, 2019) 022004.
- [82] E. Aprile et al., *Simultaneous measurement of ionization and scintillation from nuclear recoils in liquid xenon as target for a dark matter experiment*, *Phys. Rev. Lett.* **97** (2006) 081302, [[astro-ph/0601552](#)].
- [83] **XENON** Collaboration, E. Aprile et al., *Search for Light Dark Matter Interactions Enhanced by the Migdal effect or Bremsstrahlung in XENONIT*, *Phys. Rev. Lett.* **123** (2019), no. 24 241803, [[arXiv:1907.12771](#)].
- [84] **PandaX-II** Collaboration, X. Cui et al., *Dark Matter Results From 54-Ton-Day Exposure of PandaX-II Experiment*, *Phys. Rev. Lett.* **119** (2017), no. 18 181302, [[arXiv:1708.06917](#)].
- [85] **LUX** Collaboration, D. Akerib et al., *Results from a search for dark matter in the complete LUX exposure*, *Phys. Rev. Lett.* **118** (2017), no. 2 021303, [[arXiv:1608.07648](#)].

- [86] **DarkSide** Collaboration, P. Agnes et al., *Low-Mass Dark Matter Search with the DarkSide-50 Experiment*, *Phys. Rev. Lett.* **121** (Aug., 2018) 081307.
- [87] M. Ibe, W. Nakano, Y. Shoji, and K. Suzuki, *Migdal Effect in Dark Matter Direct Detection Experiments*, *JHEP* **03** (2018) 194, [[arXiv:1707.07258](#)].
- [88] J. Billard, L. Strigari, and E. Figueroa-Feliciano, *Implication of neutrino backgrounds on the reach of next generation dark matter direct detection experiments*, *Phys. Rev.* **D89** (2014), no. 2 023524, [[arXiv:1307.5458](#)].
- [89] F. Ruppin, J. Billard, E. Figueroa-Feliciano, and L. Strigari, *Complementarity of dark matter detectors in light of the neutrino background*, *Phys. Rev. D* **90** (2014), no. 8 083510, [[arXiv:1408.3581](#)].
- [90] **CDEX** Collaboration, Z. Z. Liu et al., *Constraints on Spin-Independent Nucleus Scattering with sub-GeV Weakly Interacting Massive Particle Dark Matter from the CDEX-1B Experiment at the China Jinping Underground Laboratory*, *Phys. Rev. Lett.* **123** (2019), no. 16 161301, [[arXiv:1905.00354](#)].
- [91] **SuperCDMS** Collaboration, R. Agnese et al., *Search for Low-Mass Dark Matter with CDMSlite Using a Profile Likelihood Fit*, *Phys. Rev.* **D99** (2019), no. 6 062001, [[arXiv:1808.09098](#)].
- [92] **CRESST** Collaboration, G. Angloher et al., *Results on MeV-scale dark matter from a gram-scale cryogenic calorimeter operated above ground*, *Eur. Phys. J. C* **77** (2017), no. 9 637, [[arXiv:1707.06749](#)].
- [93] **DAMA** Collaboration, R. Bernabei et al., *First results from DAMA/LIBRA and the combined results with DAMA/NaI*, *Eur. Phys. J. C* **56** (2008) 333–355, [[arXiv:0804.2741](#)].
- [94] C. Savage, G. Gelmini, P. Gondolo, and K. Freese, *Compatibility of DAMA/LIBRA dark matter detection with other searches*, *JCAP* **04** (2009) 010, [[arXiv:0808.3607](#)].
- [95] **DAMIC** Collaboration, A. Aguilar-Arevalo et al., *Search for low-mass WIMPs in a 0.6 kg day exposure of the DAMIC experiment at SNOLAB*, *Phys. Rev. D* **94** (2016) 082006, [[arXiv:1607.07410](#)].
- [96] **DarkSide** Collaboration, P. Agnes et al., *DarkSide-50 532-day dark matter search with low-radioactivity argon*, *Phys. Rev. D* **98** (Nov., 2018) 102006.
- [97] **EDELWEISS** Collaboration, E. Armengaud et al., *Searching for low-mass dark matter particles with a massive Ge bolometer operated above-ground*, *Phys. Rev.* **D99** (2019), no. 8 082003, [[arXiv:1901.03588](#)].
- [98] **EDELWEISS** Collaboration, L. Hehn et al., *Improved EDELWEISS-III sensitivity for low-mass WIMPs using a profile likelihood approach*, *Eur. Phys. J. C* **76** (2016), no. 10 548, [[arXiv:1607.03367](#)].

- [99] **LUX** Collaboration, D. S. Akerib et al., *Results of a Search for Sub-GeV Dark Matter Using 2013 LUX Data*, *Phys. Rev. Lett.* **122** (2019), no. 13 131301, [[arXiv:1811.11241](#)].
- [100] **NEWS-G** Collaboration, Q. Arnaud et al., *First results from the NEWS-G direct dark matter search experiment at the LSM*, *Astropart. Phys.* **97** (2018) 54, [[arXiv:1706.04934](#)].
- [101] **SuperCDMS** Collaboration, R. Agnese et al., *Search for Low-Mass Weakly Interacting Massive Particles with SuperCDMS*, *Phys. Rev. Lett.* **112** (2014), no. 24 241302, [[arXiv:1402.7137](#)].
- [102] **XENON100** Collaboration, E. Aprile et al., *XENON100 Dark Matter Results from a Combination of 477 Live Days*, *Phys. Rev. D* **94** (2016), no. 12 122001, [[arXiv:1609.06154](#)].
- [103] **XENON** Collaboration, E. Aprile et al., *Dark Matter Search Results from a One Ton-Year Exposure of XENON1T*, *Phys. Rev. Lett.* **121** (2018), no. 11 111302, [[arXiv:1805.12562](#)].
- [104] F. Aubin et al., *Discrimination of nuclear recoils from alpha particles with superheated liquids*, *New J. Phys.* **10** (2008) 103017, [[arXiv:0807.1536](#)].
- [105] **PICO** Collaboration, C. Amole et al., *Dark Matter Search Results from the Complete Exposure of the PICO-60 C₃F₈ Bubble Chamber*, *Phys. Rev. D* **100** (2019), no. 2 022001, [[arXiv:1902.04031](#)].
- [106] **MIMAC** Collaboration, Q. Riffard et al., *First detection of radon progeny tracks by MIMAC*, *JINST* **12** (2017) P06021, [[arXiv:1504.05865](#)].
- [107] T. Ikeda et al., *Results of a directional dark matter search from the NEWAGE experiment*, *J. Phys.: Conf. Ser.* **1458** (2020) 012042.
- [108] **DMTPC** Collaboration, C. Deaconu et al., *Measurement of the directional sensitivity of DMTPC detectors*, *Phys. Rev. D* **95** (2017) 122002, [[arXiv:1705.05965](#)].
- [109] **DRIFT** Collaboration, J. B. R. Battat et al., *Low Threshold Results and Limits from the DRIFT Directional Dark Matter Detector*, *Astropart. Phys.* **91** (2017) 65, [[arXiv:1701.00171](#)].
- [110] S. E. Vahsen et al., *CYGNUS: Feasibility of a nuclear recoil observatory with directional sensitivity to dark matter and neutrinos*, [arXiv:2008.12587](#).
- [111] P. N. Luke et al., *Calorimetric ionization detector*, *Nucl. Instrum. Meth.* **A289** (1990) 406–409.
- [112] M. J. Dolan, F. Kahlhoefer, and C. McCabe, *Directly detecting sub-GeV dark matter with electrons from nuclear scattering*, *Phys. Rev. Lett.* **121** (2018), no. 10 101801, [[arXiv:1711.09906](#)].

- [113] B. Cabrera, L. M. Krauss, and F. Wilczek, *Bolometric Detection of Neutrinos*, *Phys. Rev. Lett.* **55** (1985) 25.
- [114] J. Monroe and P. Fisher, *Neutrino Backgrounds to Dark Matter Searches*, *Phys. Rev. D* **76** (2007) 033007, [[arXiv:0706.3019](#)].
- [115] L. E. Strigari, *Neutrino Coherent Scattering Rates at Direct Dark Matter Detectors*, *New J. Phys.* **11** (2009) 105011, [[arXiv:0903.3630](#)].
- [116] A. Gutlein et al., *Solar and atmospheric neutrinos: Background sources for the direct dark matter search*, *Astropart. Phys.* **34** (2010) 90–96, [[arXiv:1003.5530](#)].
- [117] **COHERENT** Collaboration, D. Akimov et al., *Observation of Coherent Elastic Neutrino-Nucleus Scattering*, *Science* **357** (2017), no. 6356 1123–1126, [[arXiv:1708.01294](#)].
- [118] **COHERENT** Collaboration, D. Akimov et al., *First Detection of Coherent Elastic Neutrino-Nucleus Scattering on Argon*, [arXiv:2003.10630](#).
- [119] D. Z. Freedman, *Coherent Neutrino Nucleus Scattering as a Probe of the Weak Neutral Current*, *Phys. Rev. D* **9** (1974) 1389–1392.
- [120] D. Z. Freedman, D. N. Schramm, and D. L. Tubbs, *The Weak Neutral Current and Its Effects in Stellar Collapse*, *Ann. Rev. Nucl. Part. Sci.* **27** (1977) 167–207.
- [121] A. Drukier and L. Stodolsky, *Principles and Applications of a Neutral Current Detector for Neutrino Physics and Astronomy*, .
- [122] L. Vietze, P. Klos, J. Menéndez, W. Haxton, and A. Schwenk, *Nuclear structure aspects of spin-independent WIMP scattering off xenon*, *Phys. Rev. D* **91** (2015), no. 4 043520, [[arXiv:1412.6091](#)].
- [123] J. N. Bahcall, A. M. Serenelli, and S. Basu, *New solar opacities, abundances, helioseismology, and neutrino fluxes*, *Astrophys. J. Lett.* **621** (2005) L85–L88, [[astro-ph/0412440](#)].
- [124] M. Honda, T. Kajita, K. Kasahara, and S. Midorikawa, *Improvement of low energy atmospheric neutrino flux calculation using the JAM nuclear interaction model*, *Phys. Rev. D* **83** (2011) 123001, [[arXiv:1102.2688](#)].
- [125] J. F. Beacom, *The Diffuse Supernova Neutrino Background*, *Ann. Rev. Nucl. Part. Sci.* **60** (2010) 439–462, [[arXiv:1004.3311](#)].
- [126] W. Haxton, R. Hamish Robertson, and A. M. Serenelli, *Solar Neutrinos: Status and Prospects*, *Ann. Rev. Astron. Astrophys.* **51** (2013) 21–61, [[arXiv:1208.5723](#)].
- [127] A. M. Serenelli, W. Haxton, and C. Pena-Garay, *Solar models with accretion. I. Application to the solar abundance problem*, *Astrophys. J.* **743** (2011) 24, [[arXiv:1104.1639](#)].

- [128] C. Pena-Garay and A. Serenelli, *Solar neutrinos and the solar composition problem*, [arXiv:0811.2424](#).
- [129] C. A. J. O’Hare et al., *Readout strategies for directional dark matter detection beyond the neutrino background*, *Phys. Rev.* **D92** (2015), no. 6 063518, [[arXiv:1505.08061](#)].
- [130] J. Billard, L. E. Strigari, and E. Figueroa-Feliciano, *Solar neutrino physics with low-threshold dark matter detectors*, *Phys. Rev. D* **91** (2015), no. 9 095023, [[arXiv:1409.0050](#)].
- [131] S. Mathimalar et al., *Characterization of neutron transmutation doped (NTD) Ge for low temperature sensor development*, *Nucl. Instrum. Meth.* **B345** (2015) 33–36, [[arXiv:1410.3934](#)].
- [132] **SuperCDMS** Collaboration, R. Agnese et al., *Energy Loss Due to Defect Formation from ^{206}Pb Recoils in SuperCDMS Germanium Detectors*, *Appl. Phys. Lett.* **113** (2018), no. 9 092101, [[arXiv:1805.09942](#)].
- [133] **EDELWEISS** Collaboration, A. Benoit et al., *Measurement of the response of heat-and-ionization germanium detectors to nuclear recoils*, *Nucl. Instrum. Meth. A* **577** (2007) 558–568, [[astro-ph/0607502](#)].
- [134] P. N. Luke, *Voltage-assisted calorimetric ionization detector*, *J. Appl. Phys.* **64** (1988), no. 6858 6858.
- [135] B. Neganov and V. Trofimov, *Colorimetric method measuring ionizing radiation*, *Otkryt. Izobret.* **146** (1985) 215.
- [136] D. Barker, W. Z. Wei, D. M. Mei, and C. Zhang, *Ionization Efficiency Study for Low Energy Nuclear Recoils in Germanium*, *Astropart. Phys.* **48** (2013) 8, [[arXiv:1304.6773](#)].
- [137] **SENSEI** Collaboration, O. Abramoff et al., *SENSEI: Direct-Detection Constraints on Sub-GeV Dark Matter from a Shallow Underground Run Using a Prototype Skipper-CCD*, *Phys. Rev. Lett.* **122** (2019), no. 16 161801, [[arXiv:1901.10478](#)].
- [138] **SuperCDMS** Collaboration, R. Agnese et al., *First Dark Matter Constraints from a SuperCDMS Single-Charge Sensitive Detector*, *Phys. Rev. Lett.* **121** (2018), no. 5 051301, [[arXiv:1804.10697](#)]. [erratum: *Phys. Rev. Lett.* 122, no. 6, 069901 (2019)].
- [139] **DAMIC** Collaboration, A. Aguilar-Arevalo et al., *Constraints on Light Dark Matter Particles Interacting with Electrons from DAMIC at SNOLAB*, *Phys. Rev. Lett.* **123** (2019), no. 18 181802, [[arXiv:1907.12628](#)].
- [140] I. M. Bloch, R. Essig, K. Tobioka, T. Volansky, and T.-T. Yu, *Searching for Dark Absorption with Direct Detection Experiments*, *JHEP* **06** (2017) 087, [[arXiv:1608.02123](#)].

- [141] **DarkSide** Collaboration, P. Agnes et al., *Constraints on Sub-GeV Dark-Matter–Electron Scattering from the DarkSide-50 Experiment*, *Phys. Rev. Lett.* **121** (2018), no. 11 111303, [[arXiv:1802.06998](#)].
- [142] H. An, M. Pospelov, and J. Pradler, *New stellar constraints on dark photons*, *Phys. Lett. B* **725** (2013) 190–195, [[arXiv:1302.3884](#)].
- [143] J. Redondo and G. Raffelt, *Solar constraints on hidden photons re-visited*, *JCAP* **08** (2013) 034, [[arXiv:1305.2920](#)].
- [144] **EDELWEISS** Collaboration, Q. Arnaud et al., *First germanium-based constraints on sub-MeV Dark Matter with the EDELWEISS experiment*, [arXiv:2003.01046](#).
- [145] **EDELWEISS** Collaboration, E. Armengaud et al., *Measurement of the cosmogenic activation of germanium detectors in EDELWEISS-III*, *Astropart. Phys.* **91** (2017) 51–64, [[arXiv:1607.04560](#)].
- [146] **EDELWEISS** Collaboration, E. Armengaud et al., *Searches for electron interactions induced by new physics in the EDELWEISS-III Germanium bolometers*, *Phys. Rev.* **D98** (2018), no. 8 082004, [[arXiv:1808.02340](#)].
- [147] A. Juillard et al., *Low-noise HEMTs for Coherent Elastic Neutrino Scattering and Low-Mass Dark Matter Cryogenic Semiconductor Detectors*, in *18th International Workshop on Low Temperature Detectors (LTD 18) Milano, Italy, July 22-26, 2019*, 2019. [arXiv:1909.02879](#).
- [148] G. D. Starkman, A. Gould, R. Esmailzadeh, and S. Dimopoulos, *Opening the Window on Strongly Interacting Dark Matter*, *Phys. Rev. D* **41** (1990) 3594.
- [149] J. Collar and F. Avignone, *Diurnal modulation effects in cold dark matter experiments*, *Phys. Lett. B* **275** (1992) 181–185.
- [150] J. Collar and I. Avignone, F.T., *The Effect of elastic scattering in the Earth on cold dark matter experiments*, *Phys. Rev. D* **47** (1993) 5238–5246.
- [151] F. Hasenbalg, D. Abriola, F. Avignone, et al., *Cold dark matter identification: Diurnal modulation revisited*, *Phys. Rev. D* **55** (1997) 7350–7355, [[astro-ph/9702165](#)].
- [152] C. Kouvaris and I. M. Shoemaker, *Daily modulation as a smoking gun of dark matter with significant stopping rate*, *Phys. Rev. D* **90** (2014) 095011, [[arXiv:1405.1729](#)].
- [153] C. Kouvaris, *Earth’s stopping effect in directional dark matter detectors*, *Phys. Rev. D* **93** (2016), no. 3 035023, [[arXiv:1509.08720](#)].
- [154] R. Bernabei et al., *Investigating Earth shadowing effect with DAMA/LIBRA-phase1*, *Eur. Phys. J. C* **75** (2015), no. 5 239, [[arXiv:1505.05336](#)].
- [155] B. J. Kavanagh, R. Catena, and C. Kouvaris, *Signatures of Earth-scattering in the direct detection of Dark Matter*, *JCAP* **01** (2017) 012, [[arXiv:1611.05453](#)].

- [156] Y. Hochberg, E. Kuflik, T. Volansky, and J. G. Wacker, *Mechanism for Thermal Relic Dark Matter of Strongly Interacting Massive Particles*, *Phys. Rev. Lett.* **113** (2014) 171301, [[arXiv:1402.5143](#)].
- [157] Y. Hochberg, E. Kuflik, H. Murayama, T. Volansky, and J. G. Wacker, *Model for Thermal Relic Dark Matter of Strongly Interacting Massive Particles*, *Phys. Rev. Lett.* **115** (2015), no. 2 021301, [[arXiv:1411.3727](#)].
- [158] I. F. Albuquerque and L. Baudis, *Direct detection constraints on superheavy dark matter*, *Phys. Rev. Lett.* **90** (2003) 221301, [[astro-ph/0301188](#)]. [Erratum: *Phys.Rev.Lett.* 91, 229903 (2003)].
- [159] J. H. Davis, *Probing Sub-GeV Mass Strongly Interacting Dark Matter with a Low-Threshold Surface Experiment*, *Phys. Rev. Lett.* **119** (2017), no. 21 211302, [[arXiv:1708.01484](#)].
- [160] B. J. Kavanagh, *Earth scattering of superheavy dark matter: Updated constraints from detectors old and new*, *Phys. Rev. D* **97** (2018), no. 12 123013, [[arXiv:1712.04901](#)].
- [161] J. Vergados and H. Ejiri, *The role of ionization electrons in direct neutralino detection*, *Phys. Lett. B* **606** (2005) 313–322, [[hep-ph/0401151](#)].
- [162] C. Moustakidis, J. Vergados, and H. Ejiri, *Direct dark matter detection by observing electrons produced in neutralino-nucleus collisions*, *Nucl. Phys. B* **727** (2005) 406–420, [[hep-ph/0507123](#)].
- [163] R. Bernabei et al., *On electromagnetic contributions in WIMP quests*, *Int. J. Mod. Phys. A* **22** (2007) 3155–3168, [[arXiv:0706.1421](#)].
- [164] R. Maisonobe, J. Billard, M. De Jesus, et al., *Vibration decoupling system for massive bolometers in dry cryostats*, *JINST* **13** (2018), no. 08 T08009, [[arXiv:1803.03463](#)].
- [165] M. Pyle, E. Feliciano-Figueroa, and B. Sadoulet, *Optimized Designs for Very Low Temperature Massive Calorimeters*, [arXiv:1503.01200](#).
- [166] E. Olivieri, J. Billard, M. De Jesus, A. Juillard, and A. Leder, *Vibrations on pulse tube based Dry Dilution Refrigerators for low noise measurements*, *Nucl. Instrum. Meth. A* **858** (2017) 73–79, [[arXiv:1703.08957](#)].
- [167] J. Billard, M. De Jesus, A. Juillard, and E. Queguiner, *Characterization and Optimization of EDELWEISS-III FID800 Heat Signals*, *J. Low Temp. Phys.* **184** (2016), no. 1-2 299–307.
- [168] S. Di Domizio, F. Orio, and M. Vignati, *Lowering the energy threshold of large-mass bolometric detectors*, *JINST* **6** (2011) P02007, [[arXiv:1012.1263](#)].
- [169] **SuperCDMS** Collaboration, R. Agnese et al., *Low-mass dark matter search with CDMSlite*, *Phys. Rev. D* **97** (2018), no. 2 022002, [[arXiv:1707.01632](#)].

- [170] **CRESST** Collaboration, G. Angloher et al., *Results on light dark matter particles with a low-threshold CRESST-II detector*, *Eur. Phys. J. C* **76** (2016), no. 1 25, [[arXiv:1509.01515](#)].
- [171] **DarkSide** Collaboration, P. Agnes et al., *Low-Mass Dark Matter Search with the DarkSide-50 Experiment*, *Phys. Rev. Lett.* **121** (2018), no. 8 081307, [[arXiv:1802.06994](#)].
- [172] **NEWS-G** Collaboration, Q. Arnaud et al., *First results from the NEWS-G direct dark matter search experiment at the LSM*, *Astropart. Phys.* **97** (2018) 54–62, [[arXiv:1706.04934](#)].
- [173] A. L. Erickcek, P. J. Steinhardt, D. McCammon, and P. C. McGuire, *Constraints on the Interactions between Dark Matter and Baryons from the X-ray Quantum Calorimetry Experiment*, *Phys. Rev. D* **76** (2007) 042007, [[arXiv:0704.0794](#)].
- [174] D. Hooper and S. D. McDermott, *Robust Constraints and Novel Gamma-Ray Signatures of Dark Matter That Interacts Strongly With Nucleons*, *Phys. Rev. D* **97** (2018), no. 11 115006, [[arXiv:1802.03025](#)].
- [175] T. Emken and C. Kouvaris, *How blind are underground and surface detectors to strongly interacting Dark Matter?*, *Phys. Rev. D* **97** (2018), no. 11 115047, [[arXiv:1802.04764](#)].
- [176] T. Emken and C. Kouvaris, *DaMaSCUS: The Impact of Underground Scatterings on Direct Detection of Light Dark Matter*, *JCAP* **10** (2017) 031, [[arXiv:1706.02249](#)].
- [177] M. S. Mahdawi and G. R. Farrar, *Closing the window on \sim GeV Dark Matter with moderate ($\sim \mu$ b) interaction with nucleons*, *JCAP* **12** (2017) 004, [[arXiv:1709.00430](#)].
- [178] M. S. Mahdawi and G. R. Farrar, *Energy loss during Dark Matter propagation in an overburden*, [arXiv:1712.01170](#).
- [179] M. S. Mahdawi and G. R. Farrar, *Constraints on Dark Matter with a moderately large and velocity-dependent DM-nucleon cross-section*, *JCAP* **10** (2018) 007, [[arXiv:1804.03073](#)].
- [180] A. Gould, *Direct and Indirect Capture of Wimps by the Earth*, *Astrophys. J.* **328** (1988) 919–939.
- [181] G. D. Mack, J. F. Beacom, and G. Bertone, *Towards Closing the Window on Strongly Interacting Dark Matter: Far-Reaching Constraints from Earth’s Heat Flow*, *Phys. Rev. D* **76** (2007) 043523, [[arXiv:0705.4298](#)].
- [182] C. Kouvaris and N. G. Nielsen, *Daily modulation and gravitational focusing in direct dark matter search experiments*, *Phys. Rev. D* **92** (2015), no. 7 075016, [[arXiv:1505.02615](#)].

- [183] V. Gluscevic and K. K. Boddy, *Constraints on Scattering of keV–TeV Dark Matter with Protons in the Early Universe*, *Phys. Rev. Lett.* **121** (2018), no. 8 081301, [[arXiv:1712.07133](#)].
- [184] **LUX** Collaboration, D. Akerib et al., *Limits on spin-dependent WIMP-nucleon cross section obtained from the complete LUX exposure*, *Phys. Rev. Lett.* **118** (2017), no. 25 251302, [[arXiv:1705.03380](#)].
- [185] **XENON** Collaboration, E. Aprile et al., *Constraining the spin-dependent WIMP-nucleon cross sections with XENON1T*, *Phys. Rev. Lett.* **122** (2019), no. 14 141301, [[arXiv:1902.03234](#)].
- [186] **PandaX-II** Collaboration, C. Fu et al., *Spin-Dependent Weakly-Interacting-Massive-Particle–Nucleon Cross Section Limits from First Data of PandaX-II Experiment*, *Phys. Rev. Lett.* **118** (2017), no. 7 071301, [[arXiv:1611.06553](#)]. [Erratum: *Phys.Rev.Lett.* 120, 049902 (2018)].
- [187] P. Klos, J. Menéndez, D. Gazit, and A. Schwenk, *Large-scale nuclear structure calculations for spin-dependent WIMP scattering with chiral effective field theory currents*, *Phys. Rev. D* **88** (2013), no. 8 083516, [[arXiv:1304.7684](#)]. [Erratum: *Phys.Rev.D* 89, 029901 (2014)].
- [188] I. F. Albuquerque and C. Perez de los Heros, *Closing the Window on Strongly Interacting Dark Matter with IceCube*, *Phys. Rev. D* **81** (2010) 063510, [[arXiv:1001.1381](#)].
- [189] G. D. Mack and A. Manohar, *Closing the window on high-mass strongly interacting dark matter*, *J. Phys. G* **40** (2013) 115202, [[arXiv:1211.1951](#)].
- [190] A. Bhoonah, J. Bramante, F. Elahi, and S. Schon, *Calorimetric Dark Matter Detection With Galactic Center Gas Clouds*, *Phys. Rev. Lett.* **121** (2018), no. 13 131101, [[arXiv:1806.06857](#)].
- [191] A. Bhoonah, J. Bramante, F. Elahi, and S. Schon, *Galactic Center gas clouds and novel bounds on ultralight dark photon, vector portal, strongly interacting, composite, and super-heavy dark matter*, *Phys. Rev. D* **100** (2019), no. 2 023001, [[arXiv:1812.10919](#)].
- [192] R. H. Cyburt, B. D. Fields, V. Pavlidou, and B. D. Wandelt, *Constraining strong baryon dark matter interactions with primordial nucleosynthesis and cosmic rays*, *Phys. Rev. D* **65** (2002) 123503, [[astro-ph/0203240](#)].
- [193] **CONNIE** Collaboration, A. Aguilar-Arevalo et al., *The CONNIE experiment*, *J. Phys. Conf. Ser.* **761** (2016), no. 1 012057, [[arXiv:1608.01565](#)].
- [194] **TEXONO** Collaboration, S. Kerman, V. Sharma, M. Deniz, et al., *Coherency in Neutrino-Nucleus Elastic Scattering*, *Phys. Rev. D* **93** (2016), no. 11 113006, [[arXiv:1603.08786](#)].

- [195] V. Belov et al., *The ν GeN experiment at the Kalinin Nuclear Power Plant*, *JINST* **10** (2015), no. 12 P12011.
- [196] **CONUS** Collaboration, H. Bonet et al., *First constraints on elastic neutrino nucleus scattering in the fully coherent regime from the Conus experiment*, [arXiv:2011.00210](#).
- [197] **MINER** Collaboration, G. Agnolet et al., *Background Studies for the MINER Coherent Neutrino Scattering Reactor Experiment*, *Nucl. Instrum. Meth. A* **853** (2017) 53–60, [[arXiv:1609.02066](#)].
- [198] R. Strauss et al., *The ν -cleus experiment: A gram-scale fiducial-volume cryogenic detector for the first detection of coherent neutrino-nucleus scattering*, *Eur. Phys. J. C* **77** (2017) 506, [[arXiv:1704.04320](#)].
- [199] B. Julien, *Probing new physics with Ricochet*, in *18th International Workshop on Low Temperature Detectors (LTD 18) Milano, Italy, July 22-26, 2019*, 2019.
- [200] **NUCLEUS** Collaboration, G. Angloher et al., *Exploring $CE\nu NS$ with NUCLEUS at the Chooz nuclear power plant*, *Eur. Phys. J. C* **79** (2019), no. 12 1018, [[arXiv:1905.10258](#)].
- [201] A. Leder et al., *Unfolding Neutron Spectrum with Markov Chain Monte Carlo at MIT Research Reactor with He-3 Neutral Current Detectors*, *JINST* **13** (2018), no. 02 P02004, [[arXiv:1710.00802](#)].
- [202] **Ricochet** Collaboration, J. Billard et al., *Coherent Neutrino Scattering with Low Temperature Bolometers at Chooz Reactor Complex*, *J. Phys. G* **44** (2017), no. 10 105101, [[arXiv:1612.09035](#)].
- [203] **STEREO** Collaboration, N. Allemandou et al., *The STEREO Experiment*, *JINST* **13** (2018), no. 07 P07009, [[arXiv:1804.09052](#)].
- [204] J. Billard, J. Johnston, and B. J. Kavanagh, *Prospects for exploring New Physics in Coherent Elastic Neutrino-Nucleus Scattering*, *JCAP* **11** (2018) 016, [[arXiv:1805.01798](#)].
- [205] G. Heusser, M. Weber, J. Hakenmüller, et al., *GIOVE - A new detector setup for high sensitivity germanium spectroscopy at shallow depth*, *Eur. Phys. J. C* **75** (2015), no. 11 531, [[arXiv:1507.03319](#)].
- [206] A. Beda, V. Brudanin, V. Egorov, et al., *Gemma experiment: The results of neutrino magnetic moment search*, *Phys. Part. Nucl. Lett.* **10** (2013) 139–143.
- [207] M. Lindner, B. Radovčić, and J. Welter, *Revisiting Large Neutrino Magnetic Moments*, *JHEP* **07** (2017) 139, [[arXiv:1706.02555](#)].
- [208] E. Bertuzzo, F. F. Deppisch, S. Kulkarni, Y. F. Perez Gonzalez, and R. Zukanovich Funchal, *Dark Matter and Exotic Neutrino Interactions in Direct Detection Searches*, [arXiv:1701.07443](#). [Erratum: *JHEP* 04, 073 (2017)].

- [209] **APEX** Collaboration, S. Abrahamyan et al., *Search for a New Gauge Boson in Electron-Nucleus Fixed-Target Scattering by the APEX Experiment*, *Phys. Rev. Lett.* **107** (2011) 191804, [[arXiv:1108.2750](#)].
- [210] **ATLAS** Collaboration, M. Aaboud et al., *Search for high-mass new phenomena in the dilepton final state using proton-proton collisions at $\sqrt{s} = 13$ TeV with the ATLAS detector*, *Phys. Lett. B* **761** (2016) 372–392, [[arXiv:1607.03669](#)].
- [211] **CMS** Collaboration, V. Khachatryan et al., *Search for narrow resonances in dilepton mass spectra in proton-proton collisions at $\sqrt{s} = 13$ TeV and combination with 8 TeV data*, *Phys. Lett. B* **768** (2017) 57–80, [[arXiv:1609.05391](#)].
- [212] A. Friedland, M. L. Graesser, I. M. Shoemaker, and L. Vecchi, *Probing Nonstandard Standard Model Backgrounds with LHC Monojets*, *Phys. Lett. B* **714** (2012) 267–275, [[arXiv:1111.5331](#)].
- [213] **CHARM** Collaboration, J. Dorenbosch et al., *Experimental Verification of the Universality of ν_e and ν_μ Coupling to the Neutral Weak Current*, *Phys. Lett. B* **180** (1986) 303–307.
- [214] J. Barranco, O. Miranda, and T. Rashba, *Low energy neutrino experiments sensitivity to physics beyond the Standard Model*, *Phys. Rev. D* **76** (2007) 073008, [[hep-ph/0702175](#)].
- [215] P. Coloma and T. Schwetz, *Generalized mass ordering degeneracy in neutrino oscillation experiments*, *Phys. Rev. D* **94** (2016), no. 5 055005, [[arXiv:1604.05772](#)]. [Erratum: *Phys.Rev.D* 95, 079903 (2017)].
- [216] **LSND** Collaboration, A. Aguilar-Arevalo et al., *Evidence for neutrino oscillations from the observation of $\bar{\nu}_e$ appearance in a $\bar{\nu}_\mu$ beam*, *Phys. Rev. D* **64** (2001) 112007, [[hep-ex/0104049](#)].
- [217] A. Studenikin and P. Pustoshny, *Neutrino evolution accounting for the longitudinal and transversal magnetic matter currents*, *PoS ICHEP2018* (2019) 927.
- [218] **Double Chooz** Collaboration, A. Onillon, *Reactor and Antineutrino Spectrum Calculations for the Double Chooz First Phase Results*, *Nucl. Data Sheets* **120** (2014) 153–156.
- [219] T. Mueller et al., *Improved Predictions of Reactor Antineutrino Spectra*, *Phys. Rev. C* **83** (2011) 054615, [[arXiv:1101.2663](#)].
- [220] P. Barbeau, J. Collar, and P. Whaley, *Design and Characterization of a Neutron Calibration Facility for the Study of sub-keV Nuclear Recoils*, *Nucl. Instrum. Meth. A* **574** (2007) 385–391, [[nucl-ex/0701011](#)].
- [221] T. Joshi, S. Sangiorgio, V. Mozin, et al., *Design and demonstration of a quasi-monoenergetic neutron source*, *Nucl. Instrum. Meth. B* **333** (2014) 6–11, [[arXiv:1403.1285](#)].

- [222] N. Coron et al., *Measurement of the differential neutron flux inside a lead shielding in a cryogenic experiment*, *J. Phys. Conf. Ser.* **375** (2012) 012018.
- [223] E. Armengaud et al., *Development of ^{100}Mo -containing scintillating bolometers for a high-sensitivity neutrinoless double-beta decay search*, *Eur. Phys. J. C* **77** (2017), no. 11 785, [[arXiv:1704.01758](#)].
- [224] A. E. Robinson, *The Coherent Photon Scattering Background in Sub-GeV/c² Direct Dark Matter Searches*, *Phys. Rev. D* **95** (2017), no. 2 021301, [[arXiv:1610.07656](#)]. [Erratum: *Phys.Rev.D* 95, 069907 (2017)].
- [225] M. Kreuz et al., *A Method to measure the resonance transitions between the gravitationally bound quantum states of neutrons in the GRANIT spectrometer*, *Nucl. Instrum. Meth. A* **611** (2009) 326, [[arXiv:0902.0156](#)].
- [226] H. Börner, *Precision Gamma-Ray Spectroscopy at the Institut Laue Langevin*, *AIP Conf. Proc.* **819** (2006), no. 1 511.
- [227] J. Goupy et al., *Contact-less phonon detection with massive cryogenic absorbers*, *Appl. Phys. Lett.* **115** (2019), no. 22 223506, [[arXiv:1906.10397](#)].
- [228] D. Misiak, *Semiconductor cryogenic bolometer optimization for low-energy neutrino physics*. PhD thesis, Lyon University, 2021.
- [229] M. Galeazzi and D. McCammon, *A microcalorimeter and bolometer model*, *J. Appl. Phys.* **93** (2003) 4856, [[astro-ph/0304397](#)].
- [230] K. D. Irwin, *Phonon-mediated particle detection using superconducting tungsten transition-edge sensors*. PhD thesis, Stanford U., 1995.
- [231] W. Shockley, *Currents to conductors induced by a moving point charge*, *J. Appl. Phys.* **9** (1938), no. 10 635–636.
- [232] S. Ramo, *Currents induced by electron motion*, *Proc. Ire.* **27** (1939) 584–585.
- [233] **EDELWEISS** Collaboration, Q. Arnaud et al., *Signals induced by charge-trapping in EDELWEISS FID detectors: analytical modeling and applications*, *JINST* **11** (2016), no. 10 P10008, [[arXiv:1606.08097](#)].
- [234] K. McCarthy, *Detector Simulation and WIMP Search Analysis for the Cryogenic Dark Matter Search Experiment*. PhD thesis, Massachusetts Institute of Technology, 2013.
- [235] S. Marnieros, *Détecteurs cryogéniques et leurs applications en Astrophysique et Astroparticules*. PhD thesis, Université Paris Sud, 2014.
- [236] N. Kurinsky, D. Baxter, Y. Kahn, and G. Krnjaic, *Dark matter interpretation of excesses in multiple direct detection experiments*, *Phys. Rev. D* **102** (2020), no. 1 015017, [[arXiv:2002.06937](#)].

- [237] S. Caparrelli, E. Majorana, V. Moscatelli, et al., *Vibration-free cryostat for low-noise applications of a pulse tube cryocooler*, *Rev. Sci. Instrum.* **77** (2006), no. 9 095102.
- [238] A. van Haan, G. Wijts, F. Galli, et al., *Atomic resolution scanning tunneling microscopy in a cryogen free dilution refrigerator at 15 mK*, *Rev. Sci. Instrum.* **85** (2014) 035112, [[arXiv:1312.6011](#)].
- [239] A. D’Addabbo, C. Bucci, L. Canonica, et al., *An active noise cancellation technique for the CUORE Pulse Tube Cryocoolers*, *Cryogenics* **93** (2018) 56–65, [[arXiv:1712.02753](#)].
- [240] S. Pirro, *Further developments in mechanical decoupling of large thermal detectors*, *Nucl. Instrum. Meth. A* **559** (2006) 672–674.
- [241] **CUORE** Collaboration, C. Ligi et al., *The CUORE Cryostat: A 1-Ton Scale Setup for Bolometric Detectors*, *J. Low Temp. Phys.* **184** (2016), no. 3-4 590–596, [[arXiv:1603.03306](#)].
- [242] **CUORE** Collaboration, D. Santone et al., *The CUORE cryostat and its bolometric detector*, *JINST* **12** (2017), no. 02 C02055.
- [243] M. Pelliccione, A. Sciambi, J. Bartel, A. Keller, and D. Goldhaber-Gordon, *Design of a scanning gate microscope in a cryogen-free dilution refrigerator*, *Rev. Sci. Instrum.* **84** (2013) 033703, [[arXiv:1211.6546](#)].
- [244] R. F. Barron, *Cryogenic Systems, 2nd Edition, 1985*, .
- [245] **SuperCDMS** Collaboration, D. Amaral et al., *Constraints on low-mass, relic dark matter candidates from a surface-operated SuperCDMS single-charge sensitive detector*, [arXiv:2005.14067](#).
- [246] **SuperCDMS** Collaboration, I. Alkhatib et al., *Light Dark Matter Search with a High-Resolution Athermal Phonon Detector Operated Above Ground*, [arXiv:2007.14289](#).
- [247] J. Schieck et al., *Direct Dark Matter Search with the CRESST II Experiment*, *PoS ICHEP2016* (2016) 217, [[arXiv:1611.02113](#)].
- [248] R. Strauss et al., *A prototype detector for the CRESST-III low-mass dark matter search*, *Nucl. Instrum. Meth. A* **845** (2017) 414–417, [[arXiv:1802.08639](#)].
- [249] R. Strauss et al., *Gram-scale cryogenic calorimeters for rare-event searches*, *Phys. Rev. D* **96** (2017), no. 2 022009, [[arXiv:1704.04317](#)].
- [250] Q. Dong, *HEMTs Cryogéniques à faible puissance dissipée et à bas bruit*. PhD thesis, Université Paris Sud, 2013.
- [251] L. Torres, C. Arcambal, C. Delisle, et al., *First Measurement of the Intrinsic Noise of a HEMT at Sub-Kelvin Temperatures*, *J. Low Temp. Phys.* **184** (2016), no. 1-2 466–472.

- [252] A. Phipps, A. Juillard, B. Sadoulet, B. Serfass, and Y. Jin, *A HEMT-Based Cryogenic Charge Amplifier with sub-100 eVee Ionization Resolution for Massive Semiconductor Dark Matter Detectors*, *Nucl. Instrum. Meth. A* **940** (2019) 181–184, [[arXiv:1611.09712](#)].

